TFBP-TR-194

for U.S. Nuclear Regulatory Commission

FRAP-T3 — A COMPUTER CODE FOR THE TRANSIENT ANALYSIS OF OXIDE FUEL RODS

August 1977

EG&G Idaho, Inc.

IDAHO NATIONAL ENGINEERING LABORATORY

ENERGY RESEARCH AND DEVELOPMENT ADMINISTRATION

IDAHO OPERATIONS OFFICE UNDER CONTRACT EY-76-C-07-1570

70-624

TFBP-TR-194

FRAP-T3 -- A COMPUTER CODE FOR THE TRANSIENT ANALYSIS OF OXIDE FUEL RODS

Approved:

J. A. Dearien, Manager
FARAD Branch

J. G. Crocker, Manager
Thermal Fuels Behavior Division

ABSTRACT

Fuel Rod Analysis Program - Transient (FRAP-T3) is a FORTRAN IV computer code which can be used to solve for the transient response of a light water reactor fuel rod during accidents such as a loss-of-coolant accident or a power-cooling-mismatch. The coupled effects of mechanical, thermal, internal gas, and material property response on the behavior of the fuel rod are considered. The phenomena modeled by the code include: (1) heat conduction, (2) elastic-plastic cladding deformation, (3) fuel-cladding mechanical interaction, (4) transient fuel rod gas pressure, (5) heat transfer between fuel and cladding, (6) cladding oxidations, and (7) heat transfer from cladding to coolant.

FRAP-T3 is coupled to a material property subcode, MATPRO, which is used to provide gas, fuel, and cladding properties to the FRAP-T computational subcodes. No material properties need to be supplied by the code user. The needed water properties are obtained from the 1967 ASME steam tables, which are linked to the code. Critical heat flux and heat transfer correlations for a wide range of coolant conditions are contained in modular subroutines.

FRAP-T is a modular code with each major computational model isolated within the code and coupled to the main code by subroutine calls and data transfer through argument lists. The argument lists are completely defined by comment statements at the beginning of each subroutine.

The code is presently programmed and running on the CDC 7600 computer.

This volume consists of two reports. Report I describes the analytical models and the input user's manual of the third version of the FRAP-T code, which is designated FRAP-T3. Whenever the designation FRAP-T appears, FRAP-T3 is implied. Report II describes the analytical verification of the code.

REPORT I

FRAP-T3 ANALYTICAL MODELS AND INPUT MANUAL

John A. Dearien
Larry J. Siefken
Michael P. Bohn

CONTENTS

FIGURES

FIGURES (continued)

FIGURES (continued)

TABLES

TABLES (continued)

FRAP-T3 ANALYTICAL MODELS AND INPUT MANUAL

I. INTRODUCTION

Fuel Rod Analysis Program - Transient (FRAP-T) is a FORTRAN IV computer code developed to describe the transient behavior of nuclear fuel rods during accidents such as a loss-of-coolant accident (LOCA) and a power-cooling-mismatch (PCM). FRAP-T includes the coupled effects of thermal, mechanical, internal gas, and material properties in the analysis of fuel rod transient behavior. This code is part of a continuing development program by the Nuclear Regulatory Commission designed to produce analytical tools for accurate prediction of nuclear reactor system behavior during normal and abnormal operating conditions. The code described in this report (FRAP-T MOD003) is the third of a series of fuel rod codes planned for release at one year intervals, with each succeeding version incorporating the advancements made in fuel rod response analysis models during that year. Wherever the designation FRAP-T appears, FRAP-T3 is implied. The code is presently programmed and running on the CDC 7600 computer. A steady state fuel rod analysis code, FRAP-S[1], is being developed at EG&G Idaho, Inc., to generate the steady state operating parameters required as initial conditions to FRAP-T. Both codes are being developed with common subcodes and compatible input-output features.

FRAP-T is a modular code with each type of computation and analytical model, such as internal gas pressure, being in a separate module or subroutine. This configuration is designed to allow maximum flexibility in developing and modifying the code with minimum impact on the unmodified portion of the code.

A major portion of FRAP-T is the subcode MATPRO[2]. This subcode is comprised of modular function subprograms and subroutines which define the material properties required by the computational subcodes of FRAP-T. Each function subprogram or subroutine defines only one material property.

The developmental process of FRAP-T includes a verification effort[3] designed to test the analytical capability of the code. Experimental data on fuel rod response parameters such as centerline temperature and cladding deformation are compared with FRAP-T calculated values.

A configuration control procedure is used at EG&G Idaho, Inc., to maintain FRAP-T as a consistent, completely defined tool. This configuration control consists of maintaining a file on all changes to the code and identifying the code by version number on all output.

This report describes the fuel rod response parameters considered and how the code operates (Section II), the individual computational models in the code (Section III), and the numerical techniques involved in obtaining the analytical solution (Section IV). Appendices to the report include a description of the input requirements and sample problem to illustrate code operation and output features.

II. PROGRAM SUMMARY DESCRIPTION

1. PURPOSE

The FRAP-T code is designed to predict the response of light water nuclear reactor fuel rods to changes in reactor power and coolant flow. The code will predict the state of fuel rods during loss of coolant accidents, power-cooling-mismatch accidents, reactivity initiated accidents (RIA), and flow blockage accidents. The code is restricted to analysis of fuel rods containing oxide fuel and zirconium alloy cladding. The code can be applied to other types of fuel rods by linking a different material properties package to the code. The code is restricted to analysis of fuel rods cooled by water. To apply the code to another type of coolant, a different coolant properties package and heat transfer correlation package must be inserted into the code.

FRAP-T prints or plots the following fuel rod variables as a function of time:

(1) Fuel rod radial temperature distribution at an arbitrary number of axial positions

(2) Fuel OD, gas gap thickness, and cladding OD at an arbitrary number of axial positions

(3) Length change of fuel stack and cladding

(4) Pressure of internal fuel rod gas

(5) Time and location of cladding rupture

(6) Cladding surface heat transfer coefficient

(7) Critical heat flux at fuel rod surface

(8) Gas gap heat transfer coefficient.

2. FUEL ROD ANALYTICAL MODELS

FRAP-T has analytical models for the following components of fuel rod behavior:

(1) Radial and azimuthal heat conduction

(2) Internal fuel rod gas pressure

(3) Fuel stack length change

(4) Fuel stack diameter change

(5) Transient plenum gas temperature

(6) Elastic-plastic fuel cladding interaction

(7) Local ballooning of cladding

(8) Cladding length change

(9) Cladding diameter change

(10) The following modes of heat transfer from fuel rod surface:

(a) Forced convection to liquid

(b) Nucleate boiling

(c) Forced convection vaporization

(d) Flow transition boiling

(e) Flow film boiling

(f) Pool transition boiling

(g) Pool film boiling

(h) Forced convection to gas

(i) Low pressure film boiling

(j) Radiation heat transfer.

(11) Flow of gas between plenum and gas gap

(12) Conductance of open and closed gas gaps

(13) Cladding oxidation

(14) Fuel and cladding melting

(15) Effect on heat transfer of change in area of cladding surface exposed to coolant

(16) Failure of cladding

All of the analytical models listed above are coupled in the solution process.

3. PROGRAMMING FEATURES

3.1 Programming of Analytical Models

FRAP-T is programmmed so that each basic component of fuel rod behavior is computed by a modular subcode. Separate subcodes calculate response for each of the following:

(1) Temperature distribution

(2) Cladding surface temperature; this subcode contains heat transfer and critical heat flux correlations

(3) Coolant conditions

(4) Heat generation in fuel

(5) Gap heat transfer coefficient

(6) Internal fuel rod pressure

(7) Deformation

(8) Plenum gas temperature

(9) Cladding failure

(10) Cladding ballooning

(11) Cladding oxidation.

The subroutines composing each of the subcodes are listed in Table I.

3.2 Link to Material Properties Package

FRAP-T is linked to a modular material properties package, MATPRO-9. This package contains correlations for all fuel, cladding, and gas properties needed by the code. Each correlation is contained in a separate function subprogram or subroutine. No material properties need to be specified by the code user. The cladding properties obtained from MATPRO-9 and the parameters the properties are correlated with are shown in Table II. Similarly, the fuel and gas properties obtained from MATPRO-9 are shown in Tables III and IV, respectively. The tables also show the name of the function or subroutine in MATPRO-9 which computes each listed property.

TABLE I

SUBROUTINES COMPOSING SUBCODES

Surface Temperature Subcode	Gap Conductance Subcode	Temperature Calculation Subcode	Fuel Rod Deformation Subcode	Gas Pressure Subcode	Coolant Condition Subcode	Plenum Temperature Subcode	Heat Generation Subcode
HTRC	GAPHTC	HT1SST	FRACAS	GSFLOW	COOL	PLNT	POWR
PCHF	GAPHTR	HT1TDP	CLADF	GAPPRS			PAZAV
QDOT	EMSSF2	HT1INP	CLOSE	GPRINP			
PROFAC	GPCINP	MADATA	COUPLE				
ROOT1		THMPRP	CYLDST				
SURFBC		ARYMDI	DEPCAL				
VISC		ASET	FCMI				
VOID		ASTOR	GAPT				
THCON		IDXGN1	REPACK				
EMSSF1		IDXGN2	STACK				
SLIPR		KTABLE	STRAIN				
SLP2		QCON	STRESS				
		STARTI	SWLCHK				
		TZSET	VSWELL				

TABLE I (continued)

Cladding Ballooning Subcode	Cladding Failure Subcode	Metal-Water Reaction Subcode
BALOON	FRAIL	CHITOX
RADII	BDTR	
WRITE	BFRAC	
	CDTR	
	CRERUP	
	DFRAC	
	DLGAM	
	EVMELT	
	FSIGT	
	FSTEMP	
	FSTRS	
	HCFF	
	LCFF	
	MELT	
	NDTR	

TABLE II

CLADDING MATERIAL PROPERTY CORRELATIONS USED BY FRAP-T3

Property	Function or Subroutine Name	Independent Variables in Correlation
Axial thermal expansion	CATHEX	Temperature
Diametrical thermal expansion	CDTHEX	Temperature
Heat capacity	CCP	Temperature
Thermal conductivity	CTHCON	Temperature
Zirconium oxide emissivity	ZØEMIS	Temperature
Elastic modulus	CELMØD	Temperature
Meyer hardness	CMHARD	Temperature
Poisson ratio	CPØIR	Temperature
Uniaxial stress-strain relation	CSTRES	Temperature, fast neutron dosage, cold work, peak temperature after cold working, strain rate
Uniaxial stress-strain relation	CSIGMA[a]	Temperature, fast neutron dosage, cold work, peak temperature after cold working, strain rate
Uniaxial strain-stress relation	CSTRAN	Temperature, fast neutron dosage, cold work, peak temperature after cold working, strain rate
Yield strength	CMLIMT	Temperature, fast neutron dosage, cold work, peak temperature after cold working, strain rate
Strain at yield	CMLIMT	Temperature, fast neutron dosage, cold work, peak temperature after cold working, strain rate

TABLE II (continued)

Property	Function or Subroutine Name	Independent Variables in Correlation
Instability strain	CMLIMT	Temperature, fast neutron dosage, cold work, peak temperature after cold working, strain rate
Ultimate strength	CMLIMT	Temperature, fast neutron dosage, cold work, peak temperature after cold working, strain rate
Heat of fusion	PHYPRØ	No independent variables
Melting temperature	PHYPRØ	No independent variables

[a] The subroutine CSIGMA is restricted to the plastic deformation portion of the stress-strain curve.

TABLE III

FUEL MATERIAL PROPERTY CORRELATIONS USED BY FRAP-T3

Property	Function or Subroutine Name	Independent Variables in Correlation
Heat capacity	FCP	Temperature, burnup, plutonium content
Thermal conductivity	FTHCØN	Temperature, density, burnup, plutonium content
Emissivity	FEMISS	Temperature
Heat of fusion	PHYPRØ	No independent variables
Melt temperature	PHYPRØ	Burnup, plutonium content
Thermal expansion	FTHEXP	Temperature, burnup, plutonium content

TABLE IV

GAS PROPERTY CORRELATIONS USED BY FRAP-T3

Property	Function or Subroutine Name	Independent Variables in Correlation
Thermal Conductivity	GTHCON	Temperature, pressure, gap thickness, gas content
Viscosity	GVISCØ	Temperature, gas content

1570 277

3.3 Link to Water Properties Package

FRAP-T is linked to the Wagner water properties package[4], which was developed for the RELAP4[5] code. This package defines subcooled, saturated, and superheated water properties. This package finds water properties by interpolating in a table of numbers generated on the basis of the 1967 ASME steam tables. The subroutines that read the table to find water properties for a specified set of coolant conditions are shown in Table V. The tables are generated by subroutine STH2ØG for specified ranges of water temperature and pressure.

TABLE V

SUBROUTINES IN WATER PROPERTY PACKAGE

Subroutine Name	Function
STH2ØI	Initialization
STH2ØO	Computes saturation pressure as a function of temperature
STH2Ø1	Computes saturated properties as a function of temperature and quality
STH2Ø2	Computes saturated properties as a function of pressure and quality
STH2Ø3	Computes single-phase properties as a function of temperature and pressure
STH2ØG	Generates table of numbers used by above subroutines
VISC[a]	Computes viscosity of water as a function of temperature and density
THCON[a]	Computes thermal conductivity of water as a function of temperature and density

[a] Subroutine is addition to Wagner water properties package. It is based on 1967 ASME steam tables.

3.4 Array Dimensions

The size of all code arrays are specified in the main subroutine. If array sizes are to be changed to handle a bigger problem or reduce core requirements, array dimensions need to be changed only in the main subroutine. The arrays have been dimensioned to handle 1 fuel rod, 20 axial nodes, and a mesh of 20 radial nodes at each axial node.

4. OPERATIONAL FEATURES

FRAP-T requires input data which specify cold state fuel rod geometry, transient power, transient condition of coolant surrounding fuel rod, and amount and type of gas in fuel rod. This allows the user to model fuel rods of arbitrary size subjected to arbitrary power and coolant histories. Input data are needed which specify mesh generation, time step, and accuracy. This permits the code user to have some control over the numerical solution.

Transient coolant conditions can be specified in four different ways. The options are:

(1) Use card input to specify enthalpy histories of upper and lower plenums and core average enthalpy, pressure, flow rate, and bulk temperature histories.

(2) Use card input to specify enthalpy histories of upper and lower plenums and core average pressure and flow rate histories. The local enthalpy and bulk temperatures are computed using a steady state energy balance equation. The enthalpy and bulk temperature are related to fuel rod surface heat flux. This option is intended for use in scoping problems in which coolant conditions change slowly with time.

(3) Use a data storage device, such as a magnetic tape, to specify transient spatially varying coolant conditions. The coolant

conditions are assumed to have been generated earlier by a thermal hydraulic computer code such as RELAP4. The data storage device must contain enthalpy histories of lower and upper plenums, and pressure, enthalpy, mass flux, and bulk temperature histories in an arbitrary number of core regions overlaying the fuel rod to be analyzed.

(4) Use card input to prescribe transient spatially varying heat transfer coefficients.

Code printout, which occurs at input-specified time intervals, includes fuel rod temperature distribution, gap thickness, internal pressure, power, surface heat transfer coefficient, gap heat transfer coefficient, surface heat flux, and cladding hoop strain. The code can be instructed to generate plots of the above output variables as a function of time.

Two options are available for specifying initial conditions. In one option, steady state fuel rod conditions are calculated at an input-specified power level. The steady state solution is then used as the initial conditions for a transient solution. The second option directs the code to read a restart tape for initial conditions. The restart tapes used in this option can be generated by either FRAP-S[6] or FRAP-T.

An output subcode developed for FRAP-T generates 16-mm microfilm plots of data in a time sequence. When these plots are projected through a standard 16-mm movie projector, a motion picture of the output, with time as the third dimension, is shown. Use of this option is limited to computer facilities with access to microfilm plotting capabilities.

III. DESCRIPTION OF ANALYTICAL MODELS

The overall fuel rod response is divided into the six major components of behavior listed below:

(1) Temperature

(2) Internal fuel rod pressure

(3) Cladding deformation

(4) Fuel deformation

(5) Fuel rod failure

(6) Cladding-to-coolant heat transfer.

The equations and models used to predict fuel rod behavior are described in the following sections. An optional model to predict the change in coolant conditions caused by heat transferred from fuel rods is also described.

Asterisks (*) mark those assumptions representing known model simplification and for which tasks are presently under way to develop more advanced models.

1. FUEL ROD TEMPERATURE

The transient heat conduction model plays the lead role in predicting fuel rod temperature distribution. Ancillary models are:

(1) Fuel rod surface temperature model

(2) Gas gap heat transfer model

(3) Cladding oxidation model.

1.1 Assumptions

The analytical models used to predict fuel rod temperature are based on the following assumptions:

(1) No heat conduction in longitudinal direction

(2) Steady state critical heat flux correlations are valid during transient conditions

(3) Steady state cladding surface heat transfer correlations are valid during transient conditions

(4) No convective mode of heat transfer across gas gap

(5) Cladding oxidation does not influence cladding thermal properties.

1.2 Heat Conduction

Heat conduction in the radial direction within a fuel rod is considered to be governed by the equation

$$\frac{1}{r}\frac{\partial}{\partial r}\left(kr\frac{\partial T_n(r)}{\partial r}\right) + q_n(r) = C_p\,\rho\,\frac{\partial T_n(r)}{\partial t} \qquad (1)$$

where

$T_n(r)$ = temperature at axial node n and radial coordinate r

t = time

r = radius

$q_n(r)$ = heat generation rate per unit volume at axial node n and radial coordinate r

C_p = specific heat

ρ = density

k = coefficient of thermal conductivity.

The parameters C_p and k are temperature-dependent.

The following boundary conditions are used with Equation (1):

$$\left.\frac{\partial T_n}{\partial r}\right|_{r = 0} = 0 \qquad (2)$$

$$\left. T_n \right|_{r = r_o} = T_s \qquad (3)$$

where

r_o = outer radius of fuel rod

T_S = fuel rod surface temperature (computed by the surface temperature model).

The numerical solution to Equation (1) is performed by a modularized version of the HEAT-1 code[7].

Optionally, heat conduction in both the radial and azimuthal direction is considered. In this case, the one-dimensional (radial) HEAT-1 subcode is still used to determine the fuel rod temperature distribution. The heat generation rate for each HEAT-1 mesh is modified

to account for heat addition (or loss) due to azimuthal heat conduction. HEAT-1 then determines the radial temperature distribution in each azimuthal sector. The calculations are cycled until a negligible change in the radial temperature distribution of each azimuthal sector occurs between two successive iterations.

The only new equations required to model two-dimensional R-θ heat conduction are those that compute the heat added (or subtracted) from each HEAT-1 subcode mesh by azimuthal heat conduction. In continuous form, azimuthal heat conduction is computed by the equation

$$q(r,\theta) = \frac{k}{r}\frac{\partial T}{\partial \theta} \qquad (4)$$

where

$q(r,\theta)$ = rate of azimuthal heat conduction at radial coordinate r and azimuthal coordinate θ (W/m^2)

k = thermal conductivity ($W/m \cdot K$)

T = temperature (K).

Referring to the mesh configuration shown in Figure 1, the finite difference form of Equation (4) is

$$q_{\ell,n+1/2} = \frac{k_{\ell,n+1/2}}{r_\ell}\frac{(T_{\ell,n+1} - T_{\ell,n})}{\Delta\theta} \qquad (5)$$

where

$q_{\ell,n+1/2}$ = rate at which heat is conducted in azimuthal direction at mesh point $\ell,n+1/2$

$k_{\ell,n+1/2}$ = thermal conductivity = $0.5\,(k_{\ell,n} + k_{\ell n+1})$

r_ℓ = radial coordinate of radial node ℓ

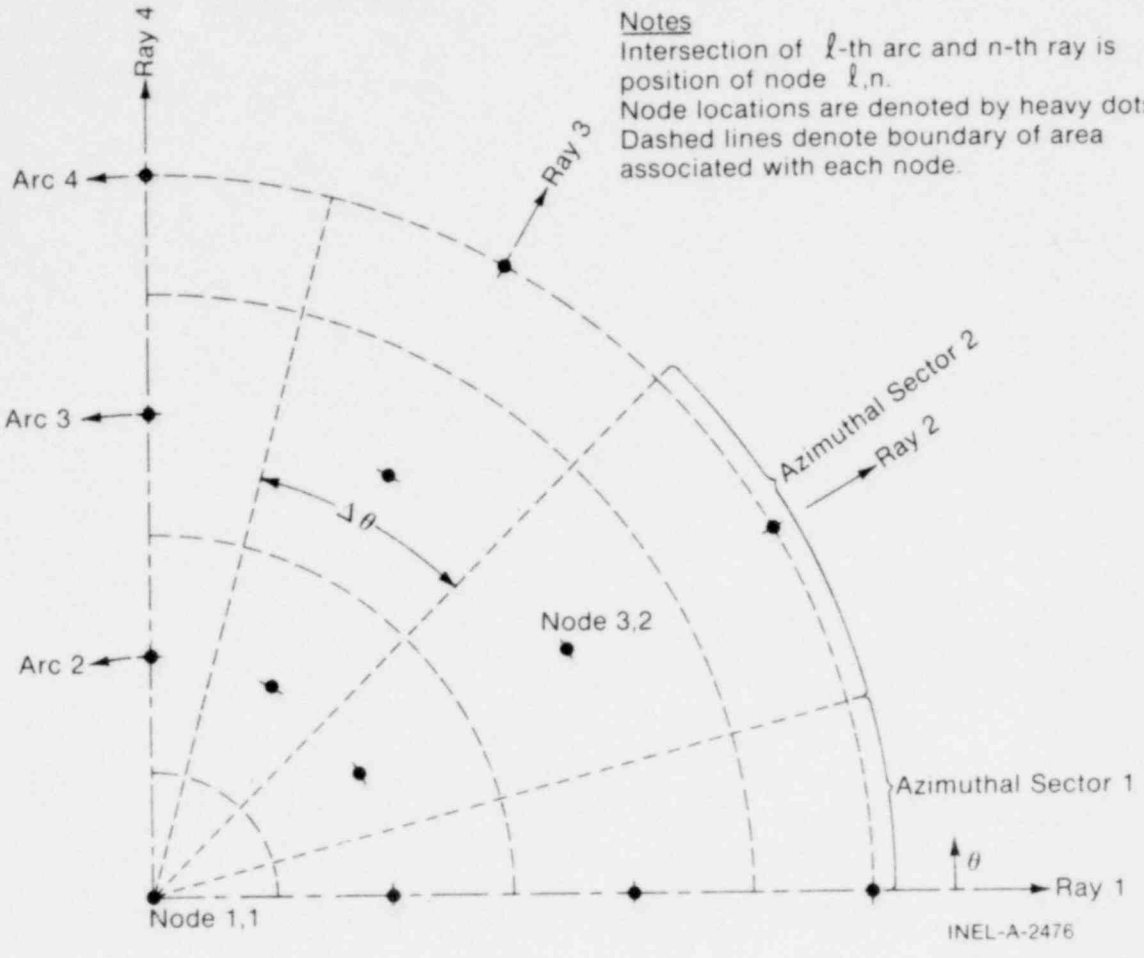

Fig. 1 Mesh configuration for R-θ heat conduction.

$T_{\ell,n}$ = temperature at radial coordinate ℓ and azimuthal coordinate n

$\Delta\theta$ = azimuthal span of each azimuthal sector (radians).

The volumetric rate at which heat is added (or subtracted) by azimuthal heat conduction into the control volume centered about the node ℓ,n

with corners at nodes ℓ-1/2, n-1/2; ℓ+1/2, n-1/2; ℓ+1/2, n+1/2; and ℓ-1/2, n+1/2 15

$$q_{\ell,n} = \frac{0.5(r_{\ell+1,n} - r_{\ell-1,n})}{r_{\ell,n}\Delta\theta\ A}\left[k_{\ell,n+1/2}\ (T_{\ell,n+1} - T_{\ell,n}) + k_{\ell,n-1/2}(T_{\ell,n-1} - T_{\ell,n})\right] \quad (6)$$

where

$\bar{q}_{\ell,n}$ = rate at which heat is added by azimuthal heat conduction to control volume centered about node ℓ,n (W/m^3)

A = area of mesh

$$= (\Delta\theta/2)\left\{\left[0.5(r_{\ell,n} + r_{\ell+1,n})\right]^2 - \left[0.5(r_{\ell,n} + r_{\ell,n-1})\right]\right\}^2$$

The quantity $\bar{q}_{\ell,n}$ is added to the heat generation term at the ℓ^{th} radial node in the HEAT-1 subcode equations to account for azimuthal heat conduction. This equation is used for all radial nodes except the center node.

For the control volume associated with the center node, the heat generation term in the HEAT-1 subcode is modified in a different manner. The first radial node of each azimuthal sector must be at the same temperature. To force this condition, the heat generation required at the first radial node of the n^{th} azimuthal sector to bring the temperature at this coordinate to the average center node temperature at the end of the past time step is computed. It is computed according to the equation

$$\bar{q}_{1n} = \rho C_p\ (T_{ave} - T_{1n})/\Delta t \quad (7)$$

where

ρ = fuel density

C_p = fuel specific heat at temperatue T_{ave}

Δt = time step

$T_{ave} = (1/N) \sum_{n=1}^{N} T_{1n}$

N = number of azimuthal sectors.

1.3 Fuel Rod Surface Temperature

The surface temperature of a fuel rod at each new time step is computed prior to computing the internal fuel rod temperature distribution. This surface temperature is then used as an up-to-date boundary condition in the calculation for internal fuel rod temperature distribution. Since boundary conditions for the temperature distribution calculations do not need to be approximated from previous time step or iteration values, iteration procedures and numerical instabilities at the onset of nucleate boiling and burnout are avoided.

Details of the method for computing surface temperature are covered in Appendix C.

1.4 Gas Gap Heat Transfer

Two models are available for calculating gap heat transfer. The first model is a modification of the Ross and Stoute[8] model. The second model[2] is based on a cracked pellet geometry.

1.4.1 Ross and Stoute Model.

(1) Assumptions.

(a) uniform geometry of the open gap between the fuel and cladding

(b) elastic cladding deformation at the points of fuel and cladding contact after the gap is closed.

(2) Open Gap. If the fuel and cladding are not in contact, heat is transferred across the gas gap by conduction through the gas and radiation. Heat transfer across the gas gap is considered to be governed by the equation

$$h_g = \frac{K_g}{t_g + (g_1 + g_2) + 1.98\,(R_f + R_c)} + h_r \qquad (8)$$

where

h_g = gap conductance
K_g = conductivity of gas in gas gap
t_g = gap thickness
g_1 = temperature jump distance at cladding inside surface
g_2 = temperature jump distance at fuel outside surface
h_r = radiant heat transfer conductance
R_c = arithmetic mean roughness height of cladding
R_f = arithmetic mean roughness height of fuel.

Radiant heat transfer conductance is computed using the following equation:

$$h_r = \sigma F_e (T_f^2 + T_c^2)(T_f + T_c) \qquad (9)$$

where

h_r = radiant heat transfer conductance

σ = Stefan-Boltzman constant
F_e = emissivity factor
T_f = temperature of outside surface of fuel
T_c = temperature of inside surface of cladding.

The emissivity factor is computed by the equation

$$F_e = \left[\frac{1}{e_f} + \frac{r_f}{r_c} \left(\frac{1}{e_c} - 1 \right) \right]^{-1} \qquad (10)$$

where

F_e = emissivity factor
e_f = emissivity of fuel surface
e_c = emissivity of cladding inside surface
r_f = outside radius of fuel
r_c = inside radius of cladding.

The temperature jump distance is computed by an empirically derived equation presented in the GAPCON code report[9]. The equation is

$$g_1 + g_2 = 5.448 \left[\frac{\mu}{P} \left(\frac{T}{M} \right)^{1/2} \right] \qquad (11)$$

where

$(g_1 + g_2)$ = jump distance (cm)
μ = viscosity of gas (gm/cm-sec)
P = pressure of gas (psi)
T = temperature of gas (K)
M = molecular weight of gas.

(3) Closed Gap. If the fuel and cladding are in contact, the GAPCON code equation for contact conductance is used. This equation

agrees with gap conductance data presented by Ross and Stoute[8]. The equation is

$$h_g = \frac{K_m P_i}{a_o R^{0.5} H} + \frac{K_g}{c(R_f+R_c) + (g_1 + g_2)} + h_r \qquad (12)$$

where

h_g = gap conductance (cal/sec-cm^2-c)

$K_m = \frac{2K_fK_c}{K_f+K_c}$

K_f = fuel conductivity (cal/sec-cm-c)

K_c = cladding conductivity (cal/sec-cm-c)

P_i = interfacial pressure between fuel and cladding (psi)

a_o = a constant - 0.5 cm$^{1/2}$

$R = \left(\frac{R_f^2 + R_c^2}{2}\right)^{1/2}$

R_c = arithmetic mean roughness height of cladding (cm)

R_f = arithmetic mean roughness height of fuel (cm)

H = Meyer-Hardness of cladding (psi)

k_g = thermal conductivity of gas (cal/sec-cm-c).

The coefficient, c, in Equation (12) is computed by the empirical equation

$$c = 1.98\, e^{-0.00125\, P_i} \qquad (13)$$

where P_i = interfacial pressure between fuel and cladding (kg/cm^2).

1.4.2 Cracked Pellet Model.

(1) Assumptions.

(a) nonuniform geometry of the open gap between the fuel and cladding

(b) both plastic and elastic deformation occur at the fuel and cladding contact points when the gap is closed.

(2) Open Gap. If the fuel and cladding are not in contact, a nonuniform cladding-fuel geometry is assumed. The fraction of the pellet circumference in contact with the cladding is considered to be governed by the equations

$$F = \frac{1}{\left(a_1 \left[\frac{\Delta D \cdot 100}{D_F}\right]^{a_2} + a_3\right)} + a_4 \qquad (14)$$

and

$$\frac{1}{a_3} + a_4 = 1 \qquad (15)$$

where

F = fraction of pellet in contact with the cladding

ΔD = hot diameteral gap (in.)

D_F = hot diameter of the fuel pellet (in.)

a_1, a_2, a_3, and a_4 = emperical constants adjusted so that FRAP-S1[6] fuel temperature calculations matched measurements of fuel temperatures.

The constant, a_4, represents the minimum fraction of pellet-cladding contact for large diametral gaps. The functional form of the model, Equations (14) and (15), permits a very large fraction of pellet-cladding contacts ($F > 0.98$) for a small, but calculated finite diametral gap ($\sim$ 0.75 mils). The justification for this is that internal cracks (radial and circumferential) form in the fuel pellets. The gas volume generated by these cracks is approximately equal to the gas volume of the original gas gap. Thus, the gas gap is mostly closed,

even when the fuel thermal expansion is small. Plots of the fraction of fuel pellet surface in contact with the cladding for beginning-of-life and end-of-life cases are shown in Figure 2.

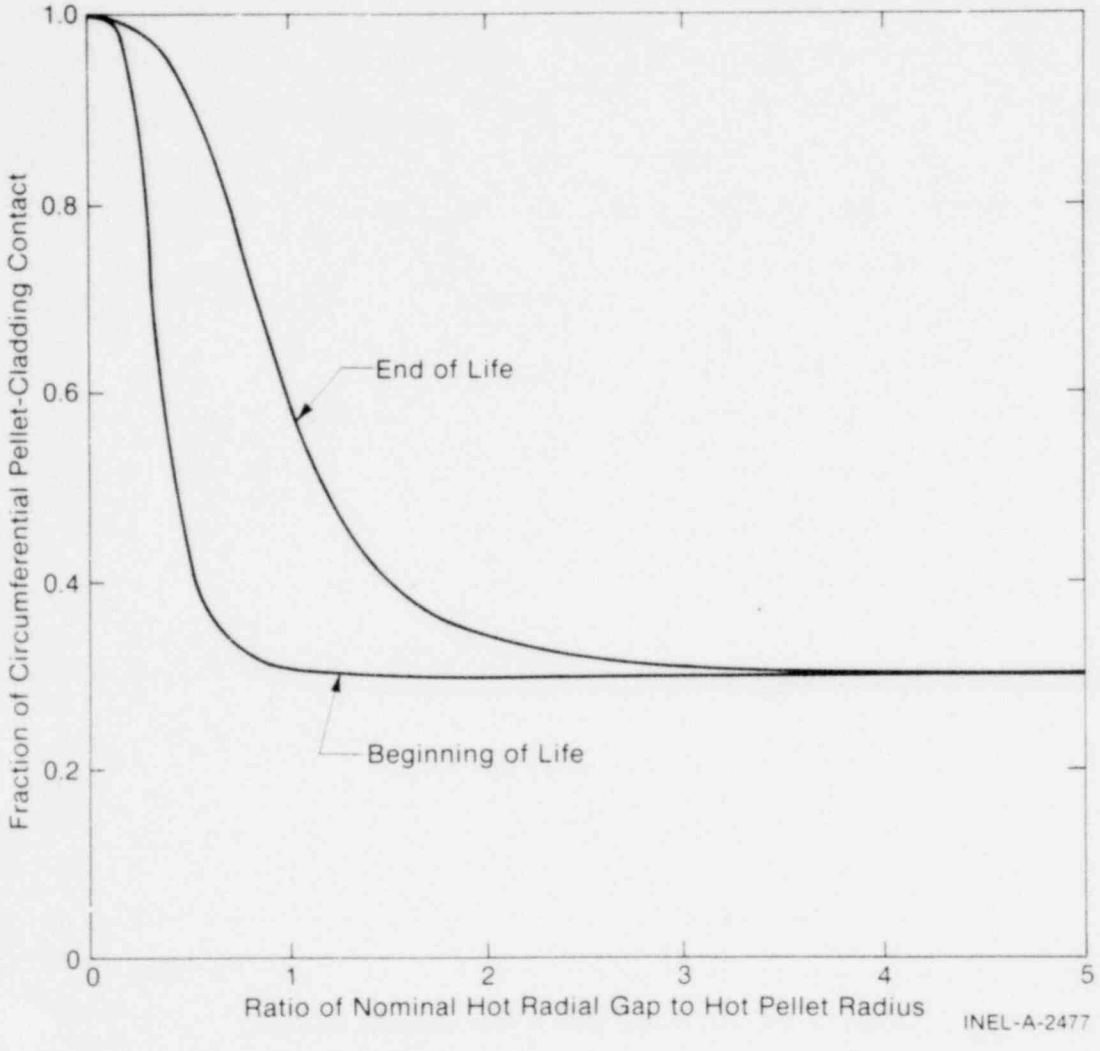

Fig. 2 Fraction of pellet circumference in contact with cladding.

Heat transfer across the gas gap is considered to be by conduction through the gas in the open gap and zero pressure contact conductance over that fraction of the gap circumference with pellet-cladding contact. Heat transfer across the gas gap is, therefore, governed by the equation

$$h_{gap} = (1 - F)\, h_1 + F\, h_2 + h_r \qquad (16)$$

where

h_{gap} = net gap conductance (Btu/hr-ft^2-°F)

h_1 = open gap conductance (Btu/hr-ft^2-°F)

h_2 = zero pressure contact conductance (Btu/hr-ft^2-°F)

hr = radiant heat transfer conductance [computed the same as shown by Equation (9)].

The open gap conductance is determined from the equation

$$h_1 = \frac{k_{mix}}{\Delta r' + \delta} \qquad (17)$$

where

k_{mix} = thermal conductivity of gas mixture (Btu/hr-ft°F)

$\Delta r'$ = average hot radial gap thickness of eccentric gas gap (ft)

δ = root mean square of the fuel cladding surface roughness. A value of 4.39 microns is assumed.

r_1 = hot-calculated inside radius of cladding (ft)

r_2 = hot-calculated radius of fuel (ft).

(3) Closed Gap. When the fuel and cladding are in contact, the theory of thermal contact conductance for ceramic fuel elements developed by Jacobs and Todreas[10] is used. The governing equation for contact conductance is

$$h_{gap} = C_1 \, p^n + \frac{k_{mix}}{w} \qquad (18)$$

where

h_{gap} = net gap conductance (Btu/hr-ft^2°F)

C_1 = 0.475 for stainless steel cladding, and 0.600 for Zr-2 and Zr-4 cladding.

P = pellet-cladding contact pressure (psi)

n = 1.0 for $0 \leq P \leq 1000$ psi, and 1/2 for $P \leq 1000$.

The value of the exponent, n, is governed by the material behavior at the interface of the fuel and cladding contact points. An exponents of 1.0 is valid only if the surface peaks of one of the materials are flowing plastically. This is consistent with the Ross and Stoute theory of contact conductance. If the contact points of both materials are behaving elastically, the correct value for the exponent, n, is approximately 1/2. The experimental results of French and Rohsenow[11] support this value and also indicate that for metal-cermic pairs, the transition pressure from plastic to elastic flow is approximately 1000 psi. Plastic flow occurs before elastic deformation because the surface peaks of the fuel and cladding are narrow. The narrow peaks are first mashed down by plastic flow. This increases the contact area and reduces the stress at the fuel-cladding interface so that only elastic deformation subsequently occurs. The parameter, k_{mix}/δ, accounts for the heat conduction through the gas in the gaps between contact points.

1.5 Transient Plenum Temperature Model

To calculate the internal pressure, the temperature for all gas volumes in the fuel rod must be calculated. Under steady state and transient reactor conditions, approximately 40 to 50% of the gas in a fuel rod is located in the fuel pellet expansion chamber (plenum) provided for in the fuel rod. The plenum temperature model has the purpose of computing the temperatures of this gas. This model includes all thermal interactions between the plenum gas and the end pellet surface, hold-down spring, and cladding wall.

1.5.1 Assumptions.

(1) The temperature of the top surface of the fuel stack is independent of the plenum gas temperature

(2) The plenum gas is well mixed by natural convection

(3) Temperature gradients in the spring and cladding are small.

The first assumption allows the end pellet temperature to be treated as an independent variable. The second assumption permits the gas to be modeled by one lumped mass with average properties. Using the third assumption, the temperature response of the cladding and spring can be represented by a small number of lumped masses.

1.5.2 Plenum Energy Equations. The plenum thermal model, PLNT, calculates the energy exchange between the plenum gas and structural components. The structural components consist of the hold-down spring, end pellet, and cladding. Energy exchange between the gas and structural components occurs by natural convection, conduction, and radiation. A schematic of these energy exchange mechanisms is shown in Figure 3. The spring is modeled by two nodes of equal mass; center and surface (Figure 4). The cladding is modeled by three nodes; two surface nodes

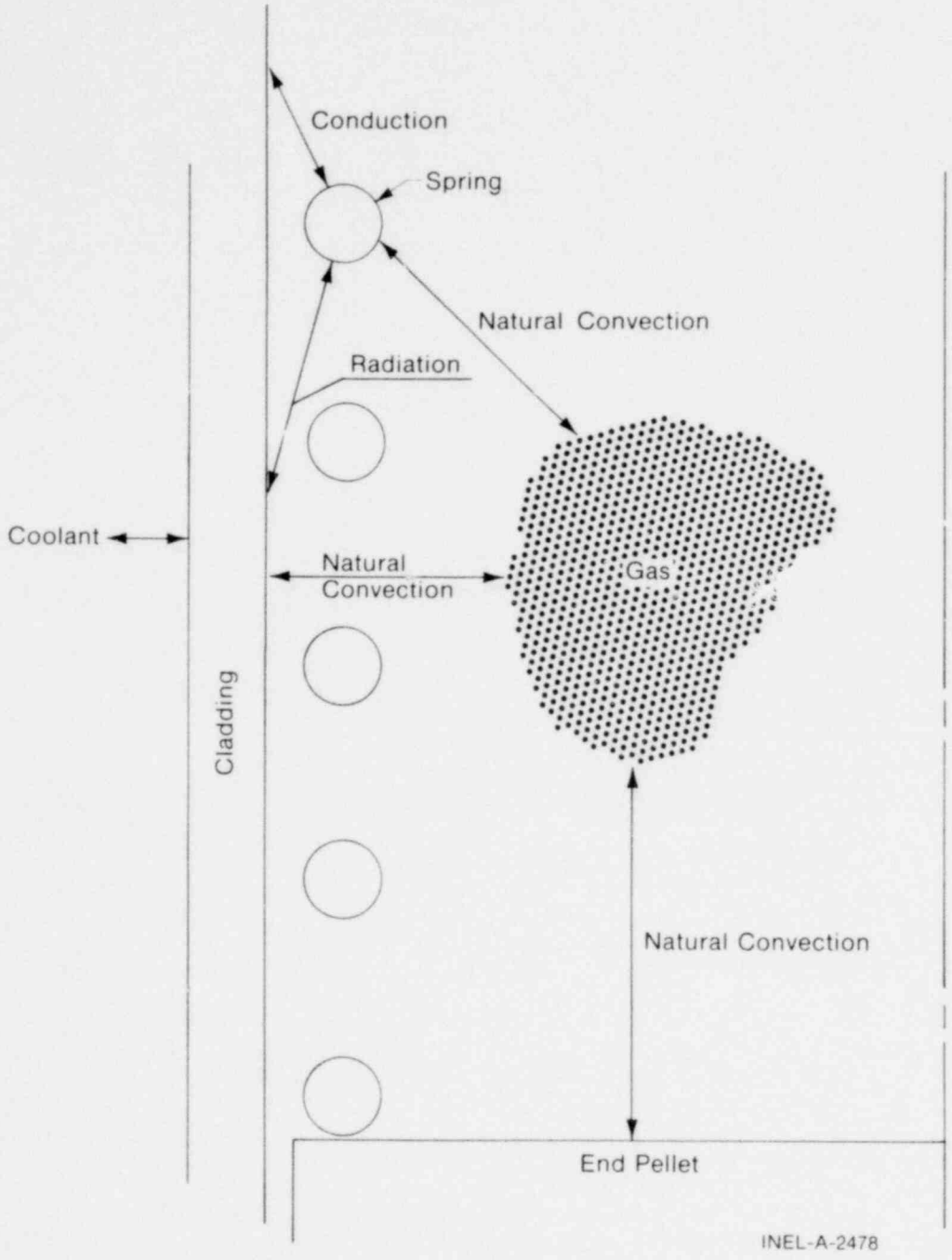

Fig. 3 Plenum energy flow model.

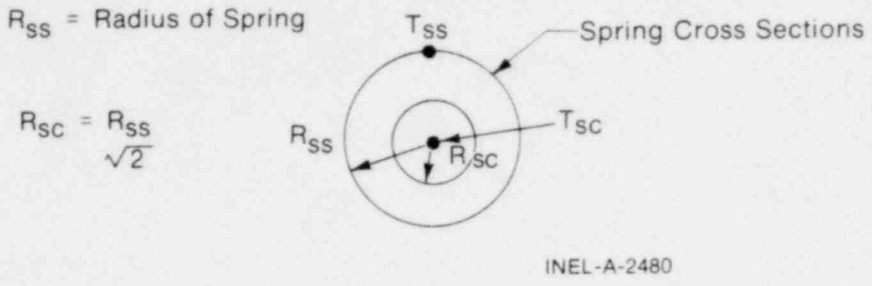

Fig. 4 Spring noding.

and one center node. The center node has twice the mass of the surface nodes (Figure 5). This nodalization scheme results in a set of six

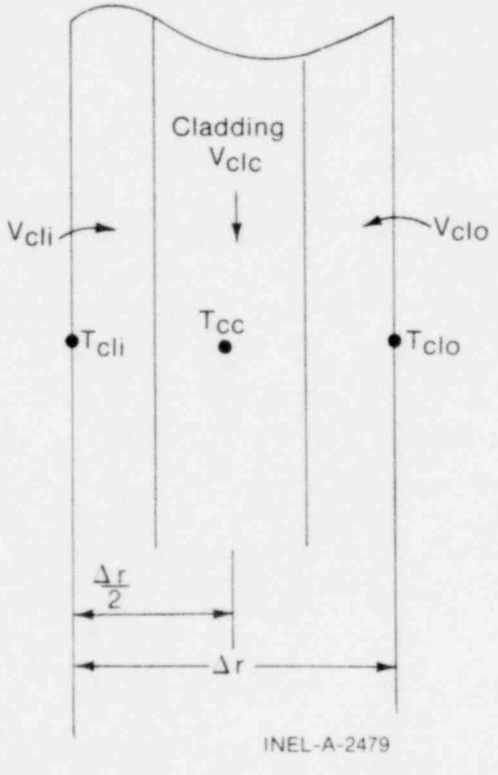

Fig. 5 Cladding noding.

energy equations from which the plenum thermal response can be calculated. The transient energy equations for the gas, spring, and cladding are as follows (Table VI defines nomenclature for PLNT equations):

(1) Plenum gas:

$$\rho_g V_g C_g \frac{\partial T_g}{\partial t} = A_{ep} h_{ep} (T_{ep} - T_g) + A_{cl} h_{cl} (T_{cli} - T_g) + A_{ss} h_s (T_{ss} - T_g) . \quad (19)$$

(2) Spring center node:

$$V_{sc} C_s \rho_s \frac{\partial T_{sc}}{\partial t} = \bar{q} V_{sc} + \frac{A_{sc} K_s (T_{ss} - T_{sc})}{R_{ss}} . \quad (20)$$

(3) Spring surface node:

$$V_{ss} C_s \rho_s \frac{\partial T_{ss}}{\partial t} = \bar{q} V_{ss} + A_{sc} K_s (T_{sc} - T_{ss}) + A_{ss} h_{rads} (T_{cli} - T_{ss}) + A_{ss} h_s (T_g - T_{ss}) + A_{ss} h_{cons} (T_{cli} - T_{ss}) \quad (21)$$

where h_{cons} is the conductance between the spring and cladding. The conductance, h_{cons}, is only used when a stagnant gas condition exists; i.e., when the natural convection heat transfer coefficient for the spring (h_s) is zero.

(4) Cladding interior node:

$$\rho_{cl} C_{cl} V_{\varepsilon li} \frac{\partial T_{cli}}{\partial t} = A_{cl} h_{radc} (T_{ss} - T_{cli}) + A_{cl} h_{cl} (T_g - T_{cli}) + A_{cl} h_{conc} (T_{ss} - T_{cli}) + \frac{A_{cl} K_{cl}}{\Delta r/2} (T_{clc} - T_{cli}) + \bar{q} V_{cli} . \quad (22)$$

(5) Cladding central node:

$$\rho_{cl} C_{cl} V_{clc} \frac{\partial T_{clc}}{\partial t} = \bar{q} \quad V_{clc} + \frac{A_{cl} K_{cl}}{\Delta r/2} \quad (T_{cli} - T_{clc})$$

$$+ \frac{A_{cl} K_{cl}}{\Delta r/2} \quad (T_{clo} - T_{clc}) \quad . \qquad (23)$$

(6) Cladding exterior node:

$$T_{clo} = T_{cool} \quad . \qquad (24)$$

For steady state, the time derivatives of temperature on the left side of Equations (19) through (23) are set to zero, and the temperature distribution in the spring and cladding is assumed uniform.

To solve Equations (19) through (24), they are rewritten in the Crank-Nicolson[12] implicit finite difference form. This formulation results in a set of six equations and six unknowns.

The details of the difference formulation of Equations (19) through (23) and the programming logic of subroutine PLNT are given in Appendix D.

1.5.3 Natural Convection Heat Transfer Coefficient for the Plenum Model. The natural convection film coefficients for the end pellet, spring, and cladding (h_{ep}, h_s, and h_{cl}, respectively) are calculated in subroutine PLNT. The correlations used for these coefficients are those given by Kreith[13] and McAdams[14] for laminar and turbulent natural convection from flat plates, horizontal cylinders, and vertical surfaces.

TABLE VI

NOMENCLATURE FOR PLNT MODEL

Quantities	
A	= surface area
C	= heat capacitance
DIAC	= diameter of the spring coil
DIAS	= diameter of the spring wire
$\bar{F}_{1-2}$	= gray-body shape factor from body 1 to body 2
F_{1-2}	= view factor from body 1 to body 2
Gr	= Grashof number
h	= surface heat transfer coefficient
I	= radiation flux
ID	= inside diameter of the cladding
K	= thermal conductivity
L	= length
OD	= outside diameter of the cladding
Pr	= Prandtl number
q	= energy
$\bar{q}''$	= surface heat flux
$\bar{q}'''$	= volumetric heat generation
R	= radius
Δr	= thickness of the cladding (OD-ID)/2.0
T	= temperature
V	= volume
σ	= Stefan-Boltzmann constant

TABLE VI (continued)

Quantities	
C_g	= heat capacitance of gas. It is a constant set equal to the value of 1.24 Btu/lb-°F, which is the heat capacitance of helium. (Other gas properties vary with temperature and pressure.)
ρ	= density
Σ	= absorption coefficient
ε	= emissivity
δ	= spring to cladding spacing (ID-DIAC)/2.0

Subscripts	Meaning
cl	= cladding
clc	= cladding center node
cli	= cladding interior node
clo	= cladding outside node
cool	= coolant
conc & cons	= conduction between the spring and cladding
conv	= convective heat transfer to coolant
ep	= end pellet
g	= gas
p	= plenum
sc	= spring center node
ss	= spring surface node
s	= spring
rads & radc	= radiation heat transfer between the spring and cladding

TABLE VI (continued)

Superscripts	Meaning
m, m+1	= old and new time step

The flat plate natural convection coefficients used for the end pellet surface heat transfer are:

(1) For laminar conditions on a heated surface

$$h_{ep} = 0.54\ K_g\ (Gr \times Pr)^{0.25}/ID \quad . \tag{25}$$

(2) For turbulent conditions, Grashof number (Gr) greater than 2.0×10^7, on a heated surface

$$h_{ep} = 0.14\ K_g\ (Gr \times Pr)^{0.33}/ID \quad . \tag{26}$$

(3) For laminar conditions on a cooled surface

$$h_{ep} = 0.27\ K_g\ (Gr \times Pr)^{0.25}/ID \quad . \tag{27}$$

The following natural convection coefficients for horizontal cylinders are used for the film coefficient for the spring:

(1) For laminar condition

$$h_s = 0.53\ K_g\ (Gr \times Pr)^{0.25}/DIAS \quad . \tag{28}$$

(2) For turbulent conditions, Gr from 10^9 to 10^{12}

$$h_s = 0.18\ (T_g - T_{ss})^{0.33} \quad . \tag{29}$$

The vertical surface natural convection coefficients used for the cladding interior surface are given by:

(1) For laminar conditions

$$h_{cl} = 0.55\ K_g\ (Gr \times Pr)^{0.25}/L_p \quad . \tag{30}$$

(2) For turbulent conditions, Gr greater than 10^9

$$h_{cl} = 0.021\ K_g\ (Gr \times Pr)^{0.4}/L_p \quad . \tag{31}$$

The natural convection correlations described above were derived for flat plates, horizontal cylinders, and vertical surfaces in an infinite gas volume. Heat transfer coefficients calculated using these correlations are expected to be higher than those actually existing within the confined space of the plenum. However, until plenum temperature experimental data are available, these coefficients are believed to provide a best-estimate of the true values.

1.5.4 Conduction Heat Transfer Between the Spring and Cladding. Conduction of energy between the spring and cladding is represented by the heat transfer coefficients, h_{cons} and h_{conc}, in Equations (24) and (22). These coefficients are calculated in subroutine PLNT when stagnant gas conditions exist. The conduction coefficients are calculated based on the spring and cladding geometries shown in Figure 6, and the assumptions that:

(1) The cladding and spring surface temperature are uniform

(2) Energy is conducted only in the direction perpendicular to the cladding wall (heat flow is one-dimensional).

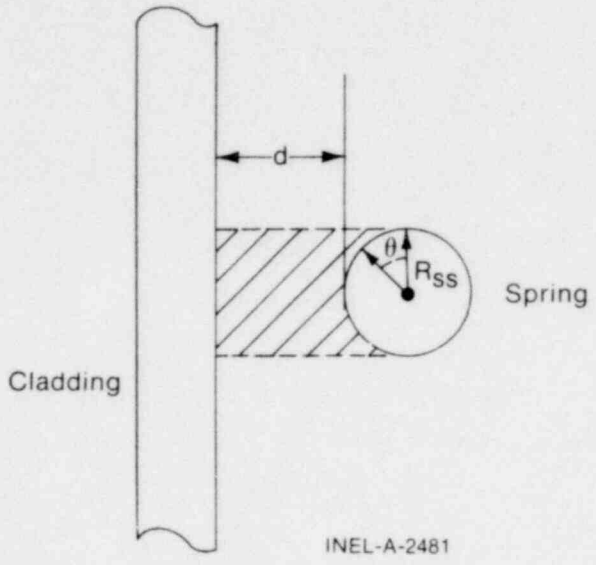

Fig. 6 Geometrical relationship between the cladding and spring.

Using the above assumptions and the geometry given in Figure 6, the energy (q) conducted from an elemental surface area of the spring ($L_s R_s d\theta$) to the cladding is

$$dq = -\frac{K_g(T_{ss} - T_{cli}) \quad (L_s . R_s \sin(\theta)\, d\theta)}{(\delta + R_s - R_s \sin\theta)} \quad . \tag{32}$$

Integrating Equation 32 over the surface area of the spring facing the cladding, the total flow of energy is

$$q = \frac{K_g A_{ss}}{\pi} (T_{ss} - T_{cli}) \left[\frac{-\pi}{2 R_s} + \frac{2}{R_s} \left\{ \frac{1}{\frac{1-R_s^2}{(\delta+2R_s)^2}} + \text{Tan}^{-1} \text{Tan}(\theta/2) - \frac{R_s}{(\delta+2R_s)} \Big/ \left(1 - \frac{R_s^2}{(\delta+2R_s)^2} \right) \right\} \right]_{\theta=0.0}^{\theta=\pi/2} \quad (33)$$

The two conduction heat transfer coefficients are given by

$$h_{cons} = q/A_{ss} (T_{ss} - T_{cli}) \quad (34)$$

and

$$h_{conc} = h_{cons} A_{ss}/A_{cl} \quad . \quad (35)$$

When natural convection heat transfer exists, h_{cl} or $h_s > 0.0$, it is assumed that energy flows to the gas from the spring and then from the gas to the cladding wall, or vice versa. Under these conditions, h_{cons} and h_{conc} are set to zero. Therefore, in the current version of PLNT, h_{cons} and h_{conc} are used only when the temperature is uniform throughout the plenum. Future plenum data or analytical analysis may indicate that natural convection flow between spring and cladding does not exist. If this is true, the conduction coefficient will be used at all times.

1.5.5 Radiation Heat Transfer Between Spring and Cladding. Transport of energy by radiation between the spring and cladding is included in the plenum model by use of the heat transfer coefficients, h_{rads} and h_{radc}, in Equations (21) and (22). These coefficients are calculated in

subroutine PLNT. They are derived from the radiant energy exchange equation for two gray bodies in thermal equilibrium[13] as follows:

$$q_{1-2} = A_1 \bar{F}_{1-2} \sigma(T_1^4 - T_2^4) \tag{36}$$

where q_{1-2} is the net rate of heat flow by radiation between bodies 1 and 2.

The gray-body factor ($\bar{F}_{1-2}$) is related to the geometrical view factor (F_{1-2}) from body 1 to body 2 by

$$A_1\bar{F}_{1-2} = \frac{1}{(1-\varepsilon_1)/A_1\varepsilon_1 + 1/A_1F_{1-2} + (1-\varepsilon_2)/A_2\varepsilon_2} \quad . \tag{37}$$

Using Equations (36) and (37) and approximating the geometric view factor from the cladding to the spring (F_{cl-s}) by

$$F_{cl-s} = \frac{A_{ss}}{2\,A_{cl}} + \frac{(2A_{cl} - A_{ss})\,A_{ss}}{4A_{cl}^{\,2}} \tag{37a}$$

the net radiant energy exchange between the cladding and spring is written as

$$q_{cl-s} = A_{cl} \bar{F}_{cl-s} \sigma(T_{cli}^{\,4} - T_{ss}^4) \quad . \tag{38}$$

The radiation heat transfer coefficients, h_{radc} and h_{rads}, are calculated by

$$h_{radc} = q_{cl-s}/A_{cl} \star (T_{cli} - T_{ss}) \tag{39}$$

and

$$h_{rads} = (h_{radc} \star A_{cl})/A_{ss}. \tag{40}$$

1.5.6 Gamma Heating of the Spring and Cladding. The volumetric power generation term, $\bar{q}$, shown in Equations (20) through (23), represents the gamma radiation heating of the spring and cladding. A simple relationship is used to calculate $\bar{q}$ in subroutine PLNT. The relationship used is derived from the gamma flux attentuation equation

$$-dI(x) = \Sigma_\gamma I(x)\, dx \tag{41}$$

where I(x) is the gamma flux, Σ_γ is the gamma ray absorption coefficient, and x is the spatial dimension of the solid on which the gamma radiation is incident. Since the cladding and spring are thin in cross section, it can be assumed that the gamma ray flux is constant (I) throughout the volume. Of the gamma flux (I) incident on the spring and cladding, the portion absorbed (ΔI) can be described by

$$-\Delta I = \Sigma_\gamma I\bar{x} \tag{42}$$

where $\bar{x}$ is the thickness of the spring or cladding. Therefore, the volumetric gamma ray absorption rate is given by

$$\frac{\Delta I}{\bar{x}} = \Sigma_\gamma I \quad . \tag{43}$$

Equation (43) can also represent gamma volumetric energy deposition by letting I represent the energy flux associated with the gamma radiation. Approximately 10% of the energy released in the fissioning of uranium is in the form of high energy gamma radiation. Therefore, the gamma energy flux leaving the fuel rod would be approximately equal to 10% of the thermal flux. The gamma energy flux throughout the reactor can then be estimated by

$$I = 0.10\, \bar{q}_{rod} \tag{44}$$

where $\bar{q}_{rod}$ is the average fuel rod power. For zirconium, Σ_γ is approximately 11.0 ft^{-1}. Therefore, the gamma energy deposition rate is given by

$$-\frac{\Delta I}{\overline{X}} = \bar{q} = 1.1\ \bar{q}_{rod} . \qquad (45)$$

Equation (45) is an estimate of the gamma heating rate for the spring and cladding.

1.6 Metal-Water Reaction Model

If metal-water chemical reaction is occurring in the cladding, the heat generated by this reaction must be accounted for in the heat conduction model. The Cathcart model[15] is used to compute this heat generation.

2. FUEL ROD INTERNAL PRESSURE

Static and transient fuel rod internal pressure models are in FRAP-T. During the initial steady state calculations, the static pressure model is used. After that, the transient pressure model is used.

2.1 Assumptions

The static fuel rod internal pressure model is based on the following assumptions:

(1) Perfect gas law holds

(2) Gas pressure is the same throughout the fuel rod

(3) Gas in the fuel rod cracks at temperature of fuel at a radius of 2/3 fuel pellet radius

(4) No fission gas release during transient*.

The transient fuel rod pressure model is based on the following assumptions:

(1) Gas behaves as a perfect gas

(2) Gas flow past the fuel column is a quasi-steady-state process

(3) Gas flow is compressible and laminer

(4) Gas flow past the fuel column can be analyzed as Poiseuille flow (i.e., by force balance only)

(5) Gas expansion in the plenum and ballooning zone is isothermal

(6) Entire gas gap can be represented as one volume containing gas at a uniform pressure*

(7) Flow distance of gas is equal to distance from plenum to centroid of gas gap*

(8) Minimum cross-sectional area of flow is equivalent to an annulus with inner radius equal to that of fuel pellet radius and a radial thickness of 0.01 mils.

2.2 Static Fuel Rod Internal Pressure

Internal fuel rod pressure is computed by

$$P_G = \frac{M_G R}{\frac{V_p}{T_p} + \sum_{n=1}^{N} \left[\Delta Z_n \quad \pi(r_{cn}^2 - r_{fn}^2) + \frac{V_{cn}}{T_{cn}} + \frac{V_{DN}}{T_{Fn}} + \frac{V_{pn}}{T_{aven}} \right]} \qquad (46)$$

where

P_G = internal fuel rod pressure

M_g = moles of gas in fuel rod

R = universal gas constant

V_p = plenum volume (defined from plenum volume model)

T_p = temperature of gas in plenum

n = axial node number

N = number of axial nodes into which fuel rod is descretized for numerical solution

r_{cn} = radius of inside surface of cladding at axial node n

r_{fn} = radius of outside surface of fuel at axial node n

T_{Gn} = temperature of gas in gas gap at axial node n

ΔZ_n = fuel rod length associated with axial node n

V_{cn} = fuel crack volume per unit length at axial node n

T_{cn} = temperature of gas in fuel cracks at axial node n

V_{Dn} = volume of fuel pellet dishes per unit length of fuel stack at axial node n

T_{Fn} = centerline temperature of fuel stack at axial node n

V_{pn} = volume of gas in fuel open pores per unit length at axial node n

T_{aven} = volumetric average fuel temperature at axial node n.

T_{Fn} = centerline temperature of fuel stack at axial node n.

2.3 Transient Internal Gas Flow

Transient flow of fill gas between the plenum and gas gap of a fuel rod is calculated with

$$\dot{m} = \frac{\pi (P_p^2 - P_s^2)}{R\mu \sum_{i=I_s}^{I_p} \frac{\ell_i T_i Ha}{D_g D_h^3}} \qquad (47)$$

where

$\dot{m}$ = mass flow rate

π = 3.14159

μ = gas viscosity at temperature T_A

T_i = gas temperature at node i

T_A = volume averaged temperature of gas in gas gap

ℓ_i = axial length of node i

t_{gi} = gap thickness (radial) at node i

I_p = number of top axial node

I_s = number of axial node closest to centroid of gas gap (see Figure 7)

Ha = Hagen number (defined below)

P_p = fuel rod plenum pressure

P_s = pressure in gas gap

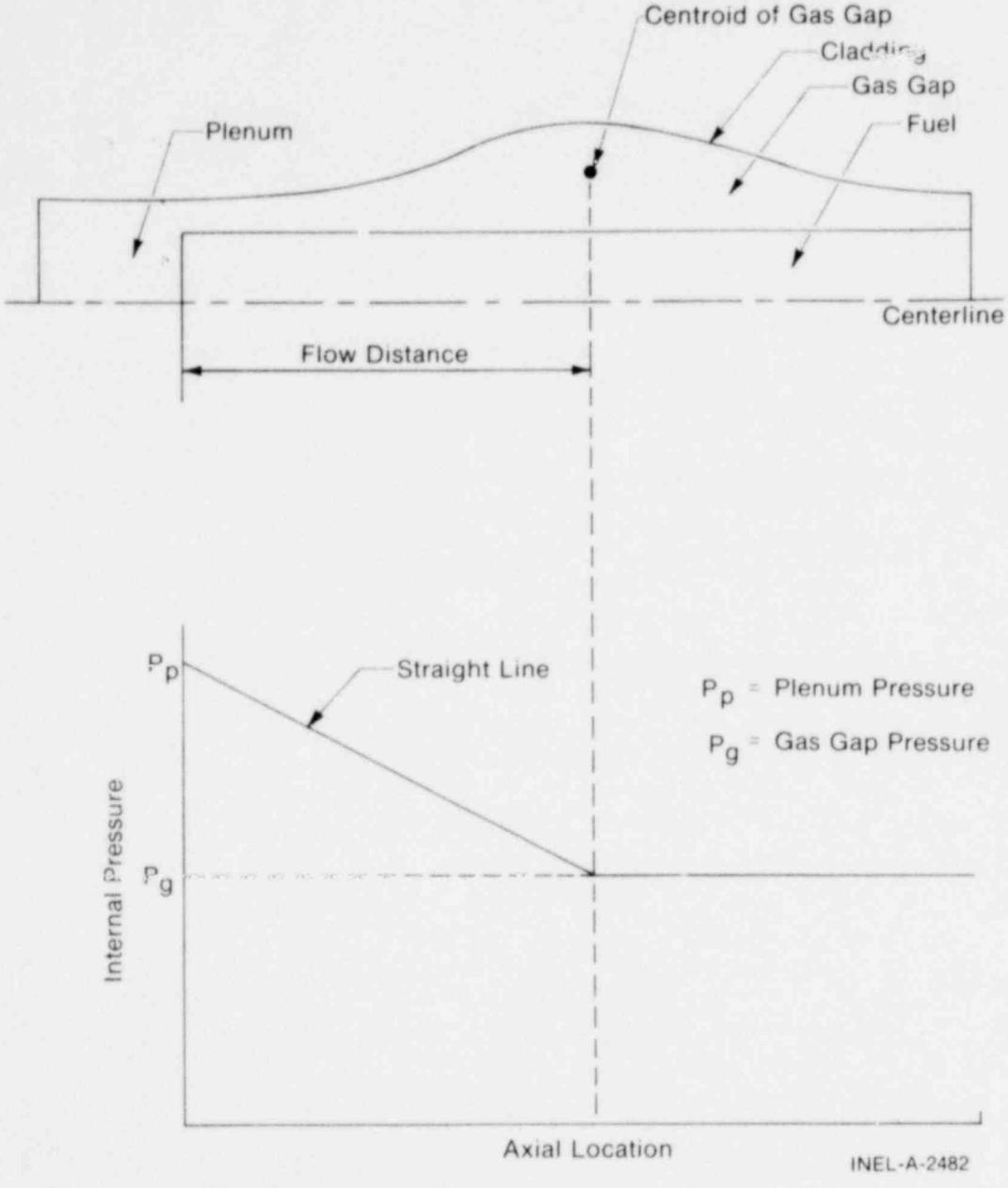

Fig. 7 Internal pressure distribution model.

D_g = mean diameter of gas gap

D_h = hydraulic diameter of gas gap = $2t_{gi}$ for a small gap

The Hagen number is computed by the equation

$$Ha = 22 + 0.24558/(2t_{gi} - 0.0007874). \quad (48)$$

A plot of the relation between Hagen number and gap thickness given by Equation (48) is shown in Figure 8. For gaps smaller than 1 mil, the function is cut off to a value of 1177.

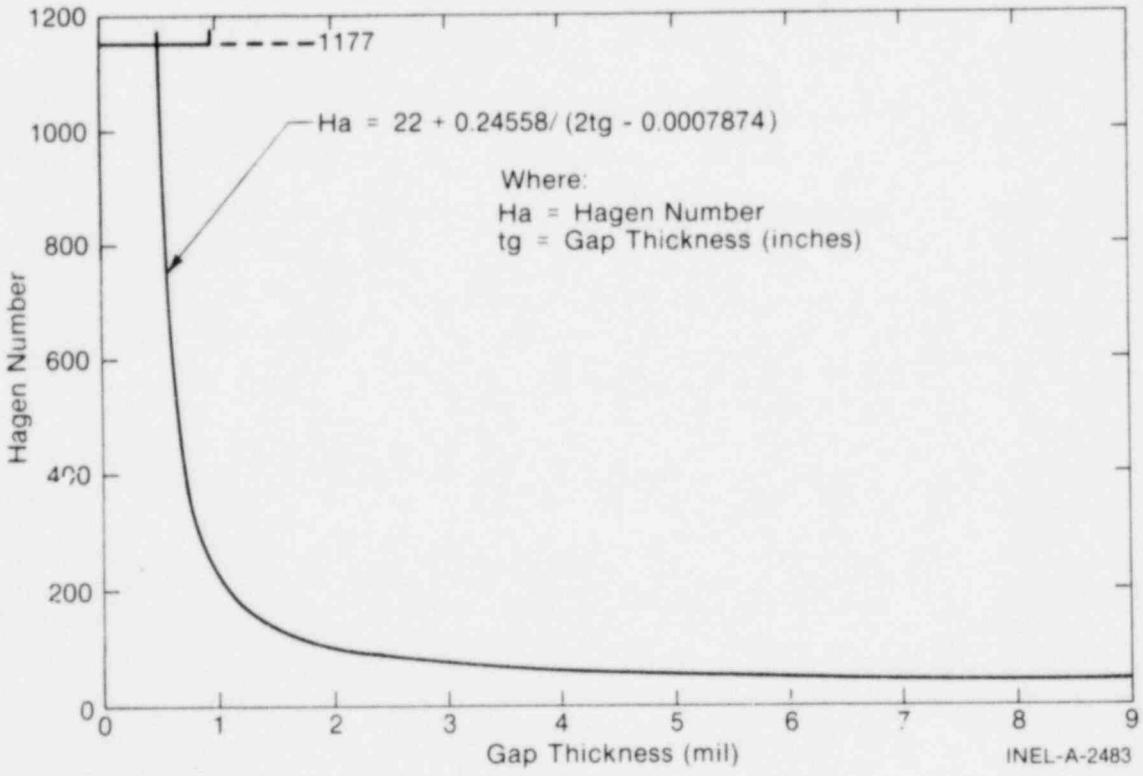

Fig. 8 Hagen number versus gap thickness.

To calculate the gas gap pressure, a modified form of Equation (46) is used. The plenum term is deleted and the moles of gas in the gas gap substituted in place of the moles of gas in the fuel rod.

The subroutine GSFLOW is programmed to solve Equation (47) and calculate the transient gas flow within a fuel rod. Operation of the computer model is as follows:

(1) During each iteration step of FRAP-T, the subroutine GSFLOW is called to calculate the pressure distribution over the length of the fuel rod

(2) At each call, FRAP-T supplies the following information to GSFLOW:

(a) Moles of gas in plenum at start of time step

(b) Moles of gas in gas gap at start of time step

(c) Fuel-cladding gap at each node

(d) Gas temperature at each node

(e) Axial length of each node

(f) Volume of plenum

(g) Volume of gas gap

(h) Axial location of centroid of gas gap (see Figure 7)

(i) Time over which flow is to occur (FRAP-T time step).

(3) Using the above input data, the subroutine GSFLOW calculates the following:

(a) Plenum pressure at the end of the time step

(b) Gas gap pressure at the end of the time step

(c) Moles of gas in plenum and gas gap at end of time step

(d) Axial pressure distribution as a function of the plenum pressure and gas gap pressure (this distribution is shown in Figure 7).

3. CLADDING DEFORMATION

3.1 Assumptions

The cladding deformation model is based on the following assumptions:

1. Incremental theory of plasticity
2. Prandtl-Reuss flow rule
3. Isotropic work-hardening
4. No creep deformation of cladding*
5. Thin wall cladding (stress, strain, and temperature uniform through cladding thickness)
6. If fuel and cladding are in contact, no slippage occurs at fuel-cladding interface
7. Bending strains and stresses in cladding are insignificant
8. Axisymmetric loading and deformation of cladding
9. No axial gaps in the fuel stack.

3.2 Introduction

In analyzing the deformation of fuel rods, three physical situations are considered. First, the fuel pellets and cladding are not in contact. Here, the problem of a cylindrical shell (the cladding) with specified internal and external pressures, and a specified cladding temperature distribution must be solved. This situation is called the "open gap" regime. Heat conduction calculations show that the temperature drop across the cladding is not large. During steady state

operation, for example, a drop of 60 to 100°F is typical. During a LOCA, the drop is even less. Hence, it is reasonable to compute the thermal strains in the cladding on the basis of a single average cladding temperature.

Second, the situation is encountered where the fuel pellets (which are considerably hotter than the cladding) have expanded so as to be in contact with the cladding. Further heating of the fuel results in "driving" the cladding outward. This sit ation is called the "closed gap" regime.

Finally, a third situation occurs in which a number of pellets in contact with the cladding are trapped between the lower end of the fuel rod and a fuel pellet which is in firm contact with the cladding. Then, the axial expansion of the stack of trapped fuel pellets is imparted to the cladding. Here, the problem of a thin cylindrical shell with not only prescribed internal and external pressures, but also a prescribed total change in length must be solved. This situation is called the "trapped stack" regime.

3.3 An Overview of the FRACAS Subcode

The FRACAS (Fuel Rod And Cladding Analysis Subcode) consists of six individual subroutines, each of which is independent of the others. Hence, the model contained in each subroutine can be modified or replaced without requiring changes in any part of the subcode.

Deformation and stresses in the cladding in the open gap regime are computed in subroutine CLADF. The model considered is that of a thin cylindrical shell with specified internal and external pressures and a prescribed uniform temperature.

Calculations for the closed gap regime are made in subroutine COUPLE. The model considered is a thin cylindrical shell with prescribed external pressure and a prescribed radial displacement of its

inside surface. The prescribed displacement is obtained from the fuel thermal expansion models contained in another subcode of FRAP-T. Further, since no slip is assumed to take place when the fuel and cladding are in contact, the axial expansion of the fuel is transmitted directly to the cladding, and hence, the change in axial strain in the shell is also prescribed.

Calculations for the trapped stack regime are made in subroutine STACK. The model considered is a thin cylindrical shell with prescribed internal and external pressures and a prescribed total change in length of the cylinder. In contrast to CLADF and COUPLE, which solve for the stresses and strains at only one axial location at a time, subroutine STACK simultaneously solves for the stresses and strains in all axial nodes which are being strained axially by the trapped stack of fuel pellets.

The decision whether the gap is open or closed, and whether to call COUPLE, STACK, or CLADF is made in the executive subroutine FCMI, (Fuel-Cladding Mechanical Interaction). This is the only subroutine which must be called by FRAP-T to initiate the fuel-cladding interaction analysis. At the completion of this analysis, FCMI returns either a new gap size or a new interface pressure between fuel and cladding for use in the next iteration of the thermal calculations.

In each of COUPLE, STACK, and CLADF, an elastic-plastic solution is obtained. Two additional subroutines, STRAIN and STRESS, compute changes in yield stress with work-hardening, given a uniaxial stress-strain curve. This stress-strain curve is obtained from the material properties package subcode MATPRO[2]. Subroutine STRAIN computes the effective total strain and new effective plastic strain, given a value of effective stress and the effective plastic strain at the end of the last loading increment. Subroutine STRESS computes the effective stress, given an increment of plastic strain and the effective plastic strain at the end of the last loading increment. Depending on the work-hardened value of yield stress, loading can be either elastic or plastic, and unloading is constrained to occur elastically. (Isotropic work-hardening is assumed in these calculations.)

Section 3.4 presents a discussion of the general problem of elastic-plastic analysis in biaxial stress fields. It will be indicated there how the formulation of the problem naturally leads to the Method of Successive Substitutions as a means of obtaining a solution to the coupled, nonlinear elastic-plastic continuum equations. Section 3.5 describes the individual subroutines and the specific equations which are solved.

3.4 General Considerations in Elasto-Plastic Analysis

Problems involving elastic-plastic deformation and multiaxial states of stress involve a number of aspects which do not need to be considered in a uniaxial problem. In the following, an attempt is made to briefly outline the structure of incremental plasticity, and to outline the Method of Successive Substitutions (also called the Method of Successive Elastic Solutions) which has been used so successfully in treating multiaxial elastic-plastic problems[16].

In a problem involving only uniaxial stress, σ_1, the strain, ε_1, is related to the stress by an experimentally determined stress-strain curve as shown in Figure 9, and Hookes's law is taken as

$$\varepsilon_1 = \frac{\sigma_1}{E} + \varepsilon_1^P + \int \alpha \, dT \qquad (49)$$

where ε_1^P is the plastic strain and E is the modulus of elasticity. The onset of yielding occurs at the yield stress, which can be determined directly from Figure 9. Given a load (stress) history, the resulting deformation can be determined in a simple fashion. Increase of yield stress with work-hardening is easily computed directly from Figure 9.

In a problem involving multiaxial states of stress, however, the situation is not so clear cut. Here there must be a method of relating the onset of plastic deformation to the results of a uniaxial test, and further, when plastic deformation occurs, there must be some means of determining how much plastic deformation has occurred, and how it is

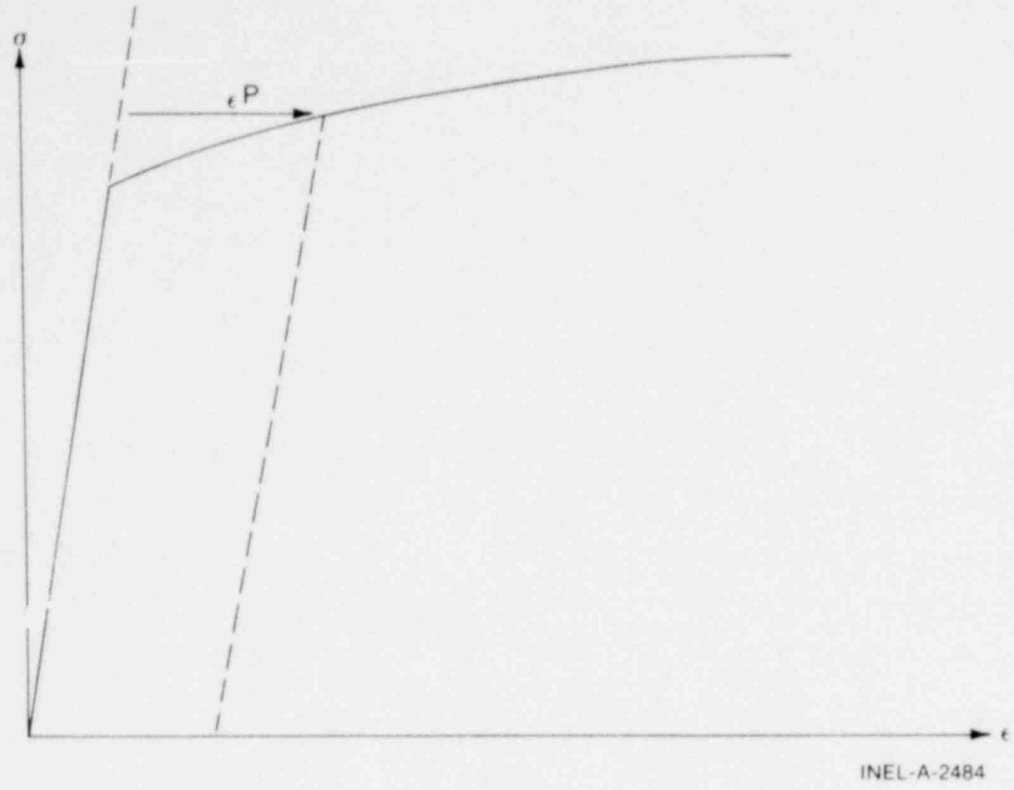

Fig. 9 Typical isothermal stress-strain curve.

distributed among the individual components of strain. These two complications are taken into account by use of the so-called "Yield Function" and "Flow Rule," respectively.

A considerable wealth of experimental evidence exists on the onset of yielding in a multiaxial stress state. The bulk of this evidence supports the von Mises yield criteria, which asserts that yielding occurs when the stress state is such that

$$0.5\,[(\sigma_1 - \sigma_2)^2 + (\sigma_2 - \sigma_3)^2 + (\sigma_3 - \sigma_1)^2] = \sigma_y^2 \qquad (50)$$

where σ_i are the principal stresses, and σ_y is the yield stress as determined in a uniaxial stress-strain test. The square root of the left side of this equation is referred to as the "effective stress", σ_e, and this effective stress is one commonly used type of yield function.

To determine how the yield stress changes with permanent deformation, it is hypothesized that the yield stress is a function of the equivalent plastic strain, ε^P. An increment of equivalent plastic strain is determined at each load step and ε^P is defined as the sum of all increments incurred

$$\varepsilon^P \underset{=}{\Delta} \int d\varepsilon^P \ . \tag{51}$$

Each increment of effective plastic strain is related to the individual plastic strain components by

$$d\varepsilon^P = \frac{2}{3}\left[(d\varepsilon_1^P - d\varepsilon_2^P)^2 + (d\varepsilon_2^P - d\varepsilon_3^P)^2 + (d\varepsilon_3^P - d\varepsilon_1^P)^2\right]^{1/2} \tag{52}$$

where the $d\varepsilon_i^P$ are the plastic strain components in principal coordinates. It is a well-known experimental result that at pressure on the order of the yield stress, plastic deformation occurs with no change in volume. This implies that

$$d\varepsilon_1^P + d\varepsilon_2^P + d\varepsilon_3^P = 0 \tag{53}$$

and hence, in a uniaxial test with $\sigma_1 = \sigma$, $\sigma_2 = \sigma_2 = 0$, the plastic strain increments are

$$d\varepsilon_2^P = d\varepsilon_3^P = -1/2\ d\varepsilon_1^P$$

so that in a uniaxial test, Equations (50) and (52) reduce to

$$\sigma_e = \sigma$$

$$d\varepsilon^P = d\varepsilon_1^P \quad . \tag{54}$$

Thus, when it is assumed that the yield stress is a function of the total effective plastic strain (called the Strain Hardening Hypothesis), the functional relationship between yield stress and plastic strain can be taken directly from a uniaxial stress-strain curve by virtue of Equation (54).

The relationship between the magnitudes of the plastic strain increments and the effective plastic strain increment is provided by the Prandtl-Reuss Flow Rule:

$$d\varepsilon_i^P = \frac{3\, d\varepsilon^P}{2\, \sigma_e} \quad S_i \qquad i = 1, 3 \tag{55}$$

where S_i are the deviatoric stress components (in principal coordinates) defined by

$$s_i = \sigma_i - \frac{1}{3}(\sigma_1 + \sigma_2 + \sigma_3) \qquad i = 1, 3 \quad . \tag{56}$$

Equation (55) embodies the fundamental observation of plastic deformation, that the plastic strain increments are proportional to the deviatoric stresses. It may be shown[16] that the constant of proportionality is determined by the choice of the yield function. Direct substitution shows that Equations (50), (51), (52), (53), and (54) are consistent with one another.

Once the plastic strain increments have been determined for a given load step, the total strains are determined from a generalized form of Hooke's law given by

$$\left.\begin{aligned}
\varepsilon_1 &= \frac{1}{E}\{\sigma_1 - \nu(\sigma_2 + \sigma_3)\} + \varepsilon_1^P + d\varepsilon_1^P + \int \alpha dT \\
\varepsilon_2 &= \frac{1}{E}\{\sigma_2 - \nu(\sigma_1 + \sigma_3)\} + \varepsilon_2^P + d\varepsilon_2^P + \int \alpha dT \\
\varepsilon_3 &= \frac{1}{E}\{\sigma_3 - \nu(\sigma_2 + \sigma_1)\} + \varepsilon_3^P + d\varepsilon_3^P + \int \alpha dT
\end{aligned}\right\} \qquad (57)$$

in which ε_1^P, ε_2^P, and ε_3^P are the total plastic strain components at the end of the previous load increment.

The remaining continuum field equations of equilibrium, strain displacement, and strain compatibility are unchanged. The complete set of governing equations is presented in Table VII, written in terms of rectangular Cartesian coordinates and employing the usual indicial notation in which a repeated Latin index implies summation. This set of equations is augmented by experimentally determined uniaxial stress-strain relation.

3.4.1 The Method of Solution. When the problem under consideration is statically determinate, so that stresses can be found from equilibrium conditions alone, the resulting plastic deformation can easily be determined. However, when the problem is statically indeterminate, and the stresses and deformation must be found simultaneously, then the full set of plasticity equations proves to be quite formidable even in the case of simple loadings and geometries.

One numerical procedure which has been used with considerable success is the Method of Successive Substitutions. This can be applied to any problem for which an elastic solution can be obtained, either in closed form or numerically. A full discussion of this technique, including a number of technologically useful examples is contained in Reference 16.

TABLE VII

FRACAS GOVERNING EQUATIONS

Equilibrium

$$\sigma_{ji,j} + \rho f_i = 0$$

where σ = stress tension

ρ = mass density

f_i = components of body force per unit mass

Stress Strain

$$\varepsilon_{ij} = \frac{1+\nu}{E}\sigma_{ij} - \delta_{ij}\left(\frac{\nu}{E}\sigma_{kk} - \int \alpha dT\right) + \varepsilon^P_{ij} + d\varepsilon^P_{ih}$$

Compatibility

$$\varepsilon_{ij,k\ell} + \varepsilon_{k\ell,ij} - \varepsilon_{ik,j\ell} - \varepsilon_{j\ell,ik} = 0$$

Definitions Used in Plasticity

$$\sigma_e \triangleq \sqrt{\frac{3}{2} S_{ij} S_{ij}}$$

$$S_{ij} \triangleq \sigma_{ij} - \frac{1}{3}\sigma_{kk}$$

$$d\varepsilon^P \triangleq \sqrt{\frac{2}{3} d\varepsilon^P_{ij}\, d\varepsilon^P_{ij}}$$

Prandtl-Reuss Flow Rule

$$d\varepsilon^P_{ij} = \frac{3}{2}\frac{d\varepsilon^P}{\sigma_e} S_{ij}$$

Briefly, the method involves breaking the loading path up into a number of small increments. For example, in the present application, the loads are external pressure, temperature, and either internal pressure or prescribed displacement of the inside surface of the cladding. These loads all vary during the operating history of the fuel rod. For each new increment of the loading, the solution to all the plasticity equations listed in Table VII is obtained as follows.

First, an initial estimate of the plastic strain increments, $d\varepsilon_{ij}^{P}$, is made. Based on these values, the equations of Equilibrium, Hooke's Law, and Strain-Displacement and Compatibility are solved as for any elastic problem. From the stresses so obtained, the deviatoric stresses, S_{ij}, may be computed. This represents one path in the computational scheme.

Independently, using the assumed $d\varepsilon_{ij}^{P}$ values, the increment of effective plastic strain, $d\varepsilon^{P}$, may be computed, and from this and the stress-strain curve, a value of the effective stress, σ_e, is obtained.

Finally, a new estimate of the plastic strain increments is obtained from the Prandtl-Reuss flow rule

$$d\varepsilon_{ij}^{P} = \frac{3}{2} \frac{d\varepsilon^{P}}{\sigma_e} S_{ij} \tag{58}$$

and the entire process is continued until the $d\varepsilon_{ij}^{P}$ converge. A schematic of the iteration scheme is shown in Figure 10.

The mechanism by which improved estimates of $d\varepsilon_{ij}^{P}$ are obtained results from the fact that the effective stress obtained from $d\varepsilon^{P}$ and the stress-strain curve will not be equal to the effective stress which would be obtained from the stresses from the elastic solution; they will only agree when convergence is obtained.

The question of convergence is one that cannot, in general, be answered a priori. However, it can be shown[16] that convergence will be obtained for sufficiently small load increments. For the problem at

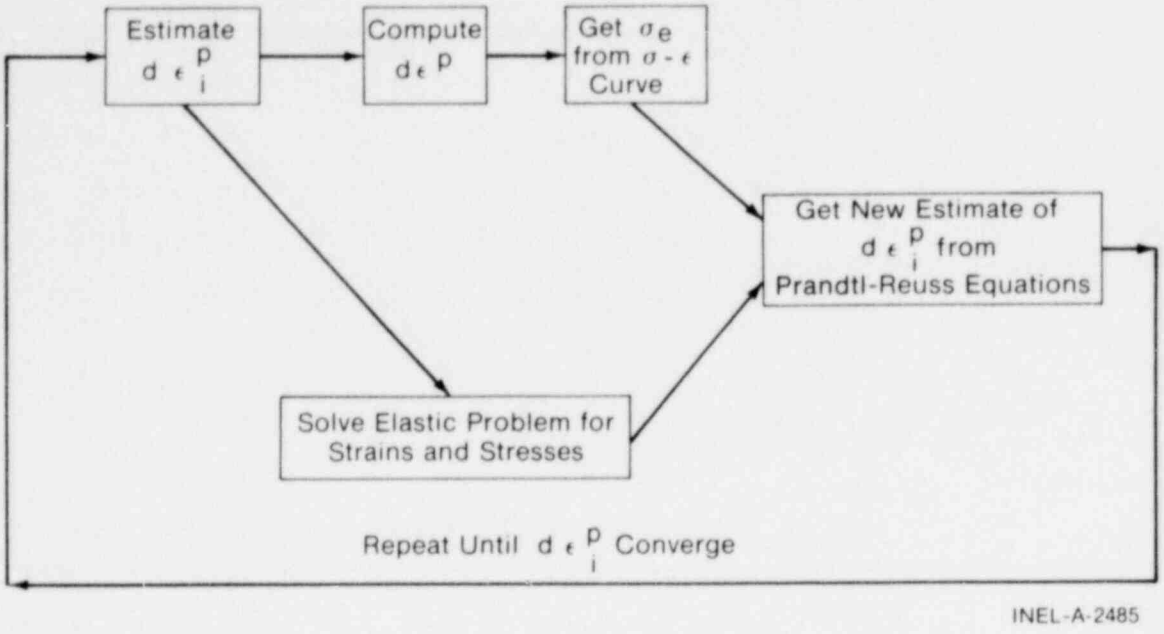

Fig. 10 Schematic of the method of successive elastic solutions.

hand, it has been found that incrementing the average fuel temperature by 100°F is not too large. Thus, it is clear that unreasonably small load increments are not required. The details of this computational scheme, as applied to driven cladding deformation, are presented in Subsections 3.5.3 and 3.5.4.

3.5 Description of Individual Subroutines

The package of subroutines which perform the Fuel-Cladding Mechanical Interaction analysis consists of six. FCMI is the executive subroutine, and it calls either COUPLE, STACK, or CLADF, as appropriate. STRESS and STRAIN are called by either CLADF or COUPLE to obtain the necessary mechanical properties. These six subroutines are described in detail below.

3.5.1 Subroutine FCMI. Subroutine FCMI performs the basic function of determining whether or not the fuel pellets and the cladding are in contact. The radial expansion of the fuel is obtained from models contained externally to the fuel-cladding interaction subroutines, and is passed to FCMI in the calling sequence. Stress effects on the fuel expansion are known to be small relative to thermal expansion and swelling, and so the fuel expansion is assumed to be uncoupled from the cladding deformation.

The decision whether or not the fuel is in contact with the cladding is made by comparing the radial displacement of the fuel with the radial displacement which would occur in the cladding due to the prescribed external (coolant) pressure and the prescribed internal (fission and fill gas) pressure. Both of these values are passed to FCMI through the calling sequence. This free cladding radial displacement is obtained in CLADF. Then, if

$$u_r^{fuel} \geq u_r^{clad} + \delta \qquad (59)$$

where δ is the initial (as-fabricated) gap between the fuel and the cladding, the fuel is determined to be in contact with the cladding. The as-fabricated gap, δ, is a constant which does not change throughout the loading history of the rod. The loading history enters into this decision by virture of the permanent plastic cladding strains which are used in the CLADF solution, and which are updated at each call to CLADF or COUPLE. These plastic strains (and total effective plastic strain, ε^P) are stored in the main calling program, and are passed to FCMI through the calling sequence.

If the fuel and cladding displacements are such that Equation (59) is not satisfied, the gap has not closed during the current load step, and the solution obtained by CLADF is the appropriate solution. The current value of the gap is computed and passed back to the main calling program. The plastic strain values may be changed in the solution obtained by CLADF if additional plastic straining has occurred.

If Equation (59) is satisfied, however, the fuel and the cladding have come into contact during the current loading increment. At the contact interface, radial continuity requires that

$$u_r^{clad} = u_r^{fuel} - \delta \qquad (60)$$

while in the axial direction it is assumed that no slip occurs between the fuel and the cladding.

It must be noted that only the additional strain which occurs in the fuel after "lock-up" has occurred is transferred to the cladding. Thus, if $\varepsilon_{z,o}^{clad}$ is the axial strain in the cladding just prior to contact, and $\varepsilon_{z,o}^{fuel}$ is the corresponding axial strain in the fuel, then the no-slip condition in the axial direction becomes

$$\varepsilon_z^{clad} - \varepsilon_{z,o}^{clad} = \varepsilon_z^{fuel} - \varepsilon_{z,o}^{fuel} \quad . \qquad (61)$$

The values of the "pre-strains", $\varepsilon_{z,o}^{fuel}$ and $\varepsilon_{z,o}^{clad}$, are set equal to the values of the strains which existed in the fuel and cladding at the time of gap closure and are stored in the main calling program and passed to FCMI in the calling sequence. They are updated at the end of any load increment during which the gap closed.

After u_r^{clad} and ε_z^{clad} have been computed in FCMI, they are passed to subroutine COUPLE, which considers a thin cylindrical shell with prescribed axial strain, external pressure, and prescribed radial displacement of its inside surface. After the solution to this problem is obtained in COUPLE, subroutine FCMI passes a value of the interface pressure back to the main calling program, along with new plastic strains and stresses.

3.5.2 Subroutine CLADF. This subroutine considers a thin cylindrical shell loaded by both internal and external pressures. Axisymmetric loading and deformation are assumed. Loading is also restricted to being uniform in the axial direction; and no bending is considered. The geometry and coordinates are shown in Figure 11. The displacements

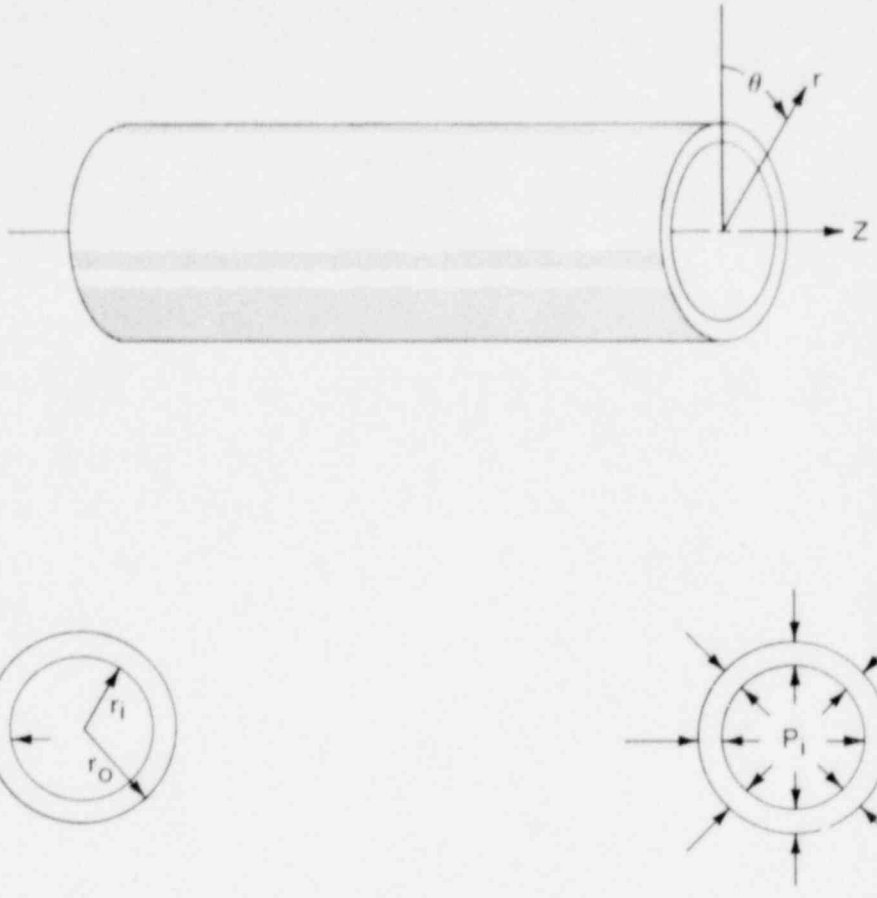

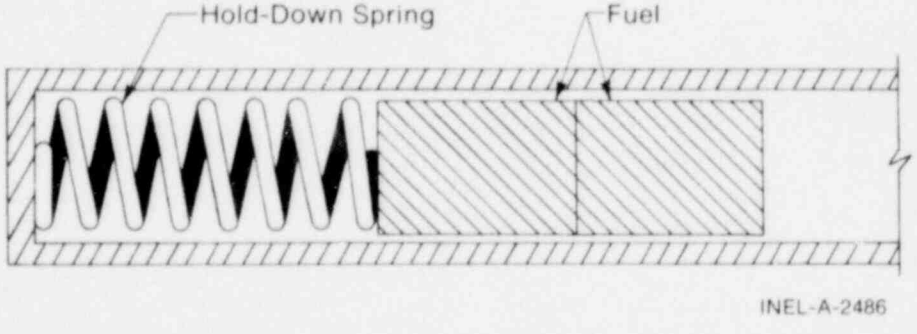

Fig. 11 Fuel rod geometry and coordinates.

of the midplane of the shell are u and w in the radial and axial directions, respectively.

Then, as is well-known, the equilibrium equations simplify considerably, and are identically satisfied by

$$\sigma_\theta = \frac{r_i P_i - r_o P_o}{t} \tag{62}$$

$$\sigma_z = \frac{\pi r_i^2 P_i - \pi r_o^2 P_o}{\pi(r_o^2 - r_i^2)} \tag{63}$$

where

σ_θ = hoop stress

σ_z = axial stress

r_i = inside radius of cladding

r_o = outside radius of cladding

P_i = internal pressure of fuel rod

P_o = coolant pressure

$t = r_o - r_i$ = cladding thickness.

For membrane shell theory[17], the strains are related to the midplane displacements by

$$\varepsilon_z = \frac{\partial w}{\partial z} \tag{64}$$

$$\varepsilon_\theta = \frac{u}{r} \tag{65}$$

where $\bar{r}$ is the radius of the midplane. Strain across the thickness of the shell will be allowed. In shell theory, since the radial stress can be neglected, and since the hoop stress, σ_θ, and axial stress, σ_z, are uniform across the thickness when bending is not considered, the radial strain is due only to the Poisson's effect, and is uniform across the thickness. (Normally, radial strains are not considered in a shell theory, but when plastic deformations are to be considered, plastic radial strains must be included.)

The stress-strain relations are written in the incremental form

$$\varepsilon_\theta = \frac{1}{E}\{\sigma_\theta - \nu\,\sigma_z\} + \varepsilon_\theta^P + d\varepsilon_\theta^P + \int_{T_o}^{T} \alpha\, dT \qquad (66)$$

$$\varepsilon_z = \frac{1}{E}\{\sigma_z - \nu\,\sigma_\theta\} + \varepsilon_z^P + d\varepsilon_z^P + \int_{T_o}^{T} \alpha\, dT \qquad (67)$$

$$\varepsilon_r = -\frac{\nu}{E}\{\sigma_\theta + \sigma_z\} + \varepsilon_r^P + d\varepsilon_r^P + \int_{T_o}^{T} \alpha\, dT \qquad (68)$$

in which T_o is the strain-free reference temperature, α is the coefficient of thermal expansion, T is the current average cladding temperature, E is the modulus of elasticity, and ν is Poisson's ratio. The terms ε_θ^P, ε_z^P, and ε_r^P are the plastic strains at the end of the last load increment, and $d\varepsilon_\theta^P$, $d\varepsilon_r^P$, and $d\varepsilon_z^P$ are the additional plastic strain increments which occur due to the new load increment.

As discussed in Section 3.4, the magnitudes of the additional plastic strain increments are determined by the effective stress and the Prandtl-Reuss Flow rule, namely

$$\sigma_e = \frac{1}{2}\left\{(\sigma_\theta - \sigma_z)^2 + (\sigma_z)^2 + (\sigma_\theta)^2\right\}^{1/2} \tag{69}$$

$$\left.\begin{aligned} d\varepsilon_\theta^P &= \frac{3}{2}\,\frac{S_\theta}{\sigma_e}\,d\varepsilon^P \\ d\varepsilon_z^P &= \frac{3}{2}\,\frac{S_z}{\sigma_e}\,d\varepsilon^P \\ d\varepsilon_r^P &= -\,d\varepsilon_\theta^P - d\varepsilon_z^P \end{aligned}\right\} \tag{70}$$

$$\left.\begin{aligned} S_\theta &= \sigma_\theta - \frac{1}{3}(\sigma_\theta + \sigma_z) \\ S_z &= \sigma_z - \frac{1}{3}(\sigma_\theta + \sigma_z) \\ S_r &= -\frac{1}{3}(\sigma_\theta + \sigma_z) \quad . \end{aligned}\right. \tag{71}$$

The solution in CLADF proceeds as follows. At the end of the last load increment the plastic strain components, ε_r^P, ε_θ^P, and ε_z^P are known, and also the total effective plastic strain, ε^P, is known.

The loading is now incremented with the prescribed values of P_i, P_o, and T. The new stresses can be determined immediately from Equations (62) and (63), and a new value of effective stress is obtained from Equation (69).

The increment of effective plastic strain, $d\varepsilon^P$, which results from the current increment of loading, can now be determined from the uniaxial stress-strain curve at the new value of σ_e, as shown in Figure 12. (The new elastic loading curve depends on the value of ε^P.) This computation is performed by subroutine STRAIN.

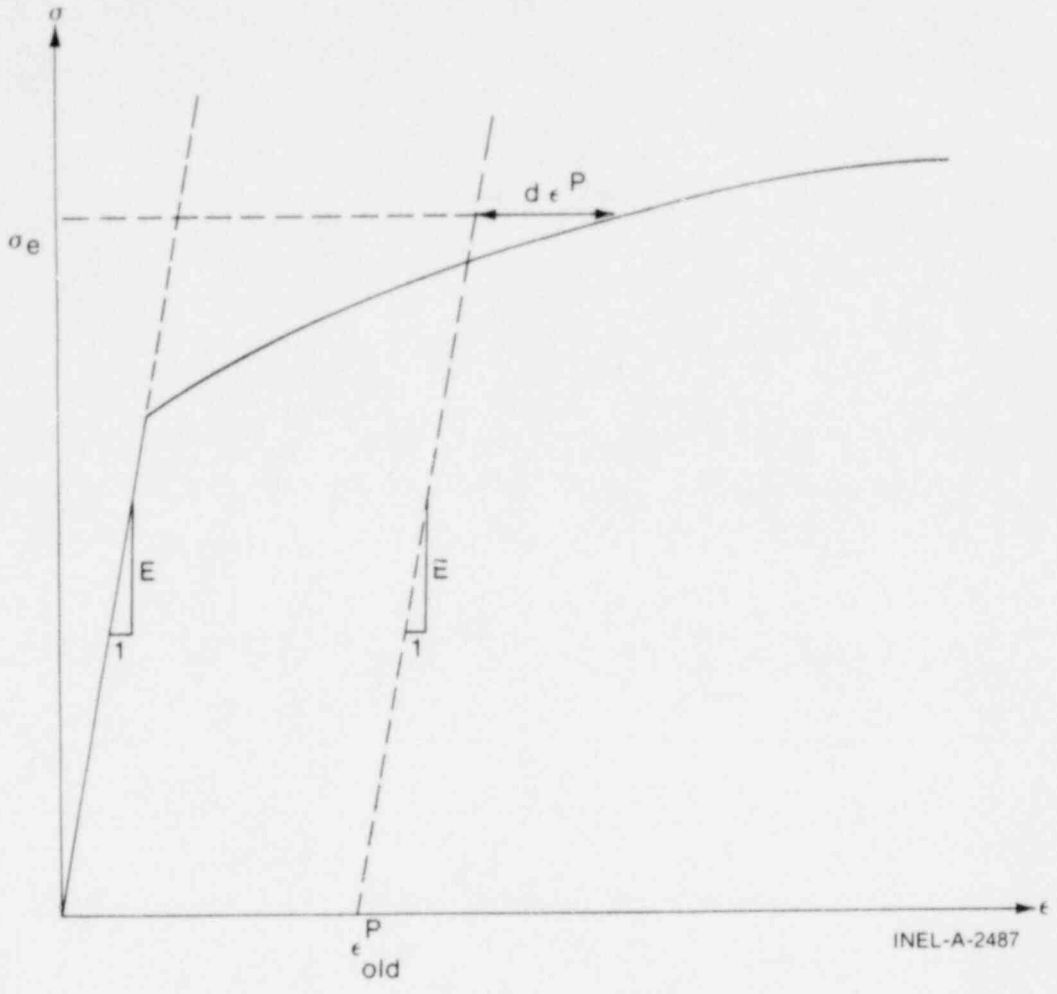

Fig. 12 Calculation of effective stress σ_e from $d\varepsilon^p$.

Once $d\varepsilon^P$ is determined, the individual plastic strain components are found from Equation (70), and the total strain components are obtained from Equations (66) through (68).

The displacement of the inside surface of the shell must be determined so that a new gap width can be computed. The radial displacement of the inside surface is given by

$$u(r_i) = \bar{r}\,\varepsilon_\theta - \frac{t}{2}\,\varepsilon_r \qquad (72)$$

where the first term is the radial displacement of the midplane [from Equation (65)] and ε_r is the uniform strain across the thickness, t.

The cladding thickness, t, is computed by the equation

$$t = (1 + \varepsilon_r)\, t_o$$

$$t_o = \text{cold state, unstressed thickness of cladding.} \qquad (73)$$

The final step performed by CLADF prior to returning control to FCMI is to add the plastic strain increments to the previous plastic strain values, i.e.,

$$\begin{aligned}
(\varepsilon_\theta^P)_{new} &= (\varepsilon_\theta^P)_{old} + d\varepsilon_\theta^P \\
(\varepsilon_z^P)_{new} &= (\varepsilon_z^P)_{old} + d\varepsilon_z^P \\
(\varepsilon_r^P)_{new} &= (\varepsilon_r^P)_{old} + d\varepsilon_r^P \qquad (74) \\
(\varepsilon^P)_{new} &= (\varepsilon^P)_{old} + d\varepsilon^P
\end{aligned}$$

and these values are returned to FCMI for use at the next load increment.

Thus, all the stresses and strains can be computed directly since, in this case, the stresses are determinant. In the case of the driven cladding displacement, the stresses depend on the displacement, and such a straightforward solution is not possible.

3.5.3 Subroutine COUPLE. This subroutine considers the problem of a cylindrical shell for which the radial displacement of the inside surface and axial strain are prescribed. Here the stresses cannot be computed directly since the pressure at the inside surface (the interface pressure) must be determined as part of the solution.

As in CLADF, the displacement at the inside surface is given by

$$u(r_i) = u - \frac{t}{2}\,\varepsilon_r \tag{75}$$

where u is the radial displacement of the midplane. From Equation (65), $u = \bar{r}\,\varepsilon_\theta$ and, hence

$$u(r_i) = \bar{r}\,\varepsilon_\theta - \frac{t}{2}\,\varepsilon_r \ . \tag{76}$$

Thus, prescribing the displacement of the inside surface of the shell is equivalent to a constraining relation between ε_θ and ε_r. As before, Hooke's law is taken in the form

$$\varepsilon_\theta = \frac{1}{E}\,(\sigma_\theta - \nu\,\sigma_z) + \varepsilon_\theta^P + d\varepsilon_\theta^P + \int_{T_o}^{T} \alpha\,dT \tag{77}$$

$$\varepsilon_z = \frac{1}{E}\,(\sigma_z - \nu\,\sigma_\theta) + \varepsilon_z^P + d\varepsilon_z^P \int_{T_o}^{T} \alpha\,dT \tag{78}$$

$$\varepsilon_r = -\frac{\nu}{E}\,(\sigma_\theta + \sigma_z) + \varepsilon_r^P + d\varepsilon_r^P + \int_{T_o}^{T} \alpha\,dT \ . \tag{79}$$

Using Equations (76) and (79) in Equation (77) yields a relation between the stresses σ_θ, σ_z, and the prescribed displacement $u(r_i)$,

$$\frac{u(r_i)}{\bar{r}} + \frac{1}{2}\,\left(\frac{t}{r}\right)\,\{\varepsilon_r^P + d\varepsilon_r^P + \int_{T_o}^{T} \alpha\,dT\}$$

$$- \{\varepsilon_\theta^P + d\varepsilon_\theta^P + \int_{T_o}^{T} \alpha\,dT\} = \frac{1}{E}\,[(1 + \frac{\nu}{2}\,\frac{t}{r})\,\sigma_\theta$$

$$+ \nu\,(\frac{1}{2}\,\frac{t}{r} - 1)\,\sigma_z\,]. \tag{80}$$

Equations (78) and (80) are now a pair of simultaneous algebraic equations for the stresses σ_θ and σ_z, which may be written as

$$\begin{bmatrix} A_{11} & A_{12} \\ A_{21} & A_{22} \end{bmatrix} \begin{bmatrix} \sigma_\theta \\ \sigma_z \end{bmatrix} = \begin{bmatrix} B_1 \\ B_2 \end{bmatrix}$$

where

$$A_{11} = 1 + \frac{\nu}{2} \frac{t}{r}$$

$$A_{12} = \nu \left(\frac{1}{2} \frac{t}{r} - 1\right)$$

$$A_{21} = -\nu$$

$$A_{22} = 1$$

$$B_1 = E \frac{u(r_i)}{r} + \frac{E}{2} \left(\frac{t}{r}\right) \left[e_r^P + d\varepsilon_r^P + \int_{T_o}^{T} \alpha dT\right]$$

$$-E \left\{\varepsilon_\theta^P + d\varepsilon_\theta^P + \int_{T_o}^{T} \alpha dT\right\}$$

$$B_2 = E \varepsilon_z - E\left\{\varepsilon_z^P + d\varepsilon_z^P + \int_{T_o}^{T} \alpha dT\right\} .$$

Then the stresses can be written explicitly as

$$\sigma_\theta = \frac{B_1 A_{22} - B_2 A_{12}}{A_{11} A_{22} - A_{12} A_{21}} \tag{81}$$

$$\sigma_z = \frac{B_2 A_{11} - B_1 A_{21}}{A_{11} A_{22} - A_{12} A_{21}} . \tag{82}$$

These equations relate the stresses to $u(r_i)$ and ε_z, which are prescribed, and to $d\varepsilon_\theta^P$, $d\varepsilon_z^P$, and $d\varepsilon_r^P$, which are to be determined. The remaining equations which must be satisfied are

$$\sigma_e = \frac{1}{\sqrt{2}} \{(\sigma_\theta - \sigma_z)^2 + (\sigma_\theta)^2 + (\sigma_z)^2\}^{1/2} \tag{83}$$

$$d\varepsilon_p = \frac{2}{3} \{(d\varepsilon_r^P - d\varepsilon_\theta^P)^2 + (d\varepsilon_\theta^P - d\varepsilon_z^P)^2 + (d\varepsilon_z^P - d\varepsilon_r^P)^2\}^{1/2} \tag{84}$$

and the Prandtl-Reuss Flow Equations [defined in Equation (70)]

$$d\varepsilon_\theta^P = \frac{3}{2} \frac{d\varepsilon^P}{\sigma_e} [\sigma_\theta - \frac{1}{3} (\sigma_\theta + \sigma_z)]$$

$$d\varepsilon_z^P = \frac{3}{2} \frac{d\varepsilon^P}{\sigma_e} [\sigma_z - \frac{1}{3} (\sigma_\theta + \sigma_z)] \tag{85}$$

$$d\varepsilon_r^P = - d\varepsilon_\theta^P - d\varepsilon_z^P \ .$$

The effective stress, σ_e, and the plastic strain increment, $d\varepsilon^P$, must, of course, be related by the uniaxial stress-strain law. Equations (81) through (85) must be simultaneously satisfied for each loading increment.

As discussed in Section 3.3, a straightforward numerical solution to these equations can be obtained via the Method of Successive Substitutions. Here, arbitrary values are initially assumed for the increments of plastic strain, and Equations (81) through (85) are used to obtain improved estimates of the plastic strain components. The steps performed by COUPLE are as follows for each increment of load:

(1) Values of $d\varepsilon_\theta^P$, $d\varepsilon_z^P$, and $d\varepsilon_r^P$ are assumed. Then, $d\varepsilon^P$ is computed from Equation (76) and the effective stress is obtained from the stress-strain curve at the value of ε^P by calling subroutine STRESS.

(2) From Hooke's law, still using the assumed plastic strain increments and the prescribed values of $u(r_i)$ and ε_z, values for the stresses can be obtained from Equations (81) and (82).

(3) New values for $d\varepsilon_\theta^P$, $d\varepsilon_z^P$, and $d\varepsilon_r^P$ are now computed from the Prandtl-Reuss relations,

$$d\varepsilon_i^P = \frac{3}{2}\frac{d\varepsilon^P}{\sigma_e}\left[\sigma_i - \frac{1}{3}(\sigma_\theta + \sigma_z)\right] \qquad i = 1, 3$$

using σ_e as computed in Step (1), and σ_i as computed in Step (2).

(4) The old and new values of $d\varepsilon_\theta^P$, $d\varepsilon_z^P$, and $d\varepsilon_r^P$ are compared and the process continued until convergence is obtained.

(5) Once convergence has been obtained, the interface pressure is computed from Equation (62)

$$P_{int} = \frac{t\,\sigma_\theta + r_o\,P_o}{r_i} \quad . \tag{86}$$

When Steps (1) through (5) have been accomplished, the solution is complete, provided that the interface pressure is not less than the local gas pressure.

Due to unequal amounts of plastic straining in the hoop and axial directions, however, it often happens upon unloading that the interface pressure as obtained in Step (5) is less than the gas pressure, even though the gap has not opened. When this situation occurs, the frictional "locking" mechanism (which is assumed to constrain the cladding axial deformation to equal the fuel axial deformation) can no longer act. The axial strain and stress adjust themselves so that the interface pressure just equals the gas pressure, at which point the axial strain is again "locked". Thus, upon further unloading, the axial strain and the hoop and axial stresses continually readjust themselves to maintain the interface pressure equal to the gas pressure until the

gap opens. Since the unloading occurs elastically, a solution for this portion of the fuel-cladding interaction problem can be obtained directly as follows.

Since the external pressure and the interface pressure are known, the hoop stress is obtained from Equation (55) as

$$\sigma_\Theta = \frac{r_i P_{int} - r_o P_o}{t} \quad . \tag{87}$$

From Equation (76) it is possible to write

$$\varepsilon_\Theta = \frac{u_r^{fuel} - \delta + t/2\ \varepsilon_r}{\bar{r}} \quad . \tag{88}$$

Substituting ε_Θ and ε_r, as given by Equations (77) and (79), into Equation (88) gives an explicit equation for σ_z as

$$\nu\, r_i\, \sigma_z = (\bar{r} + \nu\, t/2)\, \sigma_\Theta + \bar{r}\, E \left(\int \alpha dT + \varepsilon_\Theta^P \right) - \frac{t}{2} E \left(\int \alpha dT + \varepsilon_r^P \right) - E\, u\, (r_i) \tag{89}$$

in which σ_Θ is known from Equation (87). With σ_z and σ_Θ known, the strains may be computed from Hooke's law, Equations (77) through (79). This set of equations is included in subroutine COUPLE and is automatically invoked when a value of P_{int} less than the local gas pressure is computed.

As in CLADF, the last step performed by COUPLE before returning control to FCMI is to set the plastic strain components and total effective strain, ε^P, equal to their new values by adding in the computed increments $d\varepsilon_i^P$ and $d\varepsilon^P$.

3.5.4 Subroutine STACK. Subroutine STACK is called when one or more fuel pellet nodes are trapped between the lower end of the cladding and a pellet in firm contact with the cladding, as shown in Figure 13. In this case, the axial expansion of the fuel will be imparted to the cladding even though the cladding and fuel are not in contact.

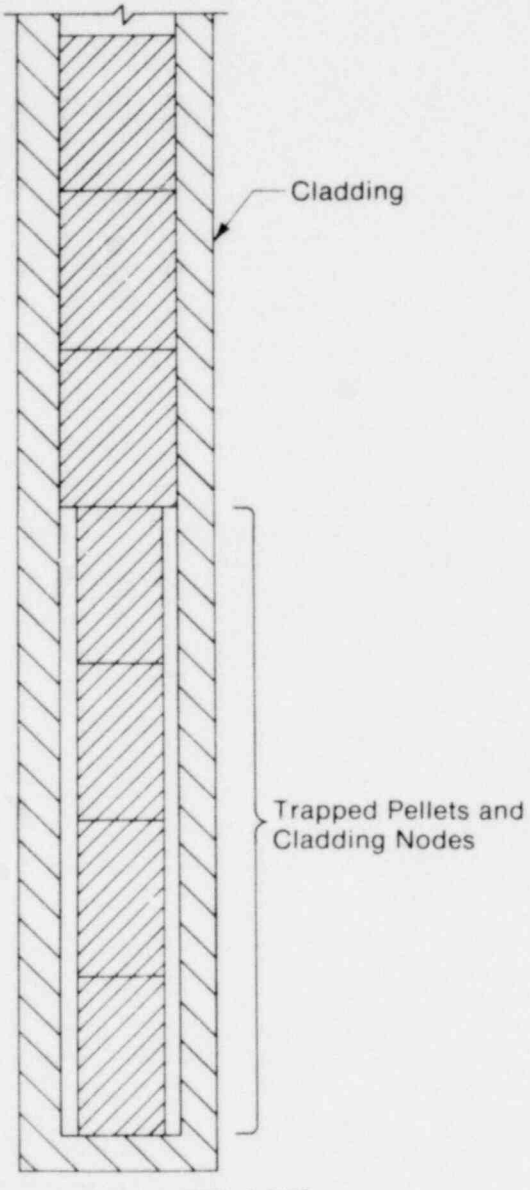

Fig. 13 Schematic of trapped stack.

The total change in length of the trapped cladding is computed in FCMI, and passed to STACK in the calling sequence. For each axial node in the trapped cladding, the axial strain is given by

$$\varepsilon_z(i) = \frac{1}{E(i)} \left[\sigma_z - \nu(i)\, \sigma_\theta(i) \right] + \varepsilon_z^P(i) + d\varepsilon_z^P(i) + \int_{T_o}^{T(i)} \alpha dT \quad (90)$$

in which i denotes the axial node number. Axial force equilibrium requires that σ_z be the same in each node. Since the total length change is prescribed, it is possible to write

$$\Delta\ell = \sum_{i=1}^{n} \left[\varepsilon_z(i) - \varepsilon_z^o(i) \quad dz(i) \right] \quad (91)$$

in which dz(i) are the axial cladding node lengths, and ε_z^o are the axial strains in the cladding at the end of the last load step. Inserting Equation (92) in the above equation yields

$$\sigma_z = \left[\sum_{i=1}^{N} \frac{E(i)}{dz(i)} \right] \left\{ \Delta\ell + \sum_{i=1}^{N} dz(i) \left[\frac{\nu(i)\, \sigma_\theta(i)}{E(i)} + \varepsilon_z^o(i) - \varepsilon_z^P(i) - d\varepsilon_z^P(i) - \int_{T_c}^{T(i)} \alpha dT \right] \right\} . \quad (92)$$

The equation for effective cladding stress [defined in Equation (69)] is

$$\sigma_e(t) = \sigma_z^2 + \sigma_\theta^2(i) - \sigma_z\, \sigma_\theta(i) \quad (93)$$

The equation for increment of effective plastic strain (defined in Equation (52)) is

$$d\varepsilon^P(i) = \sqrt{\frac{2}{3}} \left\{ \left[d\varepsilon_z^P(i) - d\varepsilon_r^P(i) \right]^2 + \left[d\varepsilon_z^P(i) - d\varepsilon_\theta^P(i) \right]^2 + \left[d\varepsilon_r^P(i) - d\varepsilon_\theta^P(i) \right]^2 \right\}^{1/2} . \quad (94)$$

As defined in Equation (70), the equations for the components of plastic strain increment are

$$d\varepsilon_z^P(i) = \frac{3}{2}\frac{d\varepsilon^P(i)}{\sigma_e(i)}\left\{\sigma_z - \frac{1}{3}\left[\sigma_z + \sigma_\theta(i)\right]\right\}$$

$$d\varepsilon_\theta^P(i) = \frac{3}{2}\frac{d\varepsilon^P(i)}{\sigma_e(i)}\left\{\sigma_\theta - \frac{1}{3}\left[\sigma_z + \sigma_\theta(i)\right]\right\} \qquad (95)$$

$$d\varepsilon_r^P(i) = -\,d\varepsilon_\theta^P(i) - d\varepsilon_z^P(i) \quad .$$

Equations (92) through (95) must be simultaneously satisfied for all the trapped axial cladding nodes. And since the nodes may have different temperatures, different stress-strain curves are used at different nodes.

As before, the Method of Successive Elastic Solutions is used. In contrast to subroutine COUPLE, however, the method is applied simultaneously to several axial nodes. Because more than one node is being considered, two additional possibilities arise.

The first is the possibility that, due to the axial stretching and Poisson's effect, some (or all) of the cladding nodes may come into contact with the fuel pellets, although contact would not occur due to internal and external pressure alone. In this case, the hoop stress in Equation (92) is no longer given by Equation (62), but now depends on σ_z and the radial displacement of the fuel. While contact occurs, however, radial compatibility as expressed in Equation (76) requires that

$$\bar{r}\,\varepsilon_\theta(i) - 0.5\,t\,\varepsilon_r(i) = u_r^{\text{fuel}}(i) - \delta \quad . \qquad (96)$$

Substituting for ε_θ (i) and ε_r (i) from Hooke's law, Equations (66) and (68), there results a single equation relating $\sigma_\theta(i)$ at each node to the axial stress σ_z, which can be solved for $\sigma_\theta(i)$ explicitly to obtain

$$\left[\frac{\bar{r}}{E(i)} + \frac{0.5\nu(i)\ t}{E(i)}\right] \sigma_\theta(i) = u_r^{\text{fuel}}(i) - \delta - \bar{r}\left[\frac{-\nu(I)}{E(i)}\ \sigma_z + \varepsilon_\theta^P(i) + d\varepsilon_\theta^P(i) + \int_{T_o}^{T(i)} \alpha_\theta dT\right] + \frac{t}{2}\left[\frac{-\nu(i)}{E(i)}\ \sigma_z + \varepsilon_r^P(i) + d\varepsilon_r^P(i) + \int_{To}^{T(i)} \alpha_r dT\right] \qquad (97)$$

which applies at each node where contact has occurred. Finally, Equation (97) is used to eliminate $\sigma_\theta(i)$ from Equation (92) for those nodes at which contact has occurred. Thus, an equation is obtained for σ_z involving summations over all nodes not in contact plus summations over all nodes, denoted j*, where contact has occurred. This equation, solved explicity for σ_z, is shown below.

$$\left\{\sum_i \frac{dz(i)}{E(i)} - \sum_{i=j^*} \frac{dz(i)\ \nu(i)}{E(i)}\left[\frac{(\bar{r}-0.5t)\ \nu(i)}{(\bar{r}+0.5t)\ \nu(i)}\right]\right\} \sigma_z = \Delta\ell + \sum_i \varepsilon_z^o(i)\ dz(i) - \sum_i \left[\varepsilon_z^P(i) + d\varepsilon_z^P(i) + \int_{T_o}^{T(i)} \alpha_z dT\right] dz(i) + \sum_{i\neq j^*} \frac{\nu(i)}{E(i)}\left[\frac{P_i(i)\ r_i - P_o(i) r_o}{r_o - r_i}\right] dz(i)$$

$$+ \sum_{i=j^*} \frac{\nu(i)dz(i)}{(r+0.5t)\nu(i)}\left\{u_r^{\text{fuel}}(i) - \delta - \bar{r}\left[\varepsilon_\theta^P(i) + d\varepsilon_\theta^P(i) + \int_{T_o}^{T(i)} \alpha_\theta dT\right] + 0.5t\left[\varepsilon_r^P(i) + d\varepsilon_r^P(i) + \int_{T_o}^{T(i)} \alpha_r dT\right]\right\} . \qquad (98)$$

This modified equation for σ_z allows for an arbitrary number of contacting nodes, and is solved for σ_z at each step in the iteration for the plastic strain increments. Of course, it is not known a priori which nodes may be in contact. However, for given values of the plastic strain increments (the iterates in the Method of Successive Elastic Solutions), the governing equations are linear. Thus, one can solve for σ_z assuming no pellets are in contact, then compute the gaps, and if any negative gaps are found, recompute σ_z with those nodes now assumed to be in contact. This process is repeated until all calculated gaps are either positive or zero. At most, N steps are required since the equations are linear, where N is the number of nodes in the stack.

The second possibility to be considered is that in the iteration for the plastic strain increments, some of the nodes may only be strained elastically. Here, the plastic strain increments for these nodes approach zero, which causes difficulties when a check for convergence is made. This difficulty is circumvented by checking the absolute values of the plastic strain increments at each iteration, and when they become smaller than some predetermined value, those nodes are deleted from the iteration scheme.

Thus, in this application, the Method of Successive Elastic Solutions becomes an iteration within an iteration, and one in which the set of variables iterated upon is determined as the solution progresses.

3.5.5 Subroutines STRAIN and STRESS. These two subroutines are called by COUPLE and CLADF to relate stress and plastic strain, taking into consideration the direction of loading and the previous plastic deformation. A typical stress-strain curve is shown in Figure 14. This curve represents the results of a uniaxial stress strain experiment, and may be interpreted (beyond initial yield) as the locus of work-hardened yield stresses. The equation of the curve is provided by MATPRO[2] at each temperature.

To utilize this information, the usual idealizations of the mechanical behavior of metals are made. Thus, linear elastic behavior is

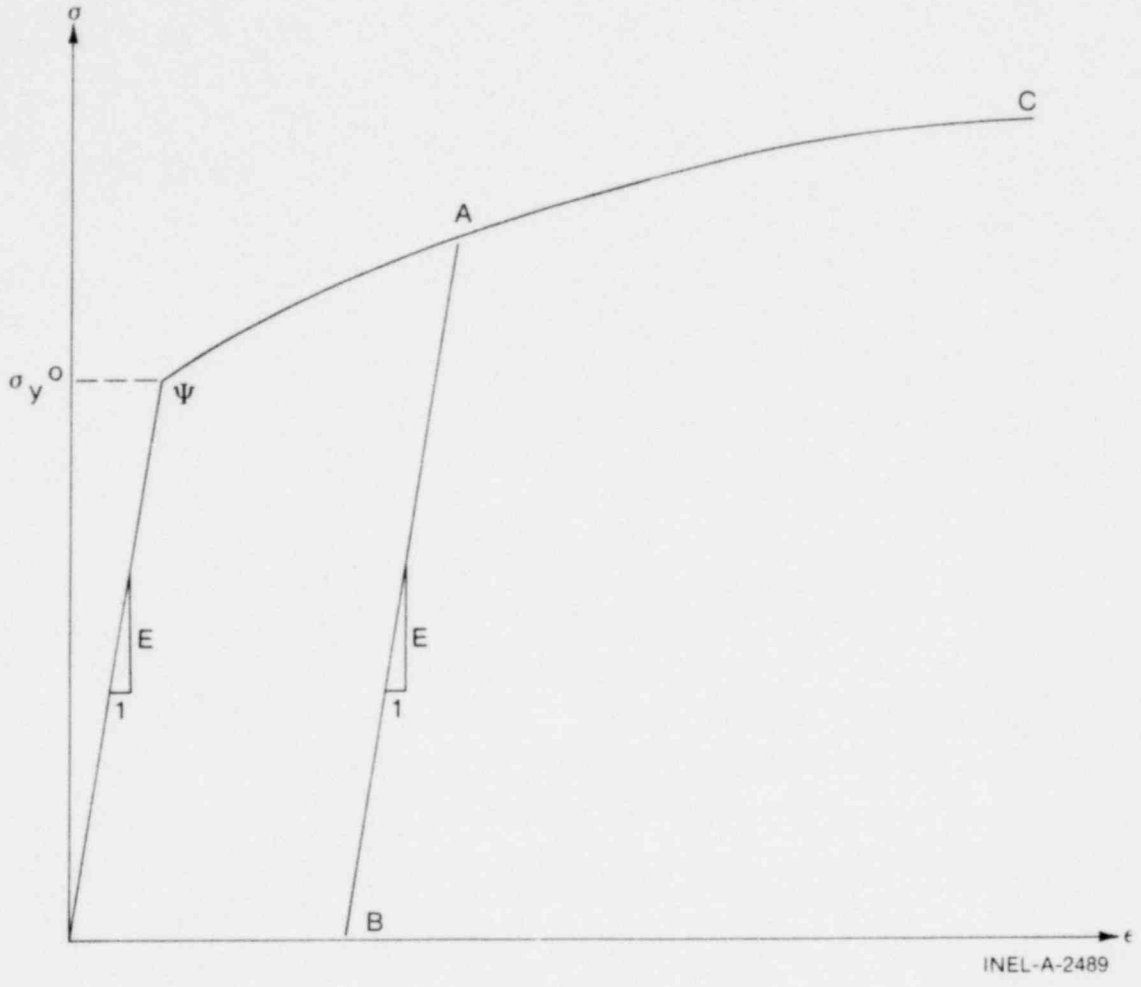

Fig. 14 Typical isothermal stress-strain curve.

assumed until a sharply defined yield stress is reached, after which plastic (irrecoverable) deformation occurs. Unloading from a state of stress beyond the initial yield stress, σ_y^o, is assumed to occur along a straight line having the elastic modulus for its slope. When the (uniaxial) stress is removed completely, a residual plastic strain remains, and this completely determines the subsequent yield stress. That is, it is assumed that when the specimen is loaded again, loading will occur along line BA, and no additional plastic deformation will occur until point A is again reached. Point A is the subsequent yield stress. If $\sigma = f(\varepsilon)$ is the equation of the plastic portion of the stress-strain curve (YAC), then for a given value of plastic strain, the subsequent yield stress is found by solving simultaneously the pair of equations

$$\sigma = f(\varepsilon)$$

$$\sigma = E(\varepsilon - \varepsilon^P) \qquad (99)$$

which may be written as

$$\sigma = f(\frac{\sigma}{E} + \varepsilon^P) \quad . \qquad (100)$$

The solution to this nonlinear equation may be computed very efficiently by Newton's Iteration Scheme

$$\sigma^{(m+1)} = f(\frac{\sigma^{(m)}}{E} + \varepsilon^P) \qquad m = 0, 1, 2, \ldots \qquad (101)$$

The initial iterate, $\sigma^{(o)}$, is arbitrary, and, without loss of generality, is taken as 5000 psi. It can be proven that, for any monotonically increasing stress-plastic strain relation, the iteration scheme in Equation (101) converges uniformly and absolutely. Normally, convergency to within a specified accuracy of 1×10^6 occurs after less than six iterations.

The computations in STRAIN and STRESS are described below. It is to be noted that STRESS is only called when additional plastic deformation has occurred.

(1) Subroutine STRAIN. Values of plastic strain, ε^P, temperature and stress are passed to STRAIN through the calling sequence.

(a) For given temperature, obtain $\sigma = f(\varepsilon)$ from MATPRO function CSIGMA

(b) Obtain yield stress σ_y for given ε^P from Equation (101)

(c) For given value of stress, σ,

(i) if $\sigma \leq \sigma_y$, $\varepsilon = \frac{\sigma}{E} + \varepsilon^P$

$$\varepsilon^P_{new} = \varepsilon^P_{old}$$

where E is computed by MATPRO function CELMØD.

(ii) if $\sigma > \sigma_y$, $\varepsilon = f(\sigma)$

$$\varepsilon^P_{new} = \varepsilon - \sigma/E$$

$$d\varepsilon^P = \varepsilon^P_{new} - \varepsilon^P_{old}$$

(d) Return.

(2) Subroutine STRESS. Values of plastic strain, ε^P, temperature, and plastic strain increment, $d\varepsilon^P$, are passed to STRESS through the calling sequence

(a) For given temperature, obtain $\sigma = f(\varepsilon)$ from MATPRO function CSIGMA

(b) Obtain yield stress σ_y for given ε^P from Equation (101)

(c) Given $d\varepsilon^P$ (see Figure 15)

$$\varepsilon^P_{new} = \varepsilon^P_{old} + d\varepsilon^P$$

Since $d\varepsilon^P > 0$, the new value of stress and strain must lie on the plastic portion of the stress-strain curve $\sigma = f(\varepsilon)$. So, σ and ε are obtained by simultaneously solving, as before,

$$\sigma = f(\varepsilon)$$

$$\sigma = E(\varepsilon - \varepsilon^P_{new})$$

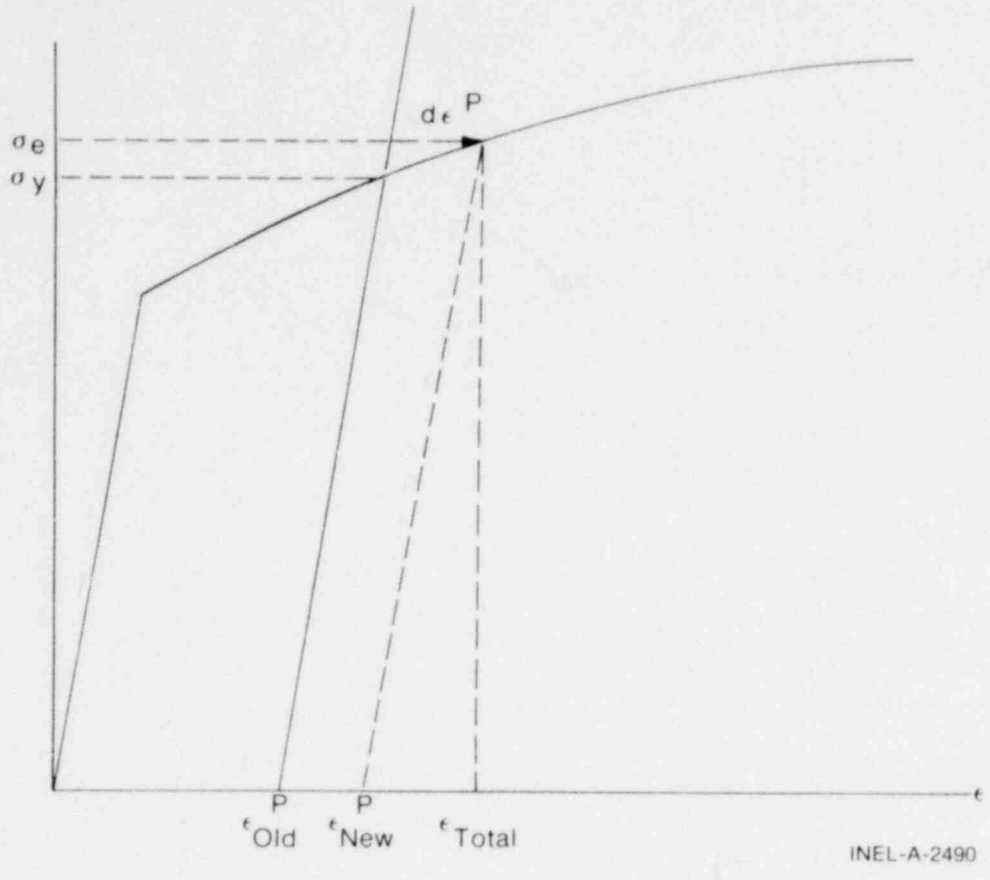

Fig. 15 Computations in subroutines STRESS.

(d) Return.

3.6 Cladding Buckling

3.6.1 Assumptions.

(1) Elastic cladding deformation

(2) Cladding is a thin-walled cylinder.

The coolant pressure required to buckle the cladding is computed by the elastic, thin-walled cylinder buckling Equation[18]. This equation is

$$P_{Bn} = P_{Gn} + \frac{E\,(T_{cn})\,t_n^{\,3}}{4\,r_{mn}^{\,3}\,(1-\nu^2(T_{cn}))} \qquad (102)$$

where

P_{Bn} = coolant pressure required to buckle cladding at axial node n

P_{Gn} = internal gas pressure at axial node n

$E(T_{cn})$ = modulus of elasticity of cladding at temperature T_{cn}

t_n = cladding thickness at axial node n

r_{mn} = radius to midplane of cladding at axial node n

$\nu(T_{cn})$ = Poisson's ratio of cladding at temperature T_{cn}.

3.7 Cladding Local Strain Model

A model is included in FRAP-T to calculate cladding strain over fuel cracks after gas gap closure has occurred.

3.7.1 Assumptions.

(1) After fuel contacts cladding, no slippage occurs between fuel and cladding

(2) After contact, all additional cladding hoop strain due to radial expansion of fuel is concentrated in portion of cladding that spans fuel radial cracks.

3.7.2 Governing Equations. Radial cracks are formed in the fuel pellet surface due to the high thermal gradient across the pellet and the low fracture strength of the fuel. The total width of these cracks can be calculated as the difference between pellet circumference due to radial thermal expansion and pellet circumference due to thermal expansion of the pellet surface only, i.e.,

$$w = 2\pi \left\{ \int_0^{r_f} \left[F_T(T(r)) \right] dr - r_f \, F_T(T(r_f)) \right\} \qquad (103)$$

where

w = total width of fuel cracks at pellet surface

r_f = outside radius of fuel pellet

$F_T(T)$ = thermal strain of fuel at temperature T (function supplied by MATPRO function FTHEXP)

T_o = cold state fuel temperature.

The additional hoop strain in the cladding during fuel cladding lock-up with no slippage is concentrated over the fuel cracks and equal to

$$\varepsilon' = U_I / W \qquad (104)$$

where

ε' = effective concentrated cladding strain

U_I = fuel cladding interference as calculated by the FRACAS subcode.

The effective strain calculated by this model is printed in the output for user information only. Failure models which will use this type of information are planned for development and inclusion in later versions of FRAP.

3.8 Cladding Ballooning Model

The ballooning model[19] computes the extent and shape of the large localized cladding deformation that occurs between the time that the cladding effective strain exceeds the instability strain and the time of cladding rupture. For this model, the cladding is assumed to consist of a network of membrane elements subjected to a pressure difference between the inside surface and the outside surface, as shown in Figure 16. The equations for the model are derived by applying the equation of equilibrium and geometric constraints. In addition, the model has an equation to account for the extra cooling the cladding undergoes as it bulges outward.

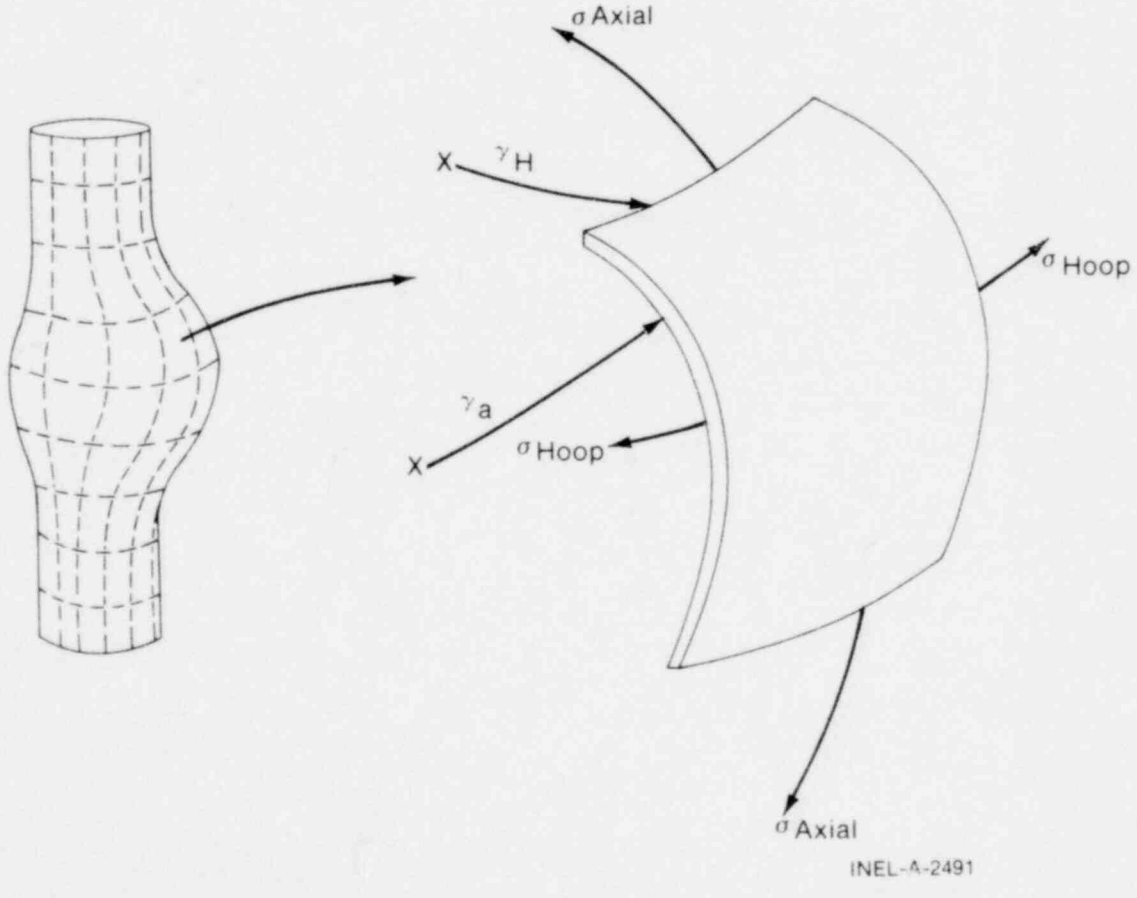

Fig. 16 Membrane swelling model.

3.8.1 Assumptions. The ballooning model is based on the following assumptions:

(1) Stability of the deformed shape can be described by membrane theory (in-plane force only)

(2) Stresses and temperatures are uniform through the cladding thickness

(3) Axial and circumferential stresses at a point can be defined as a function of temperature, strain, and strain rate by one relationship.

(4) The centroid of each nodal element remains on an extension of the radial vector to the original centroid

(5) Cladding hoop stress and axial stress are equal

(6) No change in cladding volume due to deformation

(7) No heat conduction in axial or azimuthal directions

(8) Heat flux through cladding changes slowly with time

(9) At ballooning region, surface heat transfer coefficient is a factor of two higher than that just outside of the ballooning region

(10) Cladding thickness at point of initiation of ballooning (cladding weak spot) is 95% of input-specified cladding thickness

(11) Length of cladding balloon region is four inches.

3.8.2 Equilibrium Equation. The equilibrium equation for the membrane element in Figure 16 is

$$\frac{\sigma_a}{r_a} + \frac{\sigma_\theta}{r_c} = \frac{p}{t_c} \tag{105}$$

where

p = differential pressure
σ_a = axial stress
σ_θ = hoop stress
r_a = axial radius of curvature
r_c = circumferential radius of curvature
t_c = cladding thickness.

Considering the assumption that no significant deformation is obtained until both axial and radial stresses have exceeded yield stress, Equation (105) is expressed as

$$\sigma_y\left(\frac{1}{r_a} + \frac{1}{r_c}\right) \Big/ \frac{p}{t_c} = f \tag{106}$$

where

σ_y = yield stress of cladding
f = node stability factor.

For a given internal pressure, P, cladding thickness, t_c, cladding yield stress, σ_y, and local curvatures, r_a and r_c, the value of f given by solution of Equation (106) determines whether an element is stable or will deform under the applied pressure. If the value of f is less than one, the element will displace outward. Otherwise, the element remains stable. When an unstable element is detected, the cladding is deformed in such a manner as to make the system more stable. This adjustment in the geometry of the cladding is described in the following paragraphs.

3.8.3 Geometric Models. To compute the radius of curvature in the axial direction, the configuration shown in Figure 17 is assumed. The angle between the chord connecting nodes i-1 and i+1 and the fuel rod centerline is given by the equation

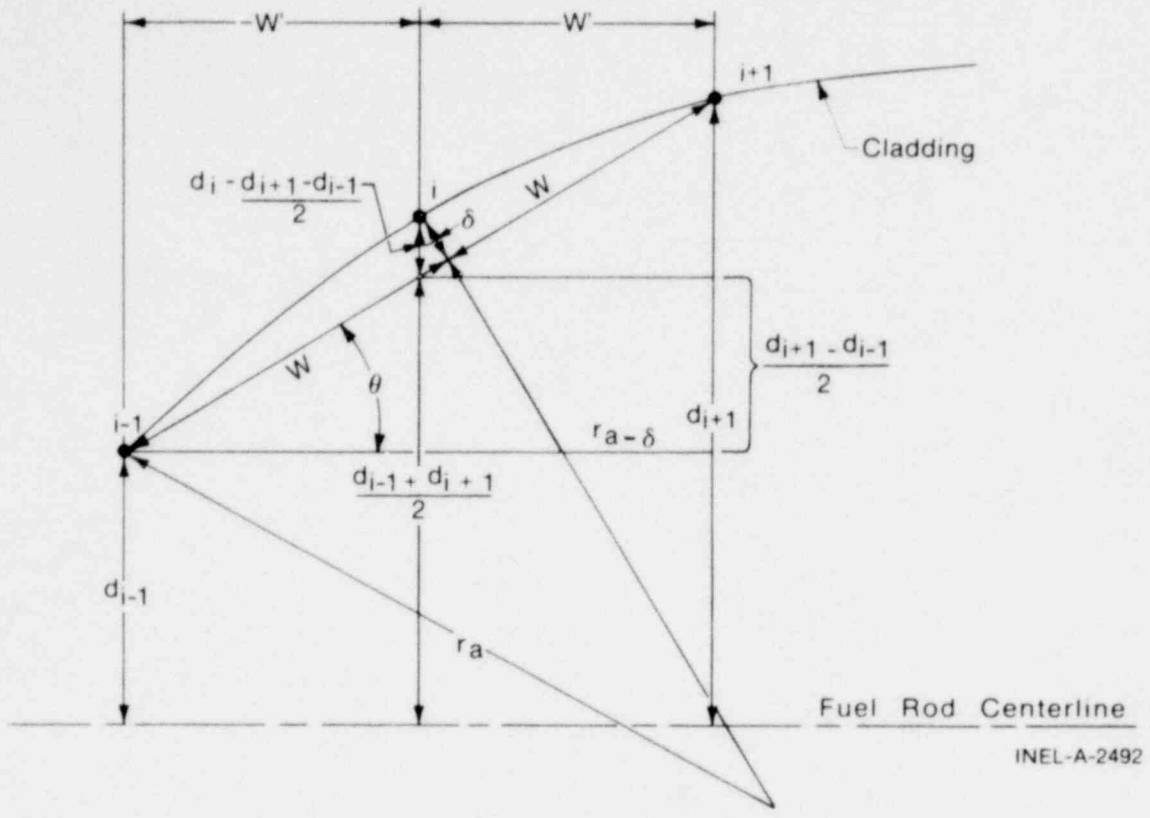

Fig. 17 Radius of curvature in axial direction.

$$\theta = \tan^{-1}\left(\frac{d_{i+1} - d_{i-1}}{2w'}\right) \qquad (107)$$

where

d_i = perpendicular distance between node i and fuel rod centerline

w' = specified mesh spacing in axial direction (set to 0.2 inches in balloon model subcode).

One-half the length of the chord connecting nodes i-1 and i+1 is

$$w = w'/\cos\theta \quad . \qquad (108)$$

If the radius of curvature, r_a, is assumed to be constant between nodes i-1 and i+1, the radius of curvature at node i and the chord connecting nodes i-1 and i+1 are perpendicular to each other. Then, the perpendicular distance between node i and the chord connecting nodes i-1 and i+1 is given by the equation

$$\delta = \cos\theta \left[d_i - \left(\frac{d_{i+1} - d_{i-1}}{2}\right)\right] . \tag{109}$$

Application of the Pythagorean theorem gives the following relation between the radius of curvature r_a, chord length 2w, and δ:

$$(r_a - \delta)^2 + w^2 = r_a^2 .$$

Solving for r_a,

$$r_a = \frac{w^2 + \delta^2}{2\delta} . \tag{110}$$

To compute the radius of curvature in the circumferential direction, the configuration shown in Figure 18 is assumed. By assuming that the local radius of curvature can be computed by averaging the radial coordinates d_{i-1} and d_{i+1}, one-half the length of the chord connecting nodes i-1 and i+1 is

$$w = \sin \phi \left(\frac{d_{i-1} + d_{i+1}}{2}\right) \tag{111}$$

where

- w = one-half length of chord connecting nodes i-1 and i+1
- ϕ = angular mesh spacing (set to $\pi/7$ in balloon model subcode)
- d_i = distance from fuel rod center to node i.

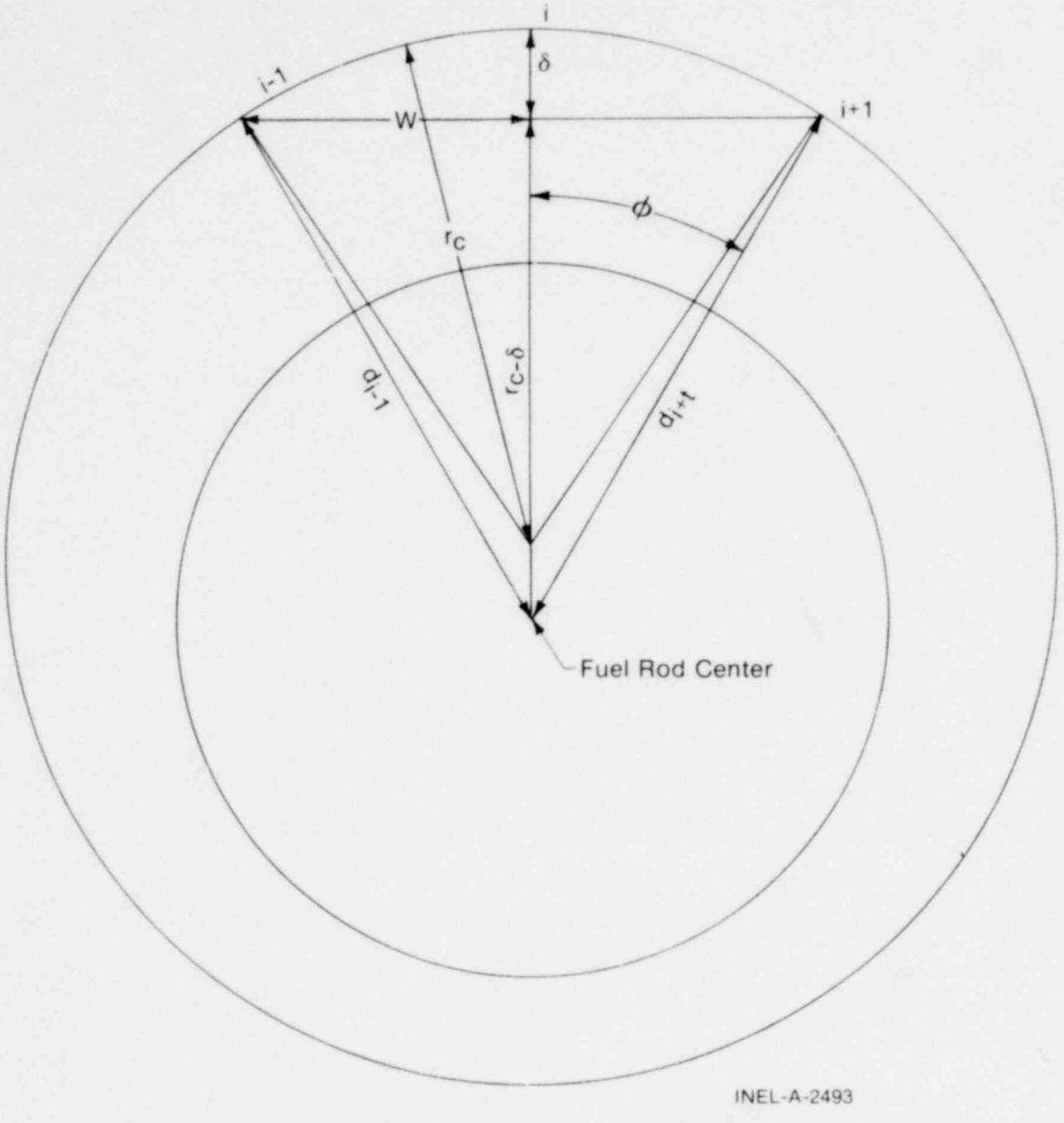

Fig. 18 Radius of curvature in circumferential direction.

The perpendicular distance between node i and the chord connecting nodes i-1 and i+1 is

$$\delta = d_i - \frac{d_{i-1} + d_{i+1}}{2} \cos\phi \, . \qquad (112)$$

By applying the Pythagorean theorem, the radius of curvature at node i is related to δ and w by the equation

$$(r_c - \delta)^2 + w^2 = r_c^2 \quad .$$

Solving for r_c gives the equation

$$r_c = \frac{\delta^2 + w^2}{2\delta} \quad . \tag{113}$$

Calculation of the surface area and cladding thickness at each node is based on the assumption that the volume of the cladding does not change with deformation. The calculations assume the configuration shown in Figure 19. The surface area of node i in the deformed state is calculated by the equation

$$A_{D_i} = d_i \emptyset \omega \tag{114}$$

where

A_{D_i} = cladding surface area at node i
d_i = radial coordinate of node i
$\emptyset$ = circumferential nodal spacing (radians)
ω = axial node spacing after swelling (see Figure 17).

Assuming constant element volume, the following relation is obtained for local cladding thickness

$$t_c = r_o \phi \omega' t_o / A_{D_i} \tag{115}$$

where

t_c = cladding thickness at node i
r_o = original cladding radius
l' = axial mesh spacing (see Figure 17)
t_o = original cladding thickness.

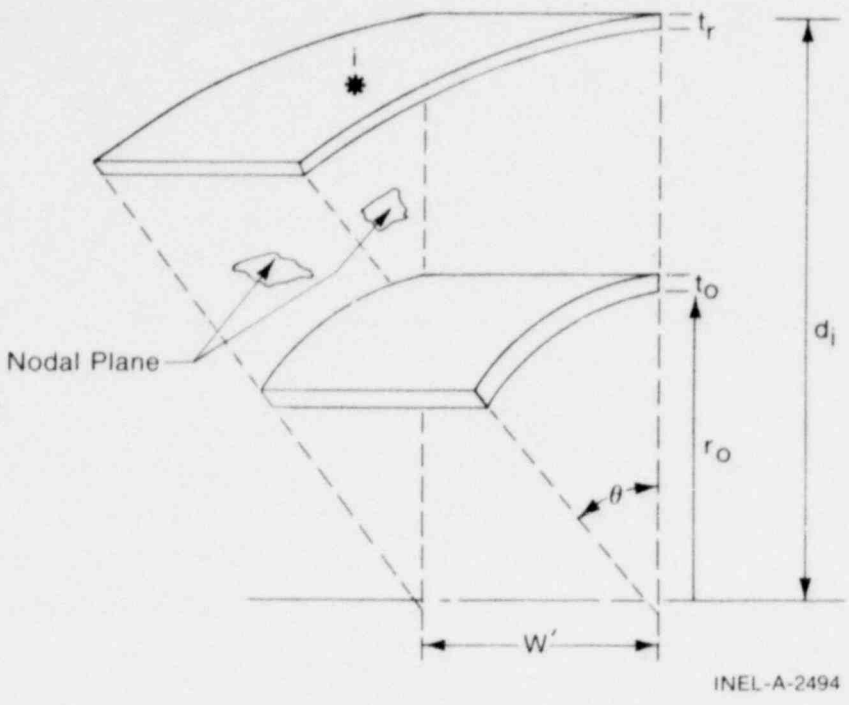

Fig. 19 Surface area and cladding thinning model.

Volume of the region inside the cladding is required for input to the fuel rod pressure model. Incremental nodal volumes are calculated as the node is displaced and summed to produce a new, swelled volume for each time step. The relationship defining the incremental nodal volume is

$$\Delta V_i = d_i \phi \omega' \delta_i \qquad (116)$$

where

δ_i = incremental displacement of node i during the time step.

Total swelling volume for the time step is then

$$V = V_o + \sum_{1=1}^{n} \Delta V_i \qquad (117)$$

where

n = number of nodes

V_o = volume from previous time step.

3.8.4 Numerical Analysis. The analytical sequence used in the cladding ballooning model consists primarily of

(1) Solving for the stability of each nodal point on the cladding using Equation (106)

(2) Modifying the cladding geometry as a function of cladding instability.

Stability of each node is checked by solving Equation (106) for the local stability factor f_i, with $f_i < 1$ indicating a node with insufficient strength to resist the applied pressure, p, and $f_i > 1$ indicating a stable node.

With the assumption that unstable nodes ($f_i < 1$) will deform, the solution process of the swelling model is to specify a deformation for these unstable nodes. Specification of deformations are based on the following assumptions:

(1) Nodal deformations are a function of the nodal instability at that node which is the most unstable (F_m = maximum f_i) and will deform the most

(2) The specified displacements must be small enough that adjacent stable nodes are not unrealistically effected.

The process of specifying deformations consists of adding a finite deformation to the nodal deformation calculated during the last time step as

$$d_i = d_{i_o} + dh_i \qquad (118)$$

where

d_i = the new radial coordinate of node i
d_i = the old radial coordinate of node i
dh_i^o = specified incremental radial displacement of node i.

The effect of adding an incremented deformation to node i is shown in Figure 20 as decreasing the radius of curvature at i. Examining Equation (106) shows this decrease in curvature to increase the stability function f_i and, thus, the local stability at node i. An additional effect to be noted from Figure 20 is that an increase in deformation at node i causes an increase in curvature at nodes i+1 and i-1 (possibly to the point of producing negative curvature).

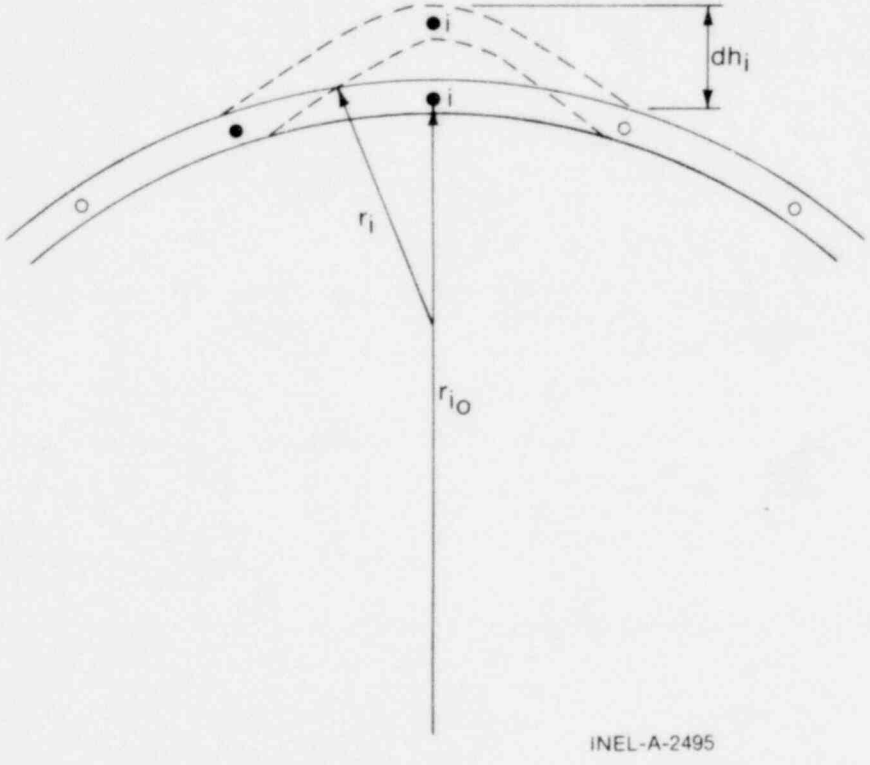

Fig. 20 Incremental deformation at node i.

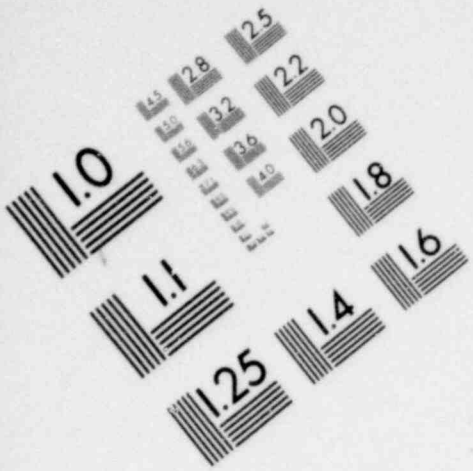

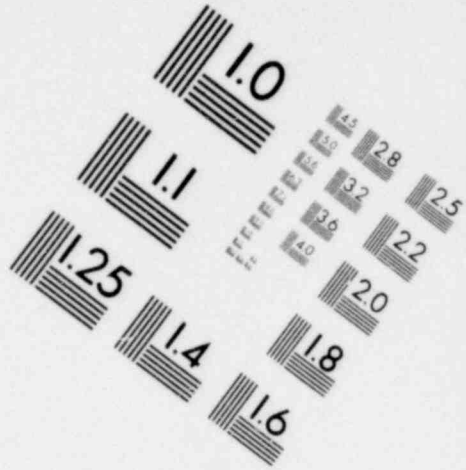

IMAGE EVALUATION TEST TARGET (MT-3)

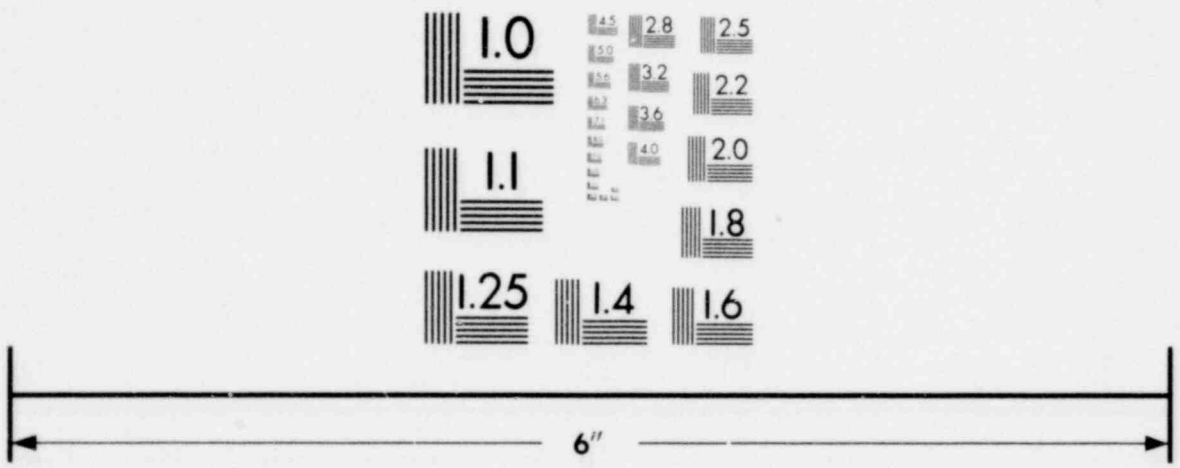

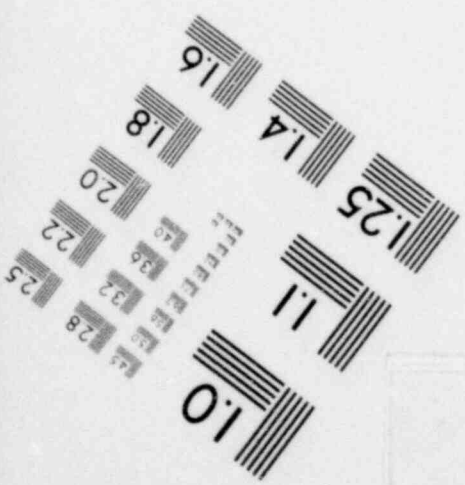

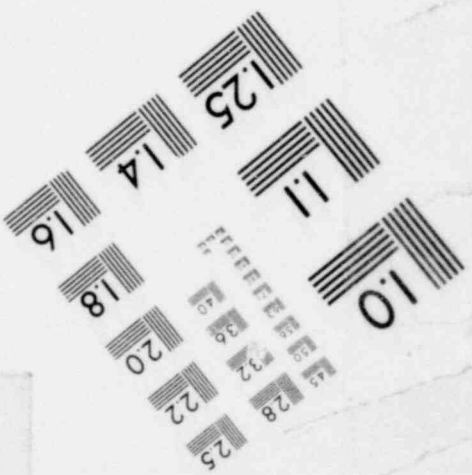

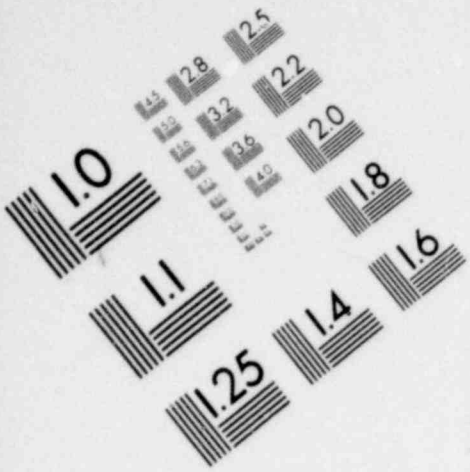

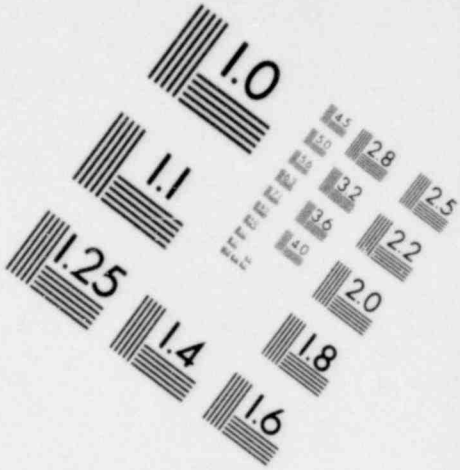

IMAGE EVALUATION TEST TARGET (MT-3)

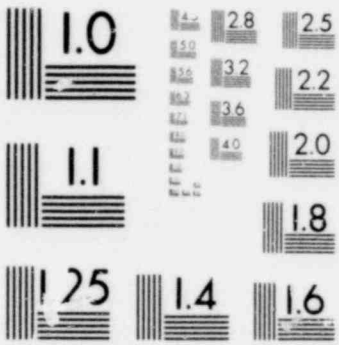

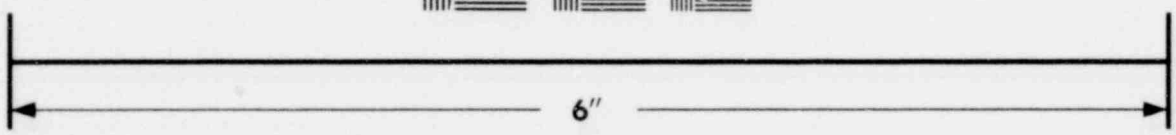

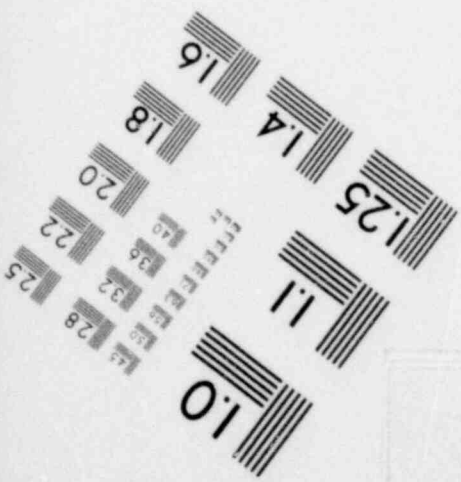

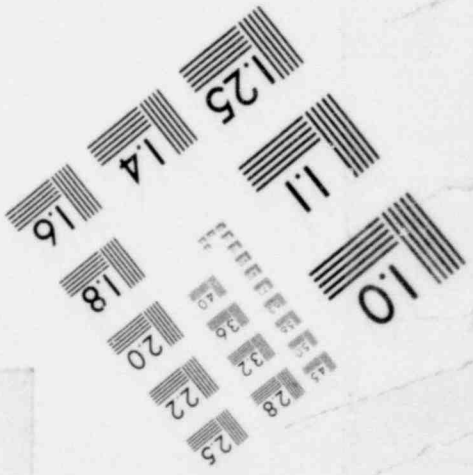

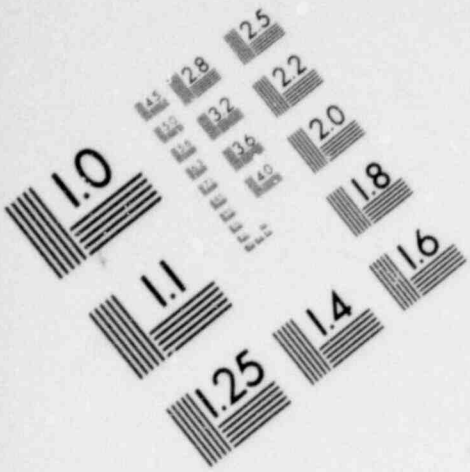

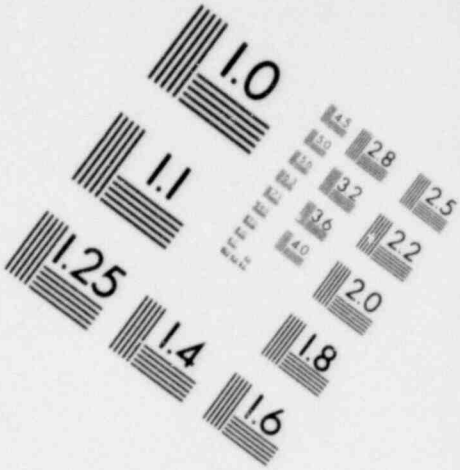

IMAGE EVALUATION TEST TARGET (MT-3)

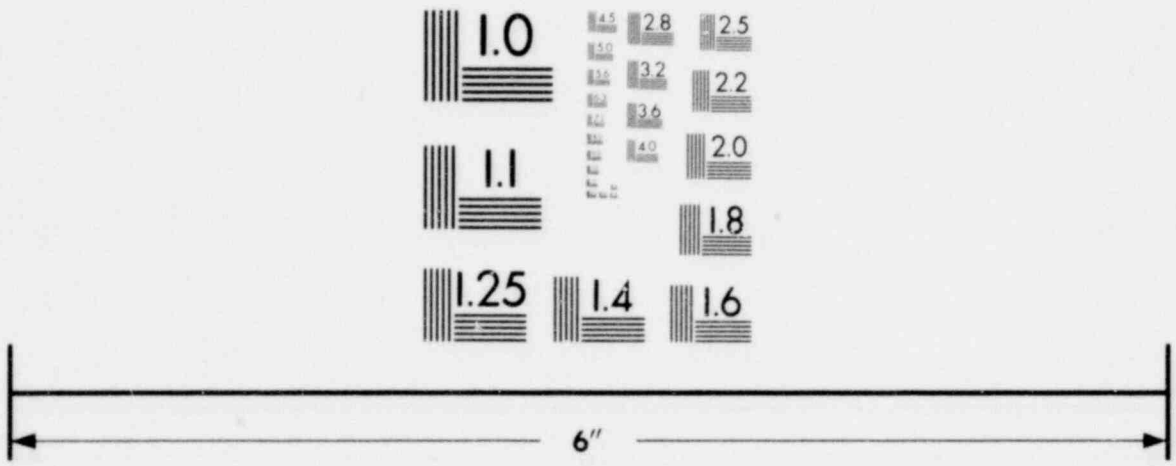

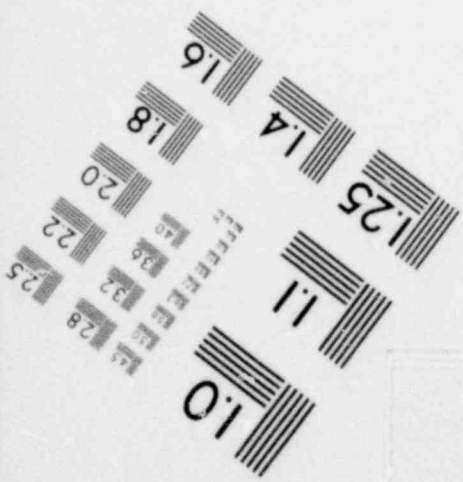

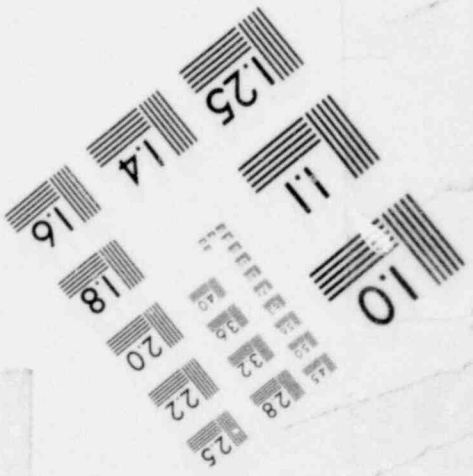

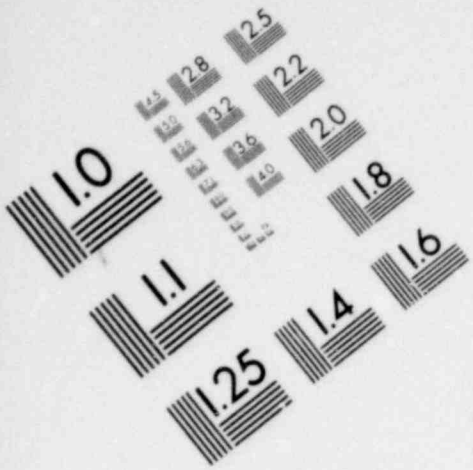

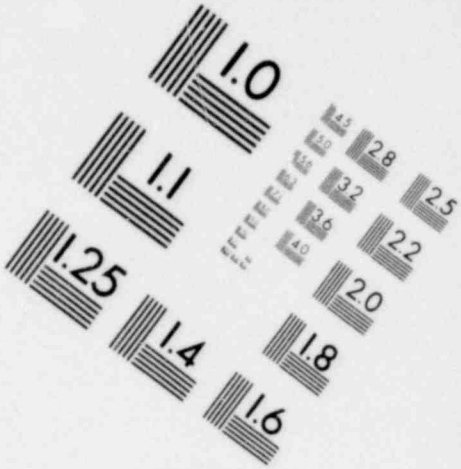

IMAGE EVALUATION TEST TARGET (MT-3)

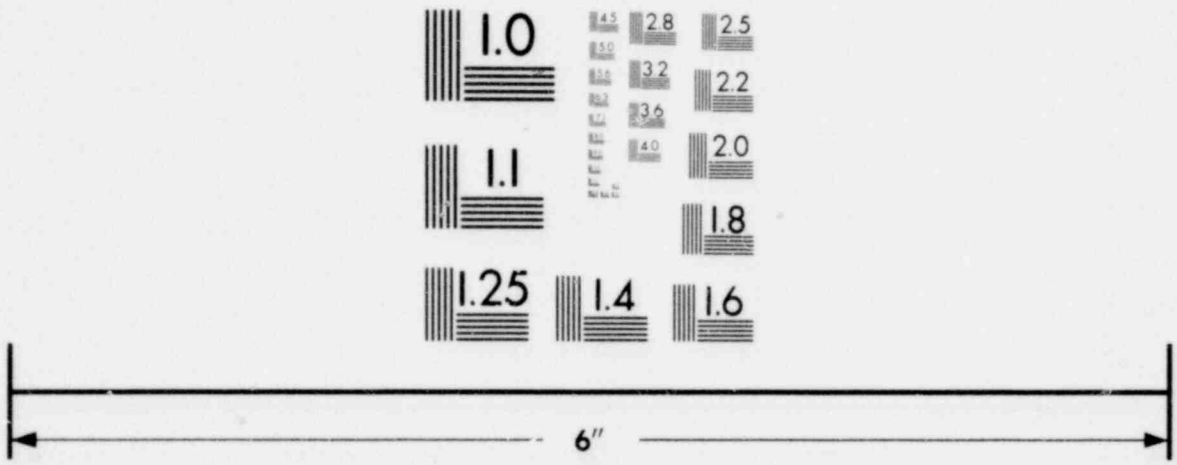

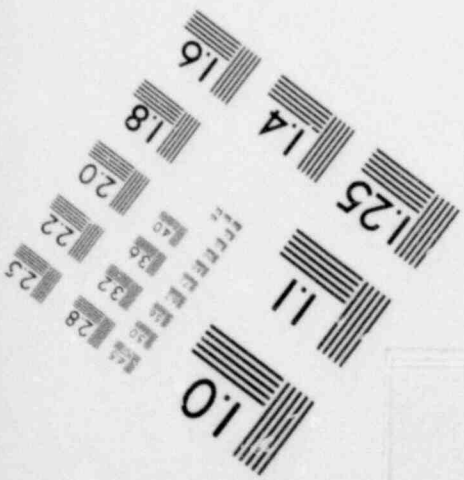

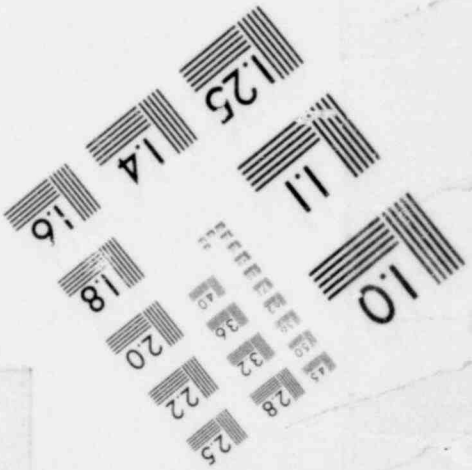

An examination of Equation (106) shows an increase in curvature to decrease the stability function and, thus, local cladding stability. The effect, therefore, of locally deforming a weak spot is to strengthen the weak spot but propagate the weakness into the surrounding material, possibly causing additional new instability and further propagation. Careful examination of membrane instabilities, such as blisters on tires and ballooning tubes, indicates that initial deformation is quite localized and then proceeds to either rupture or an enlarged stable geometry.

Deformations are specified according to the relation

$$dh_i = dh_m \left(\frac{(1-f_i)^2}{1-F_m} + 0.1 \right) \qquad (119)$$

where

dh_i = incremental radial displacement of node i
dh_m = maximum displacement to be added to any node
f_i = instability factor at node i
F_m = maximum instability factor.

A value of dh_m equal to the cladding thickness has been found to produce a rapid convergence with no apparent numerical or structural instabilities. The 0.1 factor in Equation (119) is there to "push" the function past the stability point since corrections very close to stability are very small. The overall numerical procedure for the balloon model is shown in Figure 21.

3.8.5 Conduction Model. As the cladding extends away from the hot fuel pellet surface, the cladding temperature will change under the combined effects of:

(1) Decreased gap conductance from increasing gap thickness

(2) Increased surface cooling due to increased area

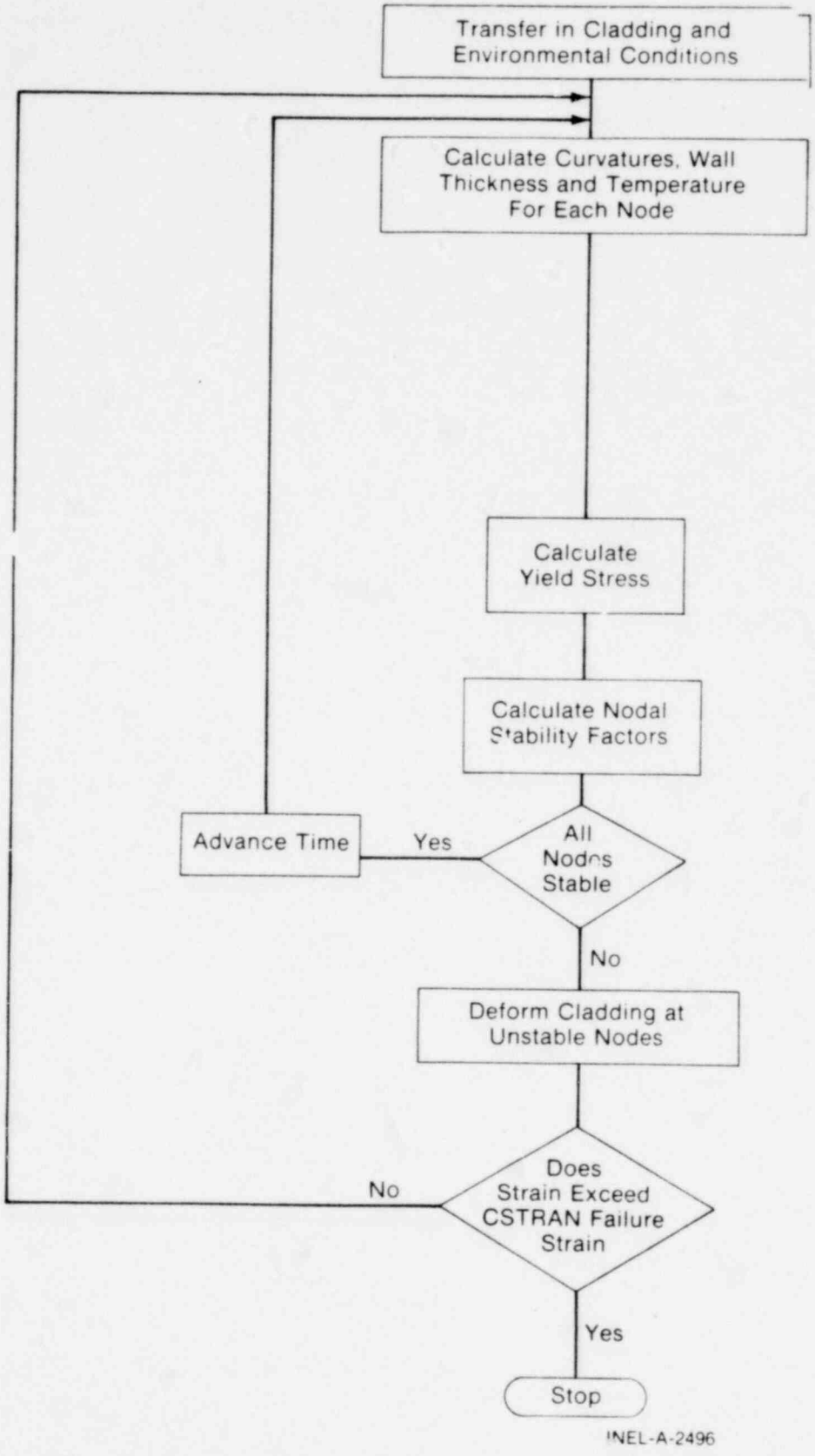

Fig. 21 Balloon model flow diagram.

(3) Increased surface cooling due to local flow phenomena

(4) Increased fuel surface temperature due to decreased gap conductance

(5) Heat capacitance of cladding.

The conduction model formulated to include these combined effects considers the cladding temperature as a function of the local power or surface heat flux value. The major assumption of the model is that the heat flux, $\ddot{q}$, from an area of the fuel, A_f, is transferred through a corresponding area of cladding, A_{cl}, throughout the transient. Considering this assumption, the temperature of the cladding is governed by

$$\rho C_p V_{cl} \frac{\partial T_{cl}}{\partial t} = \ddot{q} A_f + A_{cl} h_s (T_B - T_{cl}) \qquad (120)$$

where

C_p = cladding heat capacity
ρ = cladding density
V_{cl} = cladding nodal volume
T_{cl} = cladding average temperature
T_B = bulk coolant temperature
h_s = cladding surface heat transfer coefficient (see following section)
A_{cl} = cladding nodal area
A_f = fuel nodal area
$\ddot{q}$ = fuel surface heat flux
t = time.

Solution to Equation (120) for the time-dependent cladding temperature gives

$$T_{cl} = (T_o - B/A)\, e^{-At} + B/A \qquad (121)$$

where

T_o = cladding initial temperature

$A = A_{cl}/(\rho C_p V_{cl})$

$B = (\dot{q}'' A_f + A_{cl}\ h\ T_B)/(\rho C_p V_{cl})$.

Additional cladding cooling will result as the cladding swells into the coolant channel[20]. This additional cooling is modeled as an increase in the surface heat transfer coefficient by the relation

$$h_s = h_o(1 + C_1 d_i/r_o) \tag{122}$$

where

h_s = cladding heat transfer coefficient for expanded cladding

h_o = cladding heat transfer coefficient calculated by the HTRC subcode of FRAP-T

d_i = radial location of i^{th} node

r_o = initial radius of of i^{th} node

C_1 = heat transfer factor (assumed to be 2.0).

4. FUEL DEFORMATION

4.1 Assumptions

The analytical models used to compute fuel deformation are based on the following assumptions:

(1) Thermal expansion is the only source for fuel deformation*

(2) The fuel is assumed to expand under zero stress*

(3) Axial thermal expansion of fuel stack is equal to thermal expansion of line projected through shoulder of fuel pellets (this model is illustrated in Figure 22)

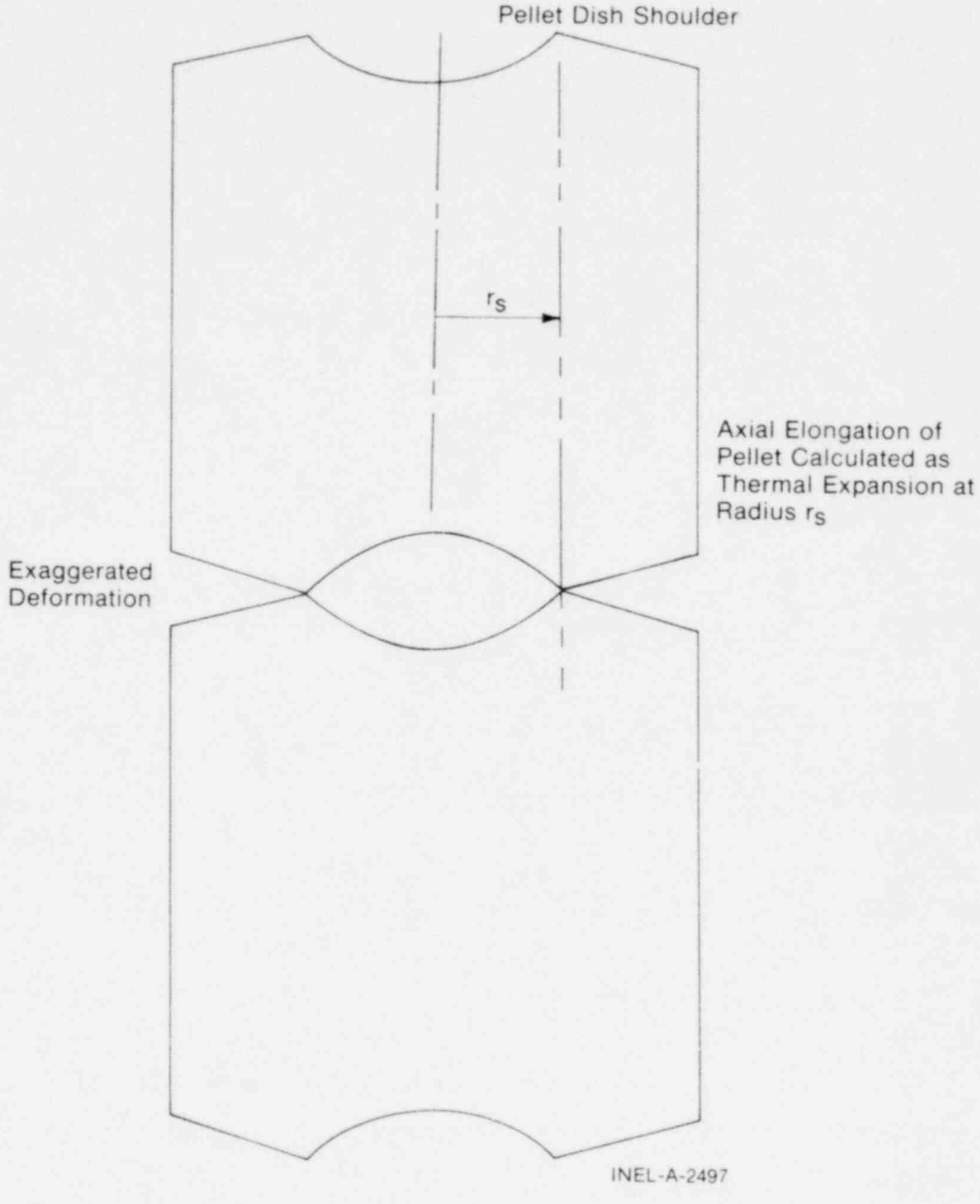

Fig. 22 Axial thermal expansion.

(4) No creep deformation of fuel during transient

(5) Stress resistance to fuel thermal expansion is negligible

(6) Isotropic fuel properties.*

4.2 Fuel Stack Length Change

The length change of the fuel stack is modeled by the equation

$$\Delta L_f = \sum_{n=1}^{N} [\, F_T(T_{sn}) - F_T(T_o)] \, \Delta Z_n \qquad (123)$$

where

ΔL_f = fuel stack length change

$F_T(T)$ = thermal expansion of fuel at temperature T (function supplied by FRAP-T material properties package)

T_{sn} = fuel temperature at pellet shoulder

T_o = cold state fuel temperature

ΔZ_n = fuel stack length associated with axial node n.

4.3 Fuel Radial Displacement

Fuel radial displacement is computed with a free thermal expansion model which considers the fuel to be extensively cracked in the radial direction.

Radial displacement of the fuel is calculated by the equation

$$U_n(r) = \int_0^{r_f} (F_T(T(r)) - F_T(T_o)] \; dr + U_c \qquad (124)$$

where

r_f = radial coordinate of fuel at outside surface
$T(r)$ = fuel temperature at radial coordinate r
U_c = 0.0025 r_f (constant addition to radial displacement to account for fuel relocation due to cracking).

4.4 Fuel Crack Volume

Fuel radial cracks are opened by the hot inner core expanding the cold outer section of the pellets radially. These cracks become space that is occupied by the fuel rod internal gas. The larger the radial displacement of the fuel inner core, the wider the radial cracks become. Thermal expansion of fuel in the outer region tends to reduce the width of the radial cracks. The volume of the radial cracks per unit length of fuel rod is computed by the equation

$$V_{cn} = 2\pi \int_0^{r_f} [U_n(r) - r(F_T(T(r)) - F_T(T_o))]\, dr \qquad (125)$$

where

V_{cn} = volume of radial cracks per unit length of axial node n.

4.5 Fuel Open Porosity

An empirical correlation with fuel density is used to compute the open porosity of the fuel. The open porosity is multiplied by the fuel volume to determine the volume of gas in the fuel pores that is connected to the fuel rod gas gap. This quantity is used in the calculation of fuel rod internal pressure.

Depending on fuel density, one of the following correlations is used to compute fuel open porosity.

$$P = 16.9297 - 0.232855\,(D-1.25) - 8.71836 \times 10^{-4}\,(D-125)^2 + 1.52442\,10^{-5}\,(D-1.25)^3 \qquad (D < 92.5)$$

$$P = 1.20196 \times 10^{-3}\,(95.25-D) \qquad (92.5 \leq D \leq 95.25)$$

$$P = 0 \qquad (D > 95.25)$$

where

P = open porosity of fuel (fraction of theoretical volume)
D = fuel density (percentage of theoretical maximum density).

5. FUEL ROD FAILURE MODEL

The determination of whether or not the fuel rod cladding has failed (suffered loss of integrity) is made by the FRAIL[21] subcode. Models for predicting four types of fuel rod failure are contained in the subcode. The failure types are: (a) overstress, (b) overstrain, (c) oxide layer wall thinning, and (d) eutectic melt. The models assume fuel rod failure to be a function of the following parameters:

(1) Temperature history

(2) Cold work

(3) Irradiation dosage

(4) Effective strain

(5) Effective stress

(6) Strain rate.

Because of scatter in the experimental data and uncertainties in experiment specimens, the FRAIL subcode uses a probabilistic approach. Instead of simply computing whether or not a fuel rod has failed, the subcode computes the probability of fuel rod failure.

5.1 Model for Overstress Failure

5.1.1 Assumptions.

(1) Mean hoop stress at failure correlated with temperature by least-squares fitting of a function to failure stress data

(2) Beta probability distribution of failure stress about the mean failure stress

(3) Failure stress is not a function of cladding hydrogen, cessium, iodine, or oxygen content*

(4) Failure stress is not a function of stress rate*

(5) Failure stress is not a function of neutron irradiation*.

5.1.2 Description. The overstress model is based on an empirical correlation which relates average failure stress to cladding temperature. The data used to develop the correlation is taken from a number (305) of isothermal and transient temperature burst tests[22 through 29]. These tests include burst tests on tubing with varying degrees of irradiation and cold work. Since hoop stress at failure was not a measured quantity for these tests, it is computed using the maximum measured internal pressure and the equation of static equilibrium for a cylinder. The empirical correlation was generated by least-squares fitting of the

failure stress data. All points were assigned a weight of one since the experimental errors were not reported. The best fit (minimum standard deviation) was found to be given by the equation

$$\log \sigma_f = 5.00 + 3.27 \times 10^{-4} T - 1.14 \times 10^{-6} T^2 + 2.56 \times 10^{-10} T^3 \qquad (126)$$

σ_f = failure stress (psi)

T = temperature (°F).

This correlation is plotted in Figure 23.

To compute the probability of failure as a function of stress and temperature, a distribution of failure stress about the mean line must be defined. The beta distribution was chosen because it is limited to a finite interval. Estimates of the shape parameters of the beta distribution were found from the equations

$$n = \frac{(1 - \bar{x})}{s^2} \left(\bar{x}\,(1-\bar{x}) - s^2\right) \qquad (127)$$

and

$$\gamma = \frac{\bar{x}\, n}{1-\bar{x}} \qquad (128)$$

where

$\bar{x}$ = normalized failure stress

s = normalized standard deviation

n, γ = shape parameters.

The normalized failure stress is found from the expression

$$\bar{x} = \frac{\sigma_F - B}{T - B}, \quad B \leq \sigma_F \leq T, \quad 0 \leq \bar{x} \leq 1 \qquad (129)$$

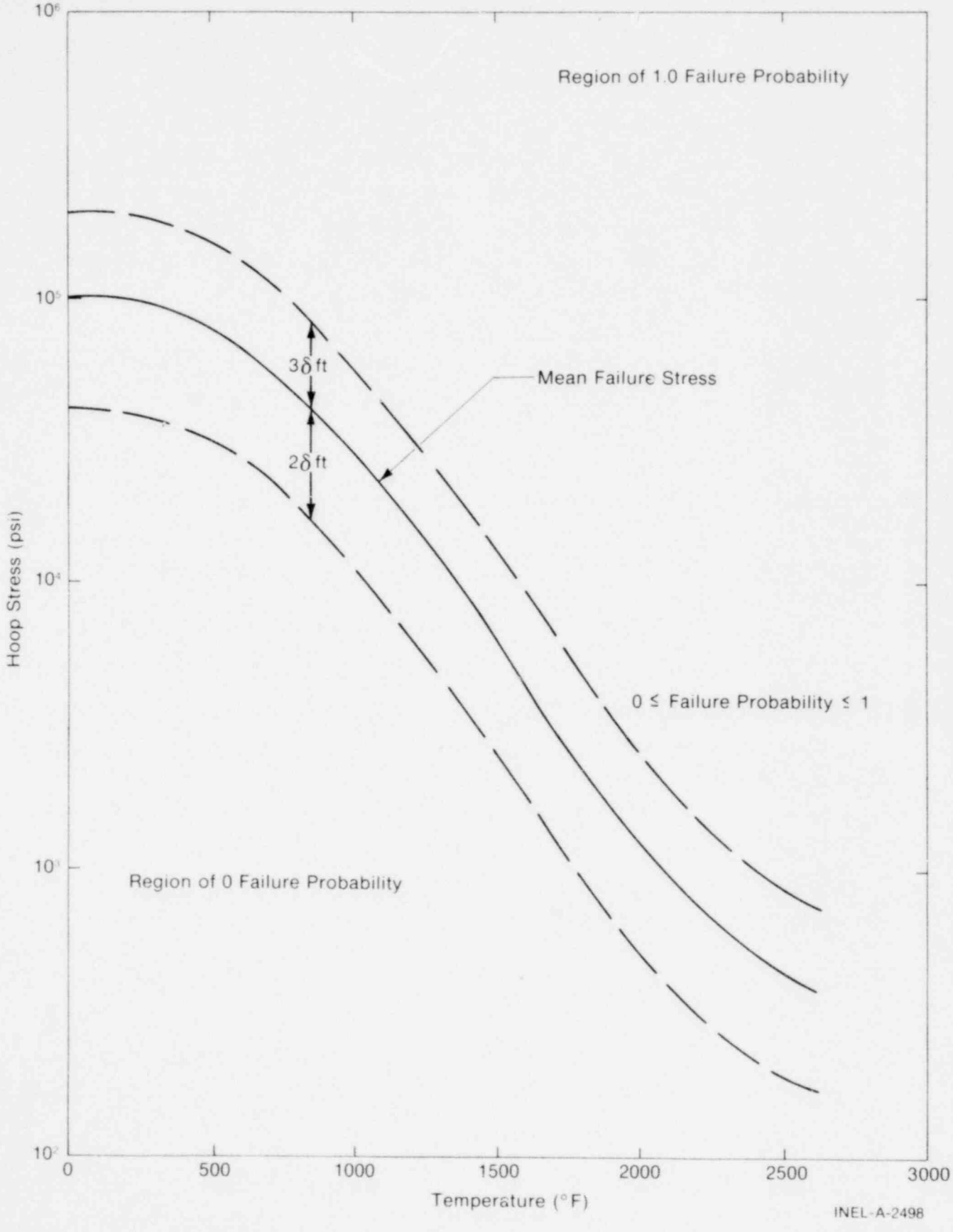

Fig. 23 Mean failure stress versus temperature.

where

$\bar{x}$ = normalized failure stress

σ_F = mean failure stress

and B and T define the interval of allowable failure stresses. This interval was chosen to be three standard deviations above and two standard deviations below the mean failure stress. These limits are depicted in Figure 23.

The normalized standard deviation is found from the equation

$$s = s' \left(\frac{\partial \bar{x}}{\partial \sigma_F}\right) = \frac{s'}{T - B} \qquad (130)$$

where

s = normalized standard deviation, i.e., standard deviation of $\bar{x}$

s' = standard deviation of σ_F = $0.305\ \sigma_F$.

Because of the large spread in the failure stress data, the overstress failure model does not currently distinguish between the failure of irradiated and unirradiated fuel rods. In order to clearly account for the effect of irradiation, the spread in measured failure stress needs to be reduced to about 1000 psi.

5.2 Model for Overstrain Failure

5.2.1 Assumptions.

(1) Mean failure strain correlated with temperature by least-squares fitting to failure strain data

(2) Beta probability distribution of failure strain about the mean failure strain

(3) Failure strain is not a function of cladding hydrogen, oxygen, cesium, or iodine content*.

5.2.2 Description. The overstrain failure model calculates the probability of failure as a function of strain and temperature. The strain at failure is assumed to be distributed according to the beta distribution. The upper and lower limits are set at +2 and -2 standard deviations, respectively, from the mean failure strain. The standard deviation is calculated to be 16% of the mean failure strain.

The mean failure strain as a function of temperature is determined by the MATPRO[2] subroutine CMLIMT. The effects of cold work and irradiation level are taken into account.

5.3 Model for Oxide Layer Wall Thinning Failure

If the thickness of the oxide layer is greater than 17% of the original cladding wall thickness, failure of the cladding is assumed to occur. No probability of failure by this mode is computed. If the oxide layer thickness is less than 17% of the original wall thickness, the probability for failure is zero. If greater, the probability for failure is one.

5.4 Model for Eutectic Melt

This model requires the cladding temperature at the point of contact with the spacer grids. Since the temperature distribution subcode only computes cladding temperature in the absence of spacer grids, this model contains an equation to estimate temperature at spacer grids. Basically, the equation modifies the temperature calculated in the temperature distribution subcode in the vicinity of the spacer grids according to the ratio of the heat transfer coefficient at the spacer grids, to that in the absence of spacer grids.

5.4.1 Assumptions.

(1) The fuel rod heat transfer coefficient at a spacer grid is 1.4 times bigger than that in absence of a spacer grid[30,31]

(2) The total heat transferred at a spacer grid is 1.06 times bigger than that transferred in absence of a spacer grid

(3) The cladding temperature at a spacer grid is governed by the equation

$$\frac{T_2 - T_1}{T_1 - T_c} = \frac{h_1 q_2}{h_2 q_1}$$

where

T = temperature
h = heat transfer coefficient
q = total heat transferred

and the subscripts

c = coolant
1 = fuel rod cladding at a spacer grid
2 = fuel rod cladding in absence of spacer grid.

(4) At the position of a spacer grid, there is no oxide layer on the surface of the cladding because of fretting

(5) Nickel from the spacer grids is the only material that can react with cladding to form a eutectic

(6) The melting temperature of the zircaloy-nickel eutectic is 1760°F

(7) If the cladding temperature reaches 1760°F at a spacer grid, the zircaloy-nickel eutectic forms instantly, which results simultaneously in localized cladding melting.

5.4.2 Application of Assumptions. By applying assumptions (1) and (2) to the equation of assumption (3), the equation for cladding temperature at a spacer grid is

$$T_1 = 0.666\ (T_2 + 0.5\ T_c) \qquad (131)$$

where

T_1 = cladding temperature at a spacer grid
T_2 = cladding temperature in absence of spacer grid (temperature computed by surface temperature subcode)
T_c = coolant temperature.

By applying assumptions (6) and (7), the cladding is assumed to fail if T_1 exceeds 1760°F.

No probability of failure by this mode is computed. If the cladding temperature at the spacer grids is less than 1760°F, the probability of failure is zero. If greater than 1760°F, the probability of failure is one.

6. COOLANT MODELS

Fuel rod heatup and cladding deformation are governed by the conditions of the coolant surrounding the fuel rod. The coolant conditions are assumed to be known prior to FRAP-T calculations, so that they can be prescribed by card or tape input.

Heat transfer correlations are used to compute the rate at which heat is transferred from fuel rod to coolant by convection. FRAP-T has at least one correlation for each convection mode of heat transfer. The convection mode of heat transfer in effect is determined by the code. Several correlations for critical heat flux are contained in the code.

6.1 Criteria for Determining Mode of Heat Transfer

The convection mode of heat transfer in effect at a given surface of a fuel rod is determined by comparing the heat fluxes given by the various applicable heat transfer correlations. The coolant void fraction, mass flux, and pressure are also factors in determining the heat transfer mode. The scheme used to determine the heat transfer mode is outlined in Table VIII. This scheme is taken from RELAP4[5]. The scheme of Table VIII is programmed in subroutine HTRC.

6.2 Heat Transfer and Critical Heat Flux Correlations

Most of the heat transfer and critical heat flux correlations in FRAP-T were taken from the RELAP code. In some cases, more than one correlation is available for a given heat transfer mode. In these cases, the particular correlation to be used is specified by the input data. The available correlations are shown in Table VIII.

TABLE VIII

HEAT TRANSFER MODE SELECTION AND CORRELATIONS

	Heat Transfer Mode	Range[a]	Heat Transfer Correlation[b]
1.	Forced convection to liquid	$T_w < T_{sat}$ or $Q_2 < Q_1 < Q_{crit}$	Dittus-Boelter[31]
2.	Nucleate boiling	$Q_1 < Q_2 < Q_{crit}$; $T_w > T_{sat}$; $\gamma<0.9$	Thom[32]
3.	Forced convection vaporization	$Q < Q_{crit}$; $\gamma > 0.9$	Shrock-Grossman[33]
4.	Flow transition boiling	Q_2 or $Q_3 > Q_{crit}$; $Q_4 > Q_5$;	McDonough, Milich, and King[34]
		$G > 200{,}000$; $P > 500$ or $Q_4 < Q_9$	Tong-Young[38]
			Condie-Bengston[37]
5.	Flow film boiling	Q_2 or $Q_3 > Q_{crit}$; $Q_5 > Q_4$	Groeneveld[35]
		$G > 200{,}000$ or $Q_5 > Q_6$ ($\alpha\leq 0.6$)	Dougall-Rohsenow[36]
		or Q_7 ($\alpha > 0.6$)	Tong-Young[38]
			Condie-Bengston[37]
6.	Pool film boiling	Q_2 or $Q_3 > Q_{crit}$; $G< 200{,}000$	modified Bromley[39]
		$Q_6 > Q_5$; $\alpha\leq 0.6$	
7.	Free convection	Q_2 or $Q_3 > Q_{crit}$; $G < 200{,}000$	free convection[39]
		and $Q_7 > Q_5$; $\alpha > 0.6$	
8.	Forced convection to gas	$X \geq 1$	Dittus-Boelter[31]

[a] The symbols used are:

Q_i = surface heat flux for ith heat transfer mode

Q_{crit} = critical heat flux

T_w = cladding surface temperature

T_{sat} = saturation temperature of coolant

γ = coolant void fraction

X = coolant quality

G = mass flux (lbm/hr-ft^2)

P = coolant pressure (psia)

[b] For each heat transfer mode shown, only one of the listed correlations next to the parameter limits describing the range of the heat transfer mode is used. The correlation to be used is specified on the card input. There is one exception; for heat transfer mode 5. If Groeneveld is selected and P < 500. the lesser heat flux given by Dougall-Rohsenow or Groeneveld is used.

The following critical heat flux correlations are available:

(1) B&W-2[1]

(2) Barnett[32]

(3) Modified Barnett[33]

(4) General Electric[34]

(5) Savannah River[35]

(6) W-3[36]

(7) Preliminary LOFT[37].

The B&W-2 correlation is multiplied by the axial power profile factor of Gellerstedt[1]. The W-3 correlation is multiplied by the axial power profile factor and cold-wall factor of Tong[36]. The preliminary LOFT correlation is also multiplied by the axial power profile factor of Tong.

Both the B&W-2 and the W-3 correlations are restricted to high pressure conditions. The B&W-2 correlation is restricted to coolant pressures greater than 1500 psia. If the coolant pressure is less than 1300 psia, the B&W-2 correlation is replaced with the Barnett correlation. A combination of the two correlations is used for intermediate pressures. Similarly, the W-3 correlation is restricted to coolant pressures greater than 1000 psia. If the coolant pressure is less than 725 psia, the W-3 correlation is replaced with the Barnett correlation. A combination of the two correlations is used for intermediate pressures.

6.3 Void Fraction

The void fraction of the coolant is computed by the equation

$$\alpha = XV_g / [\,(1-X)V_f\alpha + XV_g\,] \qquad (132)$$

where

α = void fraction
X = coolant quality
V_f = specific volume of saturated liquid
V_g = specific volume of saturated gas
γ = slip velocity ratio.

The slip velocity ratio is computed by the modified Marchatree-Hoglund correlation[38].

6.4 Coolant Enthalpy Model

In cases where the coolant flow is quasi-steady-state, coolant conditions can be specified by a combination of card input and coolant enthalpy model. The coolant inlet enthalpy and transient spatially uniform coolant pressure and mass flux are prescribed by card input. The coolant enthalpy and temperatures are then computed by the enthalpy model. This input option is included in the code as a user convenience in scoping problems where coolant conditions from a thermal hydraulic code are not readily available. It is not meant to replace the calculations of thermal hydraulic codes, especially in cases where accurate coolant conditions are required.

The coolant enthalpy model is based on the principle of energy balance. The enthalpy increase of the coolant is related to the heat received from the fuel rods. The model consists of equations which calculate the following quantities: (a) the rate at which heat is added to each flow channel, (b) enthalpy increase of the coolant in each flow channel, and (c) temperature of the coolant in each flow channel.

The rate at which heat is added to the flow channel is computed by the equation

$$q_i(z) = \pi \sum_{m=1}^{M} f_{im} \int_0^z d_m(z)\, \phi_m(z)\, dz \qquad (133)$$

where

$q_i(z)$ = rate at which heat is added to flow channel i from flow inlet to distance z from flow inlet

f_{im} = fraction of perimeter of fuel rod m that borders flow channel i

M = number of fuel rods that border flow channel i

$d_m(z)$ = diameter of fuel rod m at distance z from flow inlet

$\phi_m(z)$ = surface heat flux of fuel rod m at distance z from flow inlet.

The coolant enthalpy is computed by the equation

$$h_i(z) = h_o + q_i(z)/GA_i(z) \tag{134}$$

where

$h_i(z)$ = enthalpy of coolant in flow channel i at distance z from flow inlet

h_o = enthalpy of coolant at flow inlet

G = mass flux

$A_i(z)$ = cross-sectional area of flow channel i.

The coolant quality and temperature are computed by the following equations:

$$\text{Case 1.} \quad \begin{aligned} &h_i(z) \leq H_F(P) \\ &X_i(z) = 0 \\ &T_i(z) = \theta(h_i(z), P) \end{aligned} \tag{135}$$

Case 2. $H_F(P) \leq h_i(z) \leq H_G(P)$

$$X_i(z) = (h_i(z) - H_F(P))/(H_G(P) - H_F(P))$$

$$T_i(z) = T_s(P) \qquad (136)$$

Case 3. $h_i(z) \geq H_G(P)$

$$x_i(z) = 1$$

$$T_i(z) = \theta(h_i(z), P)) \qquad (137)$$

where

x_i = quality of coolant in flow channel i at distance z from flow inlet

$T_i(z)$ = temperature of coolant in flow channel i at distance z from flow inlet

$H_F(P)$ = enthalpy of saturated liquid at coolant pressure P

$H_G(P)$ = enthalpy of saturated gas at coolant pressure P

$T_s(P)$ = saturation temperature at coolant pressure P

$\theta(h,P)$ = function specifying temperature of coolant as a function of enthalpy and pressure.

The functions H_F, H_G, $\theta(h,P)$, and T_s, are supplied by the Wagner steam tables[4].

IV. NUMERICAL SOLUTION PROCEDURE

Since a simultaneous solution of all of the equations that govern fuel rod behavior is not possible, an iteration procedure is used by the FRAP-T program. The major aspects of fuel rod behavior are solved independently of each other. For example, fuel rod temperature distribution, internal pressure, and deformation are solved by different uncoupled subcodes. There is a modular subcode for each analytical model described in Section III. The subcodes treat quantities that are calculated by another subcode as independent variables. For example, the gap conductance subcode treats the gap thickness as an independent variable, since this quantity is computed by the deformation subcode. Iterations continue until all the quantities passed to each subcode as independent variables agree with the values computed for those quantities in the subcodes in which they are the dependent variables. The iteration procedure is illustrated in Figure 24. The symbols used in Figure 24 are defined in Table IX.

The potential for convergence of the temperature, deformation, and pressure iterates is related to time step size. The larger the time step, the more difficult convergence is. If convergence does not occur after 40 iterations in the deformation-pressure loop, or 30 iterations in the overall temperature-deformation-pressure loop, the time step is reduced a factor of four, and claculations are continued. If the time step is reduced a factor of four, ten times in succession without convergence, the program is stopped. If convergence occurs with a reduced time step, time is advanced the size of the input-prescribed time step, not the size of the time step at which convergence occurred. The automatic time step reduction eliminates most of the guesswork involved in determining the time step history to be input to the code. The main criterion of the prescribed time step history is that it specify a time step about 1/10 the size of the periods of oscillation of coolant conditions and power. If this criterion is not met, the code will still converge, but inaccuracy of calculations will result because details in the coolant condition or power histories will be overlooked.

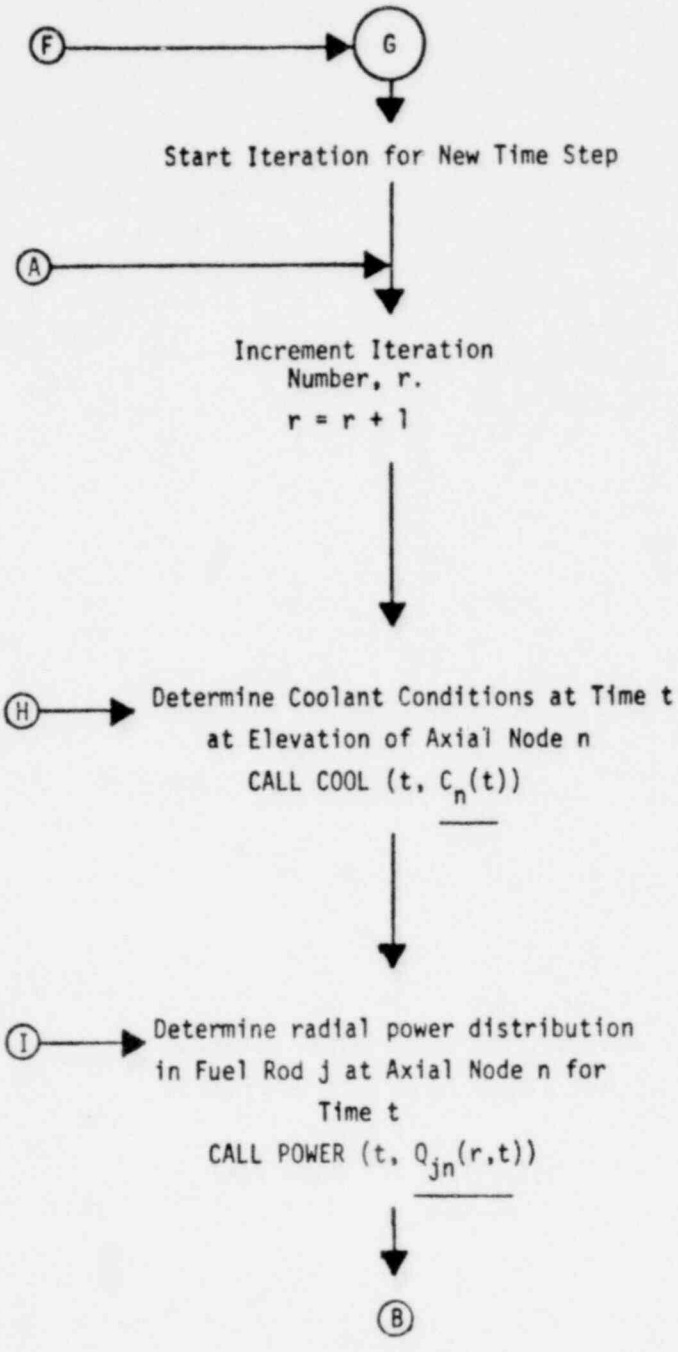

Fig. 24 Solution procedure flow chart.

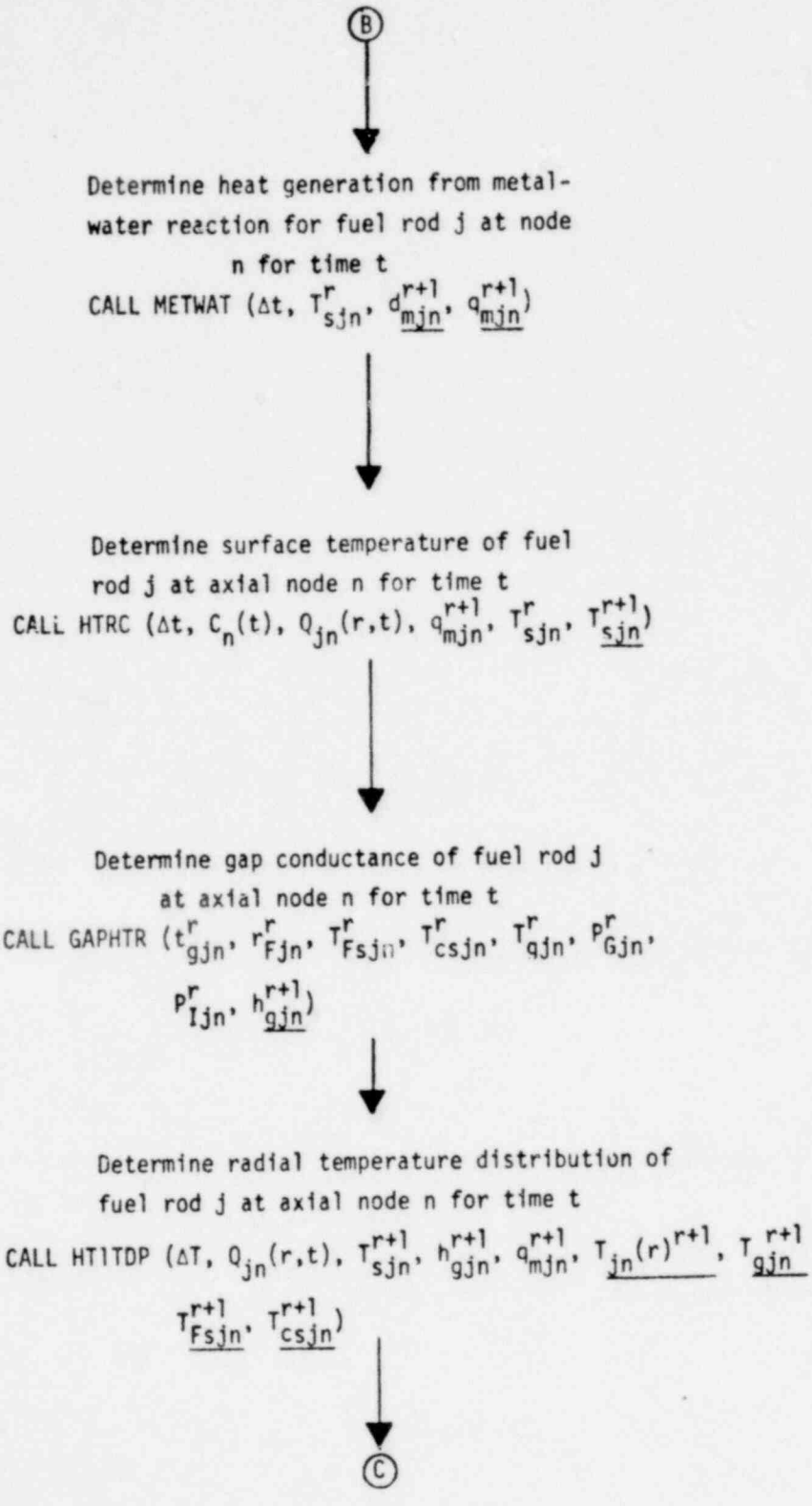

Fig. 24 Solution procedure flow chart (continued).

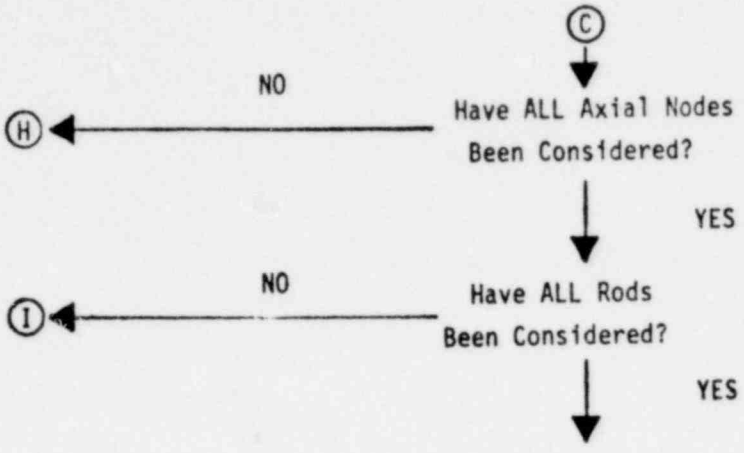

Compute temperature of gas in plenum for time t

CALL PLNT (Δt, Q_{jn}, T_{psjn}^{r+1}, T_{pj}^{r+1})

Start deformation-pressure iteration loop

Initialize iteration number s for this loop, s = 0

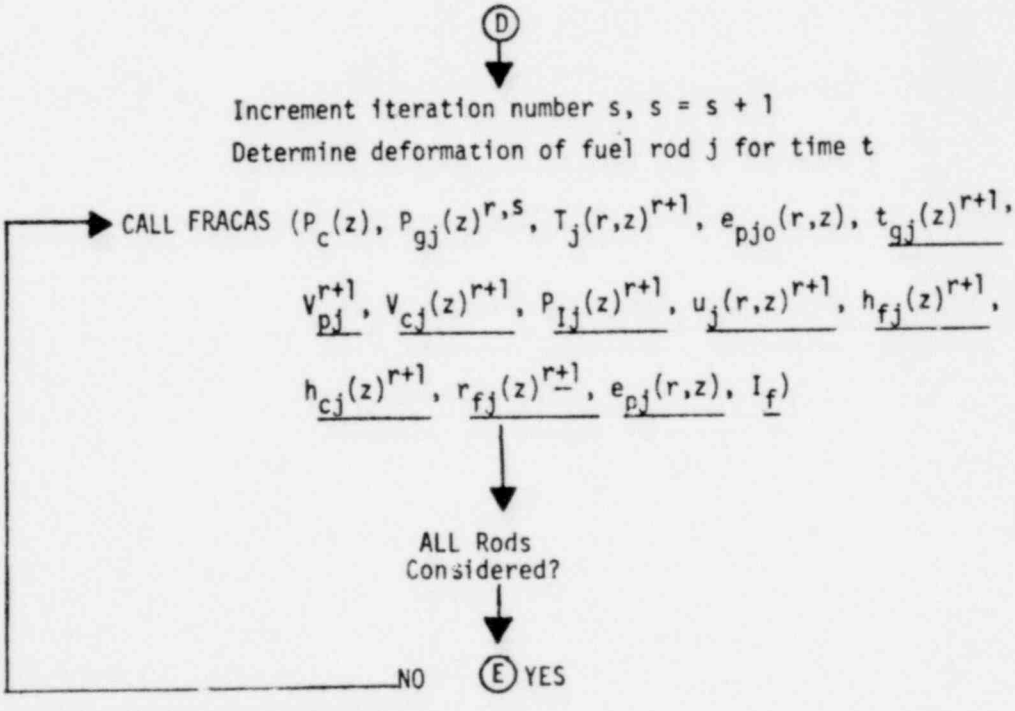

Fig. 24 Solution procedure flow chart (continued).

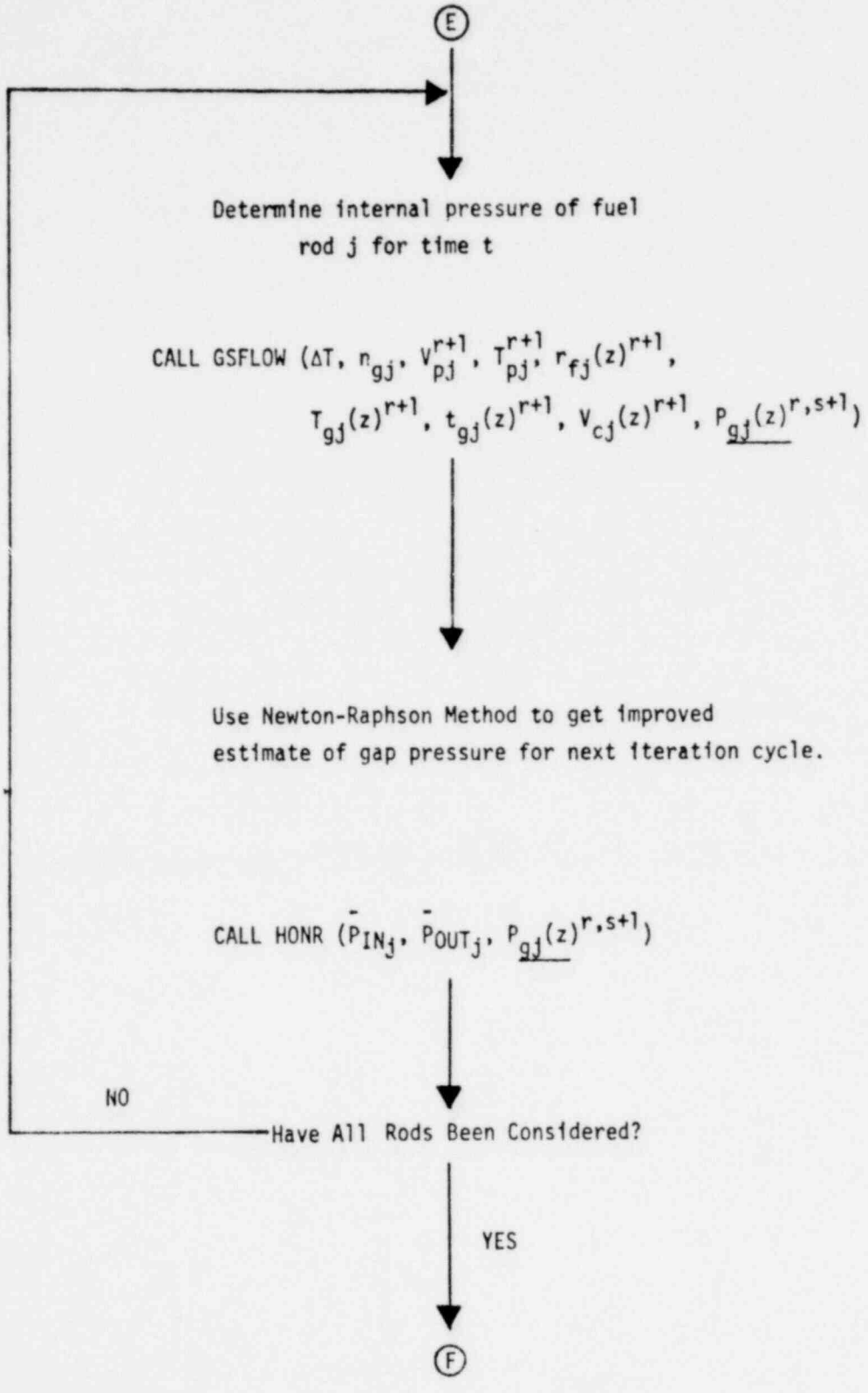

Fig. 24 Solution procedure flow chart (continued).

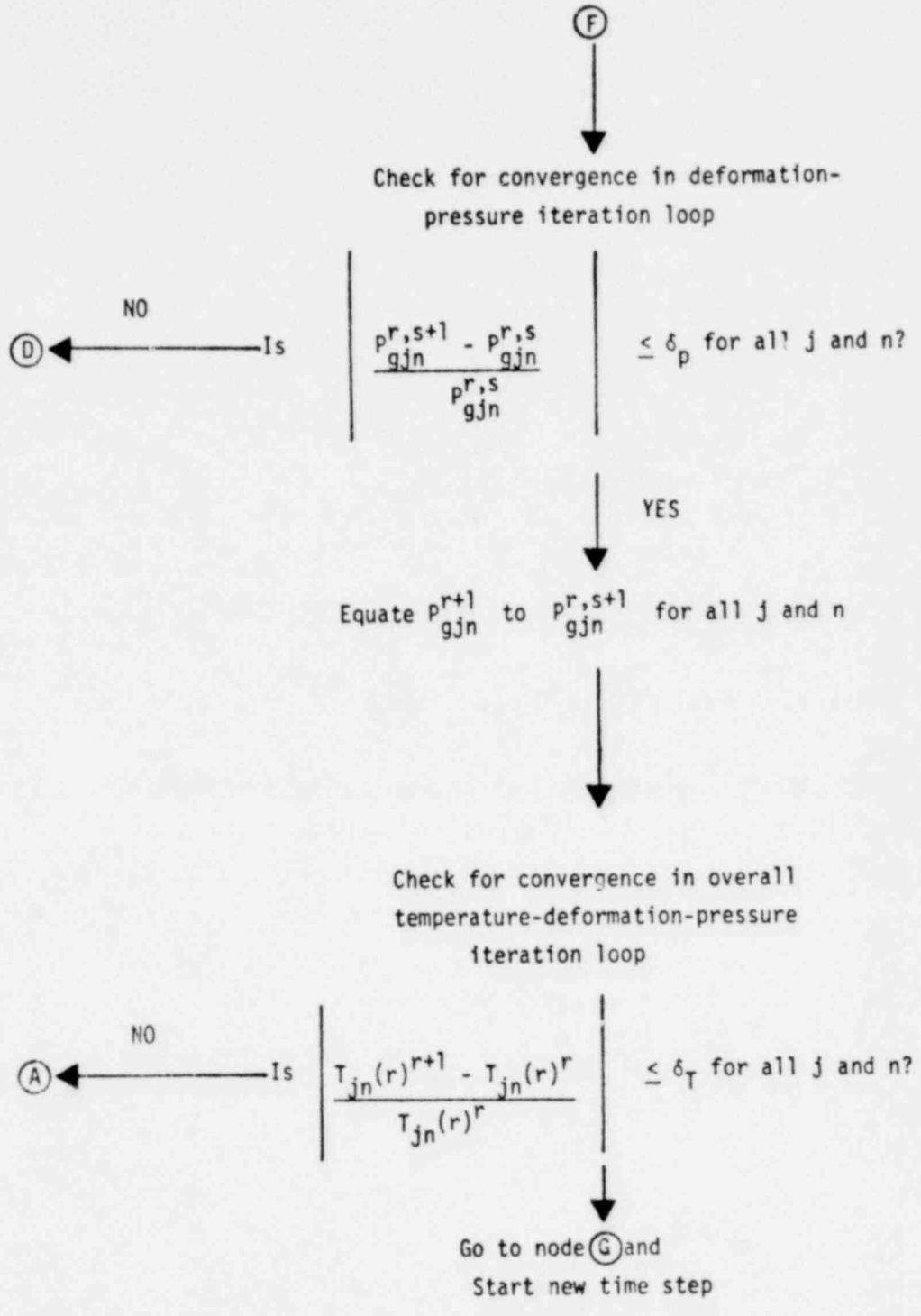

Fig. 24 Solution procedure flow chart (continued).

TABLE IX

DEFINITION OF SYMBOLS USED IN FIGURE 24

General Denotation

(1) Variables with a superscript r are iterates, where r denotes iteration number

(2) Nonunderlined variables in argument list of subcodes are input arguments (independent variables)

(3) Underlined variables in argument list of subcodes are output arguments (dependent variables)

(4) Subscripts j and n indicate fuel rod number and axial node number, respectively. Subscript N indicates top axial node

(5) t = current time; Δt = time step

(6) Superscript s denotes iteration cycle in deformation-pressure iteration loop

(7) Variables shown as a function of r or z are actually a collection of values at radial nodes or axial nodes.

Definition of Symbols in Subcode Argument Lists

C = coolant conditions

Q = radial power distribution

T_s = fuel rod surface temperature

d_m = depth of oxide layer formed by metal-water reaction

TABLE IX (continued)

q_m = heat generation rate per unit length from metal-water reaction

t_g = gas gap thickness

r_F = outer radius of fuel stack

T_{Fs} = surface temperature of fuel

T_{cs} = temperature of inside surface of cladding

T_g = temperature of gas in gas gap

P_g = pressure of gas in gas gap

P_I = fuel-to-cladding interfacial pressure

h_g = conductance of gas gap

$T(r)$ = radial temperature distribution in fuel rod

n_s = moles of gas in fuel rod

V_p = plenum volume

T_p = temperature of gas in plenum

T_{ps} = cladding surface temperature in plenum region

$r_{F_j}(z)$ = axial distribution of fuel stack outer radius (defined by collection of r_{FJn} values)

TABLE IX (continued)

$t_{gj}(z)$ = axial distribution of gas gap thickness (defined by collection of t_{gjn} values)

$T_{gh}(z)$ = axial distribution of gas gap temperature (defined by collection of T_{gjn} values)

$V_{ch}(z)$ = axial distribution of fuel crack volume (defined by collection of V_{cjn} values)

$P_{gj}(z)$ = axial distribution of gas gap pressure (defined by collection of P_{gjn} values)

P_c = coolant pressure (P_c is one of the quantities in output argument C of subcode COOL)

V_c = volume of fuel cracks per unit length

$u(r)$ = radial displacement distribution

Δh_f = fuel stack length change

Δh_c = cladding length change

I_F = failure indicator

δ_T = accuracy stipulated for temperature calculations

δ_P = accuracy stipulated for pressure calculations

$\bar{P}_{INJ}$ = vector whose i^{th} element consists of the guessed value of gap pressure in rod j at start of i^{th} iteration cycle

TABLE IX (continued)

P_{OUTj} = vector whose i^{th} element consists of the calculated value of gap pressure in rod j at end of i^{th} iteration cycle

e_{PO} = plastic strain tensor at end of last time step

e_p = plastic strain tensor at end of current time step.

Definition of Subcodes

COOL = Subcode which determines coolant conditions

POWER = Subcode which determines fuel rod power

METWAT = Subcode which determines heat generated by metal-water reaction

HTRC = Subcode which determines fuel rod surface temperature

GAPHTR = Subcode which determines gap conductance

HT1TDP = Subcode which determines fuel rod radial temperature distribution

GSFLOW = Subcode which determines fuel rod internal pressure

FRACAS = Subcode which determines fuel rod deformation

HONR = Subroutine which uses Newton's method to get better value of iterate in next iteration cycle

PLNT = Subcode which determines temperature of gas in plenum.

The convergence of the deformation-pressure iterates is accelerated by making an improved guess of fuel rod internal pressure using a modified form of the method of Newton. The improved guess is performed in subroutine HONR. This subroutine has three input arguments: (a) guessed values of internal pressure for all previous iterations at the current time step, (b) computed values of internal pressure after computation of fuel rod response to the guessed values of internal pressure, and (c) number of previous iterations. The subroutine has one output argument, which is the improved guess of internal pressure. It makes this improved guess by performing the following operations. First, generate a curve of the relation between guessed pressure and computed pressure. This is done by assuming the points established by arguments (a) and (b) above are connected by straight lines, as shown in Figure 25.

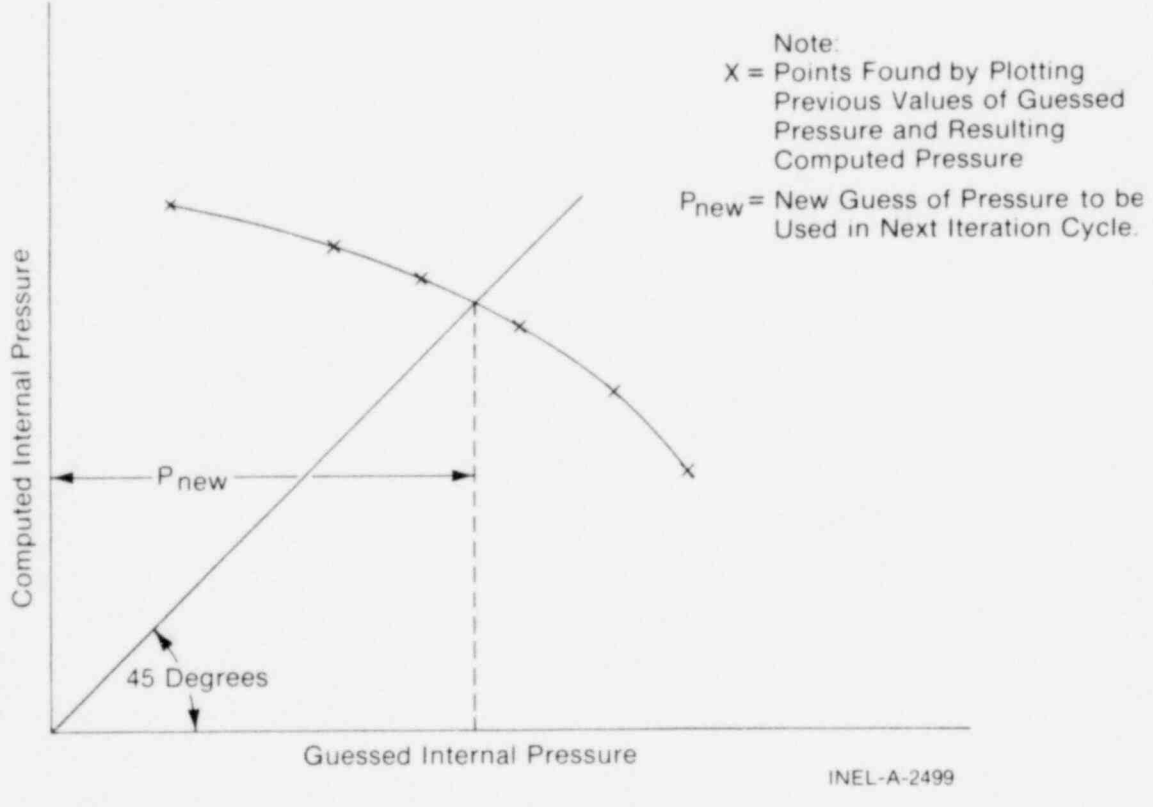

Fig. 25 Method used to make improved guess of fuel rod internal pressure.

Second, find guessed pressure that will give some value of computed pressure. This is done by finding the point at which a 45-degree line to the abscissa and through the origin intersects the generated curve. This is shown in Figure 25.

V. SUMMARY

FRAP-T3 contains improvements over FRAP-T2 in areas such as cladding failure prediction, cladding ballooning, and cladding material properties. Improvements of FRAP-T3 are presently underway and will be incorporated in the version, FRAP-T4. Differences between various versions of the code are shown in Table X. If programming errors are detected in the use of this version of FRAP-T, notification of the authors would be greatly appreciated.

TABLE X

DIFFERENCES IN VERSIONS OF FRAP-T

Phenomenon	FRAP-T1	FRAP-T2	FRAP-T3
Heat conduction	Stacked 1-D radial	Stacked 1-D radial	Stacked 1-D radial, 2-D r-e
Gap conductance	Modified Ross and Stoute	Modified Ross and Stoute, Cracked pellet	Modified Ross and Stoute, Cracked pellet
Plenum gas temperature	Coolant temperature + 10°F	Six-node transient energy balance, boundary conditions from surface temperature subcode	Six-node transient energy balance, simplified boundary conditions
Metal-water reaction	Baker-Just	Baker-Just	Cathcart
Internal pressure	Compressible, laminer gas flow, constant Hagen number (64)	Compressible, laminer gas flow, constant Hagen number (64)	Ideal gas law, compressible, laminer gas flow, variable Hagen number open porosity considered
Cladding deformation	Uncoupled stress-strain equations, no fuel-cladding interaction, no ballooning model, no creep	Triaxial coupled plastic stress-strain equations, fuel-cladding interaction, intermediate balloon model, no creep	Triaxial coupled plastic stress-strain equations, fuel-cladding interaction, advanced balloon model, strain-rate effects, cold-work and fast neutron flux effects, computation optimization, no creep.
Decay heat	No model	No model	ANS model

TABLE X (continued)

Phenomenon	FRAP-T1	FRAP-T2	FRAP-T3
Cladding failure	Failure if instability strain exceeded	Failure if total circumferential strain exceeded	Failure probability computed, overstress, overstrain, eutectic melting, and oxidation failure types modeled
Fuel deformation	GAPCØN-I Model	GAPCØN-I Model, free thermal expansion model	GAPCON-I Model, free thermal expansion model
High flow film boiling heat transfer correlations	Groeneveld	Groeneveld Dougall-Rohsenow Tong-Young Condie-Bengston	Groeneveld Dougall-Rohsenow Tong-Young Condie-Bengston
Low flow film boiling heat transfer correlations	Berenson	Groeneveld	Modified Bromley ($\alpha<0.6$) free convection ($\alpha\geq0.6$)
Critical heat flux correlations	B&W-2 Barnett Modified Barnett	B&W-2 W-3 Barnett Modified Barnett General Electric	B&W-2 W-3 Barnett Modified Barnett General Electric
Slip ratio correlation	Homogeneous	Modified Bankoff-Jones	Marchattree-Hoglund
Water properties	RELAP3 tables	Wagner steam tables	Wagner steam tables
Fuel, cladding and gas properties	MATPRO-2	MATPRO-6	MATPRO-9

VI. REFERENCES

1. J. S. Gellerstedt et al, "Correlation of Critical Heat Flux in a Bundle Cooled by Pressurized Water," *Two-Phase Flow and Heat Transfer in Rod Bundles, Symposium presented at the Winter Annual Meeting of the American Society of Mechanical Engineers, Los Angeles, California* (November 1969) pp 63-71.

2. P. E. MacDonald et al, *MATPRO-Version -- A Handbook of Materials Properties For Use in The Analysis of Light Water Reactor Fuel Rod Behavior*, TREE-NUREG 1005 (December 1976).

3. D. R. Coleman et al, *FRAP-T2 - A Computer Code for the Transient Analysis of Oxide Fuel Rods - Report II, FRAP-T2 Model Verification Report*, TREE-NUREG-1040 (March 1977).

4. Internal Manual.

5. K. R. Katsma et al, *RELAP4/MOD5 -- A Computer Program for Transient Thermal-Hydraulic Analysis of Nuclear Reactors and Related Systems*, ANCR-NUREG-1335 (September 1976).

6. J. A. Dearien et al, *FRAP-S1: A Computer Code for the Steady State Analysis of Oxide Fuel Rods - Report I, Analytical Models and Input Manual*, TREE-NUREG-1060 (to be published).

7. R. J. Wagner, *HEAT- 1: A One-Dimensional Time Dependent or Steady State Heat Conduction Code*, IDO-16887 (1963).

8. A. M. Ross and R. L. Stoute, *Heat Transfer Coefficient Between UO_2 and Zircaloy-2*, AECL-1552 (June 1962).

9. C. R. Hann, C. E. Beyer, L. J. Parchen, *GAPCON-THERMAL-1: A Computer Program for Calculating the Gap Conductance in Oxide Fuel Pins*, BNWL-1778 (September 1973).

10. C. Jocobs and N. Todreas, "Thermal Contact Conductance in Reactor Fuel Elements," *Nuclear Science and Engineering, 50* (1973).

11. H. French and W. M. Rohsenow, "Prædicition of Thermal Conductance of Metallic Surfaces in Contact," *Journal of Heat Transfer* (March 1973).

12. J. Crank and P. Nicolson, "A Practical Method for Numerical Evaluation of Solutions of Partial Differential Equations of the Heat Conduction Type," *Proceedings, Cambridge Philosophical Society, 43* (1974) pp 50-64.

13. F. Kreith, *Principles of Heat Transfer*, 8th edition, Scranton: International Text Book Company, 1964.

14. W. H. McAdams, *Heat Transmission*, 3rd edition, New York: McGraw-Hill Book Company, Inc., 1954.

15. J. V. Cathcart, *Quarterly Progress Report on Zirconium Metal-Water Oxidation*, Kinetics Program Sponsored by the NRC, Division of Reactor Safety Research, April-June 1976, ORNL/NUREG/TM-41 (August 1976).

16. A. Mendelson, *Plasticity: Theory and Applications*, New York: The MacMillian Company, 1968.

17. C. Wang, *Applied Elasticity*, New York: McGraw-Hill Book Company, Inc., 1953.

18. S. Timoshenko, *Theory of Elastic Stability*, New York: McGraw-Hill Book Company, Inc., 1963.

19. Internal Report.

20. Internal Report.

21. J. D. Kerrigan, *FRAIL3: A Fuel Rod Failure Subcode*, TFBP-TR-189 (April 1977).

22. C. C. Busby and K. B. March, *High Temperature Deformation and Burst Characteristics of Recrystallized Zircaloy-4 Tubing*, WAPD-T-900 (January 1970).

23. D. O. Hobson and P. L. Rittenhouse, *Deformation and Rupture Behavior of Light Water Reactor Fuel Cladding*, ORNL-4727 (October 1971).

24. M. R. Osborne and G. W. Parker, *The Effect of Irradiation on the Failure of Zircaloy-clad Fuel Rods*. ORNL-3626 (January 1972).

25. D. O. Hobson, M. F. Osborne, G. W. Parker, "Comparison of Rupture Data from Irradiated Fuel Rods and Unirradiated Cladding," *Nuclear Technology, 11* (August 1971).

26. D. G. Hardy, "The Effect of Neutron Irradiation on the Mechanical Properties of Zirconium Alloy Fuel Cladding in Uniaxial and Biaxial Tests," *Symposium on Irradiation Effects on Structural Alloys for Nuclear Reactor Application, Niagara Falls, Canada, June 29-July 1, 1970*, ASTM-STP 484 (1971) pp 215-216.

27. W. J. Langford, "Metallurgical Properties of Cold-Worked Zircaloy-2 Pressure Tubes Irradiated Under CANDU-PHW Power Reactor Conditions," *Symposium on Irradiation Effects on Structural Alloys for Nuclear Reactor Application, Niagara Falls, Canada, June 29-July 1, 1970*, ASTM-STP 484 (1971) pp 259-286.

28. W. R. Smalley, *Saxton Core II Fuel Performance Evaluation Material*, WCAP-3385-56 (September 1971) pp 4-84, 4-65; W. R. Smalley, *Evaluation of Saxton Core III Fuel Materials Performance*, WCAP-3385-57 (July 1974) pp 3-69, 3-132, 3-134.

29. D. G. Hardy, "Burst Testing of Zircaloy Cladding from Irradiated Pickering-Type Fuel Bundles," *Symposium on the Effects of Radiation on Substructure and Mechanical Properties of Metals and Alloys, Los Angeles, June 25-30, 1972*, ASTM-STP 529 (1973) pp 415-435.

30. W. A. Sutherland, "Experimental Heat Transfer in Rod Bundles," *Heat Transfer in Rod Bundles, ASME* (1968).

31. Internal Report.

32. P. G. Barnett, *A Correlation of Burnout Data for Uniformly Heated Annuli and Its Use for Predicting Burnout in Uniformly Heated Rod Bundles*, AEEW-R463 (1966).

33. E. D. Hughes, *A Correlation of Rod Bundle Critical Heat Flux for Water in the Pressure Range 150 to 725 psia*, IN-1412 (July 1970).

34. B. C. Slifer and J. E. Hench, *Loss-of-Coolant Accident and Emergency Core Cooling Models for General Electric Boiling Water Reactors*, NEDO-10329 (April 1971).

35. D. H. Knoegel et al, *Forced Convection Subcooled Critical Heat Flux, D_2O and H_2O Coolant with Aluminum and Stainless Steel Heaters*, DP-1306 (February 1973).

36. L. S. Tong, *Boiling Crisis and Critical Heat Flux*, TID-25887 (August 1972).

37. Internal Report.

38. L. S. Tong and J. D. Young, "A Phenomenological Transition and Film Boiling Heat Transfer Correlation," *Fifth International Heat Transfer Conference, Japan, July 1974*, Journal of Heat Transfer (1974) pp 20-124.

39. Internal Correspondence.

APPENDIX A

JCL AND INPUT DATA REQUIREMENTS

APPENDIX A

JCL AND INPUT DATA REQUIREMENTS

The Job Control Language (JCL) cards for compiling and executing the FRAP-T3 code on the CDC 7600 computer at the Idaho National Engineering Laboratory (INEL) are shown in Section 1. The input data requirements are shown in Section 2.

1. CONTROL CARDS FOR CDC 7600 COMPUTER

The control cards below will compile the tape transmitted source cards of FRAP-T and execute an example input data deck stored on the transmittal tape.

Job Card

Account Card

```
STAGE,TRAN,PE,PRE,VSN=T91234          (Stage FRAP-T tape with
                                       ten files of data)

CØPYP,TRAN,FRAPSRC.                   (Copy source cards of
                                       FRAP-T3, which are on
                                       file 1, to data set FRAPSRC)

CØPYP,TRAN,FCOOL.                     (Copy source cards of
                                       program that converts a
                                       RELAP4 plot tape to a
                                       FRAP coolant condition
                                       tape to data set FCOOL)

CØPYP,TRAN,FRPL.                      (Copy source cards of
                                       FRAP plot code to data
                                       set FRPL)
```

```
CØPYP,TRAN,SEGDECK.
```
(Copy segment loader directive cards to data set SEGDECK)

```
CØPYP,TRAN,LIBFRAP.
```
(Copy directives needed to create library of FRAP-T object decks to data set LIBFRAP)

```
CØPYP,TRAN,LIBENVS.
```
(Copy directives needed to create library of INEL Environmental Package subroutines to data set LIBENVS)

```
CØPYP,TRAN,SAMPLBM.
```
(Copy example input data deck for FRAP-T from file 7 to data set SAMPLBM)

```
CØPYP,TRAN,SAMPJCL.
```
(Copy example control cards for executing FRAP-T program from transmittal tape)

```
COPYP,TRAN,STH2ØT.
```
(Copy water properties table to data set STH2ØT. This data set consists of one record that is several thousand words long.)

```
REWIND,FRAPSRC,STH2ØT,SEGDECK.
REWIND,LIBFRAP,LIBENVS,SAMPLBM.
```

```
UPDATE,A,R,P=TRAN,N.                    (Process the source cards
                                         of the INEL Environmental
                                         Package, which are stored
                                         on file 8 with CDC UPDATE
                                         program)

RETURN, TRAN.
UPDATE,P=NEWPL,F.                       (NEWPL contains the INEL
                                         Environmental Package
                                         source cards)

RFL,160000.                             (Reserve 160,000 octal
                                         words of storage for
                                         compiling)

FTN,I=CØMPILE,R=3,ØPT=2,S=SYSTEXT,S=PFMTEXT,RØUND,L=0.
                                        (Compile source cards
                                         of INEL Environmental
                                         Package, which was given
                                         name COMPILE by execution
                                         of UPDATE program)

REDUCE.
RETURN,CØMPILE.
RETURN,NEWPL.
LIBEDT,I=LIBENVS.                       (Create library of object
                                         decks of INEL Environmental
                                         Package subroutines.
                                         Directives are in pre-
                                         viously created data set
                                         LIBENVS.  Directives give
                                         this library the name
                                         ENVLIB)

RETURN,LGØ.
CØPYP,FRAPSRC,TAPE8.                    (Transfer source cards of
                                         FRAP-T to file TAPE 8)
```

```
REWIND,TAPE8.
RFL,160000.
FTN,I=TAPE8,ØPT=0,R=3,L=0.          (Compile FRAP-T source
                                     cards)

LDSET,PRESET=NGINF,ERR=NØNE,LIB=ENVLIB.   (Prepare to send object
                                     decks of FRAP-T and INEL
                                     Environmental Package to
                                     Loader, set all of core
                                     to negative infinity)

SEGLØAD,B=FRAPABS,I=SEGDECK.        (Create load module of
                                     entire FRAP-T program.
                                     Directives for seg-
                                     mentation are given by
                                     previously created data
                                     set SEGDECK)

LØAD,LGØ.
NØGØ.
CØPYP,STH2ØT,TAPE15.                (FRAP-T reads water
                                     properties table with
                                     FORTRAN Logical
                                     Unit 15)

RETURN,STH2ØT.

REWIND,FRAPABS,TAPE15.
REWIND, TAPE17.                     (Information for FRAP-T
RFL,160000.                          plotting program is
                                     written to file TAPE 17)

FRAPABS,SAMPLBM.                    (Execute FRAP-T with
                                     example input data deck
                                     stored in data set
                                     SAMPLBM)

EXIT,U.
```

If transient spatially varying coolant conditions are to be specified, a file for TAPE4 needs to be set up. An example of this is shown below.

```
STAGE,TAPE4,PE,E,VSN=T9aaaa.          (T9aaaa is tape number
                                       of previously created
                                       tape containing transient
                                       coolant conditions)
REWIND,TAPE4.
```

If a restart tape is to be written, a file for FORTRAN Logical Unit 1 needs to be set up. An example of this is shown below.

```
STAGE,TAPEW,PE,E,PØST.
REWIND,TAPE1.
CØPYP,TAPE1,TAPEW.
```

The directive cards for the segment loader (SEGLØAD) consist of the following cards:

```
T1        TREE      CØØL-(HT1SST,HT1TDP)
          TREE      FRAPT-(EXCINP,PØWINP,GAPPRS,PRNTØT,T1)
          GLØBAL    STH2ØC
          GLØBAL    FTBLCM
          GLØBAL    PRNTB,DFRMB,BLKI,EXCB
          GLØBAL    IØ.BUF.,Q8.IØ.,FCL.C.
          INCLUDE   INCØM=
FRAPT     INCLUDE   PLØTW,TIMSET,ZERØUT,MØVE,PHYPRØ,FTHCØN
FRAPT     INCLUDE   TIMSTP,VSWELL,FRIDAW,ERRØRI
FRAPT     INCLUDE   PLENV,PRNTMP,TIMSTP,VSWELL,FRIDAW,ERPORI
FRAPT     INCLUDE   CTHCØN,GVISCØ,STH2ØI,STH2Ø1,STH2Ø3,ERRØR1
FRAPT     INCLUDE   HØNR
EXCINP    INCLUDE   THMPRP,HT1INP,FCP,NBNDY
EXCINP    INCLUDE   INP,INP2,INP5,INP6,INP8,CVI,LINK,MØDER,INPUPK
PØWINP    INCLUDE   PLTINP,GPRINP,CØØLIN,CARDPR,GPCINP,MØDPID
```

```
CØØL      INCLUDE   PØWER,METWAT,HTRC,EMSSF2,MADATA
CØØL      INCLUDE   PCHF,PRØFAC,BDCØND,QDØT,GTHCØN
CØØL      INCLUDE   EMSSF1,RØØT1,FEMISS,CMHARD
CØØL      INCLUDE   GAPHTR,PRNTC,GAPHTC,SLP2,PLNT,SLIPR
CØØL      INCLUDE   SURTEN,THCØN,VISC,VØID
GAPPRS    INCLUDE   FRACAS,SWLCHK,CLDRUP,FTHEXP,CDTHEX
GAPPRS    INCLUDE   CPØIR,CSTRAN,CATHEX
GAPPRS    INCLUDE   CELMØD,FELMØD,FPØIR,CLADF,CLØSE
GAPPRS    INCLUDE   CØUPLE,DEPCAL,FCMI,GAPT,GSFLØW
GAPPRS    INCLUDE   FRAIL,BDTR,BFRAC,CDTR,CRERUP,DFRAC,DLGAM,EUMELT
GAPPRS    INCLUDE   REPACK,STACK,STRAIN,STRESS
GAPPRS    INCLUDE   FSIGT,FSTEMP,FSTRS,HCFF,LCFF,MELT,NDTR,BALOON,RADII
PRNTØT    INCLUDE   PAGHED,ENERGY
HT1SST    INCLUDE   SURFBC
     END  FRAPT
```

The directives for execution of program LIBEDT to make a library of the object decks of the INEL Environmental Package consist of the following cards:

```
LIBRARY(ENVLIB,NEW=2048)
REWIND(LGØ)
ADD(*,LGØ)
FINISH.
```

The directives for execution of program LIBEDT to make a library of the object decks of the FRAP-T program consist of the following cards:

```
LIBRARY(FRAPLIB,NEW=4000)
REWIND(FRAPØBJ)
ADD(*,FRAPØBJ)
REWIND(PARTØBJ)
REPLACE(*,PARTØBJ)
PCØPY(*,NEWFRAP)
REWIND(NEWFRAP)
FINISH.
```

2. INPUT DATA CARDS

For the purpose of better describing the contents of FRAP-T3 input data cards, the data deck has been divided into several data blocks. Each data block is read in by a different input subroutine of the code. The data blocks are described below in the order they follow in the input data deck. The type of data contained in each data block is identified, and the column location, format, name, and definition of each piece of input data given.

The input data can be in either the British or SI system of units. The two systems of units cannot be mixed. If SI units are specified, all data must be input in SI units. Within either system, the required unit for each input quantity is given below.

Input format is indicated by the characters F, I, and A. F denotes that floating point numbers are to be input. For this case, exponents must be right hand adjusted and a decimal point must be present. An I denotes that integer numbers are to be input. The integers must be right hand adjusted. No decimal point can be present. An A denotes that alpha-numeric characters are to be input. This input is used to specify labels for plot axes and titles.

When the restart option is used, and the problem solution starts from the end time of a previous computer run, the entire input deck must still be submitted.

Data Block 1. General Data.

Card 1.1

Columns	Format	Name	Quantity
1-5	I	NROD	Number of fuel rods (NRØD must equal 1, since arrays are dimensioned to handle only one fuel rod).

1-10	I	NCHN	Number of coolant subchannels surrounding fuel rods. Because of programming limitations, NCHN must equal 1.
11-15	I	NAXN	Number of axial nodes (NAXN $\leq$ 20). If NGSFLØ=1 (columns 31-35), NAXN $\geq$ 3. If no minus sign in format of NAXN, code generates evenly spaced mesh. An example of generated mesh is shown in Figure A-1. If minus sign input, axial node lengths are specified by card group 1.7.
16-20	I	NPLNT	If NPLNT = 0, plenum gas temperature model is used. If NPLNT = 1, plenum gas temperature set to coolant temperature at top axial node plus 10°F.
21-25	I	NDT	Number of time step - time pairs used to prescribe maximum time step that can be used during problem solution. See card group 1.5 input instruction for further clarification. NDT < 20.
26-30	I	NUNIT	If this field is zero or left blank, data are input in British units. If the integer 1 is put in column 30, data are input in SI units. Code output is in the same system of units that is selected for input.
31-35	I	NGSFLO	If NGSFLO = 0, gas flow between plenum and gas gap is not modeled. Instead, pressure equilibrium is assumed to instantly occur, so that plenum and gas gap are always at the same pressure. If NGSFLO = 1, gas flow between plenum and gas is modeled.

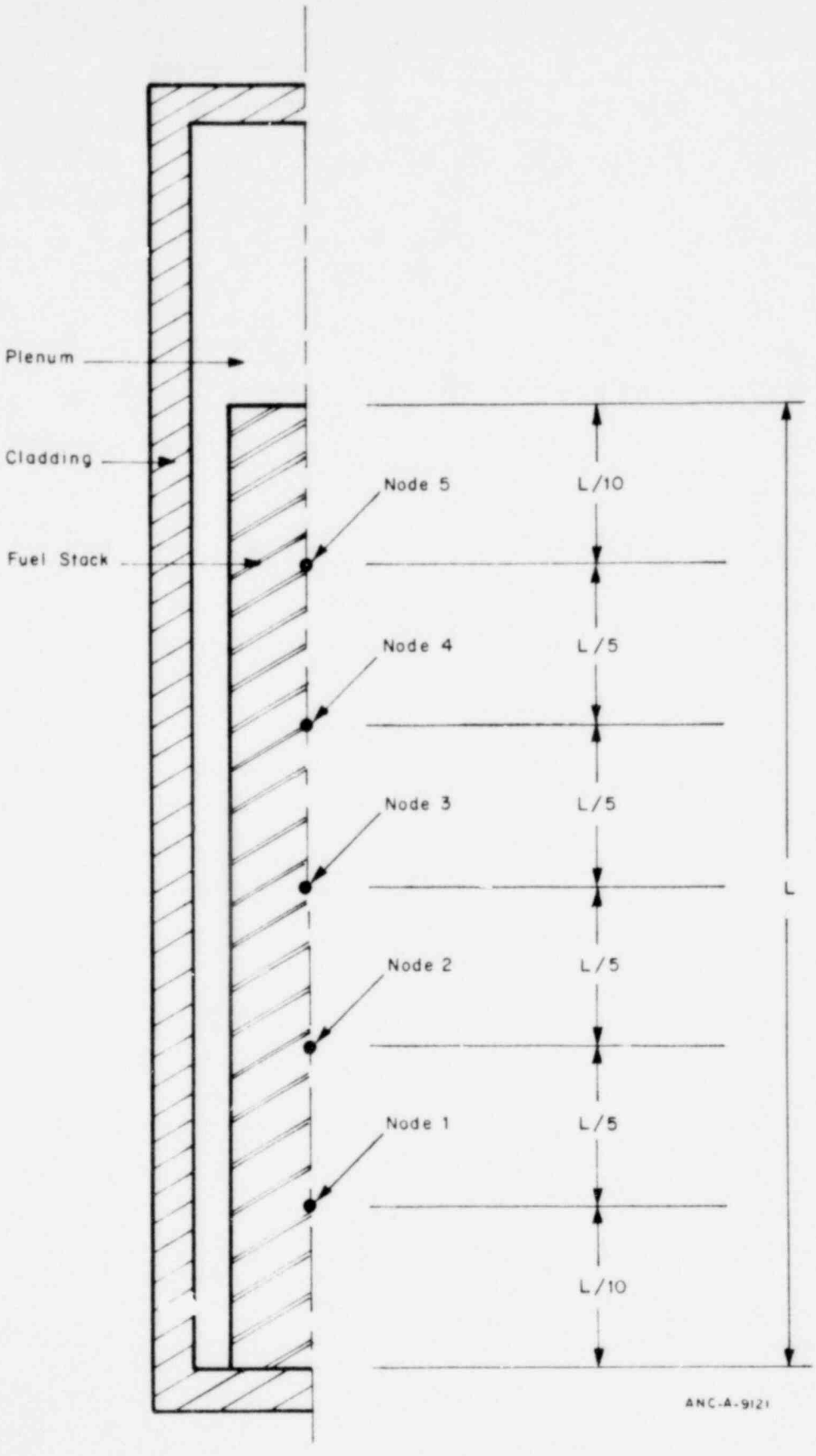

Fig. A-1 Example of evenly spaced axial node mesh for case NAXN=5.

36-40	I	MODMW	If MODMW = 0, metal-water reaction is modeled. If MODMW = 1, metal-water reaction is not modeled.
41-45	I	MODFD	If MODFD = 0, fuel deformation is modeled as if the fuel had radial cracks extending from the fuel surface to the center (free thermal expansion). If MODFD = 1, the GAPCON-1 code[A-1] fuel deformation model is used.
46-50	I	MODFPC	If MODGPC = 0, the Ross and Stoute[A-1] gap conductance model is used. If MODGPC = 1, the MacDonald-Broughton[A-2] gap conductance model is used. The MacDonald-Broughton model will predict the effects of pellet cracking on gap conductance, while the Ross and Stoute model will not.
51-55	I	NFASTF	If NFASTF = 0, fast neutron flux assumed to have same axial profile as power profile specified by card group 4.3. Otherwise, NFASTF = number of pairs of normalized fast neutron flux versus elevation used to prescribe axial distribution of fast neutron flux on card group 1.7.1. NFASTF $\leq$ 25.
56-60	I	MPDCAY	If MPDCAY = 0, ANS formula for decay heat not used to specify fuel rod power. If MPDCAY = 1, ANS formula for decay heat used to specify fuel rod power. In this case, decay heat assumed only source of fuel heat generation.

61-65	I	NFRIDW	Switch to write on disk or tape the forcing function data set required by the FRIDA[A-3] subcode. If NFRIDW = 0, data set not written. If NFRIDW = 1, data set is written.
66-70	I	NDIM	Indicator of number of dimensions in heat conduction calculations. If NDIM = 0, only radial heat conduction is considered. If NDIM = 1, R - Ø heat conduction at one or more axial nodes is considered.
71-75	I	NCONSW	Switch to permit "stacked" azimuthal temperature distribution calculations. If NCONSW=0, normal heat conduction calculations. If NCONSW=1, "stacked" calculation performed to determine azimuthal temperature variation. Radial temperature distribution in each azimuthal sector determined, but no heat transfer between azimuthal sectors assumed. This option reduces computer time. This option requires NDIM=1.
76-80	I	NEDTSW	If NEDTSW=0, strain-rate terms for MATPRO caldding property correlations not set to zero (normal procedure). If NEDTSW=1, strain-rate terms for MATPRO cladding property correlations are set to zero. An error in interpolation of cladding stress-strain state to find time of gas gap closure sometimes occurs. When this error is large, an error message stating "argument to EXP too small" is printed from subroutine CSIGMA. This error is precluded when NEDTSW=1.

Card 1.2

Columns	Format	Name	Quantity
1-10	F	TO	Initial problem time (seconds) (If restarting, TO = end time of previous calculations). As an option, TO on starting card can be set to zero. In this case, initial conditions set equal to those on restart tape at time equal to TREST (specified on card 1.4), but time is backshifted to zero. This permits one run to be made establishing steady state fuel rod conditions. Then, on second run, which has purpose of predicting fuel rod behavior following an accident, input specified power and coolant condition histories can have a time frame which has accident initiation beginning at T = 0.
11-20	F	TMAX	Final problem time (seconds)
21-30	F	DT	Time step (seconds). IF NDT > 0 on card 1.1, this field is not used. If used, DT > 0. If NDIM>0 on card 1.1 (multidimensional heat conduction calculations performed), DT should not exceed value of about 0.001. This is because the explicit numerical solution of multidimensional heat conduction is not stable for a time step much larger than 0.001 sec.
31-40	F	DTPO	Problem time intervals at which calculated fuel rod state will be printed (seconds). If printout desired at end of each time step, set DTPO to zero.
41-50	F	RL	Cold length of fuel pellet stack (ft or m)

51-60	F	DROD	Cold outer diameter of fuel rod (ft or m)
61-70	F	TEMPO	Cold state temperature of fuel rod (°F or K). The fuel rod dimensions given in the input must correspond with this temperature.
71-80	F	COLDW	Fraction of cross-sectional area reduction of cladding done by cold working process. COLDW = $(A_o-A)/A_o$ Where A_o = cross-sectional area prior to cold working, A = cross-sectional area after cold working.

Card 1.3 Pellet Data.

Columns	Format	Name	Quantity
1-10	F	RHØF	Cold state density of fuel (lbf/ft^3 or kg/m^3)
11-20	F	RSHD	Cold state radius to pellet shoulder (ft or m). Shoulder defined to be point of primary contact at pellet interfaces. See Figure A-2.
21-30	F	DISHD	Cold state depth of pellet dish (ft or m)
31-40	F	PELH	Cold state height of fuel pellet (ft of m)
41-50	F	DISHVO	Cold state volume of pellet dish (ft^3 or m^3) (sum of top and bottom dish volumes)
51-60	F	FRPO2	Fraction by weight of fuel that is PuO_2
61-70	F	BU	Burnup of fuel (MWs/kg).

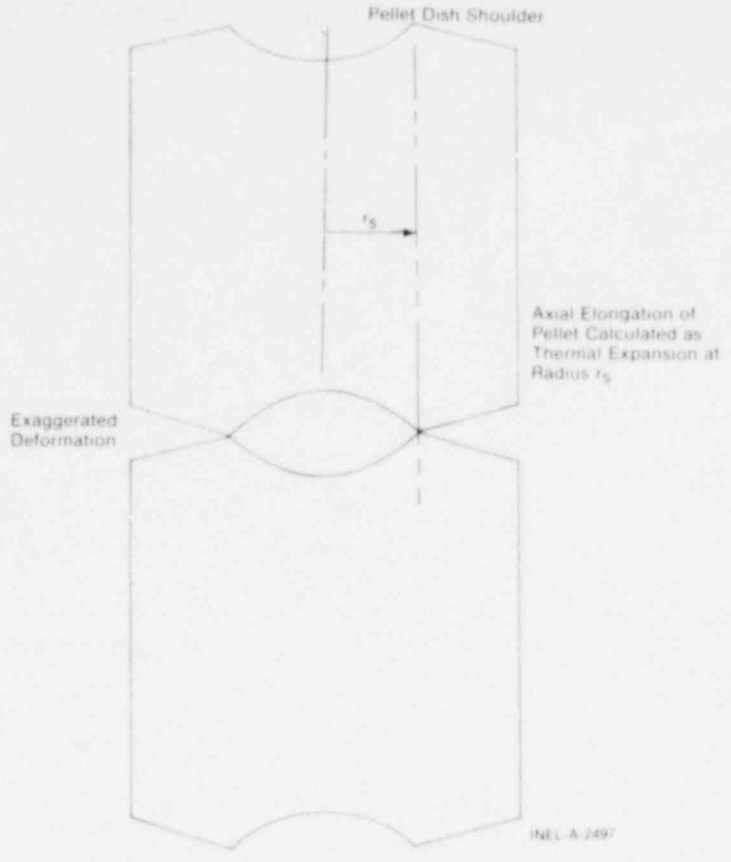

Fig. A-2 Definition of pellet shoulder radius.

Card 1.4 Numerical Solution Control and Cladding Flux History.

Columns	Format	Name	Quantity
1-10	F	PRSACC	Minimum fractional difference in internal fuel rod pressure at a given axial node calculated by two successive iterations before convergence is declared. If these columns left blank, program sets a value of 0.0005. This minimum difference must occur at every axial node before convergence is declared. The test is $(P^{r+1} - P^r) / P^r <$ PRSACC, where P^r symbolizes pressure at iteration number r.

11-20	F	TMPACC	Minimum fractional difference in temperature at a given radial node calculated by two successive iterations before convergence is declared. If these columns left blank, program sets value of 0.0005. If PRSACC > 1.0, explicit solution method used. No iterations performed. Accuracy controlled only by specified time step. For steady state solution, accuracy internally set to 0.001. If implicit solution method runs into convergence difficulties, explicit solution method should be considered.
21-30	F	FQCRIT	Factor which critical heat flux is multiplied by. If these columns left blank, program sets value of 1.0.
31-40	F	DTSS	Time step threshold (sec) for steady state heat conduction model. If time step as set by DT on card 1.2 or DTMAXA array of card group 1.5 is greater than DTSS, steady state heat conduction model used. If not, transient heat conduction model used. If DTSS left blank, transient heat conduction model always used after first time step.
41-50	F	CFLUX	Axially averaged and time averaged fast neutron flux cladding exposed to during lifetime (neutrons/m^2-sec). Fast neutron is defined to be a neutron with an energy greater than 1 Mev.

51-60	F	TFLUX	Time span of cladding exposure to fast neutron flux (sec). The quantity CFLUX*TFLUX must equal axially averaged fast neutron fluence received by cladding.
61-70	F	PFAIL	Probability for fuel rod failure above which deformation and pressure subcodes assumes fuel rod to be failed. If these columns left blank, PFAIL set to value of 0.5. Then, deformation and pressure subcodes assume fuel rod not failed until probability for failure computed by FRAIL subcode is greater than 0.5. If calculations wanted assuming fuel rod never fails, set PFAIL=1.1. If calculations wanted assuming failure does not occur until hoop strain exceeds ultimate strain, set PFAIL = 1.1.

Card 1.4.1 (Between card 1.4 and card group 1.5. Omit cards 1.4.1 through 1.4.3 if NDIM = 0. on card 1.1)

Columns	Format	Name	Quantity
1-10	F	TIMMD	Time at which multidimensional heat conduction calculations are to start (sec).

Card 1.4.2 (omit if NDIM = 0)

Columns	Format	Name	Quantity
1-5	I	NAZ	Number of azimuthal sectors in heat conduction calculations (azimuthal sector defined in Figure A-3).
6-10	I	NAZN	Number of axial nodes at which azimuthal heat conduction is to be considered

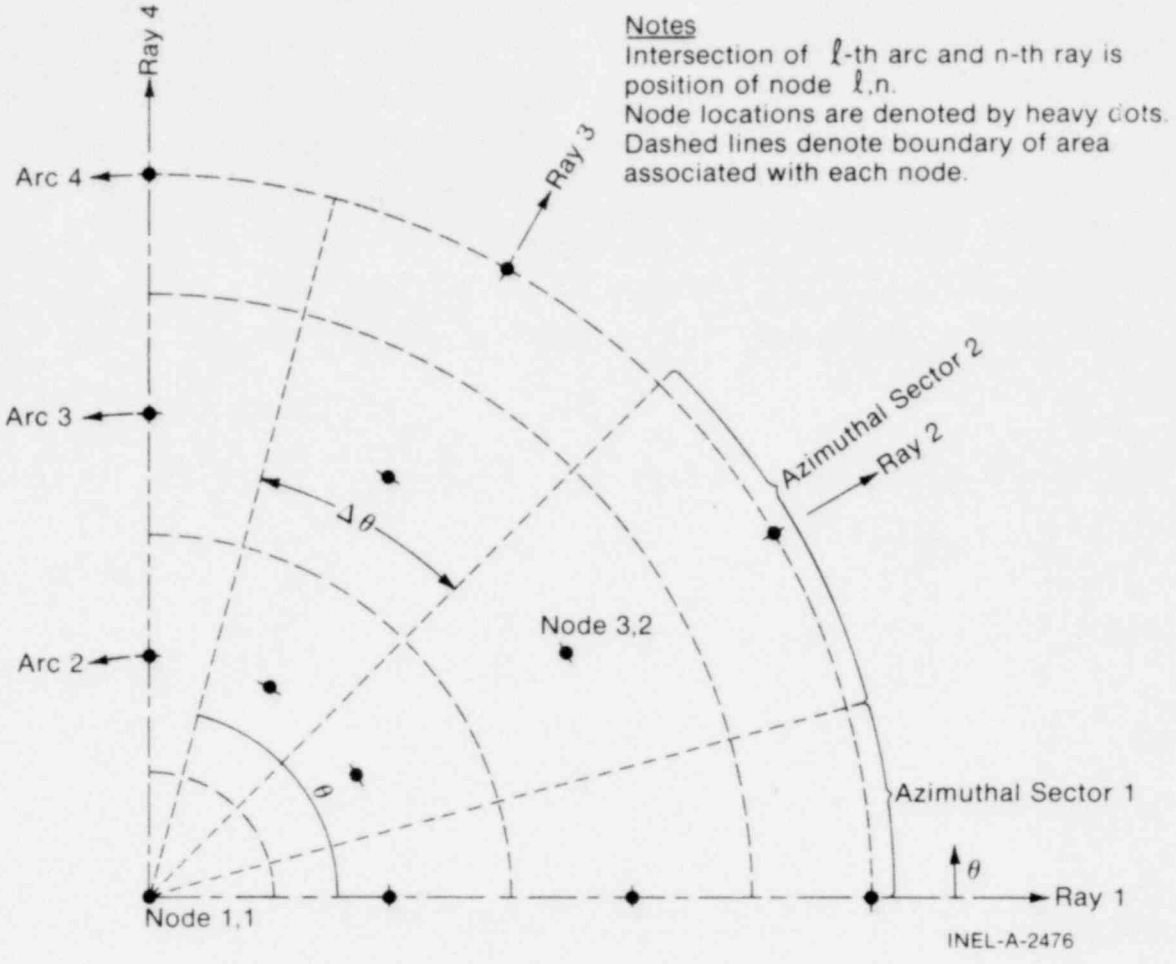

Fig. A-3 Mesh conduction for R-θ heat conduction.

11-15	I	NSYMM	Symmetry indicator. If NSYMM = 0, twofold symmetry (temperature distribution computed in quarter of fuel rod). If NSYMM=1, onefold symmetry (temperature distribution computed in half of fuel rod). If NSYMM = 2, no symmetry.

The computer core requirements increase as the spatial detail specified for the multidimensional temperature distribution increases. Storage requirements increase according to the equation $S = 5\ N_\theta\ N_Z\ N_R + 20\ N_\theta\ N_Z$, where S = words of storage required, N_θ = number of azimuthal sectors, N_Z = number of axial nodes at which azimuthal heat conduction is to be considered, and N_R = number of radial nodes. Symmetry conditions are taken advantage of to reduce storage requirements. If twofold symmetry exists, a given azimuthal spatial detail is accomplished with a quarter of the azimuthal sectors required when no symmetry exists.

Card(s) 1.4.3 (omit if NDIM = 0)

Columns	Format	Name	Quantity
1-5	I	N1	First axial node at which azimuthal heat conduction to be considered
6-10	I	N2	Second axial node at which azimuthal heat conduction is to be considered.

Repeat as necessary.

Card Group 1.5 Time Step History Cards.

These are time step history cards. If NDT $\leq$ 0 on card 1.1, no cards are input. On these cards, every other 10 column field contains the maximum time step desired at the time specified in the 10 column field immediately to the right of it. The data are entered four pairs per card in order of increasing time until NDT pairs are described. A straight line interpolation between points specified by input is performed by the code. If quantities such as mass flux or pressure are oscillating rapidly, the time step history cards should be used to enforce a program step that is small compared to the period of the oscillations. Examples of the time step history specified for several different types of accidents are shown in Table A-I. As a general rule, the time step should not exceed 0.1 sec. Cases in which the fuel rod temperature is changing slowly are an exception. If multidimensional

TABLE A-I

EXAMPLES OF TIME STEP HISTORIES

Loss-of-Coolant Accident		Power-Cooling-Mismatch Accident		Reactivity Initiated Accident		Anticipated Transient Without Scram Accident		Slow Power Ramp		Power Ramp at 0.5 kW/m-sec, 2-D rθ Heat Conduction	
Time (sec)	Time step (sec)	Time (sec)	Time step (sec)	Time (sec)	Time step (sec)	Time (sec)	Time step (sec)	Time (sec)	Time step (sec)	Time (sec)	Time step (sec)
0.0	0.02	0.0	0.1	0.0	0.001	0.0	0.05	0.0	3600.0	0.0	0.0005
0.05	0.02	100.0	0.1	2.0	0.001	10.0	0.05	36,000.0	3600.0	10.0	0.0005
0.0501	0.05					10.1	0.1				
1.9	0.05					20.0	0.1				
2.0	0.1										
30.0	0.1										

heat conduction is being computed (NDIM > 0 on card 1.1), then the time step should never exceed about 0.001 sec. The time step needs to be limited to this value in order to assure stability of the heat conduction calculations.

Columns	Format	Name	Quantity
1-10	F	DTMAXA(1)	Time step at time DTMAXA(2) (sec)
11-20	F	DTMAXA(2)	Time (sec)
21-30	F	DTMAXA(3)	Time step at time DTMAXA (4) (sec)
31-40	F	DTMAXA(4)	Time (sec) (DTMAXA(4) > DTMAXA(2).

Repeat as necessary. After first card is filled with four pairs of data, continue putting data in same manner on second card. Continue in this manner until all pairs of data have been put on cards. An example of the time step history specified by card group 1.5 is shown in Figure A-4. Maximum of 20 time step pairs.

Card Group 1.6 Rod-to-Coolant Channel Connection Data.

There must be NRØD cards in this group, with rod numbers 1 to NRØD of card 1.1. At least one coolant subchannel but no more than four coolant subchannels may be specified. The coolant channel geometry is assumed to be the same along the entire length of the fuel rods. No coolant subchannel can have an identification number greater than NCHN of card 1.1. If only one coolant subchannel, input for card group 1.6 consists of one card with a 1 in column 5, 1 in column 15, and 1.0 in columns 16-20; rest of card is blank. A pictorial explanation of data input for card group 1.6 is shown in Figure A-5.

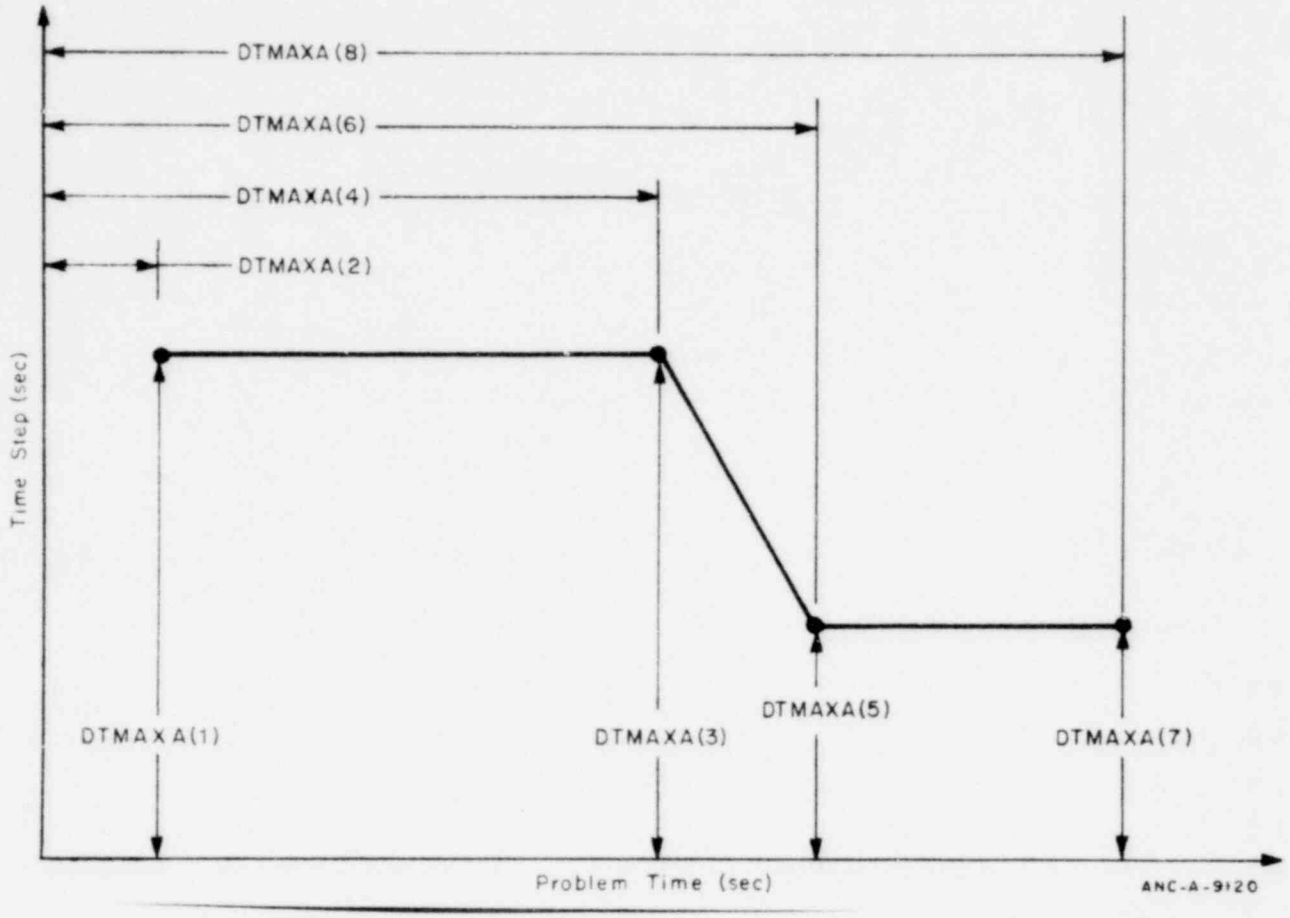

Fig. A-4 Example of time step history specified by card group 1.5.

Columns	Format	Name	Quantity
1-5	I	RØDNØ	Number of a rod in cluster being analyzed
11-15	I	CHNNØ1	Number of a subchannel cooling RØDNØ
16-20	F	FRP1	Fraction of surface area of RØDNØ bordering CHNNØ1
21-25	I	CHNNØ2	Number of a subchannel cooling RØDNØ
26-30	F	FRP2	Fraction of surface area of RØDNØ bordering CHNNØ2
31-35	I	CHNNØ3	Number of a subchannel cooling RØDNØ
36-40	F	FRP3	Fraction of surface area of RØDNØ bordering CHNNØ3

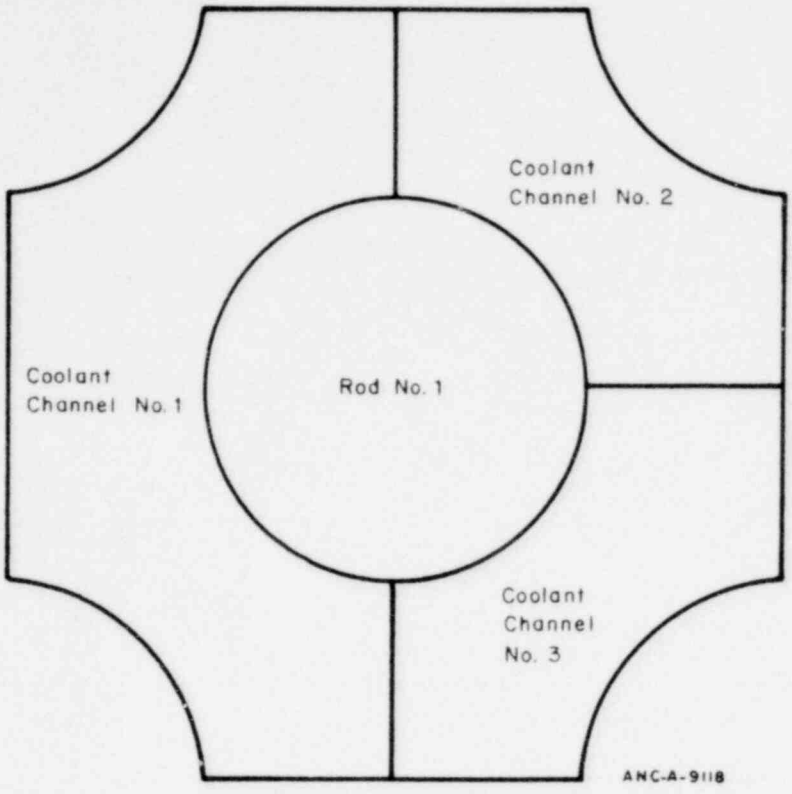

Card Group 1.6 Data

RØDNØ = 1
CHNNØ1 = 1
FRP1 = 0.5
CHNNØ2 = 2
FRP2 = 0.25
CHNNØ3 = 3
FRP3 = 0.25

Fig. A-5 Example of data input for card group 1.6 (coolant channel data).

41-45	I	CHNNØ4	Number of subchannel cooling RØDNØ
46-50	F	FRP4	Fraction of surface area of RØDNØ bordering CHNNØ4.

Card Group 1.7 Axial Node Length Data.

If no minus sign is put in front of NAXN of card 1.1, omit this card group.

Columns	Format	Name	Quantity
1-10	F	Z(1)	Length of axial node 1 (ft or m)
11-20	F	Z(2)	Length of axial node 2 (ft or m)
21-30	F	Z(3)	Length of axial node 3 (ft or m).

Continue as necessary with eight lengths per card until NAXN lengths have been put on cards. The node lengths must sum to within 0.0005 ft of RL on card 1.2. An example of the axial node mesh layout generated by card group 1.7 is shown in Figure A-6 for the case of NAXN = 5.

Card Group 1.7.1 Normalized Fast Neutron Flux Axial Distribution. (Omit this card group if NFASTF = 0 on card 1.1). Fast neutrons considered to be those with energy greater than 1 Mev.

Columns	Format	Name	Quantity
1-10	F	FLUXZ(1)	Ratio of fast neutron flux at elevation FLUXZ(2) to axially averaged fast neutron flux. FLUXZ(1) * CFLUX = fast neutron flux at elevation FLUXZ(2). (CFLUX input on card 1.4.)
11-20	F	FLUXZ(2)	Elevation above bottom of fuel stack (ft or m)
21-30	F	FLUXZ(3)	Ratio of fast neutron flux at elevation FLUXZ(4) to average fast neutron flux.
31-40	F	FLUXZ(4)	Elevation above bottom of fuel stack (ft or m)

Repeat until NFASTF pairs of data have been placed on cards, 4 pairs per card. Maximum of 6 and 1/4 cards of data. FLUXZ(4) > FLUXZ(2), etc.

Card 1.8 Restart Switches.

Columns	Format	Name	Quantity
1-5	I	NSWINR	If NSWINR = 0, no restart tape is read. If restart tape is to be read, set NSWINR equal to 1.
6-10	I	NSWINW	If NSWINW = 0, no restart tape to be written. If restart tape to be written, set NSWINW equal to 2. If minus sign in front

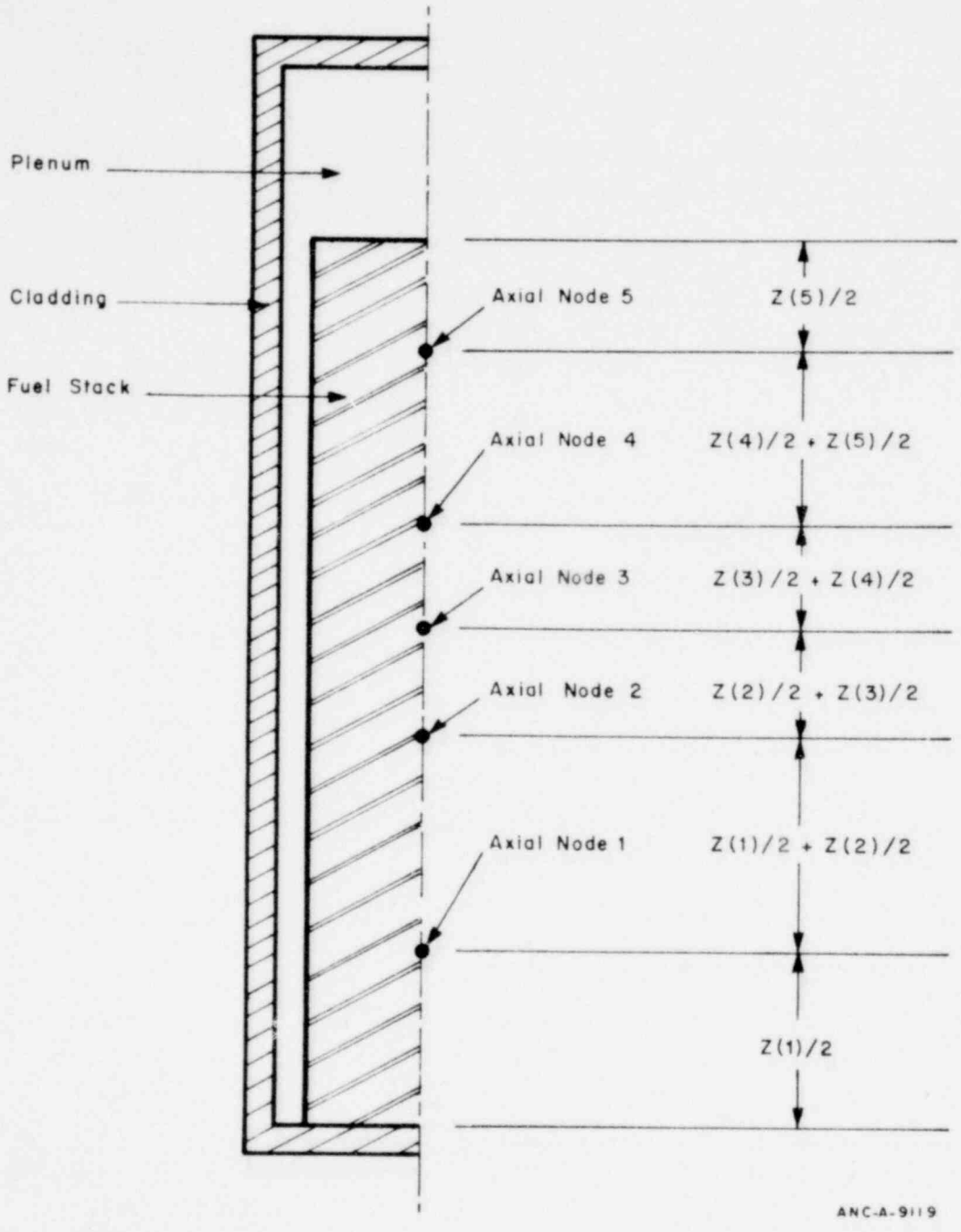

Fig. A-6 Example of axial node mesh specified by card group 1.7 for case NAXN=5.

			of NSWINW, restart records laid end to end rather than overlaid, so that problem can be restarted at anytime between 0 and TMAX.
11-15	I	NRADFS	If NRADFS=0, number of radial nodes used in calculations which created restart tape that is to be read is same as COLS on card 3.2. Otherwise, NRADFS equals numbers of radial nodes used in calculations from which a restart is to be made. This adjusts for differences in FRAP-S and FRAP-T radial nodalization. If NSWINR=0, NRADFS=0. If restarting from tape created by FRAP-T, NRADFS=0.
21-30	F	TREST	Time at which transient calculations are to begin or continue (sec).

Data Block 2. Thermal Property Data.

Card 2.1

Specification of temperature intervals at which thermal properties are put into tables. No restriction placed on the upper bound value for the quantities read in on this card. Larger values demand more core, however.

Columns	Format	Name	Quantity
1-5	I	NKF	Number of thermal conductivity versus temperature pairs to be generated by code for fuel. If NKF < 2 it is reset to 2. Normally NKF = 100.
6-10	I	NSF	Number of specific heat versus temperature pairs to be generated for fuel. Core space requirements are reduced if NSF = NKF.

11-15	I	NKC	Number of thermal conductivity versus temperature pairs to be generated for cladding. If NKC < 2 it is reset to 2. Normally, NKC = 50.
16-20	I	NSC	Number of specific heat versus temperature pairs to be generated for cladding. Core space requirements are reduced by setting NSC = NKC.
21-25	I	IDEBUG	If IDEBUG is greater than zero, thermal property tables printed.

Card 2.2

Specification of temperature bounds of thermal property tables.

Columns	Format	Name	Quantity
1-10	F	TOF	Minimum temperature in fuel thermal property tables (°F or K) (must be less than minimum fuel temperature expected during calculations)
11-20	F	TMAXF	Maximum temperature in fuel thermal property tables (°F or K) (must be greater than maximum fuel temperature expected during calculations)
21-30	F	TOC	Minimum temperature in thermal property tables of cladding (°F or K)
31-40	F	TMAXC	Maximum temperature in thermal property tables of cladding (°F or K).

Data Block 3. Temperature Computation Subcode Input Data.

Input data for this data block is processed by the INP[A-3] package. All of the input data cards must have an eight digit card number as the first entry on the card. The input data is free form.

It does not need to be placed in certain card columns. Each piece of input data must be separated on both sides by at least one blank column or a comma. A piece of input data that is integer format must not have a decimal point or an exponent. Title cards must have an "=" as the first nonblank character. Comment cards are allowed in this block of the input data and are identified by an "*" or a "$" as the first nonblank character. Data on a card may be continued on a following card by entering a plus sign as the first nonblank character on the continuation card. The last card in data block 3 must be a "." character in column 1.

Card 3.1 Title Card.

This card must have the "=" symobol as the first nonblank character, usually placed in column 1. The remainder of the card is used to specify the problem title, which will be printed out in the input listing.

Card 3.2 General Data. - Card #01010001

Data Field	Format	Name	Quantity
1	I	COLS	Number of radial mesh points at each axial node (COLS $\leq$ 20).
2	I	IGEOM	Geometry type. Always input the integer 2 (cylindrical).
3	F	XO	Left boundary coordinate. Always input 0.0.
4	F	FCTR	Source multiplication factor. Always set equal to 1.
5	I	MAXIT	Maximum number of iterations in temperature calculation subcode or steady state solution (normally about 200).
5	F	EPS	Convergence criterion for temperature calculation subcode (°F or K) (normally about 1.0).

7	I	NOITER	Maximum number of iterations on material properties for time dependent solution of temperature calculation subcode. (Normally about 200).

Card 3.3 Geometry Location and Mesh Increment Format. - Card #01010200

Radial mesh intervals for a problem are specified by defining an interval having a constant mesh spacing. Normally, intervals are defined for the fuel, gas gap, and cladding, respectively. An example of radial mesh layout is shown in Figure A-7. The mesh data are given as a sequence of pairs of numbers in one of two formats; either as the number of mesh spaces in the i^{th} interval and the right boundary coordinate (cold state) of the interval (Format 1), or as a mesh spacing and the mesh spacing number of the right boundary where the spacing changes (Format 2).

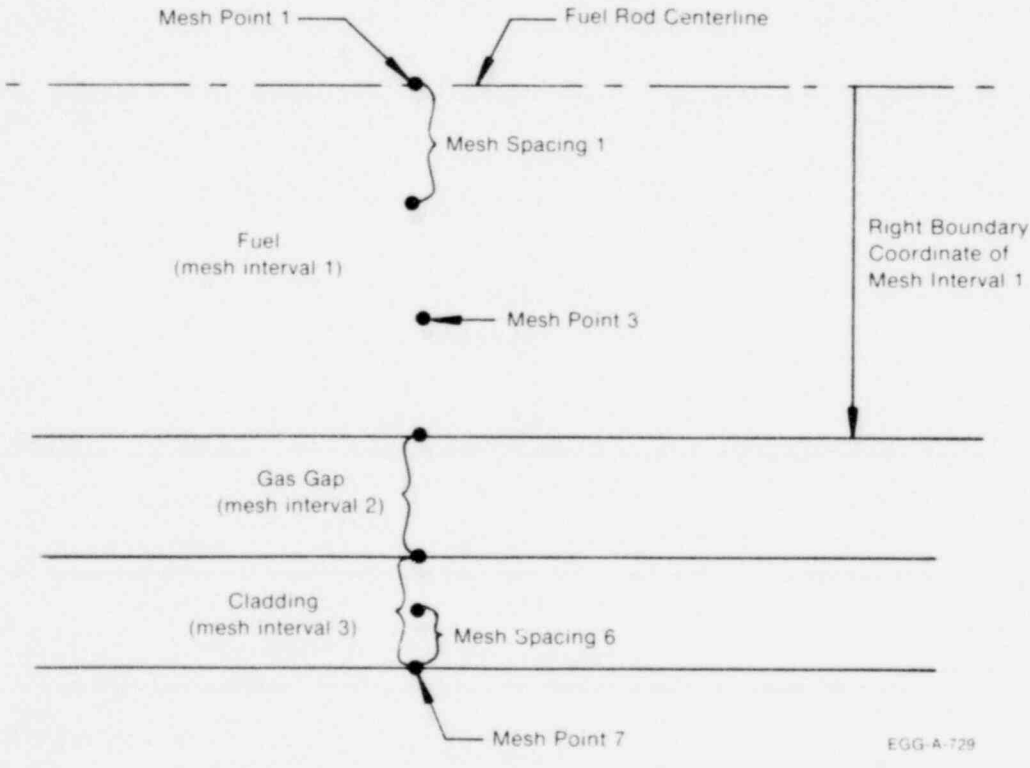

Fig. A-7 Example of radial mesh layout.

Data Field	Format	Quantity
1	I	ID of problem in which geometry data are defined. Always set equal to 0
2	I	Format of mesh spacing data (1 or 2).

Card Group 3.4 Specification of Radial Mesh. - Card(s) #010102nn

nn = card sequence number ($1 \leq nn \leq 99$)

Data in pairs according to Format 1 or Format 2 above. More than one data pair may be placed on a card. Normally the fuel is given a constant mesh spacing, the gas gap one mesh spacing equal to the size of the cold state gap, and the cladding another mesh spacing. In this case, this card will contain three pairs of data. If input in Format 1 above, the card will contain the data shown below.

Data Field	Format	Quantity
1	I	Number of mesh spaces overlaying fuel
2	F	Radius of outside surface of fuel pellets (ft or m)
3	I	Number of mesh spaces overlaying the gas gap (normally, the integer 1 is input)
4	F	Radius of inside surface of cladding (ft or m)
5	I	Number of mesh spaces overlaying cladding
6	F	Radius of outside surface of cladding (ft or m).

The integers in data fields 1, 3, and 5 cannot sum to a number greater than CØLS-1, where CØLS is specified in data field 1 of card 3.2.

Card 3.5 Composition Overlay. - Card #01010301

Compositions are defined as homogeneous material regions bounded on either side by mesh points. Composition data are input pairs of numbers in integer format; the first being the composition number, and the second the number of the last mesh spacing (not mesh point) containing material with the composition number. Mesh spacings which overlay the fuel region must be given a composition number of 1. Similarly, cladding mesh spacings must be given a composition number of 2 and the gas gap mesh spacing a composition number of 3.

Data Field	Format	Quantity
1	I	Composition of fuel region. Always input the integer 1.
2	I	The number of the farthest to the right mesh spacing which overlays fuel.
3	I	Composition of gas gap. Always input the integer 3.
4	I	The number of the mesh spacing overlaying the gas gap (usually the number in data field 2, plus 1).
5	I	Composition of cladding region. Always input the integer 2.
6	I	The number of the farthest to the right mesh spacing which overlays cladding. This number must equal CØLS-1, where CØLS is specified in field 1 of card 3.2.

Card Group 3.6 Normalized Radial Power Distribution. - Card(s) #010104nn

nn = card sequence number ($1 \leq nn \leq 99$).

The radial power profile factor is defined to be the ratio of power in a mesh spacing to the radially averaged power in the fuel[a]. Power factors for each mesh spacing are specified by pairs of numbers. The first number specifies the radial power profile factor and the second number the mesh spacings where the radial power profile factor applies. The radial power profile factor should represent the average power in the mesh spacings. All axial nodes are assumed to have the same normalized radial power distribution. This card still needed even if azimuthal variation in power specified on card 4.5 It specifies power distribution at axial nodes in which no azimuthal heat conduction is specified. If azimuthal heat conduction specified at all axial nodes, put dummy data on this card.

Data Field	Format	Name	Quantity
1	F	P(1)	Radial power profile factor for region defined by N1.
2	I	N1	The number of the farthest to the right mesh spacing for which P(1) applies.
3	F	P(2)	Radial power profile factor for region defined by N2.
4	I	N2	The number of the farthest to the right mesh spacing for which P(2) applies.

Repeat as necessary. The last mesh spacing number input must by CØL-1.

---

[a] The following equation must be satisfied:

$$\sum_{n=1}^{N} \frac{P_n(r_{n+1}^2 - r_n^2)}{r_f^2} = 1$$

where r_f = radius to outside of fuel
P_n = power profile factor for n^{th} mesh spacing
r_n = left boundary coordinate (cold state) of n^{th} mesh spacing
N = number of mesh spacings in fuel

Card Group 3.7 Initial Temperature Estimate. - Card(s) #010106nn

nn = card sequence number ($\leq$ nn $\leq$ 99).

The initial temperature distribution is input in the same format as the radial power distribution except that the temperatures are defined at mesh points rather than for mesh spacings. This input is only used to supply initial guess to steady state temperature calculations. Normally, the steady state temperature calculations will converge if the entire fuel rod is assumed to be at initial coolant temperature.

Data Field	Format	Name	Quantity
1	F	T(1)	Initial temperature of region defined by N1 (°F or K)
2	I	N1	The number of the mesh point on the right boundary of region for which T(1) applies
3	F	T(2)	Initial temperature of region defined by N2 (°F or K)
4	I	N2	The number of the mesh point on the right boundary of region for which T(2) applies.

Repeat as necessary. The last mesh point number input must be CØLS.

End card. Place period symbol, ".", in column 1.

Data Block 4. Power History and Axial Power Profile Input Data.

Card 4.1 and card groups 4.2 and 4.3 must be input for each fuel rod being analyzed. Card groups 4.2 and 4.3 are input in same format as card group 1.5.

Card 4.1

Columns	Format	Name	Quantity
1-5	I	N	Number of a fuel rod in rod bundle being analyzed ($1 \leq N \leq$ NRØD on card 1.1)
6-10	I	NH	Number of power-time pairs used to describe power history of rod ($NH \leq 50$)
11-15	I	NA	Number of power factor-position pairs used to describe axial power profile of rod N ($NA \leq 25$).
16-20	I	NAAZP	Number of radial power profile distributions input as a function of azimuthal angle to specify azimuthal power variation ($NAAZP \leq 10$). Leave blank of NDIM=0 on card 1.1.
21-25	I	NRAZP	Number of pairs of relative power versus radius in each radial power profile ($NRAZP \leq 15$). Leave blank if NDIM=0 on card 1.1.

Card Group 4.2 Power History Cards. (Omit this card group if MPDCAY=1 on card 1.1)

Columns	Format	Name	Quantity
1-10	F	PH(1)	Average linear power in fuel rod N at time PH(2) (kW/ft or kW/m)[a] Power at first time step must be low enough to not cause fuel-cladding contact
11-20	F	PH(2)	Time (sec).

Repeat until NH pairs of data have been placed on cards, 4 pairs per card. Maximum of 12 and 1/2 cards of data.

[a] If the fuel rod power at the start of problem, at which steady state calculations are performed, is near the steady state power that causes burnout, the code has difficulty converging. To avoid this problem, input an initial power at every axial node that is at least 2% less than the minimum steady state power which causes burnout.

Card Group 4.2.1 ANS Decay Heat Formula Parameters. (Omit this card group if MPDCAY=0 on card 1.1)

Columns	Format	Name	Quantity
1-10	F	PØWØP	Average linear fuel rod power just prior to accident initiation (normal operation power) (kW/ft or kW/m
11-20	F	TIMØP	Time span at which fuel rod was at operating power (sec)
21-30	F	FPDCAY	Factor applied to power given by ANS decay heat formula. If power specified by ANS formula not to be modified, set FPDCAY = 1.

Card Group 4.3 Normalized Axial Power Distribution.[a]

Columns	Format	Name	Quantity
1-10	F	PA(1)	Axial power profile factor at elevation PA(2).
11-20	F	PA(2)	Elevation (ft or m). This elevation does not need to correspond to elevation of an axial node.

Repeat until NA pairs of data have been input. PA(4) < PA(2), etc. Maximum of 6 and 1/4 cards of data. A pictorial explanation of axial power profile specified by card group 4.3 for case of NA = 4 is shown in Figure A-8.

---

[a] The axial power profile factors must satisfy the following equation:

$$\sum_{n=1}^{N} P_n \Delta\ell_n / L = 1$$

where L = fuel stack length

$P = n^{th}$ axial power profile factor

$\Delta\ell_n$ = length associated with n^{th} axial power profile factor

= 0.5 [(PA(2n+2) -PA(2n-2)]

N = NA.

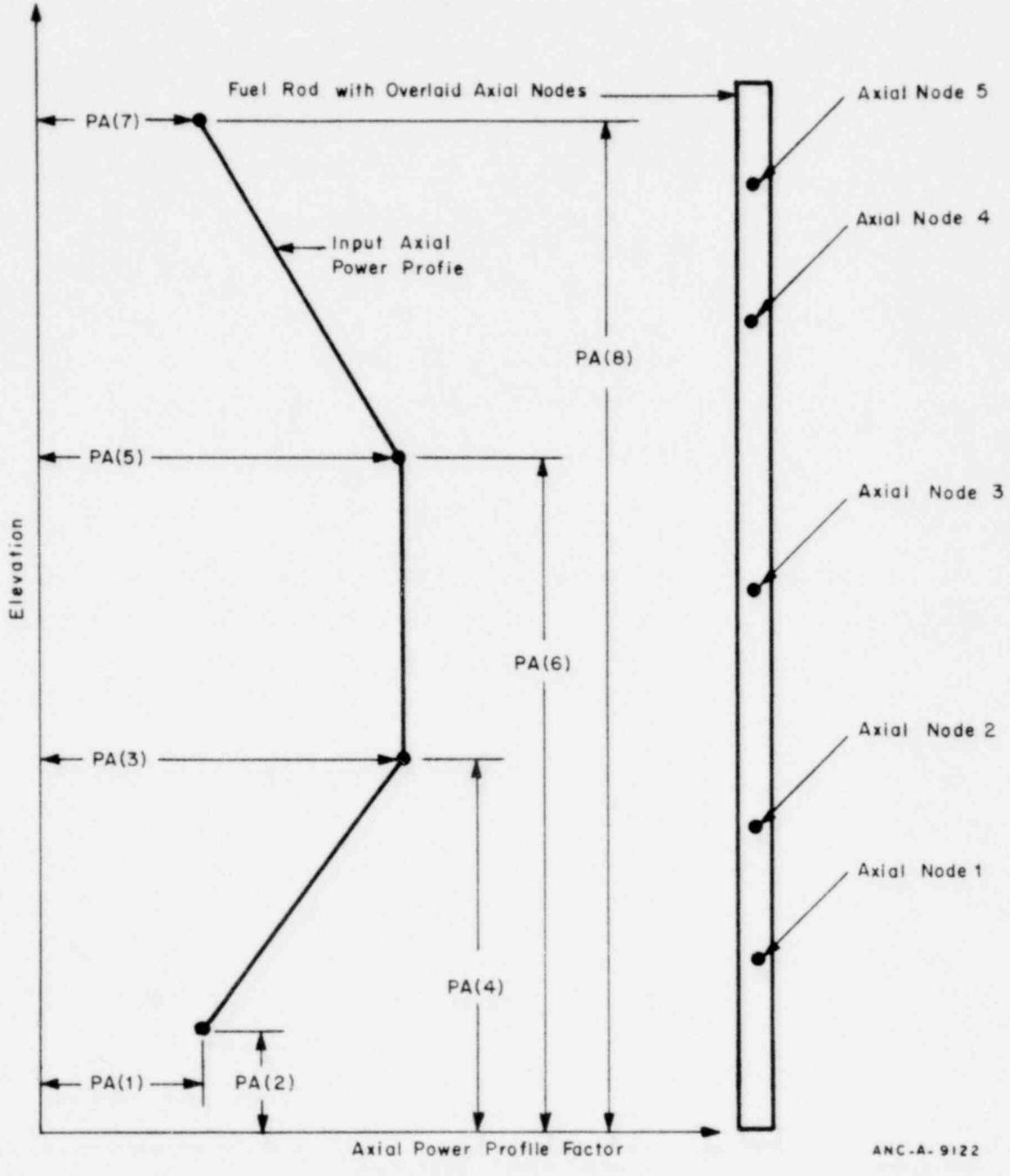

Fig. A-8 Example of axial power profile specified by data on card group 4.3.

Card groups 4.2 and 4.3 specify fuel rod power according to the equation

$$P(\bar{Z},t) = A_f(\bar{Z})\, P_h(t)$$

where

$P(\bar{Z},t)$ = fuel rod power at elevation $\bar{Z}$ and time t (kW/ft or kW/m)

$A_f(\bar{Z})$ = axial power profile factor at elevation $\bar{Z}$ (this value found by interpolating in table specified by card group 4.3).

$P_h(t)$ = average fuel rod power at time t (this value found by interpolating in table specified by card group 4.2).

Cards 4.4 and 4.5 are input as a set. There must be NAAZP (specified on card 4.1) sets of these cards. These cards are omitted if NDIM = 0 on card 1.1. These cards specify the radial power profile at various azimuthal angles.

Card 4.4 (Omit if NDIM = 0 on card 1.1)

Columns	Format	Name	Quantity
1-10	F	AZ(L)	Azimuthal angle (degrees) of L^{th} radial power profile.

Card 4.5 (Omit if NDIM = 0 on Card 1.1)

Columns	Format	Name	Quantity
1-10	F	PAZ(1,L)	Radial power profile factor at radius PAZ(2,L)
11-20	F	PAZ(2,L)	Radius (ft or m)
21-30	F	PAZ(3,L)	Radial power profile factor at radius PAZ(4,L)
31-40	F	PAZ(4,L)	Radius (ft or m)

Repeat until NRAZP (specified on card 4.1) power factor versus radius pairs has been input. The radius of the last power factor for each radial profile must equal the outer radius of the fuel.

The set of radial power profile curves must satisfy the following relation:

$$\sum_{j=1}^{NAAZP} \frac{\theta_{j+1} - \theta_{j-1}}{2\emptyset} \sum_{n=1}^{NRAZP} \left[\frac{PAZ(2n+1,j) + PAZ(2n-1,j)}{2}\right]\left[PAZ(2n+2,j)^2 - PAZ(2n,j)^2\right] = r_f^2$$

where

θ_j = azimuthal angle j^{th} radial power profile (degrees)

NAAZP = total number of radial power profiles

r_f = radius to outside surface of fuel

$\emptyset$ = 90 if NSYMM = 0

= 180 if NSYMM = 1

= 360 if NSYMM = 2.

Data Block 5. Coolant Condition History Input Data.

Four input options are available. In the first option, the enthalpy, quality, and void fraction of the coolant are computed by the code. These quantities are coupled to the calculated fuel rod surface heat flux. In the second option, core average transient coolant conditions are input on cards. In the third option, transient spatially varying coolant conditions are input by reading a data set stored on tape or disk. In the fourth option, transient spatially varying heat transfer coefficients are input on cards.

Card 5.1

Columns	Format	Name	Quantity
1-5	I	NSWC	Coolant input switch. If NSWC = 0, enthalpy histories of lower and upper vessel plenums, core average pressure history, and core average mass flux history are specified by card input. The code computes the coolant enthalpy, temperature, quality, and void fraction. These are coupled to the fuel rod surface heat flux and vary with elevation and coolant channel. If NSWC = 1, enthaply histories of lower and upper plenums, core average pressure history, mass flux history, and enthalpy history are specified by card input. The core average coolant conditions are applied at all fuel rod axial nodes. The code computes the coolant quality and void fraction. If NSWC = 2, transient coolant conditions are read from data set stored on disk or tape. With this option, different coolant conditions can be specified for each axial node. The coolant void fraction is computed by the code. If NSWC = 3, fuel rod cooling is specified by prescribing heat transfer coefficient and bulk temperature histories on cards.
6-10	I	NPBH	Number of pressure-time pairs used to describe to coolant pressure history. NPBH $\leq$ 50. Leave blank if NSWC = 2.

11-15	I	NHLP	Number of enthalpy-time pairs used to describe enthalpy history of lower plenum. NHLP $\leq$ 50. Leave blank if NSWC = 2 or 3.
16-20	I	NHUP	Number of enthalpy-time pairs to describe enthalpy history of upper plenum. NHUP $\leq$ 50. Leave blank if NSWC = 2 or 3.
21-25	I	NGBH	Number of mass flux-time pairs used to describe mass flux history in core. NGBH $\leq$ 100. Leave blank if NSWC = 2 or 3.
26-30	I	NHBH	Number of enthalpy-time pairs used to describe average enthalpy history of coolant in core. NHBH $\leq$ 25. Leave blank if NSWC = 0, 2, or 3.
31-35	I	NZØNE	Number of different zones for which coolant conditions are specified along a vertical flow path. Normally, NZØNE = number of volumes used in thermal hydraulic code calculations along the vertical flow path surrounding fuel rods being analyzed. Leave blank if NSWC = 0, 1, or 3. NZØNE $\leq$ 20. (Value set to NZONE is independent of value given NAXN on card 1.1).
36-40	I	LCHF	Option switch to control application of axial power profile factor and cold-wall factor to critical heat flux correlations. Axial power profile factor models influence of axially nonuniform heat flux on CHF. Cold-wall factor models

			influence of cold walls surrounding fuel rod on CHF. If LCHF = 0, critical heat flux correlation multiplied by both axial power profile factor and cold-wall factor. If LCHF = 1, CHF correlation is multiplied only by axial power profile factor. If JCHF (next input variable on this card) = 5; LCHF set internally to 1, independent of input value. If LCHF = 2, CHF correlation is multiplied only by cold-wall factor. If LCHF = 3, neither axial power profile factor nor cold-wall factor are applied to CHF correlation. If JCHF = 1 or 2, LCHF set internally to 3, independent of input value.
44	I	JCHF	Option switch to control critical heat flux correlation. If JCHF = 0, CHF correlation to be used is selected based on coolant-pressure. Modified Barnett correlation[A-4] is used when when coolant pressure is less than 725 psia. The Barnett correlation[A-5] is used for pressure between 1000 and 1300 psia. B&W-2 correlation[A-6] is used when coolant pressure is greater than 1500 psia. For intermediate pressures, a combination of the two adjacent correlations are used. If JCHF = 1, General Electric correlation[A-7] is used. If JCHF = 2,

			Savannah River correlation[A-8] is used. If JCHF = 3, either modifed Barnett or W-3 correlation[A-9] is used, depending on coolant pressure. Modified Barnett is used when coolant pressure is less than 735 psia. Combination of modified Barnett and W-3 is used for pressures between 725 and 1000 psia. W-3 correlation is used for pressures greater than 1000 psia. If JCHF = 5, preliminary Loss-of-Fluid Test correlation[A-10] is used. This correlation assumes the geometry of the LOFT reactor.
45	I	JFB	Option switch to control film boiling correlation. If JFB = 0, form 5.9 (cluster geometry) of Groeneveld correlation[A-11] is used when the coolant pressure is greater than 500 psia. When coolant pressure is less than 500 psia, the Dougall-Rohsenow correlation[A-12] is used. If JBF = 1, form 5.7 (open annulus geometry) of Groeneveld correlation is used when the coolant pressure is greater than 500 psia. Otherwise, the Dougall-Rohsenow correlation is used. If JBF = 2, Dougall-Rohsenow correlation is always used. If JFB = 3, Condie-Bengston correlation[A-13] is always used. If

JFB = 4, Tong-Young correlation[A-14] is always used.

Card groups 5.2 through 5.13 below complete the data input required for the coolant condition data block. Depending on the value of NSWC (input on card 5.1), not all of these card groups are input. The card groups required for each value of NSWC are shown in Table A-II.

TABLE A-II

CARD GROUPS REQUIRED FOR COOLANT CONDITION DATA BLOCK

NSWC	Required Card Groups
0	5.2-5.5, 5.7-5.9
1	5.2-5.9
2	5.7-5.9, tape of transient coolant condition, according to format shown in Appendix E
3	5.2, 5.10-5.13

Card Group 5.2

Specification of pressure history of coolant. Input in same format as card group 1.5, four pairs per card.

Columns	Format	Name	Quantity
1-10	F	PBH(1)	Average core coolant pressure at time PBH(2) (psia or N/m^2)
11-20	F	PBH(2)	Time (sec).

Repeat until NPBH pairs have been input. Maximum of 12 and 1/2 cards of data.

If NSWC = 3, do not input card groups 5.3 through 5.9.

Card Group 5.3

Specification of enthalpy history of lower plenum (coolant at bottom of fuel rods). Input in same format as card group 1.5.

Columns	Format	Name	Quantity
1-10	F	HLP(1)	Enthalpy of coolant in lower plenum at time HLP(2) (Btu/lbm or joules/kg)
11-20	F	HLP(2)	Time (sec).

Repeat until NHLP pairs have been input. Maximum of 12 and 1/2 cards of data.

Card Group 5.4

Specification of enthalpy history of upper plenum (coolant at top of fuel rods). If coolant always flows upward, enthalpy of upper plenum can be set equal to any value greater than enthalpy of lower plenum. In this case, the upper plenum enthalpy values are only used to specify that coolant is always flowing upward. If the coolant is flowing downward through the core, however, the upper plenum enthalpy must be accurately specified. The lower plenum enthalpy can then be set to any value greater than upper plenum enthalpy. Input in same manner as card group 1.5.

Columns	Format	Name	Quantity
1-10	F	HUP(1)	Enthalpy of upper plenum at time HUP(2) (Btu/lbm or joules/kg)
11-20	F	HUP(2)	Time (sec).

Repeat until NHUP pairs have been input. Maximum of 12 and 1/2 cards of data.

Card Group 5.5

Specification of mass flux history of coolant. Input in same manner as card group 1.5.

Columns	Format	Name	Quantity
1-10	F	GBH(1)	Average mass flux of coolant surrounding fuel rods at time GBH(2) (lbm/hr-ft^2 or kg/s·m^2)
11-20	F	GBH(2)	Time (sec).

Repeat until NGBH pairs have been input. Maximum of 25 cards of data.

Card Group 5.6

Specification of core average enthalpy history. Input this card group only if NSWC = 1. Input in same format as card group 1.5.

Columns	Format	Name	Quantity
1-10	F	HBH(1)	Average enthalpy of coolant surrounding fuel rods at time HBH(2) (Btu/lbm or joules/kg)
11-20	F	HBH(2)	Time (sec).

Repeat until NHBH pairs have been input. Maximum of 6 and 1/4 cards of data.

Card Group 5.7

Specification of heated equivalent diameter of flow channels. For more information on flow channels, see card group 1.6.

Columns	Format	Name	Quantity
1-10	F	DHE(1)	Heated equivalent diameter of flow channel 1 (ft or m) [4 x (flow area)/(heated perimeter)]

11-20	F	DHE(2)	Heated equivalent diameter of flow channel 2 (ft or m)
21-30	F	DHE(3)	Heated equivalent diameter of flow channel 3 (ft or m).

Repeat until NCHN numbers have been input. Specify the heated equivalent diameter of the first eight channels on first card. Then, continue with the other coolant channels in same manner on next card.

Card Group 5.8

Specification of hydraulic diameter of flow channels.

Columns	Format	Name	Quantity
1-10	F	DHY(1)	Hydraulic diameter of flow channel 1 (ft or m) [4 x (flow area)/(wetted perimeter)]
11-20	F	DHY(2)	Hydraulic diameter of flow channel 2 (ft or m).

Repeat as necessary in same manner as card group 5.7. A total of NCHN numbers must be input.

Card Group 5.9

Specification of cross-sectional area of flow channels.

Columns	Format	Name	Quantity
1-10	F	ACHN(1)	Cross-sectional area of flow channel 1 (ft^2 or m^2)
11-20	F	ACHN(2)	Cross-sectional area of flow channel 2 (ft^2 or m^2).

Repeat as necessary in same manner as card group 5.7. A total of NCHN numbers must be input.

If NSWC = 3, input cards 5.10 through 5.13. Otherwise, omit these cards.

Card Group 5.10

Columns	Format	Name	Quantity
1-5	I	NHTCZ	Number of different vertical zones for which heat transfer coefficient and bulk temperature histories will be prescribed. NHTCZ $\leq$ 10.

Cards 5.11 through 5.13 must be input as a set for each vertical zone. A total of NHTCZ sets must be supplied.

Card 5.11

Columns	Format	Name	Quantity
1-5	I	L	Number of a vertical zone (1 $\leq$ L $\leq$ NHTCZ)
6-10	I	NHPRS(L)	Number of heat transfer coefficient-time pairs specified for zone L [NHPRS(L) $\leq$ 12]
11-15	I	NTPRS(L)	Number of bulk temperature-time pairs specified for zone L [NTPRS (L) $\leq$ 12]
21-30	F	ZP(L)	Elevation of top boundary of zone L. Elevation of bottom boundary of zone L is assumed to be same as top boundary of zone L - 1. Bottom boundary boundary of zone 1 assumed to have elevation of zero. Top boundary of top vertical zone must have elevation $\geq$ active fuel stack length (ft or m).

Card(s) 5.12

Heat Transfer Coefficient (HTC) history for vertical zone L. Input in same format as card group 1.5, four pairs per card.

Columns	Format	Name	Quantity
1-10	F	HTCA(1)	Heat transfer coefficient at time HTCA(2) (Btu/hr-ft^2-°F or W/m^2·K)
11-20	F	HTCA(2)	Time (sec)
21-30	F	HTCA(3)	Heat transfer coefficient at time HTCA (4) (Btu/hr-ft^2-°F or W/m^2·K)
31-40	F	HTCA(4)	Time (sec).

Repeat until NHPRS(L) pairs have been input. Maximum of three cards.

Card(s) 5.13

Bulk temperature history for vertical zone L. Input in same format as card group 1.5, four pairs per card.

Columns	Format	Name	Quantity
1-10	F	TBLKA(1)	Coolant temperature at time TBLKA(2) (°F or K)
11-20	F	TBLKA(2)	Time (sec).

Repeat until NTPRS(L) pairs have been input. Maximum of three cards.

Repeat card groups 5.11 through 5.13 until heat transfer coefficient and coolant temperature-time pairs have been supplied for a total of NHTCZ zones.

If NSWC = 2, a data set describing the transient coolant conditions is read from disk or tape. The data set will be accessed by FORTRAN

logical unit 4. The required form of the coolant condition data set is given in Appendix E.

One program in the FRAP package has the purpose of transforming RELAP4[5] plot data sets to FRAP coolant condition data sets. The information required to use this program is given in Appendix E.

Data Block 6. Gap Conductance Subcode Input Data.

Card 6.1

Specification of surface roughness of fuel and cladding

Columns	Format	Name	Quantity
1-10	F	RC	Arithmetic mean roughness of inside surface of cladding (microns) (leave blank if MacDonald-Broughton model is specified on card 1.1)
11-20	F	RF	Arithmetic mean roughness of outside surface of fuel pellets (microns) (leave blank if MacDonald-Broughton model is specified on card 1.1).

Data Block 7. Internal Gas and Plenum Data. Cards 7.1 and 7.2 must be input as pairs for each fuel rod being analyzed.

Card 7.1

Columns	Format	Name	Quantity
1-5	I	N	Number of fuel rod in rod bundle being analyzed.
6-10	I	NC(N)	Number of coils in plenum spring of rod N (NC(N) $\geq$ 1).
11-20	F	GSMS(N)	Amount of gas in fuel rod N (gram-moles) (leave blank of TGAS0(N) > 0 in columns 71-80 of this card).

21-30	F	VPLEN(N)	Cold state plenum volume of fuel rod N (ft^3 or m^3) (include volume of spring).
31-40	F	PO(N)	Cold state pressure in fuel rod N (psia or N/m^2). If TGASO(N)=0, only use of this quantity is that of supplying guess of internal fuel rod pressure on first iteration of first time step. Accurate value, therefore, is not required. But, if TGASO(N) > 0, PO(N) is term in calculation of moles of gas in fuel rod. Accurate value, then, is required.
41-50	F	SL(N)	Height (coiled) of plenum spring of fuel rod N (ft or m).
51-60	F	CD(N)	Outer diameter of plenum spring coils of fuel rod N (ft or m).
61-70	F	DS(N)	Wire diameter of plenum spring of fuel rod N (ft or m).
71-80	F	TGASO(N)	Temperature of fuel rod gas when at cold state temperature PO(N) (°F or K). This temperature is term in calculation to compute moles of gas in fuel rod. If moles of gas input in columns 11-20, leave these columns blank.

Card 7.2 Gas Composition Data

Mole fractions of gas components specified. Total of fractions should sum to 1. If they do not, the code normalizes them so that sum is 1.

Columns	Format	Name	Quantity
1-10	F	GF(1)	Fraction of helium in fuel rod N
11-20	F	GF(2)	Fraction of argon in fuel rod N
21-30	F	GF(3)	Fraction of krypton in fuel rod N
31-40	F	GF(4)	Fraction of xenon in fuel rod N
41-50	F	GF(5)	Fraction of hydrogen in fuel rod N
51-60	F	GF(6)	Fraction of nitrogen in fuel rod N
61-70	F	GF(7)	Fraction of water vapor in fuel rod N.

Data Block 8. Plot Subcode Input Data. If plots are not wanted, omit the cards in this data block.

Card 8.1

Columns	Format	Name	Quantity
1-5	I	NPLTS	Number of axial nodes at which plots of fuel response are wanted. If no minus sign put in front of NPLTS, plots will only cover time span of current calculations. If a minus sign is put in front of NPLTS, the plot data of the current calculations will be appended to plots covering the time span of previous calculations. In this case, the previous saved plot tape must be specified for FORTRAN logical unit 17 and the write ring inserted.

Card 8.2

Columns	Format	Name	Quantity
1-5	I	N1	Number of an axial node for which temperature, deformation, and pressure histories are to be plotted

6-10	I	N2	Number of an axial node for which temperature, deformation, and pressure histories are to be plotted.

Repeat for all nodes to be plotted.

Card 8.3 Time Axis.

Columns	Format	Name	Quantity
1-10	F	TSTART	Minimum time on time axis (sec)
11-20	F	TEND	Maximum time on time axis (sec)
21-30	F	AXLT	Length of time axis (in.)
31-70	A	LABLT	Label to be given time axis.

Card 8.4 Cladding Surface Temperature Axis.

Columns	Format	Name	Quantity
1-10	F	TSMIN	Minimum cladding surface temperature on axis (°F or K)
11-20	F	TSMAX	Maximum cladding surface temperature on axis (°F or K)
21-30	F	AXLTS	Length of surface temperature axis (in.)
31-70	A	LABLTS	Label to be given surface temperature axis.

Card 8.5 Fuel Centerline Temperature Axis.

Columns	Format	Name	Quantity
1-10	F	TCLMIN	Minimum fuel centerline temperature on axis (°F or K)
11-20	F	TCLMAX	Maximum fuel centerline temperature on axis (°F or K)
21-30	F	AXLTMP	Length of centerline temperature axis (in.)
31-70	A	LABLTM	Label to be given centerline temperature axis.

Card 8.6 Gas Gap Pressure Axis.

Columns	Format	Name	Quantity
1-10	F	PMIN	Minimum gas gap pressure on axis (psia or N/m^2)
11-20	F	PMAX	Maximum gas gap pressure on axis (psia or N/m^2)
21-30	F	AXLP	Length of gas gap pressure axis (in.)
31-70	A	LABLP	Label to be given gas gap pressure axis.

Card 8.7 Cladding Hoop Strain Axis.

Columns	Format	Name	Quantity
1-10	F	EPSMIN	Minimum cladding hoop strain on axis (dimensionless)
11-20	F	EPSMAX	Maximum cladding hoop strain on axis (dimensionless)
21-30	F	AXLEPS	Length of cladding hoop strain axis (in.)
31-70	A	LABLE	Label to be given cladding hoop strain axis.

Card 8.8 Fuel Axial Displacement Axis.

Columns	Format	Name	Quantity
1-10	F	UZFMIN	Minimum fuel axial displacement on axis (in. or m)
11-20	F	UZFMAX	Maximum fuel axial displacement on axis (in. or m)
21-30	F	AXLUZF	Length of fuel axial displacement axis (in.)
31-70	A	LABLUF	Label to be given fuel axial displacement axis.

Card 8.9 Cladding Axial Displacement Axis.

Columns	Format	Name	Quantity
1-10	F	UZCMIN	Minimum cladding axial displacement on axis (in. or m)

11-20	F	UZCMAX	Maximum cladding axial displacement on axis (in. or m)
21-30	F	AXLUZC	Length of cladding axial displacement axis (in.)
31-70	A	LABLUC	Label to be given cladding axial displacement axis.

Card 8.10 Fuel Rod Power Axis.

Columns	Format	Name	Quantity
1-10	F	PMIN	Minimum linear fuel rod power on axis (kW/ft or kW/m)
11-20	F	PMAX	Maximum linear fuel rod power on axis (kW/ft or kW/m)
21-30	F	PLEN	Length of linear fuel rod power axis (in.)
31-70	A	PLABL	Label to be given linear fuel rod power axis.

Card 8.11 Fuel Surface Temperature Axis.

Columns	Format	Name	Quantity
1-10	F	TFSMIN	Minimum fuel surface temperature on axis (°F or K)
11-20	F	TFMAX	Maximum fuel surface temperature on axis (°F or K)
21-30	F	TFSLEN	Length of fuel surface temperature axis (in.)
31-70	F	TFSLAB	Label to be given fuel surface temperature axis.

Card 8.12 Gap Heat Transfer Coefficient Axis.

Columns	Format	Name	Quantity
1-10	F	HGMIN	Minmum gap heat transfer coefficient on axis (Btu/hr-F-ft^2 or J/s·K·m^2)
11-20	F	HGMAX	Maximum gap heat transfer coefficient on axis (Btu/hr-F-ft^2 or J/s·K·m^2)

21-30	F	HGLEN	Length of gap heat transfer coefficient axis (in.)
31-70	A	HGLABL	Label to be given gap heat transfer coefficient axis.

Card 8.13 Surface Heat Transfer Coefficient Axis.

Columns	Format	Name	Quantity
1-10	F	HSMIN	Minimum surface heat transfer coefficient on axis (Btu/hr-F-ft^2 or J/s·K·m^2)
11-20	F	HSMAX	Maximum surface heat transfer coefficient on axis (Btu/hr-F-ft^2 or J/s·K·m^2)
21-30	F	HSLEN	Length of surface heat transfer coefficient axis (in.)
31-70	A	HSLAB	Label to be given surface heat transfer coefficient axis.

Card 8.14 Average Cladding Temperature Axis.

Columns	Format	Name	Quantity
1-10	F	TAMIN	Minimum average cladding temperature on axis (°F or K)
11-20	F	TAMAX	Maximum average cladding temperature on axis (°F or K)
21-30	F	TALEN	Length of average cladding temperature axis (in.).

Card 8.15 Heat Per Unit Length Transferred Out of Fuel Rod Axis.
(This plot designed to overlay plot specified by card 8.10)

Columns	Format	Name	Quantity
1-10	F	QMIN	Minimum heat out value on axis (kW/ft or kW/m)
11-20	F	QMAX	Maximum heat out value on axis (kW/ft or kW/m)
21-30	F	QLEN	Length of heat out axis (in.)
31-70	A	QLABL	Label to be given heat out axis.

Card 8.16 Plenum Pressure Axis.

Columns	Format	Name	Quantity
1-10	F	PPMIN	Minimum plenum pressure on axis (psia or N/m^2)
11-20	F	PPMAX	Maximum plenum pressure on axis (psia or N/m^2)
21-30	F	PPLEN	Length of plenum pressure axis (in.)
31-70	A	PPLABL	Label to be given plenum pressure axis.

Card 8.17 Plenum Temperature Axis.

Columns	Format	Name	Quantity
1-10	F	TPMIN	Minimum plenum temperature on axis (°F or K)
11-20	F	TPMAX	Maximum plenum temperature on axis (°F or K)
21-30	F	TPLEN	Length of plenum temperature axis (in.)
31-70	A	TPLABL	Label to be given plenum temperature axis.

Card 8.18 Gas Flow Rate Axis.

(Plot of rate at which gas flows from plenum.)

Columns	Format	Name	Quantity
1-10	F	GFMIN	Minimum gas flow rate on axis (gram-moles/sec)
11-20	F	GFMAX	Maximum gas flow rate on axis (gram-moles/sec)
21-30	F	GFLEN	Length of gas flow rate axis (in.)
31-70	A	GFLABL	Label to given gas flow rate axis.

Card 8.19 Mass Flux Axis.

Plot of average mass flux in coolant channels surrounding fuel rod. (If NSWC = 3 on card 5.1, put dummy values on this card such that GMAX >GMIN and GLEN > 0.)

Columns	Format	Name	Quantity
1-10	F	GMIN	Minimum mass flux on axis (lbm/ft^2-hr or kg/s·m^2)
11-20	F	GMAX	Maximum mass flux on axis (lbm/ft^2-hr or kg/s·m^2)
21-30	F	GLEN	Length of mass flux axis (in.)
31-70	A	GLABL	Label to be given mass flux axis.

Card 8.20 Coolant Quality Axis.

Plot of average quality in coolant channel surrounding fuel rod. (If NSWC = 3, on card 5.1 put dummy values on this card such that XMAX > XMIN and XLEN > 0.)

Columns	Format	Name	Quantity
1-10	F	XMIN	Minimum quality on axis (dimensionless)
11-20	F	XMAX	Maximum quality on axis (dimensionless)
21-30	F	XLEN	Length of quality axis (in.)
31-70	A	XLABL	Label to be given quality axis.

Card 8.21 Coolant Pressure Axis.

(Plot of average pressure in coolant channel surrounding fuel rod.)

Columns	Format	Name	Quantity
1-10	F	PCMIN	Minimum pressure on axis (psia or N/m^2)
11-20	F	PCMAX	Maximum pressure on axis (psia or N/m^2)
21-30	F	PCLEN	Length of pressure axis (in.)
31-70	A	PCLABL	Label to be given coolant pressure axis.

Card 8.22 Gap Thickness Axis.

Columns	Format	Name	Quantity
1-10	F	THKMIN	Minimum gap thickness on axis (mils or m)
11-20	F	THKMAX	Maximum gap thickness on axis (mils or m)

21-30	F	THLEN	Length of gap thickness axis (in.)
31-70	A	THKLAB	Label to be given gap thickness axis.

Card 8.23 Bulk Temperature Axis.

Columns	Format	Name	Quantity
1-10	F	TBMIN	Minimum bulk temperature on axis (°F or K)
11-20	F	TBMAX	Maximum bulk temperature on axis (°F or K)
21-30	F	TBLEN	Length of bulk temperature axis (in.)
31-70	A	TBLAB	Label to be given bulk temperature axis.

3. REFERENCES

A-1. C. R. Hann, C. E. Beyer, L. J. Parchen, *GAPCON-THERMAL-1: A Computer Program for Calculating the Gap Conductance in Oxide Fuel Pins*, BNWL-1778 (September 1973).

A-2. P. E. MacDonald et al, *MATPRO-Version 09 - A Handbook of Materials Properties for Use in the Analysis of Light Water Reactor Fuel Rod Behavior*, ANCR-1263 (February 1976).

A-3. Internal Manual.

A-4. E. D. Hughes, *A Correlation of Rod Bundle Critical Heat Flux for Water in the Pressure Range 150 to 725 psia*, IN-1412 (July 1970).

A-5. P. G. Barnett, *A Correlation of Burnout Data for Uniformly Heated Annuli and Its Use for Predicting Burnout in Uniformly Heated Rod Bundles*, AEEW-R463 (1966).

A-6. J. S. Gellerstedt et al, "Correlation of Critical Heat Flux in a Bundle Cooled by Pressurized Water," *Two-Phase Flow and Heat Transfer in Rod Bundles, Symposium presented at the Winter Annual Meeting of the American Society of Mechanical Engineers, Los Angeles, California, November 1969*, pp 63-71.

A-7. B. C. Slifer and J. E. Hench, *Loss of Coolant Accident and Emergency Cooling Models for General Electric Boiling Water Reactors*, NEDO-10329 (April 1971).

A-8. D. H. Knoebel et al, *Forced Convection Subcooled Critical Heat Flux, D2O and H2O Coolant with Aluminum and Stainless Steel Heaters*, DP-1306 (February 1973).

A-9. L. S. Tong, *Boiling Crisis and Critical Heat Flux*, TID-25887 (August 1972).

A-10. Internal Report.

A-11. D. C Groeneveld, *An Investigation of Heat Transfer in a Liquid Deficient Regime*, AECL-3281 (Revised December 1968; Revised August 1969).

A-12. R. S. Dougall and W. M. Rohsenow, *Film Boiling on the Inside of Vertical Tubes with Upward Flow of The Fluid at Low Qualities*, MIT-TR-9079-26 (1963).

A-13. K. G. Condie et al, "Regression Analysis of Post-CHF Flow Boiling Data," *Fifth International Heat Transfer Conference, Japan, September 1974*, pp 115-119.

A-14. L. S. Tong and J. D. Young, "A Phenomenological Transition and Film Boiling Heat Transfer Correlation," *Fifth International Heat Transfer Conference, Japan, July 1974*, Journal of Heat Transfer (1974) pp 20-124.

APPENDIX B

SAMPLE PROBLEM

APPENDIX B

SAMPLE PROBLEM

A FRAP-T prediction of the behavior of the hot fuel rod of the hot coolant channel in a PWR after a double-ended cold leg break is shown. The input data, calculation printout, and plots of calculation results are presented. A summary description of the fuel rod analyzed is shown in Table B-I. The peak rod power at initiation of the accident was 51.9 kW/m. The internal gas in the fuel rod consisted of 0.030 gram-moles of helium.

TABLE B-I

FUEL ROD DATA (COLD STATE)

Measurement	British Units	SI Units
Fuel stack length	12 ft	3.658 m
Cladding outside diameter	0.422 in.	0.01072 m
Cladding thickness	24 mils	0.6096×10^{-3} m
Amount of internal Gas		0.030 gram-moles
Plenum volume	0.657 $in.^3$	1.076×10^{-5} m^3
Fuel density	638 lbf/ft^3	1.022×10^4 kg/m^3
Cladding density	409 lbf/ft^3	5.5602×10^3 kg/m^3
Arithmetic mean roughness of fuel		0.114×10^{-5} m
Arithmetic mean roughness of cladding		0.216×10^{-5} m
Radius to outside edge of pellet dishes	0.121 in.	0.307×10^{-2} m

A descriptive printout of the input data is shown on pages 1 to 10[a]. The data are printed out in about the same order as they are

[a] All page numbers mentioned in this appendix refer to the numbers located in the upper right corner of the computer printout sheets.

stored on the input cards. The input data of a general nature are shown on pages 1 to 3. The temperature calculation subcode input data are shown on pages 4 to 6. The radial mesh that was used by both the temperature and deformation subcodes is shown in this printout. The radial heat source distribution is also shown. The average fuel rod power history and axial power profile are shown on page 7. The input data used to specify the transient fuel rod to coolant heat transfer coefficients and coolant temperature are shown on pages 8 to 9. The heat transfer coefficients are prescribed for three axial zones. Fuel rod to coolant heat transfer is uniform within each zone. The input data for the gap conductance and gap pressure subcodes are shown on page 10.

Computer printout and plots showing the fuel rod behavior for the first 20 seconds following the cold leg break are shown next. The fuel rod state just prior to the pipe break is shown on pages 12 to 14. Localized ballooning and rupture of the cladding occurred 10 seconds after the pipe break. The rupture occurred near the point of peak fuel rod power (axial node 5). The maximum localized hoop strain at the ballooning and rupture point was 0.55. When cladding rupture occurred, the fuel rod internal pressure dropped to the value of the coolant pressure (shown in Figure B-1). The peak cladding surface temperature during the first 20 seconds following the pipe break was 1300K. It occurred 10.5 seconds after the pipe break at axial node 5. The surface temperature history at axial node 5 is shown in Figure B-2. The fuel centerline temperature continuously dropped during the LOCA. This is shown in Figure B-3. The cladding hoop strain history at axial node 5 is shown in Figure B-4. Localized bollooning and rupture occurred at axial node 5. This deformation is not shown in Figure B-4. The gap conductance history at axial node 5 is shown in Figure B-5. The plenum gas temperature is compared with the coolant temperature in Figure B-6. Length change of the cladding is shown in Figure B-7.

The calculations were performed on the CDC 7600 computer system at INEL. The run required two minutes of computer time.

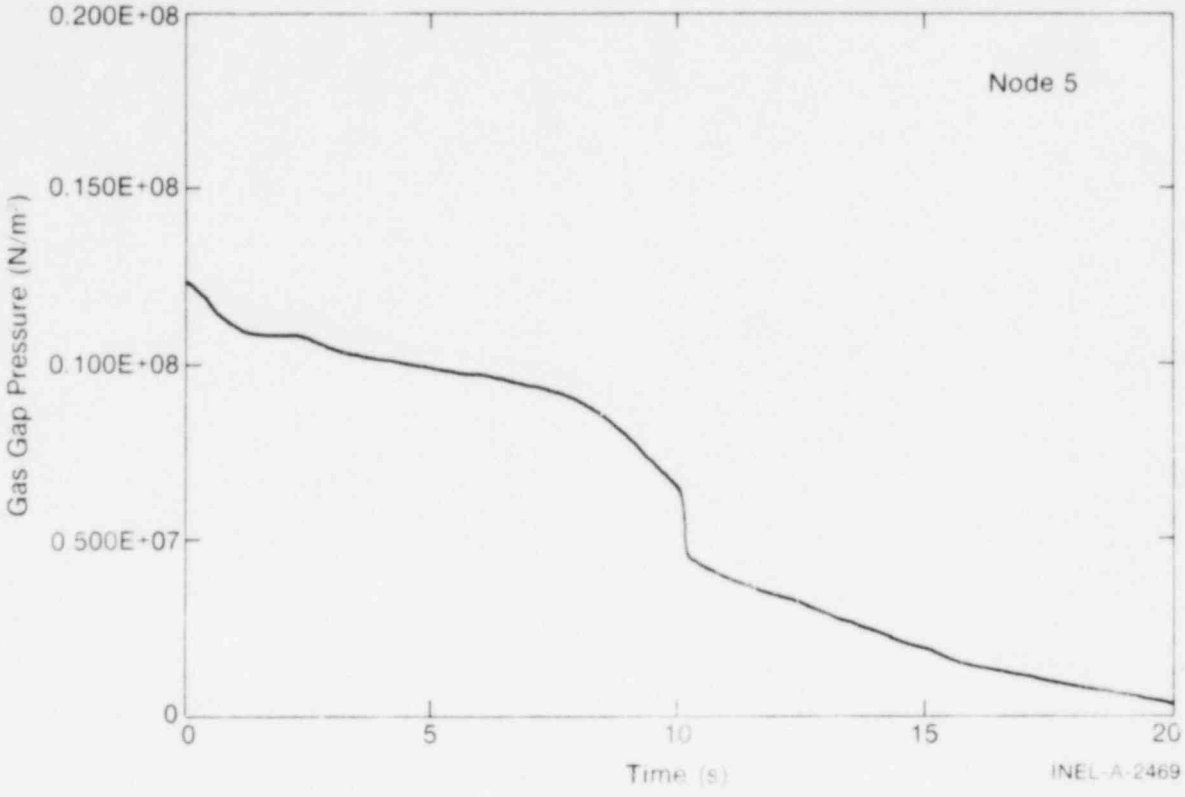

Fig. B-1 Fuel rod internal pressure history.

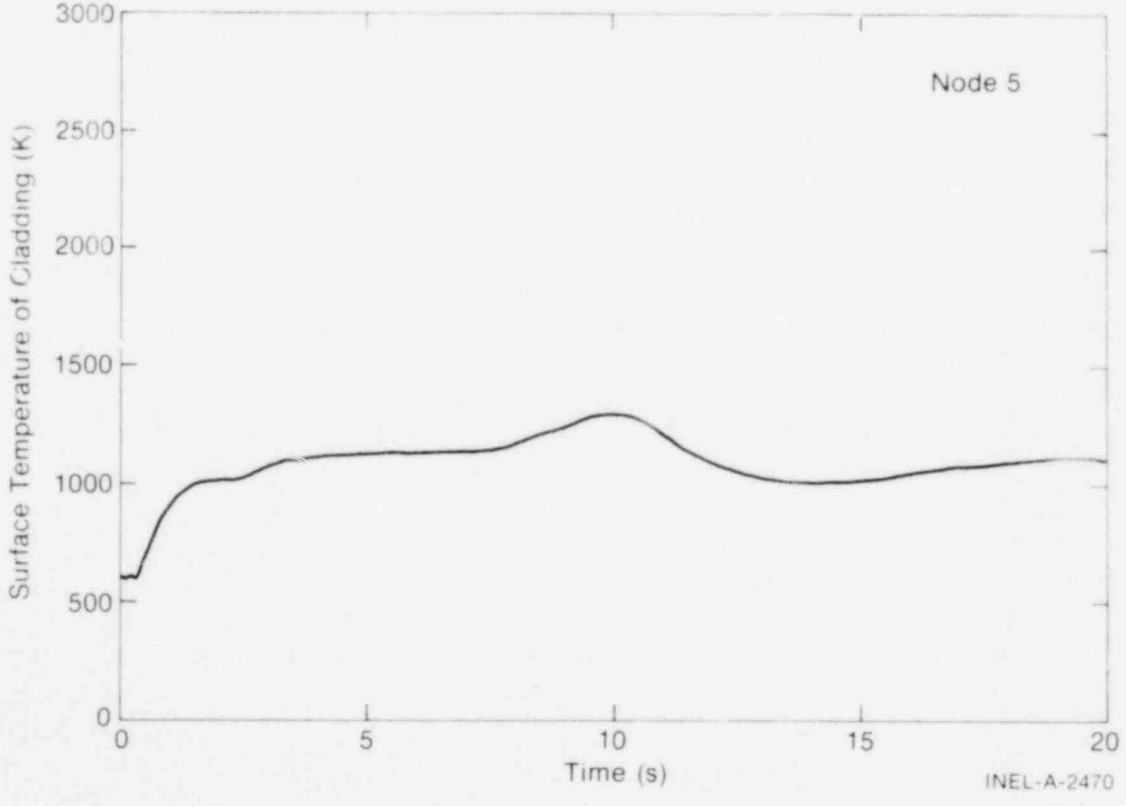

Fig. B-2 Cladding surface temperature history.

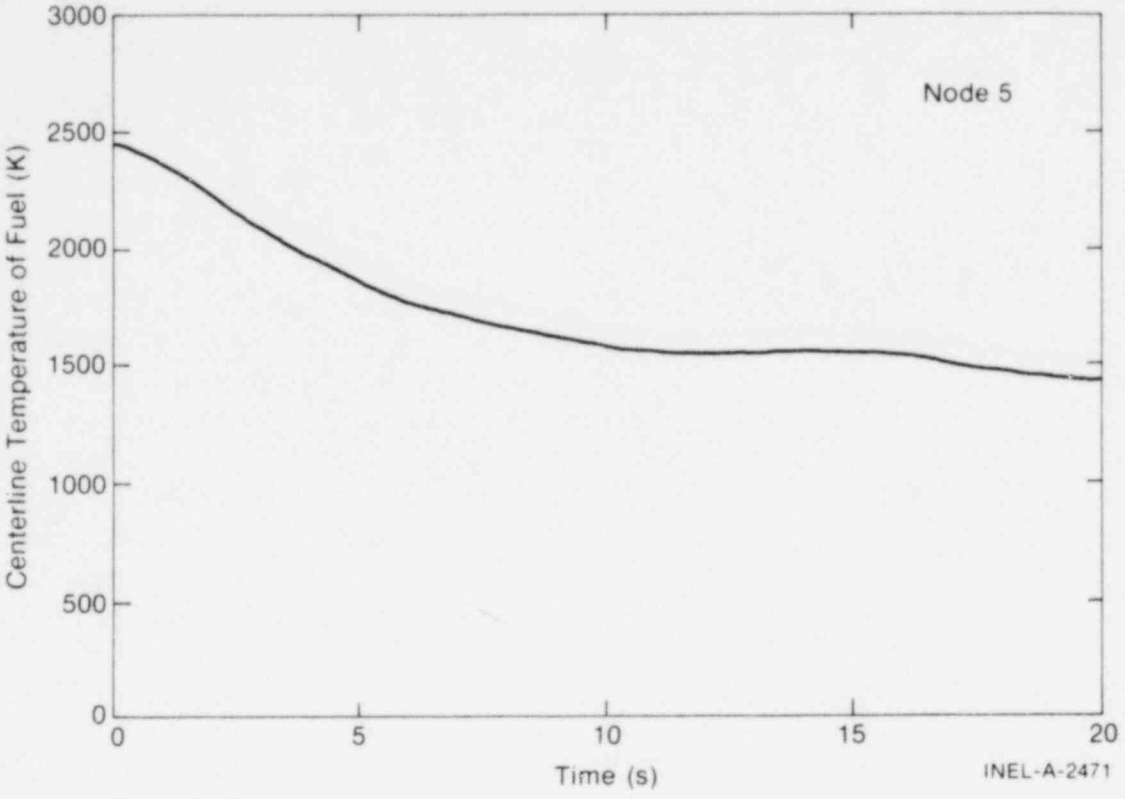

Fig. B-3 Fuel centerline temperature history.

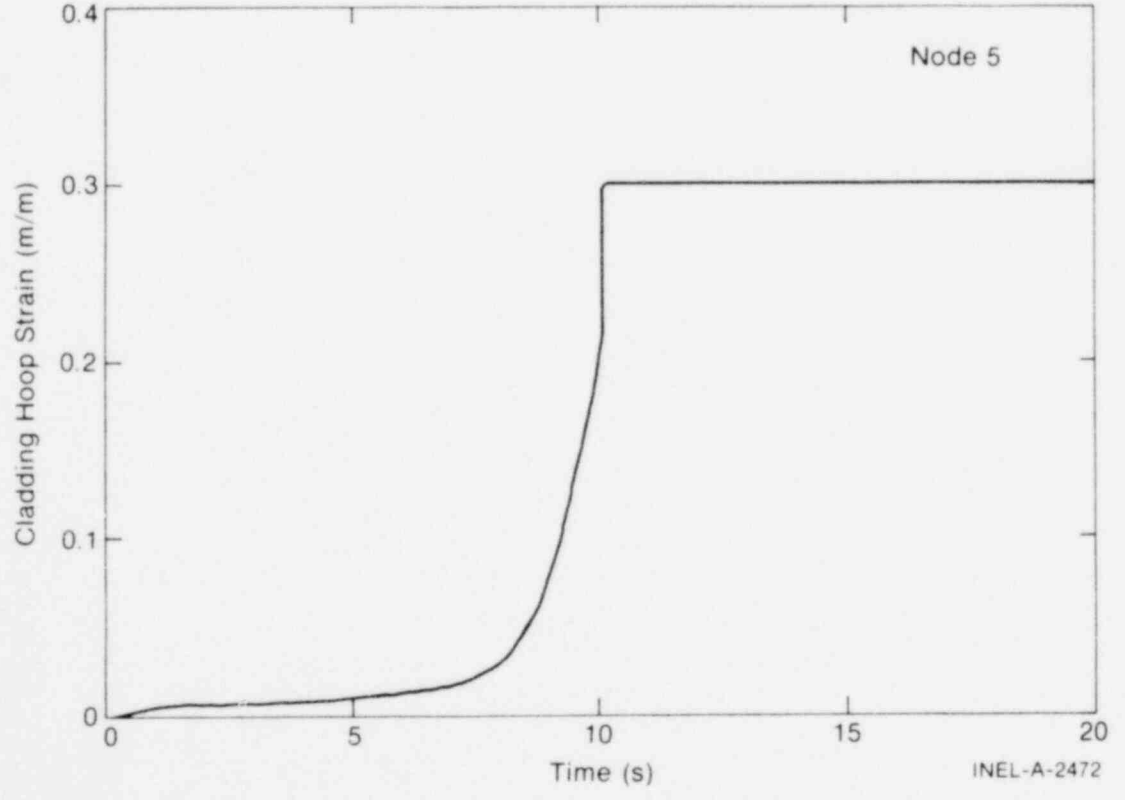

Fig. B-4 Cladding hoop strain history.

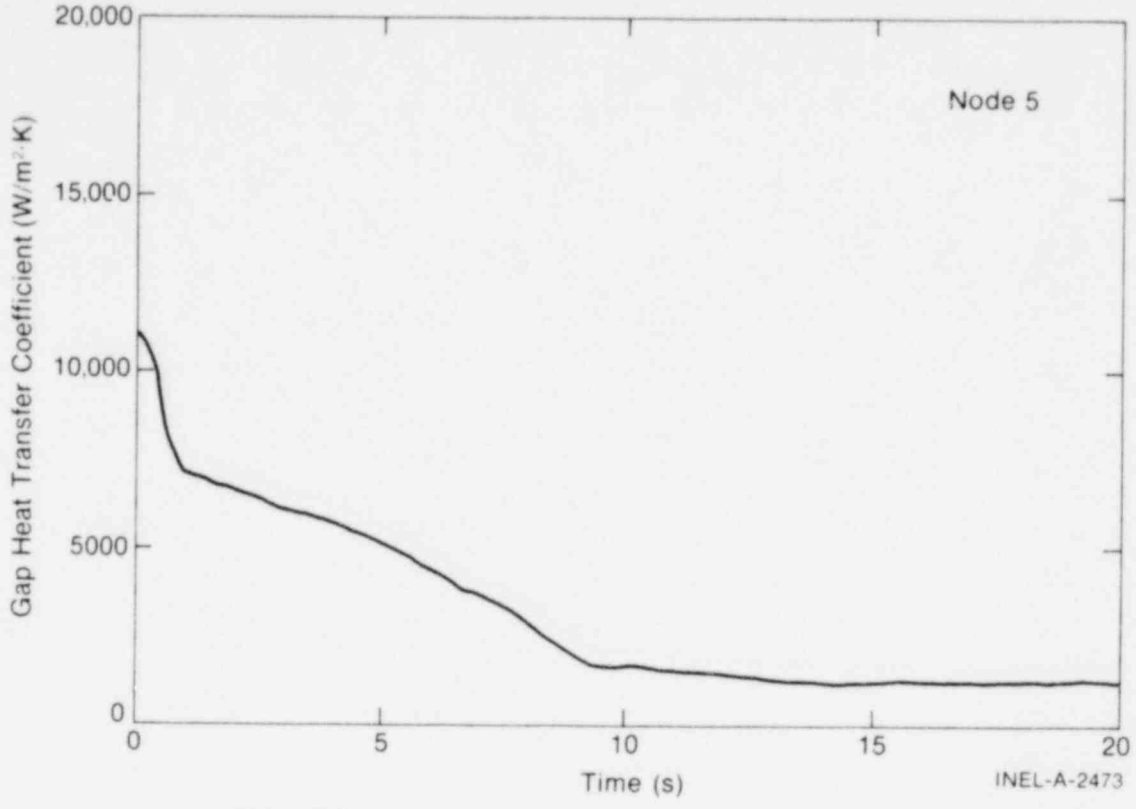

Fig. B-5 Gap conductance history.

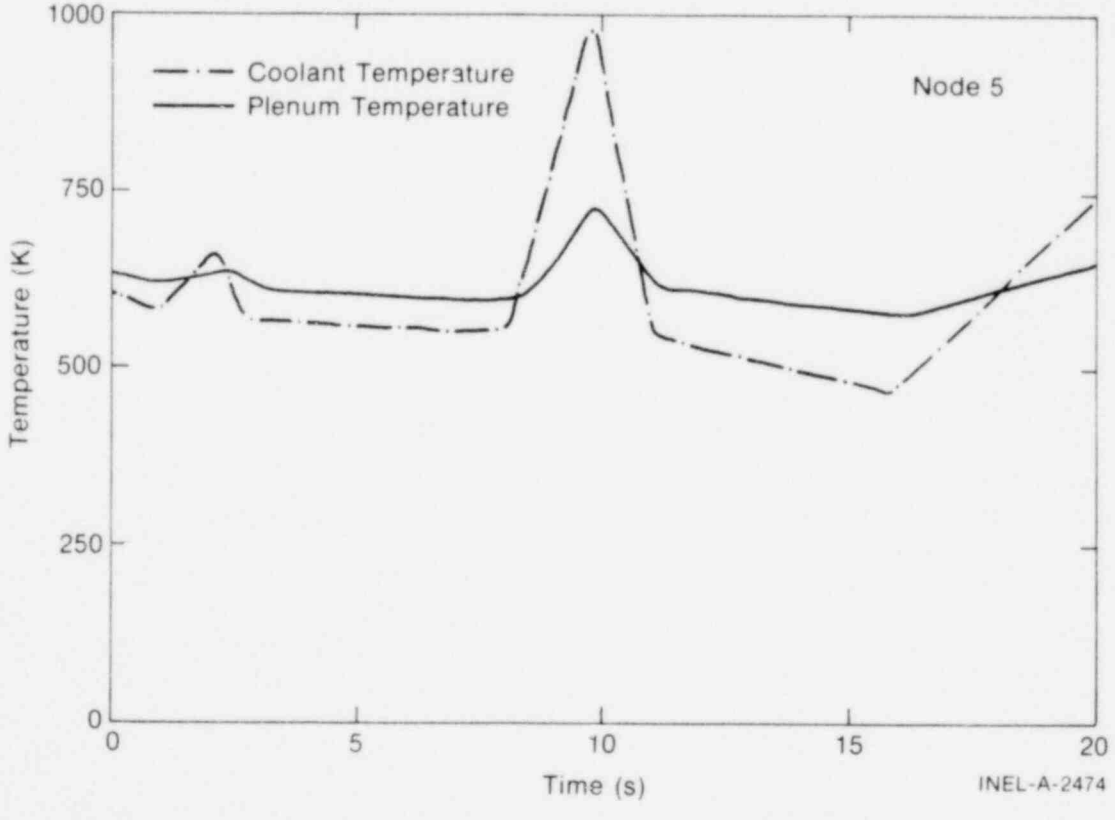

Fig. B-6 Plenum gas temperature history.

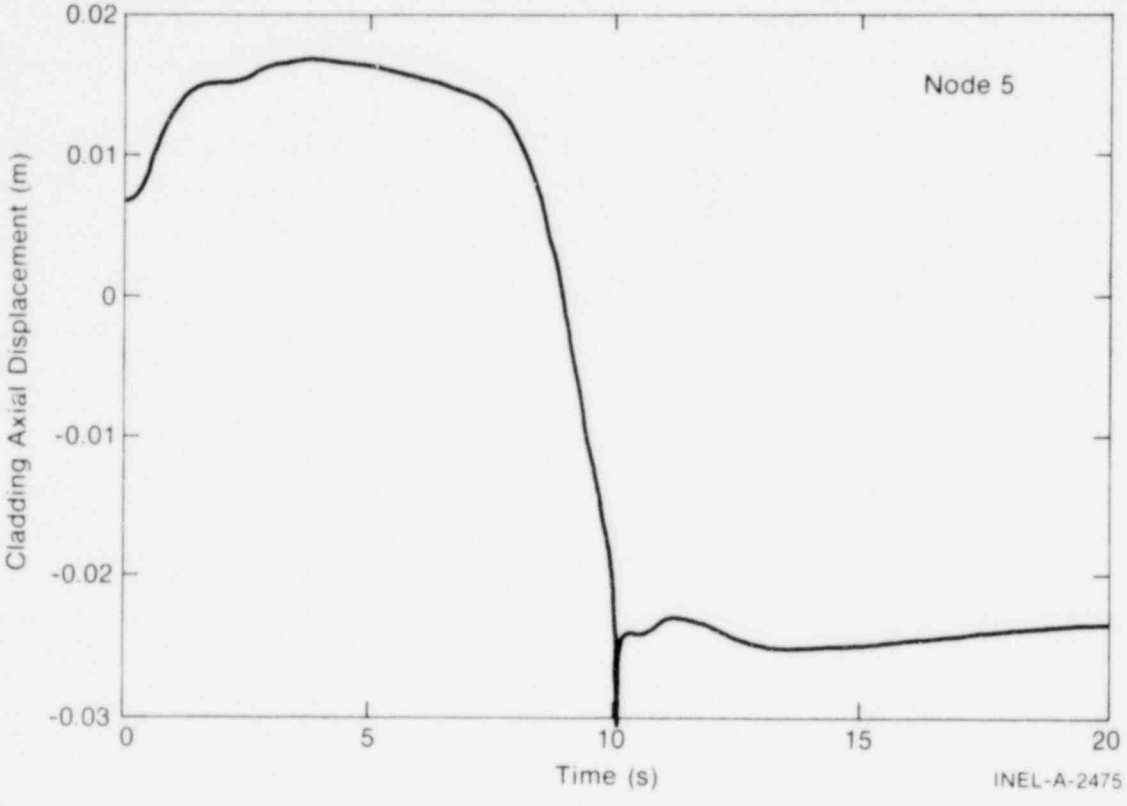

Fig. B-7 Cladding length change history.

The heat transfer mode at each axial node is identified by a code number in the computer printout. The code number of each heat transfer node is given in Table IV of the main text.

```
        1         2         3         4         5         6         7         8
12345678901234567890123456789012345678901234567890123456789012345678901234567890
    1    1  -15        00    2    1    1          0
    0
    0.        20.        .1         .5        12.        .03516     70.
  638.       .01008     .000685     .0251       .2E-06                          0.
 .001        .001                                                    1.1
    1          1 1.
    1.         1.         1.         1.         .5         .5         .5         .5
    .5         .5         .5         .5         1.         1.         1.         1.

  100  100    50   50
   70.       3500.       70.       3500.
* BLOCKDOWN ANALYSIS OF SINGLE ROD
* GENERAL DATA FOR HEAT-1
01010001     14         2          0.         1.       100          1.       100
* GEOMETRY LOCATION AND MESH INCREMENT
010:0200     0          1
* MESH INCREMENT DATA - UNITS ARE FT
01010201     10        .01525      1          .015375    2         .01750
* COMPOSITION OVERLAY
01010301     1         10          3          11         2         13
* SOURCE DISTRIBUTION CARDS
01010401     1.        10          0.         13
* INITIAL TEMPERATURE DISTRIBUTION
010:0501     650.      14
.
    1    8   11
   11.00       0.        3.695      0.6        2.01       2.3        1.413      8.7
   0.815      10.0       1.502     13.0        0.543     16.3        0.402     45.
    .56        0.045     1.17       1.6333     1.48       2.7         1.61      3.9125
  1.08         4.0       1.48       5.99166    1.34       7.075       1.15      8.15833
  0.94         9.25      0.70      10.3        0.36      11.39166
    3   12
 2273.         0.        1561.      0.51       1405.      1.01       1198.      2.15
 1163.         2.75       940.      6.95        908.      7.55        856.      8.15
  693.         8.87       508.     11.07        206.     15.07         50.     20.07
    3
    1   12   12          3.
51500.         0.        166.      0.51         36.      1.01        281.      2.15
  160.         2.75      109.      6.95         52.      7.55          5.      8.15
    5.         8.87      150.     11.07         60.     15.07         50.     20.07
 693.3         0.        601.5     0.51        587.5     1.01        743.8     2.15
1333.8         2.75      537.2     8.95        533.1     7.55        533.2     8.15
 993.8         8.87      531.     11.07        384.2     15.07       693.2     20.07
    3   12   12          3.
02300.         0.        166.      0.51         36.      1.01        281.      2.15
  113.         2.75      100.      6.95         52.      7.55          5.      8.15
    5.         8.87      150.     11.07         60.     15.07         50.     20.07
 693.3         0.        601.5     0.51        587.5     1.01        743.8     2.15
1333.5         2.75      537.2     8.95        533.1     7.55        533.2     8.15
 993.2         8.87      531.     11.07        384.2     15.07       693.2     20.07

        1         2         3         4         5         6         7         8
12345678901234567890123456789012345678901234567890123456789012345678901234567890
```

```
          1         2         3         4         5         6         7         8
12345678901234567890123456789012345678901234567890123456789012345678901234567890

   3   12    12          12.
 39300.        0.        253.       0.51       40.       1.01      281.      2.15
   128.       2.75       110.       6.95       52.       7.55        5.      3.15
     5.       9.87       100.      11.07       60.      15.87       50.     20.07
 633.3          0.      601.5       0.51      587.5       1.01      743.8     2.15
 533.5        2.75      537.2       6.95      533.1       7.55      553.2     3.15
 1333.8       9.87      531.       11.07      384.2      15.87      893.2     20.07
2.15        1.14
   7    22  3.00E-02    .30E-03   2200.       .4583      .0291     .006333

   4
   4     5     6     7
   0.          20.          10.          TIME (SEC)
     0.        3000.         6.        SURFACE TEMPERATURE OF CLAD (K)
     0.        3000.         6.        CENTERLINE TEMPERATURE OF FUEL (K)
 1.0E+05     2.0E+07         8.       GAS GAP PRESSURE (N/M**2)
     0.          .4            8.          CLADDING HOOP STRAIN (M/M)
     0.          .05          10.       FUEL AXIAL DISPLACEMENT (M)
   -.03          .02           5.0      CLADDING AXIAL DISPLACEMENT (M)
     0.          80.           8.       FUEL ROD POWER (KW/M)
     0.        2000.           8.0      FUEL SURFACE TEMP. (K)
 1.0E+03     5.0E+03           5.0      GAP HEAT TRANSFER COEFFICIENT (W/M**2-K)
 1.0E+01     1.0E+07           6.0      SURF. HEAT TRANSF. COEFF. (W/M**2-K)
     0.        2000.           8        AVERAGE CLADDING TEMP. (K)
   -20.          20.           8.0      SURFACE HEAT FLUX PER UNIT LENGTH (KW/M)
 1.0E+05     1.0E+07           5.0      PLENUM PRESSURE (N/M**2)
     0.          1000.         5.       PLENUM TEMPERATURE (K)
-1.1E-10     -1.1E-10          10.      GAS FLOW RATE (GRAM-MOLES/SEC)
 -1.E+03      2.E+03           6.       MASS FLUX (KG/M**2-SEC)
     0.           1.           5.     COOLANT QUALITY
 1.0E+05     1.0E+7             5.0    COOLANT PRESSURE (N/M**2)
0.0E-05     1.0E-06            10.     GAP THICKNESS (M)
     0.        1000.           5.      BULK TEMPERATURE (K)

          1         2         3         4         5         6         7         8
12345678901234567890123456789012345678901234567890123456789012345678901234567890
03 INPUT CARDS
```

*** ROD CODE GENERAL INPUT ***
INPUT IN BRITISH SYSTEM OF UNITS - OUTPUT IN S.I. UNITS

NUMBER OF FUEL RODS = 1

NUMBER OF FLOW CHANNELS = 1

NUMBER OF AXIAL NODES = 16

FUEL DEFORMATION MODEL TYPE = 0
FREE THERMAL EXPANSION FUEL DEFORMATION MODEL SPECIFIED

METAL-WATER REACTION CALCULATIONS SUPPRESSED

MODIFIED ROSS AND STOUTE MODEL FOR GAP CONDUCTANCE TO BE USED

GAS FLOW MODEL TURNED ON

INITIAL TIME = 0.000 SEC

FINAL TIME = 20.000 SEC

MAXIMUM TIME STEP = .10000 SEC

TIME SPAN BETWEEN EDITS = .500 SEC

FUEL ROD LENGTH = 12.0000 FT 3.658 M

ROD DIAMETER = .03516 FT .01072 M
CLADDING COLD WORK =0.00000

PROBABILITY THRESHOLD FOR FUEL ROD FAILURE =1.10000

*** FUEL PELLET DATA ***

FUEL DENSITY = .[illegible]E+03 LBM/FT3 .10220E+05 KG/M3

FRACTION OF THEORETICAL DENSITY = .932457

SHOULDER RADIUS = .01000 FT .00307 M
(AXIAL EXPANSION OF FUEL STACK IS ON A LINE THRU THIS SHOULDER)

DISH DEPTH = .62500E-03 FT .19050E-03 M

PELLET HEIGHT = .25100E-01 FT .76505E-02 M

DISH VOLUME/PELLET = .20000E-06 FT3 .56634E-08 M**3

FRACTION BY WEIGHT OF FUEL THAT PLUTONIUM OXIDE =0.000000

BURNUP OF FUEL =0. MWS/KG

AVERAGE FAST NEUTRON FLUX (N/M**2-SEC) =0.

TIME SPAN OF FAST NEUTRON FLUX (SEC) =0.

COLD STATE TEMPERATURE OF ROD = 70.0 F 294.3 K

CONVERGENCE FRACTION FOR INTERNAL PRES. = 1.00E-03

CONVERGENCE FRACTION FOR TEMPERATURES = 1.00E-03

// ROD TO COOLANT CHANNEL CONNECTIONS //.

ROD NO	CHANNEL	FRACTION	CHANNEL	FRACTION	CHANNEL	FRACTION	CHANNEL	FRACTION
1	1	1.000E+00	0	0.	0	0.	0	0.

AXIAL NODE MID-PLANE ELEVATIONS (FT)	(M)	NODE LENGTHS (FT)	(M)
.5000	.1524	1.0000	.3048
1.5000	.4572	1.0000	.3048
2.5000	.7620	1.0000	.3048
3.5000	1.0668	1.0000	.3048
4.2500	1.2954	.5000	.1524
4.7500	1.4478	.5000	.1524
5.2500	1.6002	.5000	.1524
5.7500	1.7526	.5000	.1524
6.2500	1.9050	.5000	.1524
6.7500	2.0574	.5000	.1524
7.2500	2.2098	.5000	.1524
7.7500	2.3622	.5000	.1524
8.5000	2.5908	1.0000	.3048
9.5000	2.8956	1.0000	.3048
10.5000	3.2004	1.0000	.3048
11.5000	3.5052	1.0000	.3048

NORMALIZED AXIAL VARIATION IN FAST FLUX ASSUMED SAME AS THAT OF FUEL ROD POWER

/ THERMAL PROPERTY DATA /

FUEL PROPERTY TABLES IN THE TEMPERATURE RANGE 70.0 TO 6500.0 F WILL USE 100 POINTS FOR THERMAL CONDUCTIVITY, 100 FOR HEAT CAPACITY.		294.3 TO 4977.6 K
CLAD PROPERTY TABLES IN THE TEMPERATURE RANGE 70.0 TO 3500.0 F WILL USE 50 POINTS FOR THERMAL CONDUCTIVITY, 50 FOR HEAT CAPACITY.		294.3 TO 2199.8 K
FUEL DENSITY = 5.3806E+02 LBM/FT**3 FRACTION OF THEORETICAL DENSITY = 93.25 %		1.0220E+04 KG/M**3
CLAD DENSITY = 4.0954E+02 LBM/FT**3		6.5602E+03 KG/M**3
GAS GAP HEAT CAPACITY = 1.200E-02 BTU/FT**3.F		8.046E+02 J/M**3.K
FUEL MELTING TEMPERATURE = 5144.0 F		3113.2 K
FUEL HEAT OF FUSION = 7.5156E+04 BTU/FT**3		2.8002E+09 J/M**3
CLAD MELTING TEMPERATURE = 3317.0 F		2098.2 K
CLAD HEAT OF FUSION = 3.9616E+04 BTU/FT**3		1.4760E+09 J/M**3

LISTING OF INPUT DATA FOR CASE 1

```
    1     * BLOWDOWN ANALYSIS OF SINGLE ROD
    2     * GENERAL DATA FOR HEAT-1
    3     01G10001     14          2          0.          1.        100         1.        100
    4     * GEOMETRY LOCATION AND MESH INCREMENT
          01010200      0          1
    6     * MESH INCREMENT DATA - UNITS ARE FT
    7     01011001     10       .01525        1        .015575      2        .01758
    8     * COMPOSITION OVERLAY
    9     01019301      1          10          3        11           2        13
   10     * SOURCE DISTRIBUTION CARDS
   11     01010601      1          10          0.       15
   12     * INITIAL TEMPERATURE DISTRIBUTION
   13     01010601    650.         14
   14
```

GENERAL DATA

HEAT1 PROBLEM NUMBER = 1

NUMBER OF MESH POINTS = 14

GEOMETRY TYPE = CYLINDRICAL

LEFT BOUNDARY COORD. = 0.

SOURCE SCALING FACTOR = 1.00000E+00

TOTAL INTEG. SOURCE = 7.30617E-04

DATA FOR STEADY STATE CALCULATIONS

MAX NO. OF ITERATIONS = 100

CONVERGENCE CRITERION = 1.00000E+00

DATA FOR TIME DEPENDENT CALCULATIONS

MAX NO. OF ITERATIONS = 100

MESH INTERVALS - (J(I), DELTA X(I))
MESH INCREMENT DELTA X(I), CONSTANT BETWEEN MESH POINTS J(I-1) AND J(I)

11. 1.52500E-03 12. 3.25000E-04 14. 1.00250E-03

CUMULATIVE MESH COORDINATES - (J, X(J))

1.	0.	2.	1.52500E-03	3.	3.07500E-03	4.	4.57500E-03	5.	6.10000E-03	6.	7.62500E-03
7.	9.15000E-03	8.	1.09750E-02	9.	1.22000E-02	10.	1.37250E-02	11.	1.52500E-02	12.	1.55750E-02
13.	1.65775E-02	14.	1.75800E-02								

COMPOSITION OVERLAY - (J(I), COMP ID(I))
COMPOSITION CONSTANT BETWEEN MESH POINTS J(I-1) AND J(I)

11. 1 12. 3 14. 2

SOURCE DISTRIBUTION - (J(I), Q(I))
SOURCE Q(I) CONSTANT BETWEEN MESH POINTS J(I-1) AND J(I)

11. 1.00000E+00 14. 0.

INITIAL TEMPERATURE DISTRIBUTION - (J(I), T(I))
TEMPERATURE T(I) CONSTANT BETWEEN MESH POINTS J(I-1) AND J(I)

14. 6.50000E+02

POWER HISTORY AND AXIAL PROFILE INPUT DATA FOR 1 FUEL RODS

ROD NO.	DATA PAIRS	LINEAR POWER (KW/FT)	TIME (SEC)	LINEAR POWER (KW/FT)	TIME (SEC)	LINEAR POWER (KW/FT)	TIME (SEC)	LINEAR POWER (KW/FT)	TIME (SEC)
1	8	1.1050E+01	0	3.6950E+00	6.0000E-01	2.0100E+00	2.3000E+00	1.4130E+00	8.7000E+00
		8.1500E-01	1.0000E+01	1.9020E+00	1.3000E+01	5.4300E-01	1.6300E+01	4.0200E-01	4.5000E+01

DATA PAIRS	AXIAL POWER RATIO	AXIAL DISTANCE (FT)	AXIAL POWER RATIO	AXIAL DISTANCE (FT)	AXIAL POWER RATIO	AXIAL DISTANCE (FT)	AXIAL POWER RATIO	AXIAL DISTANCE (FT)
11	5.6000E-01	5.4500E-01	1.1700E+00	1.6333E+00	1.4600E+00	2.7000E+00	1.6100E+00	3.8125E+00
	1.5800E+00	4.9000E+00	1.4800E+00	5.9817E+00	1.3400E+00	7.0750E+00	1.1500E+00	8.1583E+00
	9.4000E-01	9.2500E+00	7.0000E-01	1.0300E+01	3.6000E-01	1.1392E+01		

*** INTEGRAL OF AXIAL POWER PROFILE FACTORS OVER FUEL ROD LENGTH SUMS TO .1120E+01FOR FUEL ROD = 1 ***
SUM SHOULD BE 1.0. CHECK CARD GROUP 4.3 INPUT. FACTORS TEMPORARILY FIXED BY BEING NORMALIZED TO 1.

*** CORE PRESSURE HISTORY *** 12 PAIRS

	TIME (SEC)	PRESSURE (PSIA)	PRESSURE (N/M**2)
0		2.2730E+03	1.5672E+07
5	1.0000E-01	1.5811E+03	1.0763E+07
	1.0100E+00	1.4[illegible]E+03	9.6871E+06
2	1.5000E+00	1.[illegible]E+03	8.2599E+06
	[illegible]	1.[illegible]E+03	8.0393E+06
	[illegible]	9.[illegible]	6.[illegible]
2	[illegible]	3.[illegible]	[illegible]
8	[illegible]	8.[illegible]	5.[illegible]
	[illegible]	6.[illegible]	4.[illegible]
	1.0[illegible]	5.[illegible]	3.[illegible]
	[illegible]	2.[illegible]	1.[illegible]
2	3.0000E+01	5.0000E+01	3.4474E+05

*** TRANSIENT HEAT TRANSFER COEFFICIENT AND BULK TEMPERATURE SPECIFIED BY CARD INPUT ***

*** ZONE 1 TOP BOUNDARY ELEVATION = 3.0000 FT OR .9144 M ***

TIME(SEC)	H.T.C.(BTU/HR-F-FT2)	H.T.C.(WATT/M-K)
0	.5150E+05	.2930E+05
.5160E+00	.1665E+03	.9425E+03
.1210E+01	.3600E+02	.2044E+03
.2110E+01	.2810E+03	.1593E+04
.3760E+01	.1160E+03	.6614E+03
.5670E+01	.1000E+03	.5676E+03
.7390E+01	.5230E+02	.2953E+03
.9150E+01	.3500E+01	.2039E+02
.9970E+01	.5010E+01	.2839E+02
.1100E+02	.1600E+03	.9080E+03
.1150E+02	.6000E+02	.3407E+03
.2010E+02	.5000E+02	.2839E+03

TIME(SEC)	TEMPERATURE(F)	TEMPERATURE(K)
0	.6500E+03	.6100E+03
.5160E+00	.6210E+03	.5985E+03
.1210E+01	.5370E+03	.5019E+03
.2110E+01	.5040E+03	.4800E+03
.3760E+01	.5030E+03	.5044E+03
.5670E+01	.5330E+03	.5038E+03
.7390E+01	.5310E+03	.5026E+03
.9150E+01	.5010E+03	.5010E+03
.9970E+01	.5010E+03	.5010E+03
.1100E+02	.5070E+03	.5300E+03
.1150E+02	.4350E+03	.4600E+03
.2010E+02	.9932E+03	.7516E+03

*** ZONE 2 TOP BOUNDARY ELEVATION = 9.0000 FT OR 2.7432 M ***

TIME(SEC)	H.T.C.(BTU/HR-F-FT2)	H.T.C.(WATT/M-K)
0	.6050E+05	.3438E+05
.5160E+00	.1910E+03	.1084E+04
.1210E+01	.3600E+02	.2044E+03
.2110E+01	.2810E+03	.1593E+04
.3760E+01	.1160E+03	.6614E+03
.5670E+01	.1000E+03	.5676E+03
.7390E+01	.5230E+02	.2953E+03
.9150E+01	.3500E+01	.2039E+02
.9970E+01	.5010E+01	.2839E+02
.1100E+02	.1600E+03	.9080E+03
.1150E+02	.6000E+02	.3407E+03
.2010E+02	.5000E+02	.2839E+03

TIME(SEC)	TEMPERATURE(F)	TEMPERATURE(K)
0	.6500E+03	.6100E+03
.5160E+00	.6210E+03	.5985E+03
.1210E+01	.5370E+03	.5019E+03
.2110E+01	.5040E+03	.4800E+03
.3760E+01	.5030E+03	.5044E+03
.5670E+01	.5330E+03	.5038E+03
.7390E+01	.5310E+03	.5026E+03
.9150E+01	.5010E+03	.5010E+03
.9970E+01	.5010E+03	.5010E+03
.1100E+02	.5070E+03	.5300E+03
.1150E+02	.4350E+03	.4600E+03
.2010E+02	.9932E+03	.7516E+03

70-736

POOR ORIGINAL

*** GAP CONDUCTANCE SUBCODE INPUT ***

ARITHMETIC MEAN ROUGHNESS OF CLADDING (MICRONS) = .2160E+01

ARITHMETIC MEAN ROUGHNESS OF FUEL (MICRONS) = .1140E+01

*** GAS GAP DATA ***

XXX DATA FOR ROD 1 XXX

GAS QUANTITY = 3.000E-02 MOLES

PLENUM VOLUME = 3.300E-04 FT**3 (1.076E-05 M**3)

GAP PRESSURE = 2.200E+03 PSIA (1.517E+07 N/M**2)

SPRING LENGTH= 4.500E-01 FT (1.397E-01 M)

COIL OD SPRING = 2.910E-02 FT (8.870E-03 M)

NUMBER OF COILS = 22

WIRE OD OF SPRING = 6.333E-03 FT (1.930E-03 M)

MOLE FRACTIONS OF GAS COMPONENTS

HELIUM	ARGON	KRYPTON	XENON	HYDROGEN	NITROGEN	H2O
1.000E+01	0.	0.	0.	0.	0.	0

PLOTS REQUESTED FOR 4 NODES

4 5 6 7

MINIMUM	MAXIMUM	AXIS LENGTH	-------LABEL----------
0.	.2000E+02	.1000E+02	TIME (SEC)
0.	.3000E+04	.6000E+01	SURFACE TEMPERATURE OF CLAD (K)
0.	.3100E+04	.6000E+01	CENTERLINE TEMPERATURE OF FUEL (K)
.1000E+06	.2500E+08	.8000E+01	GAS GAP PRESSURE (N/M**2)
0.	.4000E-00	.8000E+01	CLADDING HOOP STRAIN (M/M)
0.	.1000E-01	.1000E+02	FUEL AXIAL DISPLACEMENT (M)
-.3000E-01	.3000E-01	.6000E+01	CLADDING AXIAL DISPLACEMENT (M)
0.	.1000E+02	.8000E+01	FUEL ROD POWER (KW/M)
0.	.2000E+04	.6000E+01	FUEL SURFACE TEMP. (K)
.1000E+04	.5000E+04	.5000E+01	GAP HEAT TRANSFER COEFFICIENT (W/M**2-K
.1000E+02	.1000E+00	.6000E+01	SURF. HEAT TRANSF. COEFF. (W/M**2-K)
0	.2500E+04	.8000E+06	AVERAGE CLADDING TEMP. (K)
-.2000E+02	.2000E+02	.8000E+01	SURFACE HEAT FLUX PER UNIT LENGTH (KW/M
.1000E+06	.1000E+08	.6000E+01	PLENUM PRESSURE (N/M**2)
0	.1000E+04	.5000E+01	PLENUM TEMPERATURE (K)
-.1000E-00	.1000E-10	.1000E+02	GAS FLOW RATE (GRAM-MOLES/SEC)
-.1000E+04	.2000E+04	.6000E+01	MASS FLUX (KG/M**2-SEC)
0.	.1000E+01	.5000E+01	COOLANT QUALITY
.1000E+06	.1000E+08	.5000E+01	COOLANT PRESSURE (N/M**2)
0	.1000E-05	.1000E+00	GAP THICKNESS (M)
0	.1000E+04	.5000E+01	DUCT TEMPERATURE (K)

*** LENGTH REQUIRED FOR A1 ARRAY = 1681 ***

COOLANT CONDITIONS AT TIME = 0. SEC

ELEVATION(M)	COOLANT TEMPERATURE(K)	PRESSURE(N/M**2)
.1524E+00	.6100E+03	.1567E+08
.4572E+00	.6100E+03	.1567E+08
.7620E+00	.6100E+03	.1567E+08
.1067E+01	.6100E+03	.1567E+08
.1295E+01	.6100E+03	.1567E+08
.1447E+01	.6100E+03	.1567E+08
.1600E+01	.6100E+03	.1567E+08
.1753E+01	.6100E+03	.1567E+08
.1905E+01	.6100E+03	.1567E+08
.2057E+01	.6100E+03	.1567E+08
.2210E+01	.6100E+03	.1567E+08
.2362E+01	.6100E+03	.1567E+08
.2591E+01	.6100E+03	.1567E+08
.2896E+01	.6100E+03	.1567E+08
.3200E+01	.6100E+03	.1567E+08
.3505E+01	.6100E+03	.1567E+08

FUEL ROD CONDITIONS AT TIME = 0.0000 SEC

ROD NUMBER 1 NUMBER OF ITERATIONS REQUIRED FOR CONVERGENCE = 12 ACCUMULATED CPU TIME = 0.0 S

AVERAGE FUEL ROD POWER (KW/M)	3.635E+01
ENERGY GENERATED BY METAL-WATER REACTION(KW)	0.
FUEL STACK AXIAL EXTENSION (MM)	4.085E+01
CLADDING AXIAL EXTENSION (MM)	7.050E+00
PLENUM GAS TEMPERATURE (K)	630.4
PLENUM GAS PRESSURE (N/M**2)	.1234E+08
GAS FLOW RATE FROM PLENUM (GM-MOLES/SEC)	0.
FRACTION OF MOLTEN FUEL IN FUEL ROD	0.0000
FRACTION OF FUEL RODS FAILED	0.
TOTAL FREE GAS VOLUME(MM) **3	.1587?8E+05
PLENUM VOLUME FRACTION	.433691
CRACK VOLUME FRACTION	.007578
GAP VOLUME FRACTION	.208610
OPEN POROSITY VOLUME FRACTION	.027670
DISH VOLUME FRACTION	.143401

FRAP-T MOD05 VER04/28 FUEL ROD ANALYSIS PROGRAM • 04/28/77 • EG&G MATPRO MODULE MOD008

AXIAL NODE NUMBER	1	2	3	4	5	6
ELEVATION (M)	.152	.457	.762	1.067	1.295	1.449
LOCAL FUEL ROD POWER (KW/M)	1.732E+01	3.556E+01	4.503E+01	5.090E+01	5.187E+01	5.143E+01
AVERAGE FUEL ENTHALPY (JOU/KG)	203095.3	317432.9	370439.5	394398.5	398653.0	396709.9
FUEL CENTERLINE TEMPERATURE (K)	1216.7	1931.0	2271.9	2418.7	2444.4	2432.6
GAS GAP TEMPERATURE (K)	715.5	759.7	759.4	753.5	752.2	752.8
FUEL ROD SURFACE TEMPERATURE (K)	611.7	613.6	614.6	614.3	614.3	614.3
COOLANT BULK TEMPERATURE (K)	610.0	610.0	610.0	610.0	610.0	610.0
COOLANT QUALITY	0.	0.	0.	0.	0.	0.
COOLANT MASS FLUX,KG/SEC-M2	0.	0.	0.	0.	0.	0.
SURFACE HEAT FLUX (WATT/M**2)	5.148E+05	1.054E+06	1.353E+06	1.509E+06	1.538E+06	1.525E+06
CRITICAL HEAT FLUX (WATT/M**2)	-3.155E+00	-3.155E+00	-3.155E+00	-3.155E+00	-3.155E+00	-3.155E+00
SURFACE HEAT TRANSFER COEF. (WATT/M**2.K)	2.930E+05	2.930E+05	2.930E+05	3.536E+05	3.539E+05	3.536E+05
HEAT TRANSFER MODE	1	1	1	1	1	1
GAP HEAT TRANSFER COEF. (WATT/M**2.K)	3.511E+03	5.710E+03	8.328E+03	1.059E+04	1.114E+04	1.089E+04
THERMAL RADIAL GAP GAP (MM)	.0789	.0435	.0276	.0201	.0167	.0183
STRUCTURAL RADIAL GAS GAP (MM)	.0720	.0435	.0276	.0201	.0187	.0193
GAP PRESSURE (N/M**2)	1.234E+07	1.234E+07	1.234E+07	1.234E+07	1.234E+07	1.234E+07
COOLANT PRESSURE (N/M**2)	1.567E+07	1.567E+07	1.557E+07	1.557E+07	1.567E+07	1.567E+07
RMS DISPLT. OF FUEL OUTER SURFACE (MM)	3.301E-02	6.266E-02	7.606E-02	8.648E-02	8.755E-02	8.722E-02
DISPLACEMENT OF CLAD OUTER SURFACE (MM)	7.882E-03	8.442E-03	8.755E-03	8.973E-03	8.907E-03	8.804E-03
CLADDING AXIAL STRAIN (INELASTIC)	1.433E-03	1.537E-03	1.595E-03	1.618E-03	1.623E-03	1.621E-03
CLADDING AXIAL ELASTIC STRAIN	0.	0.	0.	0.	0.	0.
CLADDING AXIAL THERMAL STRAIN	0.	0.	0.	0.	0.	0.
CLADDING HOOP INELASTIC HOOP STRAIN	0.	0.	0.	0.	0.	0.
INTERFACE PRESSURE, THERMAL GAP(N/M**2)	0.	0.	0.	0.	0.	0.
INTERFACE PRESSURE, STRUCT. GAP(N/M**2)	0.	0.	0.	0.	0.	0.
CLADDING HOOP STRESS (N/M**2)	-4.156E+07	-4.156E+07	-4.156E+07	-4.156E+07	-4.156E+07	-4.156E+07
CLADDING AXIAL STRESS (N/M**2)	-2.783E+07	-2.783E+07	-2.783E+07	-2.783E+07	-2.783E+07	-2.783E+07
EFFECTIVE CLADDING STRESS (N/M**2)	3.668E+07	3.668E+07	3.668E+07	3.668E+07	3.668E+07	3.668E+07
CLADDING YIELD STRENGTH(N/M**2)	1.950E+08	1.943E+08	1.934E+08	1.931E+08	1.931E+08	1.931E+08
CLAD STRESS AT INSTABILITY STRAIN(N/M**	3.219E+08	3.156E+08	3.124E+08	3.111E+08	3.108E+08	3.110E+08
CLADDING EFFECTIVE PLASTIC STRAIN	0.	0.	0.	0.	0.	0.
CLADDING INSTABILITY STRAIN	1.301E-01	1.319E-01	1.329E-01	1.333E-01	1.334E-01	1.334E-01
METAL-WATER REACTION DEPTH (MM)	0.	0.	0.	0.	0.	0.
METAL-WATER REACTION ENERGY (KW/M)	0.	0.	0.	0.	0.	0.

TEMPERATURES BY RADIAL MESH POINTS

NO.	MESH RADIUS (MM)	TEMPERATURES (K)					
1	0.	1216.7	1931.0	2271.9	2418.7	2444.4	2432.6
2	4.345E-01	1211.9	1917.6	2260.4	2402.5	2428.1	2416.4
3	8.691E-01	1197.3	1877.0	2209.5	2353.2	2378.5	2366.9
4	1.304E+00	1173.8	1811.8	2129.4	2269.6	2293.1	2282.0
5	1.738E+00	1142.5	1721.1	2013.6	2145.1	2168.4	2157.7
6	2.173E+00	1099.3	1608.8	1899.5	1978.8	1998.7	1989.0
7	2.607E+00	1038.8	1477.4	1675.9	1769.3	1786.7	1778.2
8	3.042E+00	958.0	1332.3	1475.2	1537.4	1548.2	1543.3
9	3.476E+00	853.0	1176.4	1284.3	1338.1	1347.4	1342.1
10	3.911E+00	730.3	1021.1	1094.0	1098.7	1058.8	1138.8
11	4.345E+00	598.8	875.3	932.4	939.0	931.2	932.9
12	4.780E+00	468.7	754.2	814.2	821.0	813.1	812.6
13	5.053E+00	621.8	853.6	894.0	899.3	893.1	892.9
14	5.188E+00	611.7	813.8	814.5	814.3	814.3	814.3

FRAP-T MOD009 VER04/28 FUEL ROD ANALYSIS PROGRAM • 04/28/77 • EOL0 MATPRO MODULE MOD008

AXIAL NODE NUMBER	7	8	9	10	11	12
ELEVATION (M)	1.500	1.753	1.905	2.057	2.210	2.362
LOCAL FUEL ROD POWER (KW/M)	5.025E+01	4.976E+01	4.898E+01	4.486E+01	4.250E+01	3.966E+01
AVERAGE FUEL ENTHALPY (JOU/KG)	391541.2	384851.1	376509.0	366454.1	354674.5	339819.7
FUEL CENTERLINE TEMPERATURE (K)	2401.4	2360.9	2310.1	2248.0	2173.9	2073.1
GAS GAP TEMPERATURE (K)	754.3	756.0	757.7	759.3	760.4	760.8
FUEL ROD SURFACE TEMPERATURE (K)	614.2	614.1	613.9	613.7	613.5	613.3
COOLANT BULK TEMPERATURE(K)	610.0	610.0	610.0	610.0	610.0	610.0
COOLANT QUALITY	0.	0.	0.	0.	0.	0.
COOLANT MASS FLUX,KG/SEC-M2	0.	0.	0.	0.	0.	0.
SURFACE HEAT FLUX (WATT/M**2)	1.490E+06	1.448E+06	1.393E+06	1.330E+06	1.250E+06	1.176E+06
CRITICAL HEAT FLUX (WATT/M**2)	-3.155E+00	-3.155E+00	-3.155E+00	-3.155E+00	-3.155E+00	-3.155E+00
SURFACE HEAT TRANSFER COEF. (WATT/M**2.K)	3.520E+05	3.530E+05	3.538E+05	3.538E+05	3.539E+05	3.532E+05
HEAT TRANSFER MODE	1	1	1	1	1	1
GAP HEAT TRANSFER COEF. (WATT/M**2.K)	1.026E+04	9.554E+03	8.808E+03	9.054E+03	7.323E+03	6.577E+03
THERMAL RADIAL GAS GAP (MM)	.0210	.0230	.0256	.0287	.0324	.0358
STRUCTURAL RADIAL GAS GAP (MM)	.0210	.0230	.0256	.0287	.0324	.0358
GAP PRESSURE (N/M**2)	1.234E+07	1.234E+07	1.234E+07	1.234E+07	1.234E+07	1.234E+07
COOLANT PRESSURE(N/M**2)	1.557E+07	1.557E+07	1.557E+07	1.557E+07	1.557E+07	1.557E+07
PEAK DISPLT. OF FUEL OUTER SURFACE (MM)	8.556E-02	8.343E-02	8.079E-02	7.763E-02	7.396E-02	6.940E-02
DISPLACEMENT OF CLAD OUTER SURFACE (MM)	8.056E-03	8.813E-03	8.758E-03	8.695E-03	8.623E-03	8.539E-03
CLADDING HOOP STRAIN (MIDPLANE)	1.614E-03	1.606E-03	1.595E-03	1.584E-03	1.571E-03	1.555E-03
CLADDING PERMANENT HOOP STRAIN	0.	0.	0.	0.	0.	0.
CLADDING MIDPLANE AXIAL STRAIN	0.	0.	0.	0.	0.	0.
CLADDING MAXIMUM LOCALIZED HOOP STRAIN	0.	0.	0.	0.	0.	0.
INTERFACE PRESSURE, THERMAL GAP(N/M**2)	0.	0.	0.	0.	0.	0.
INTERFACE PRESSURE, STRUCT. GAP(N/M**2)	0.	0.	0.	0.	0.	0.
CLADDING HOOP STRESS (N/M**2)	-4.156E+07	-4.156E+07	-4.156E+07	-4.156E+07	-4.155E+07	-4.156E+07
CLADDING AXIAL STRESS (N/M**2)	-2.783E+07	-2.783E+07	-2.783E+07	-2.783E+07	-2.783E+07	-2.783E+07
EFFECTIVE CLADDING STRESS (N/M**2)	3.668E+07	3.668E+07	3.668E+07	3.668E+07	3.663E+07	3.660E+07
CLADDING YIELD STRESS(N/M**2)	1.933E+08	1.933E+08	1.934E+08	1.936E+08	1.939E+08	1.940E+08
CLAD STRESS AT INSTABILITY STRAIN(N/M**	3.113E+08	3.116E+08	3.124E+08	3.131E+08	3.139E+08	3.148E+08
CLADDING EFFECTIVE PLASTIC STRAIN	0.	0.	0.	0.	0.	0.
CLADDING INSTABILITY STRAIN	1.333E-01	1.331E-01	1.329E-01	1.327E-01	1.325E-01	1.322E-01
METAL-WATER REACTION DEPTH (MM)	0.	0.	0.	0.	0.	0.
METAL-WATER REACTION ENERGY (KW/M)	0.	0.	0.	0.	0.	0.

TEMPERATURES BY RADIAL MESH POINTS

NO.	MESH RADIUS (MM)	TEMPERATURES (K)					
1	0.	2401.4	2360.9	2310.1	2248.0	2173.9	2073.1
2	4.849E-01	2383.3	2344.9	2294.5	2232.7	2159.0	2059.7
3	9.698E-01	2336.3	2296.5	2246.8	2185.1	2113.7	2021.2
4	1.455E+00	2268.1	2213.5	2155.4	2095.7	2036.7	1947.5
5	1.940E+00	2189.5	2092.9	2047.5	1992.1	1928.1	1843.4
6	2.425E+00	1984.2	1931.0	1889.7	1840.5	1783.8	1713.2
7	2.910E+00	1753.3	1732.8	1700.4	1651.8	1617.2	1551.3
8	3.395E+00	1530.1	1512.9	1491.1	1454.6	1433.4	1393.5
9	3.715E+00	1288.7	1284.0	1272.8	1250.2	1240.5	1216.7
10	4.155E+00	1058.4	1057.4	1055.3	1051.9	1055.5	1057.8
11	4.640E+00	857.4	862.8	863.1	865.8	868.8	868.0
12	4.767E+00	821.2	859.4	857.3	859.6	864.9	865.1
13	5.043E+00	842.1	841.2	840.0	838.7	837.2	836.4
14	5.358E+00	814.2	814.1	813.9	813.7	813.5	813.3

AXIAL NODE NUMBER	13	14	15	16
ELEVATION (M)	2.591	2.896	3.200	3.505
LOCAL FUEL ROD POWER (KW/M)	3.920E+01	2.886E+01	2.070E+01	1.059E+01
AVERAGE FUEL ENTHALPY (JOU/KG)	315305.9	276757.5	225578.0	157256.0
FUEL CENTERLINE TEMPERATURE (K)	1916.6	1682.1	1346.5	966.2
GAS GAP TEMPERATURE (K)	759.0	751.3	729.2	682.5
FUEL ROD SURFACE TEMPERATURE (K)	612.9	613.8	612.7	611.4
COOLANT BULK TEMPERATURE (K)	610.0	610.0	610.0	610.0
COOLANT QUALITY	0.	0.	0.	0
COOLANT MASS FLUX, KG/SEC-M2	0.	0.	0.	0
SURFACE HEAT FLUX (WATT/M**2)	1.044E+06	8.499E+05	6.140E+05	3.141E+05
CRITICAL HEAT FLUX (WATT/M**2)	-3.155E+00	-3.155E+00	-3.155E+00	-3.155E+00
SURFACE HEAT TRANSFER COEF. (WATT/M**2.K)	3.930E+05	2.230E+05	2.232E+05	2.232E+05
HEAT TRANSFER MODE	1	1	1	1
GAP HEAT TRANSFER COEF. (WATT/M**2.K)	5.630E+03	4.839E+03	3.789E+03	3.049E+03
THERMAL RADIAL GAS GAP (MM)	.0441	.0547	.0672	.0812
STRUCTURAL RADIAL GAS GAP (MM)	.0441	.0547	.0672	.0812
GAP PRESSURE (N/M**2)	1.234E+07	1.234E+07	1.234E+07	1.234E+07
CORE PRESSURE (N/M**2)	1.587E+07	1.587E+07	1.587E+07	1.587E+07
PLUS LIMIT OF FUEL OUTER SURFACE (MM)	6.202E-02	5.185E-02	3.861E-02	2.432E-02
DISPLACEMENT OF CLAD OUTER SURFACE (MM)	8.403E-03	8.271E-03	8.014E-03	7.690E-03
CLADDING HOOP STRAIN (INELASTIC)	1.530E-03	1.505E-03	1.457E-03	1.397E-03
CLADDING PERMANENT HOOP STRAIN	0.	0.	0.	0.
CLADDING PERMANENT AXIAL STRAIN	0.	0.	0.	0.
CLADDING MAXIMUM LOCALIZED HOOP STRAIN	0.	0.	0.	0.
INNER ACE PRESSURE, THERMAL GAP(N/M**2)	0.	0.	0.	0.
INTERFACE PRESSURE, STRUCT GAP(N/M**2)	0.	0.	0.	0.
CLADDING HOOP STRESS (N/M**2)	-4.155E+07	-4.156E+07	-4.156E+07	-4.156E+07
CLADDING AXIAL STRESS (N/M**2)	-2.783E+07	-2.783E+07	-2.783E+07	-2.783E+07
EFFECTIVE CLADDING STRESS (N/M**2)	3.859E+07	3.860E+07	3.860E+07	3.858E+07
CLADDING YIELD STRESS (N/M**2)	1.954E+08	1.947E+08	1.855E+08	1.964E+08
CLAD STRESS AT INSTABILITY STRAIN(N/M**	3.102E+08	3.176E+08	3.204E+08	3.240E+08
CLADDING EFFECTIVE PLASTIC STRAIN	0.	0.	0.	0.
CLADDING INSTABILITY STRAIN	1.318E-01	1.314E-01	1.305E-01	1.295E-01
METAL-WATER REACTION DEPTH (MM)	0.	0.	0.	0.
METAL-WATER REACTION ENERGY (KW/M)	0.	0.	0.	0.

TEMPERATURES BY RADIAL MESH POINTS

NO.	MESH RADIUS (MM)	TEMPERATURES (K)			
1	0.	1916.6	1682.1	1346.5	966.2
2	9.6[illegible]E-01	1903.4	1682.0	1340.3	963.7
3	1.92[illegible]E+00	1862.8	1682.1	1321.5	956.2
4	2.88[illegible]E+00	1788.7	1573.0	1290.0	944.0
5	3.84[illegible]E+00	1709.5	1505.9	1246.7	927.0
6	4.80[illegible]E+00	1598.4	1402.5	1196.1	905.9
7	5.76[illegible]E+00	1483.2	1302.2	1134.1	880.8
8	6.72[illegible]E+00	1356.1	1210.7	1064.9	850.6
9	7.68[illegible]E+00	1178.3	1100.2	987.7	817.0
10	8.64[illegible]E+00	1019.8	979.9	903.6	780.5
11	9.60[illegible]E+00	894.8	869.1	821.9	741.5
12	1.05[illegible]E+01	853.1	845.6	818.8	723.6
13	1.15[illegible]E+01	832.8	820.8	814.3	717.3
14	1.25[illegible]E+01	812.9	813.8	812.7	711.4

COOLANT CONDITIONS AT TIME = .99000E+01 SEC

ELEVATION(M)	COOLANT TEMPERATURE(K)	PRESSURE(N/M**2)
.1524E+00	.9852E+03	.4709E+07
.4572E+00	.9852E+03	.4709E+07
.7620E+00	.9852E+03	.4709E+07
.1067E+01	.9852E+03	.4709E+07
.1295E+01	.9852E+03	.4709E+07
.1448E+01	.9852E+03	.4709E+07
.1600E+01	.9852E+03	.4709E+07
.1753E+01	.9852E+03	.4709E+07
.1907E+01	.9852E+03	.4709E+07
.2057E+01	.9852E+03	.4709E+07
.2210E+01	.9852E+03	.4709E+07
.2362E+01	.9852E+03	.4709E+07
.2531E+01	.9852E+03	.4709E+07
.2690E+01	.9852E+03	.4709E+07
.3200E+01	.9852E+03	.4709E+07
.3500E+01	.9852E+03	.4709E+07

FUEL ROD CONDITIONS AT TIME = 9.9000 SEC

ROD NUMBER 1 NUMBER OF ITERATIONS REQUIRED FOR CONVERGENCE = 2 ACCUMULATED CPU TIME = 0

AVERAGE FUEL ROD POWER (KW/M)	2.825E+00
ENERGY GENERATED BY METAL-WATER REACTION(KW)	0.
FUEL STACK AXIAL EXTENSION (MM)	3.247E+01
CLADDING AXIAL EXTENSION (MM)	-1.588E+01
PLENUM GAS TEMPERATURE (K)	735.9
PLENUM GAS PRESSURE (N/M**2)	.6090E+07
GAS FLOW RATE FROM PLENUM (GM-MOLES/SEC)	-.3415E-10
FRACTION OF MOLTEN FUEL IN FUEL ROD	0.0000
FRACTION OF FUEL RODS FAILED	.7401E+00
MODE OF FUEL ROD FAILURE	E

TOTAL FREE GAS VOLUME(M**3)	.4165356+05
PLENUM VOLUME FRACTION	.143161
CRACK VOLUME FRACTION	.004321
GAP VOLUME FRACTION	.774828
OPEN POROSITY VOLUME FRACTION	.018359
DISH VOLUME FRACTION	.053510

AXIAL NODE NUMBER	1	2	3	4	5	6
ELEVATION (M)	.152	.457	.762	1.067	1.295	1.448
LOCAL FUEL ROD POWER (KW/M)	1.348E+00	2.763E+00	3.548E+00	3.954E+00	4.031E+00	3.956E+00
AVERAGE FUEL ENTHALPY (JOU/KG)	174083.9	268864.1	315519.6	340751.2	345399.7	343287.2
FUEL CENTERLINE TEMPERATURE (K)	930.5	1285.7	1474.9	1569.9	1587.2	1579.3
GAS GAP TEMPERATURE (K)	885.1	1143.3	1244.6	1306.3	1317.5	1312.5
FUEL ROD SURFACE TEMPERATURE (K)	881.3	1133.4	1221.8	1276.0	1285.9	1281.4
COOLANT BULK TEMPERATURE (K)	985.2	985.2	985.2	985.2	985.2	985.2
COOLANT QUALITY	0.	0.	0.	0.	0.	0.
COOLANT MASS FLUX (KG/SEC-M2)	0.	0.	0.	0.	0.	0.
SURFACE HEAT FLUX (WATT/M**2)	-5.219E+03	7.467E+03	1.192E+04	1.465E+04	1.515E+04	1.493E+04
CRITICAL HEAT FLUX (WATT/M**2)	-3.155E+00	-3.155E+00	-3.155E+00	-3.155E+00	-3.155E+00	-3.155E+00
SURFACE HEAT TRANSFER COEF (WATT/M**2.K)	5.039E+01	5.039E+01	5.039E+01	5.039E+01	5.039E+01	5.039E+01
HEAT TRANSFER MODE	1	1	1	1	1	1
GAP HEAT TRANSFER COEF (WATT/M**2.K)	3.139E+03	4.162E+03	2.509E+03	1.695E+03	1.642E+03	1.659E+03
THERMAL RADIAL GAS GAP (MM)	.0863	.1027	.2461	.7165	.9704	.8133
STRUCTURAL RADIAL GAS GAP (MM)	.0863	.1027	.2461	.7155	.9704	.8133
GAS PRESSURE (N/M**2)	6.690E+06	6.690E+06	6.690E+06	6.690E+06	6.690E+06	6.690E+06
COOLANT PRESSURE(N/M**2)	6.700E+06	6.700E+06	6.700E+06	6.700E+06	6.700E+06	6.700E+06
RELOCATION OF FUEL OUTER SURFACE (MM)	2.540E-02	4.826E-02	5.177E-02	5.695E-02	5.792E-02	5.754E-02
DISPLACEMENT OF CLAD OUTER SURFACE (MM)	2.554E-02	9.957E-02	1.878E-01	2.600E-01	2.752E-01	2.692E-01
CLADDING HOOP STRAIN (TOTAL)	4.778E-03	9.445E-03	3.035E-02	1.200E-01	1.763E-01	1.503E-01
CLADDING MECHANICAL HOOP STRAIN	0.	1.075E-03	3.202E-02	1.220E-01	1.700E-01	1.441E-01
CLADDING MECHANICAL AXIAL STRAIN	0.	-5.084E-04	-8.100E-03	-2.865E-02	-3.841E-02	-3.324E-02
CLADDING MAXIMUM LOCALIZED HOOP STRAIN	0.	1.075E-03	3.202E-02	1.220E-01	1.700E-01	1.441E-01
INTERFACE PRESSURE, THERMAL GAP(N/M**2)	0.	0.	0.	0.	0.	0.
INTERFACE PRESSURE, STRUCT. GAP(N/M**2)	0.	0.	0.	0.	0.	0.
CLADDING HOOP STRESS (N/M**2)	1.059E+07	1.074E+07	1.159E+07	1.433E+07	1.581E+07	1.522E+07
CLADDING AXIAL STRESS (N/M**2)	5.023E+06	2.550E+06	2.973E+06	4.325E+06	5.070E+06	4.775E+06
EFFECTIVE CLADDING STRESS (N/M**2)	9.674E+06	9.720E+06	1.043E+07	1.271E+07	1.395E+07	1.332E+07
CLADDING TOTAL STRESSES (N/M**2)	9.902E+07	9.816E+06	9.838E+06	1.159E+07	1.395E+07	1.332E+07
CLADDING STRESS INTENSITY STRAIN(N/M**	5.771E+07	9.800E+06	9.874E+06	1.171E+07	1.395E+07	1.332E+07
CLADDING EFFECTIVE PLASTIC STRAIN	0.	2.083E-03	3.330E-02	1.276E-01	1.788E-01	1.550E-01
CLADDING INSTABILITY STRAIN	1.783E-01	2.253E-01	1.200E-01	1.876E-01	2.900E-01	9.950E-01
METAL-WATER REACTION DEPTH (MM)	0.	0.	0.	0.	0.	0.
METAL-WATER REACTION ENERGY (KW/M)	0.	0.	0.	0.	0.	0.

TEMPERATURES BY RADIAL MESH POINTS

NO.	MESH RADIUS (MM)	TEMPERATURES (K)					
1	0	930.5	1285.7	1474.9	1569.9	1587.2	1579.3
2	4.648E-01	929.7	1283.3	1471.3	1565.7	1582.9	1575.0
3	9.295E-01	927.5	1276.5	1460.7	1553.7	1570.3	1562.6
4	1.394E+00	924.0	1266.5	1443.8	1535.7	1550.6	1543.1
5	1.859E+00	919.5	1253.8	1421.7	1512.1	1526.3	1518.8
6	2.324E+00	914.1	1238.7	1395.8	1484.7	1497.7	1490.3
7	2.788E+00	908.3	1222.7	1367.7	1455.1	1467.9	1460.5
8	3.253E+00	902.5	1206.8	1339.6	1425.5	1438.1	1430.8
9	3.718E+00	897.1	1192.0	1313.6	1397.9	1410.2	1402.9
10	4.183E+00	892.4	1179.2	1291.0	1374.0	1385.9	1378.7
11	4.648E+00	888.6	1168.8	1272.9	1354.9	1366.4	1359.2
12	5.113E+00	885.7	1160.9	1259.1	1340.3	1351.5	1344.3
13	5.578E+00	883.6	1155.2	1249.2	1329.8	1340.8	1333.6
14	6.043E+00	882.3	1151.7	1243.1	1323.3	1334.2	1327.0
15	6.508E+00	881.8	1150.4	1240.9	1320.9	1331.8	1324.6
16	6.973E+00	881.3	1149.1	1238.7	1318.6	1329.4	1322.2
17	7.438E+00	881.3	1149.1	1238.7	1318.6	1329.4	1322.2

FRAP-T MOD109 VER04/28 FUEL ROD ANALYSIS PROGRAM • 04/28/77 • EG&G MATPRO MODULE MOD009

AXIAL NODE NUMBER	7	8	9	10	11	12
ELEVATION (M)	1.800	1.753	1.805	2.057	2.210	2.362
LOCAL FUEL ROD POWER (KW/M)	3.905E+00	3.789E+00	3.649E+00	3.466E+00	3.303E+00	3.092E+00
AVERAGE FUEL ENTHALPY (JOU/KG)	337601.0	330617.5	322125.0	312334.9	301451.1	288338.8
FUEL CENTERLINE TEMPERATURE (K)	1558.5	1532.1	1499.8	1461.7	1418.1	1364.7
G.S GAP TEMPERATURE (K)	1298.7	1281.2	1260.6	1237.6	1213.7	1186.2
FUEL ROD SURFACE TEMPERATURE (K)	1269.2	1253.7	1235.7	1215.7	1195.5	1172.4
COOLANT BULK TEMPERATURE(K)	985.2	985.2	985.2	985.2	985.2	985.2
COOLANT QUALITY	0.	0.	0.	0.	0.	0.
COOLANT MASS FLUX,KG/SEC-M2	0.	0.	0.	0.	0.	0.
SURFACE HEAT FLUX (WATT/M**2)	1.431E+04	1.393E+04	1.282E+04	1.162E+04	1.050E+04	9.433E+0
CRITICAL HEAT FLUX (WATT/M**2)	-3.155E+00	-3.155E+00	-3.155E+00	-3.155E+00	-3.155E+00	-3.155E+0
SURFACE HEAT TRANSFER COEF. (WATT/M**2.K)	5.039E+01	5.039E+01	5.039E+01	5.039E+01	5.039E+01	5.039E+0
HEAT TRANSFER MODE	1	1	1	1	1	1
GAP HEAT TRANSFER COEF. (WATT/M**2.K)	1.760E+03	1.944E+03	2.234E+03	2.626E+03	3.120E+03	3.761E+0
THERMAL RADIAL GAS GAP (MM)	.5080	.4388	.3118	.2248	.1664	.1234
STRUCTURAL RADIAL GAS GAP (MM)	.6080	.4388	.3118	.2248	.1664	.1234
GAP PRESSURE (N/M**2)	6.690E+06	6.690E+06	6.690E+06	6.690E+06	6.690E+06	6.690E+0
COOLANT PRESSURE(N/M**2)	6.709E+06	6.709E+06	6.709E+06	6.709E+06	6.709E+06	6.709E+0
RELOCATION OF FUEL OUTER SURFACE (MM)	5.611E-03	5.406E-02	5.311E-02	5.110E-02	4.687E-02	4.221E-0
RELOCATION OF CLAD OUTER SURFACE (MM)	5.211E-01	3.662E-01	2.488E-01	1.675E-01	1.130E-01	7.174E-0
CLADDING T.W STRAIN (INCREASE)	1.075E-01	7.509E-02	5.092E-02	3.411E-02	2.267E-02	1.490E-0
CLADDING PERMANENT HOOP STRAIN	1.014E-01	6.923E-02	4.488E-02	2.776E-02	1.580E-02	8.803E-0
CLADDING PERMANENT AXIAL STRAIN	-2.428E-02	-1.703E-02	-1.125E-02	-7.046E-03	-4.034E-03	-1.740E-0
CLADDING MAXIMUM LOCALIZED HOOP STRAIN	1.014E-01	6.923E-02	4.488E-02	2.776E-02	1.580E-02	8.803E-0
INTERFACE PRESSURE, THERMAL GAP(N/M**2)	0.	0.	0.	0.	0.	0.
INTERFACE PRESSURE, STRUCT. GAP(N/M**2)	0.	0.	0.	0.	0.	0.
CLADDING HOOP STRESS (N/M**2)	1.385E+07	1.268E+07	1.130E+07	1.147E+07	1.113E+07	1.088E+0
CLADDING AXIAL STRESS (N/M**2)	4.000E+06	3.517E+06	3.150E+06	2.914E+06	2.744E+06	2.615E+0
EFFECTIVE CLADDING STRESS (N/M**2)	1.215E+07	1.134E+07	1.074E+07	1.033E+07	1.001E+07	9.727E+0
CLADDING YIELD STRESS(N/M**2)	1.134E+07	1.038E+07	9.824E+06	9.526E+06	9.290E+06	9.100E+0
CLADDING STRESS FOR INSTABILITY STRAIN(N/M**	1.145E+07	1.059E+07	1.013E+07	9.811E+06	9.568E+06	9.369E+0
CLADDING EFFECTIVE PLASTIC STRAIN	1.000E-01	1.059E+07	4.669E-02	2.647E-02	1.642E-02	9.668E-0
CLADDING INSTABILITY STRAIN	1.754E-01	1.602E-01	1.381E-01	1.135E-01	8.965E-02	7.010E-0
METAL-WATER REACTION DEPTH (MM)	0.	0.	0.	0.	0.	0.
METAL-WATER REACTION ENERGY (KW/M)	0.	0.	0.	0.	0.	0.

TEMPERATURES BY RADIAL MESH POINTS

NO.	MESH RADIUS (MM)	TEMPERATURES (K)					
1	0.	1558.5	1532.1	1499.8	1461.7	1418.1	1364.7
2	4.688E-01	1554.4	1529.1	1496.2	1458.2	1414.9	1361.9
3	9.288E-01	1542.2	1516.4	1485.0	1447.9	1405.5	1353.5
4	1.394E+00	1522.9	1497.9	1467.4	1431.5	1389.9	1338.5
5	1.859E+00	1497.7	1473.6	1444.5	1409.0	1368.3	1318.2
6	2.324E+00	1468.2	1444.3	1417.5	1383.2	1343.9	1295.3
7	2.789E+00	1435.5	1414.7	1388.4	1355.8	1318.0	1271.9
8	3.254E+00	1402.3	1384.0	1358.8	1328.0	1291.5	1248.2
9	3.719E+00	1374.4	1357.2	1333.0	1305.1	1270.1	1228.4
10	4.184E+00	1348.0	1332.0	1309.1	1283.7	1249.0	1208.0
11	4.649E+00	1328.0	1312.7	1290.0	1265.1	1231.1	1191.2
12	5.114E+00	1320.0	1305.0	1282.4	1258.0	1224.5	1185.0
13	5.579E+00	1320.0	1305.0	1282.4	1258.0	1224.5	1185.0
14	5.580E+00	1320.0	1305.0	1282.4	1258.0	1224.5	1185.0

AXIAL NODE NUMBER	13	14	15	16
ELEVATION (M)	2.591	2.896	3.200	3.505
LOCAL FUEL ROD POWER (KW/M)	2.735E+00	2.227E+00	1.609E+00	8.230E-01
AVERAGE FUEL ENTHALPY (JOU/KG)	267492.0	232330.6	190350.2	136391.6
FUEL CENTERLINE TEMPERATURE (K)	1279.5	1147.4	991.4	795.4
GAS GAP TEMPERATURE (K)	1140.4	1050.3	931.3	772.3
FUEL ROD SURFACE TEMPERATURE (K)	1130.7	1044.5	926.5	770.4
COOLANT BULK TEMPERATURE (K)	985.2	985.2	965.2	985.2
COOLANT QUALITY	0.	0.	0.	0
COOLANT MASS FLUX, KG/SEC-M2	0.	0.	0.	0.
SURFACE HEAT FLUX (WATT/M**2)	7.325E+03	2.985E+03	-2.961E+03	-1.082E+04
CRITICAL HEAT FLUX (WATT/M**2)	-3.155E+00	-3.155E+00	-3.155E+00	-3.155E+00
SURFACE HEAT TRANSFER COEF. (WATT/M**2.K)	5.039E+01	5.039E+01	5.039E+01	5.039E+01
HEAT TRANSFER MODE	1	1	1	1
GAP HEAT TRANSFER COEF. (WATT/M**2.K)	4.166E+03	4.020E+03	3.265E+03	2.843E+03
THERMAL RADIAL GAS GAP (MM)	.1022	.0958	.0862	.0853
STRUCTURAL RADIAL GAS GAP (MM)	.1022	.0958	.0862	.0853
GAP PRESSURE (N/M**2)	6.690E+06	6.690E+06	6.690E+06	6.690E+06
COOLANT PRESSURE(N/M**2)	4.709E+06	4.709E+06	4.709E+06	4.709E+06
RMS DISPLT. OF FUEL OUTER SURFACE (MM)	4.296E-02	3.553E-02	2.819E-02	1.947E-02
DISPLACEMENT OF CLAD OUTER SURFACE (MM)	4.870E-02	3.625E-02	2.845E-02	1.872E-02
CLADDING HOOP STRAIN (MIDPLANE)	9.302E-03	6.780E-03	5.323E-03	3.505E-03
CLADDING PERMANENT HOOP STRAIN	1.827E-03	0.	0.	0.
CLADDING PERMANENT AXIAL STRAIN	-4.704E-04	0.	0.	0.
CLADDING MAXIMUM LOCALIZED HOOP STRAIN	1.027E-03	0.	0.	0.
INTERFACE PRESSURE, RADIAL GAP(N/M**2)	0.	0.	0.	0.
INTERFACE PRESSURE, AXIAL GAP(N/M**2)	0	0.	0.	0.
CLADDING HOOP STRESS (N/M**2)	1.079E+07	1.060E+07	1.069E+07	1.068E+07
CLADDING AXIAL STRESS (N/M**2)	2.568E+06	2.523E+06	2.523E+06	2.522E+06
EFFECTIVE CLADDING STRESS (N/M**2)	9.716E+06	9.575E+06	9.674E+06	9.657E+06
CLADDING YIELD STRESS(N/M**2)	9.725E+06	9.004E+06	2.089E+07	1.192E+09
CLAD STRESS AT INSTABILITY STRAIN(N/M**	9.099E+06	1.109E+07	3.528E+07	1.649E+09
CLADDING EFFECTIVE PLASTIC STRAIN	1.693E-03	0.	0.	0.
CLADDING INSTABILITY STRAIN	2.316E-01	2.109E-01	1.888E-01	1.553E-01
METAL-WATER REACTION DEPTH (MM)	0.	0.	0.	0.
METAL-WATER REACTION ENERGY (KW/M)	0.	0.	0.	0.

TEMPERATURES BY RADIAL MESH POINTS

NO.	MESH RADIUS (MM)	TEMPERATURES (K)			
1	0	1279.5	1147.4	991.4	795.4
2	4.568E-01	1277.4	1145.7	990.4	795.1
3	1.370E+00	1270.6	1140.8	987.4	793.9
4	2.283E+00	1259.9	1132.0	982.7	792.1
5	3.196E+00	1246.9	1122.6	976.6	790.1
6	4.109E+00	1229.7	1110.7	969.5	788.9
7	5.022E+00	1212.1	1098.0	961.8	788.9
8	5.935E+00	1196.5	1087.2	955.0	790.9
9	6.848E+00	1177.3	1073.4	946.8	793.1
10	7.761E+00	1162.0	1063.3	940.5	795.8
11	8.674E+00	1149.1	1055.6	935.7	797.1
12	9.587E+00	1141.7	1049.1	931.8	797.4
13	1.050E+01	1134.3	1044.6	929.3	797.3
14	1.141E+01	1130.7	1044.5	929.3	797.4

COOLANT CONDITIONS AT TIME = .10500E+02 SEC

ELEVATION(M)	COOLANT TEMPERATURE(K)	PRESSURE(N/M**2)
.1524E+00	.7622E+03	.4303E+07
.4572E+00	.7622E+03	.4303E+07
.7620E+00	.7622E+03	.4303E+07
.1067E+01	.7622E+03	.4303E+07
.1206E+01	.7622E+03	.4303E+07
.1448E+01	.7622E+03	.4303E+07
.1600E+01	.7622E+03	.4303E+07
.1753E+01	.7622E+03	.4303E+07
.1905E+01	.7622E+03	.4303E+07
.2057E+01	.7622E+03	.4303E+07
.2210E+01	.7622E+03	.4303E+07
.2362E+01	.7622E+03	.4303E+07
.2515E+01	.7622E+03	.4303E+07
.2667E+01	.7622E+03	.4303E+07
.3200E+01	.7622E+03	.4303E+07
.3505E+01	.7622E+03	.4303E+07

FUEL ROD CONDITIONS AT TIME = 10.5000 SEC

ROD NUMBER 1 NUMBER OF ITERATIONS REQUIRED FOR CONVERGENCE = 2 ACCUMULATED CPU TIME =

AVERAGE FUEL ROD POWER (KW/M)	3.268E+00
ENERGY GENERATED BY METAL-WATER REACTION(KW)	0.
FUEL STACK AXIAL EXTENSION (MM)	3.257E+01
CLADDING AXIAL EXTENSION (MM)	-2.294E+01
PLENUM GAS TEMPERATURE (K)	891.1
PLENUM GAS PRESSURE (N/M**2)	.4303E+07
GAS FLOW RATE FROM PLENUM (GM-MOLES/SEC)	0.
FRACTION OF MOLTEN FUEL IN FUEL ROD	0.0000
FRACTION OF FUEL RODS FAILED	.1000E+01
MODE OF FUEL ROD FAILURE	7
TOTAL FREE GAS VOLUME(MM) **3	.465793E+05
PLENUM VOLUME FRACTION	.117670
CRACK VOLUME FRACTION	.003425
GAP VOLUME FRACTION	.000119
OPEN POROSITY VOLUME FRACTION	.012041
DISH VOLUME FRACTION	.055056

PEAK CLADDING OUTSIDE RADIUS AT BALLOON POINT (MM) = .9294 4E+01 ELEVATION = .1205 E+01 M)

**** FAILURE PREDICTED 1.205 M) FROM BOTTOM OF ROD ****

FRAP-T MOD008 VER04/28 FUEL ROD ANALYSIS PROGRAM • 04/28/77 • EG&G MATPRO MODULE MOD008

AXIAL NODE NUMBER	1	2	3	4	5	6
ELEVATION (M)	.152	.457	.762	1.067	1.295	1.449
LOCAL FUEL ROD POWER (KW/M)	1.581E+00	3.197E+00	4.103E+00	4.576E+00	4.564E+00	4.624
AVERAGE FUEL ENTHALPY (JOU/KG)	174748.5	269282.7	315854.5	341548.7	346226.8	344077.8
FUEL CENTERLINE TEMPERATURE (K)	925.3	1273.9	1457.5	1550.7	1567.7	1559.9
GAS GAP TEMPERATURE (K)	885.6	1145.7	1249.2	1307.8	1318.8	1313.8
FUEL ROD SURFACE TEMPERATURE (K)	883.6	1129.9	1219.4	1263.9	1273.3	1269.0
COOLANT BULK TEMPERATURE (K)	762.2	762.2	762.2	762.2	762.2	762.2
COOLANT QUALITY	0.	0.	0.	0.	0.	0.
COOLANT MASS FLUX,KG/SEC-M2	0.	0.	0.	0.	0.	0.
SURFACE HEAT FLUX (WATT/M**2)	5.854E+04	1.803E+05	2.237E+05	2.460E+05	2.505E+05	2.486
CRITICAL HEAT FLUX (WATT/M**2)	-3.155E+00	-3.155E+00	-3.155E+00	-3.155E+00	-3.155E+00	-3.155
SURFACE HEAT TRANSFER COEF. (WATT/M**2.K)	4.905E+02	4.905E+02	4.905E+02	4.905E+02	4.905E+02	4.905
HEAT TRANSFER MODE	1	1	1	1	1	1
GAP HEAT TRANSFER COEF. (WATT/M**2.K)	3.171E+03	4.178E+03	2.459E+03	1.575E+03	1.624E+03	1.654
THERMAL RADIAL GAS GAP (MM)	.0957	.1027	.2584	.8138	1.5297	.975
STRUCTURAL RADIAL GAS GAP (MM)	.0957	.1027	.2584	.8138	1.5297	.975
GAP PRESSURE (N/M**2)	4.303E+06	4.303E+06	4.303E+06	4.303E+06	4.303E+06	4.303
COOLANT PRESSURE(N/M**2)	4.303E+06	4.303E+06	4.303E+06	4.303E+06	4.303E+06	4.303
PEAK DISPLT. OF FUEL OUTER SURFACE (MM)	2.847E-02	4.219E-02	5.140E-02	5.867E-02	5.764E-02	5.715
DISPLACEMENT OF CLAD OUTER SURFACE (MM)	2.492E-02	4.609E-02	1.043E-01	7.027E-01	1.360E+00	8.477
CLADDING HOOP STRAIN (MIDPLANE)	4.651E-03	9.384E-03	4.609E-02	1.492E-01	2.819E-01	1.783
CLADDING DIFFERENT HOOP STRAIN	0.	2.126E-03	3.409E-02	1.404E-01	2.759E-01	1.704
CLADDING DIFFERENT AXIAL STRAIN	0.	-5.581E-04	-8.712E-03	-3.307E-02	-8.156E-02	-3.921
CLADDING MAXIMUM LOCALIZED HOOP STRAIN	0.	2.126E-03	3.409E-02	1.404E-01	2.759E-01	1.704
INTERFACE PRESSURE, THERMAL GAP(N/M**2)	0.	0.	0.	0.	0.	0.
INTERFACE PRESSURE, STRUCT. GAP(N/M**2)	0.	0.	0.	0.	0.	0.
CLADDING HOOP STRESS (N/M**2)	-4.303E+06	-4.303E+06	-4.303E+06	-4.303E+06	-4.303E+06	-4.303
CLADDING AXIAL STRESS (N/M**2)	-4.303E+06	-4.303E+06	-4.303E+06	-4.303E+06	-4.303E+06	-4.303
EFFECTIVE CLADDING STRESS (N/M**2)	0.	0.	0.	0.	0.	0.
CLADDING YIELD STRESS(N/M**2)	0.	0.	0.	0.	0.	0.
CLAD STRESS AT INSTABILITY STRAIN(N/M**	0.	0.	0.	0.	0.	0.
CLADDING EFFECTIVE PLASTIC STRAIN	0.	0.	0.	0.	0.	0.
CLADDING INSTABILITY STRAIN	0.	0.	0.	0.	0.	0.
METAL-WATER REACTION DEPTH (MM)	0.	0.	0.	0.	0.	0.
METAL-WATER REACTION ENERGY (KW/M)	0.	0.	0.	0.	0.	0.

TEMPERATURES BY RADIAL MESH POINTS

NO.	MESH RADIUS (MM)	TEMPERATURES (K)					
1	0.	925.3	1273.9	1457.5	1550.7	1567.7	1559.9
2	4.658E-01	885.6	1271.9	1456.4	1549.7	1566.7	1558.9
3	9.690E-01	884.1	1265.2	1446.4	1536.8	1553.1	1545.5
4	1.356E+00	881.4	1257.2	1438.9	1531.7	1548.1	1540.5
5	1.882E+00	877.9	1245.5	1426.1	1517.8	1534.1	1526.6
6	2.826E+00	873.9	1231.7	1410.2	1502.7	1518.8	1511.2
7	3.771E+00	869.5	1216.9	1393.5	1484.7	1500.8	1493.2
8	4.715E+00	864.3	1201.3	1376.4	1466.7	1482.8	1475.2
9	5.659E+00	859.3	1187.0	1359.1	1448.7	1464.8	1457.2
10	6.603E+00	854.7	1172.6	1342.7	1430.7	1446.8	1439.2
11	7.547E+00	850.2	1157.8	1325.7	1412.7	1428.8	1421.2
12	8.491E+00	845.9	1143.5	1309.3	1394.7	1410.8	1403.2
13	9.435E+00	841.4	1132.0	1295.7	1380.3	1396.4	1389.0
14	9.812E+00	839.8	1128.9	1291.4	1375.9	1391.9	1384.8

FRAP-T MOD009 VER04/28 FUEL ROD ANALYSIS PROGRAM • 04/28/77 • EG&G MATPRO MODULE MOD008

AXIAL NODE NUMBER	7	8	9	10	11	12
ELEVATION (M)	1.600	1.753	1.905	2.057	2.210	2.362
LOCAL FUEL ROD POWER (KW/M)	4.518E+00	4.384E+00	4.222E+00	4.034E+00	3.821E+00	3.565E+00
AVERAGE FUEL ENTHALPY (J/KG)	338446.4	331252.3	322528.9	312619.0	301626.3	288551.0
FUEL CENTERLINE TEMPERATURE (K)	1530.5	1513.5	1481.9	1444.8	1402.4	1350.6
GAS GAP TEMPERATURE (K)	1300.6	1284.3	1264.6	1242.1	1218.0	1189.9
FUEL ROD SURFACE TEMPERATURE (K)	1257.9	1245.4	1230.4	1212.6	1193.7	1170.3
COOLANT BULK TEMPERATURE(K)	762.2	762.2	762.2	762.2	762.2	762.2
COOLANT QUALITY	0.	0.	0.	0.	0.	0.
COOLANT MASS FLUX,KG/SEC-M2	0.	0.	0.	0.	0.	0.
SURFACE HEAT FLUX (WATT/M**2)	2.431E+05	2.370E+05	2.295E+05	2.210E+05	2.118E+05	2.001E+05
CRITICAL HEAT FLUX (WATT/M**2)	-3.155E+00	-3.155E+00	-3.155E+00	-3.155E+00	-3.155E+00	-3.155E+00
SURFACE HEAT TRANSFER COEF. (WATT/M**2.K)	4.905E+02	4.905E+02	4.905E+02	4.905E+02	4.905E+02	4.905E+02
HEAT TRANSFER MODE	1	1	1	1	1	1
GAP HEAT TRANSFER COEF. (WATT/M**2.K)	1.720E+03	1.905E+03	2.186E+03	2.532E+03	3.023E+03	3.743E+03
THERMAL RADIAL GAS GAP (MM)	.6600	.4760	.3320	.2348	.1705	.1250
STRUCTURAL RADIAL GAS GAP (MM)	.6300	.4760	.3320	.2348	.1705	.1250
GAP PRESSURE (N/M**2)	4.303E+06	4.303E+06	4.303E+06	4.303E+06	4.303E+06	4.303E+06
COOLANT PRESSURE(N/M**2)	4.303E+06	4.303E+06	4.303E+06	4.303E+06	4.303E+06	4.303E+06
BEAM DISPLT. OF FUEL OUTER SURFACE (MM)	5.603E-02	5.457E-02	5.282E-02	5.089E-02	4.850E-02	5.540E-02
DISPLACEMENT OF CLAD OUTER SURFACE (MM)	5.727E-01	3.920E-01	2.612E-01	1.728E-01	1.142E-01	7.188E-02
CLADDING HOOP STRAIN (MIDPLANE)	1.202E-01	8.148E-02	5.412E-02	3.556E-02	2.316E-02	1.423E-02
CLADDING PERMANENT HOOP STRAIN	1.144E-01	7.573E-02	4.629E-02	2.593E-02	1.654E-02	7.173E-03
CLADDING PERMANENT AXIAL STRAIN	-2.753E-02	-1.878E-02	-1.223E-02	-7.543E-03	-4.260E-03	-1.859E-03
CLADDING MAXIMUM LOCALIZED HOOP STRAIN	1.144E-01	7.573E-02	4.829E-02	2.943E-02	1.854E-02	7.173E-03
INTERFACE PRESSURE, THERMAL GAP(N/M**2)	0.	0.	0.	0.	0.	0.
INTERFACE PRESSURE, STRUCT. GAP(N/M**2)	0.	0.	0.	0.	0.	0.
CLADDING HOOP STRESS (N/M**2)	-4.303E+06	-4.303E+06	-4.303E+06	-4.303E+06	-4.303E+06	-4.303E+06
CLADDING AXIAL STRESS (N/M**2)	-4.303E+06	-4.303E+06	-4.303E+06	-4.303E+06	-4.303E+06	-4.303E+06
EFFECTIVE CLADDING STRESS (N/M**2)	0.	0.	0.	0.	0.	0.
CLADDING YIELD STRESS(N/M**2)	0.	0.	0.	0.	0.	0.
CLAD STRESS AT INSTABILITY STRAIN(N/M**	0.	0.	0.	0.	0.	0.
CLADDING EFFECTIVE PLASTIC STRAIN	0.	0.	0.	0.	0.	0.
CLADDING INSTABILITY STRAIN	0.	0.	0.	0.	0.	0.
METAL-WATER REACTION DEPTH (MM)	0.	0.	0.	0.	0.	0.
METAL-WATER REACTION ENERGY (KW/M)	0.	0.	0.	0.	0.	0.

TEMPERATURES BY RADIAL MESH POINTS

NO.	MESH RADIUS (MM)	TEMPERATURES (K)					
1	0	1539.5	1513.5	1481.9	1444.8	1402.4	1350.6
2	4.849E-01	1535.9	1510.1	1478.7	1441.8	1399.7	1348.2
3	9.698E-01	1525.5	1500.1	1468.3	1433.0	1391.7	1341.1
4	1.454E+00	1509.0	1484.3	1454.3	1419.0	1379.3	1330.3
5	1.939E+00	1487.5	1463.6	1434.7	1400.6	1360.3	1312.3
6	2.424E+00	1462.7	1439.7	1411.9	1379.4	1340.8	1293.8
7	2.909E+00	1434.1	1414.0	1387.3	1355.4	1317.6	1271.8
8	3.394E+00	1403.5	1386.2	1362.5	1332.8	1294.8	1250.2
9	3.879E+00	1369.3	1353.5	1336.0	1310.0	1272.8	1229.0
10	4.363E+00	1331.1	1340.7	1316.2	1288.3	1251.6	1208.4
11	4.848E+00	1333.9	1318.9	1297.0	1267.3	1231.2	1188.5
12	5.333E+00	1282.3	1249.7	1234.6	1217.0	1182.7	1141.4
13	5.818E+00	1269.4	1247.9	1232.8	1215.2	1181.0	1139.8
14	6.303E+00	1257.9	1245.4	1230.4	1212.6	1178.5	1137.3

AXIAL NODE NUMBER	13	14	15	16
ELEVATION (M)	2.591	2.896	3.200	3.505
LOCAL FUEL ROD POWER (KW/M)	3.165E+00	2.577E+00	1.961E+00	9.922E-01
AVERAGE FUEL ENTHALPY (JOU/KG)	267905.5	233008.4	191082.7	137054.2
FUEL CENTERLINE TEMPERATURE (K)	1268.1	1138.4	995.7	793.1
GAS GAP TEMPERATURE (K)	1142.6	1051.2	934.0	780.0
FUEL ROD SURFACE TEMPERATURE (K)	1127.0	1038.8	926.7	779.7
COOLANT BULK TEMPERATURE (K)	762.2	762.2	762.2	762.2
COOLANT QUALITY	0.	0.	0.	0.
COOLANT MASS FLUX, KG/SEC-M2	0.	0.	0.	0.
SURFACE HEAT FLUX (WATT/M**2)	1.708E+05	1.357E+05	8.059E-04	5.590E+03
CRITICAL HEAT FLUX (WATT/M**2)	-3.155E+00	-3.155E+00	-3.155E+00	-3.155E+00
SURFACE HEAT TRANSFER COEF. (WATT/M**2.K)	4.905E+02	4.905E+02	4.905E+02	4.905E+02
HEAT TRANSFER MODE	1	1	1	1
GAP HEAT TRANSFER COEF. (WATT/M**2.K)	4.180E+03	4.073E+03	3.309E+03	2.869E+03
THERMAL RADIAL GAS GAP (MM)	.1022	.0918	.0954	.0950
STRUCTURAL RADIAL GAS GAP (MM)	.1022	.0946	.0956	.0950
GAP PRESSURE (N/M**2)	4.303E+06	4.303E+06	4.303E+06	4.303E+06
COOLANT PRESSURE (N/M**2)	4.303E+06	4.303E+06	4.303E+06	4.303E+06
PEAK DISPLT. OF FUEL OUTER SURFACE (MM)	4.101E-02	3.546E-02	2.610E-02	1.051E-02
DISPLACEMENT OF CLAD OUTER SURFACE (MM)	4.089E-02	3.501E-02	2.768E-02	1.645E-02
CLADDING HOOP STRAIN (MIDPLANE)	9.237E-03	6.534E-03	5.165E-03	3.481E-03
CLADDING PERMANENT HOOP STRAIN	1.973E-03	0.	0.	0.
CLADDING PERMANENT AXIAL STRAIN	-5.184E-04	0.	0.	0.
CLADDING MAXIMUM LOCALIZED HOOP STRAIN	1.973E-03	0.	0.	0.
INTERFACE PRESSURE, THERMAL GAP(N/M**2)	0.	0.	0.	0.
INTERFACE PRESSURE, STRUCT. GAP(N/M**2)	0.	0.	0.	0.
CLADDING HOOP STRESS (N/M**2)	-4.303E+06	-4.303E+06	-4.303E+06	-4.303E+06
CLADDING AXIAL STRESS (N/M**2)	-4.303E+06	-4.303E+06	-4.303E+06	-4.303E+06
EFFECTIVE CLADDING STRESS (N/M**2)	0.	0.	0.	0.
CLADDING YIELD STRESS(N/M**2)	0.	0.	0.	0.
CLAD STRESS AT INSTABILITY STRAIN(N/M**	0.	0.	0.	0.
CLADDING EFFECTIVE PLASTIC STRAIN	0.	0.	0.	0.
CLADDING INSTABILITY STRAIN	0.	0.	0.	0.
METAL-WATER REACTION DEPTH (MM)	0.	0.	0.	0.
METAL-WATER REACTION ENERGY (KW/M)	0.	0.	0.	0.

TEMPERATURES BY RADIAL MESH POINTS

NO.	MESH RADIUS (MM)	TEMPERATURES (K)			
1	0.	1268.1	1139.4	995.7	793.1
2	4.648E-01	1266.2	1137.0	995.0	792.9
3	9.295E-01	1260.6	1133.1	992.7	792.0
4	1.394E+00	1251.0	1126.8	979.0	790.7
5	1.859E+00	1240.3	1119.7	974.3	789.0
6	2.324E+00	1228.9	1109.3	969.8	787.0
7	2.788E+00	1212.4	1099.3	963.0	785.0
8	3.254E+00	1197.6	1068.3	957.1	783.1
9	3.719E+00	1183.1	1079.7	951.6	781.5
10	4.183E+00	1168.0	1070.5	946.5	780.5
11	4.648E+00	1154.6	1060.8	941.4	780.2
12	4.747E+00	1130.6	1041.7	930.5	779.9
13	5.053E+00	1129.1	1040.5	927.0	779.8
14	5.358E+00	1127.0	1038.8	926.7	779.7

APPENDIX C

CALCULATIONS OF CLADDING SURFACE TEMPERATURE

APPENDIX C

CALCULATION OF CLADDING SURFACE TEMPERATURE

As shown in the HEAT-1 program report, the numerical solution of the heat conduction equation [Equation (1)] reduces to solving a set of tridiagonal equations. This set of equations is shown below.

$$\begin{vmatrix} b_1 & C_1 & 0 & 0 & & \\ a_2 & b_2 & C_2 & 0 & & 0's \\ 0 & a_3 & b_3 & C_3 & & \\ . & . & . & . & & . \\ . & . & . & . & & . \\ & 0's & a_{n-1} & b_{n-1} & & C_{n-1} \\ & & & a_n & & b_n \end{vmatrix} \begin{vmatrix} T_1^{m+1} \\ T_2^{m+1} \\ T_3^{m+1} \\ . \\ . \\ T_{n-1}^{m+1} \\ T_n^{m+1} \end{vmatrix} = \begin{vmatrix} d_1 \\ d_2 \\ d_3 \\ . \\ . \\ d_{n-1} \\ d_n \end{vmatrix} \qquad \text{(C-1)}$$

where a_n, b_n, c_n, d_n are terms in finite difference form of heat conduction equation at n^{th} mesh point.

T_n^{m+1} = temperature at n^{th} mesh point at time step m+1

n = number of mesh point at outer surface.

The mesh point temperatures are solved by the Gaussian elimination method.

$$T_n^{m+1} = (d_n - a_n F_{n-1})/(b_n - a_n E_{n-1})$$

$$T_j^{m+1} = -E_j T_{j+1}^{m+1} + F_j \text{ for } j = n-1, n-2, \ldots 2, 1$$

$$E_1 = C_1/b_1 \text{ and } F_1 = d_1/b_1$$

$$\left.\begin{aligned} E_j &= C_j/(b_j - a_j E_{j-1}) \\ F_j &= (d_j - a_j F_{j-1})/(b_j - a_j E_{j-1}) \end{aligned}\right\} \text{for } j = 2, 3 \ldots n-1 \qquad \text{(C-2)}$$

The next step is to get the equation for surface temperature in the form

$$A_1 T_n^{m+1} + B_1 = \phi^{m+1} \qquad \text{(C-3)}$$

where A_1, B_1 are coefficients

ϕ^{m+1} = surface heat flux at time step m+1

To determine the coefficients A_1 and B_1 in Equation (C-3), the terms in the equation for surface temperature in Equation set (C-2) must be expanded. The expanded form of these terms is as follows:

$$a_n = \frac{-0.5A_{n-1/2}\ K}{\Delta r}$$

$$b_n = \left(\frac{\rho C_p\ \Delta V}{\Delta t} + \frac{0.5A_{n-1/2}\ K}{\Delta r}\right) \qquad \text{(C-4)}$$

$$d_n = \frac{\rho C_p\ \Delta V}{\Delta t}\ T_n^m\ \frac{-0.5A_{n-1/2}\ K}{\Delta r}\ (T_n^m - T_{n-1}^m)$$

$$-0.5A_n\ (\phi^{m+1} + \phi^m) + q^{m+1/2}\ \Delta V$$

$$A_{n-1/2} = 2\pi\ (r_n - \Delta r/2)$$

$$A_n = 2\pi\ r_n$$

$$V = \pi\ (r_n\ \Delta r - \Delta r^2/4)$$

where

K = thermal conductivitiy of material in half mesh interval bordering the surface

C_p = specific heat of material in half mesh interval bordering the surface

ρ = density of material in half mesh interval bordering the surface

r_n = radius to outside surface

Δr = width of mesh interval bordering outside surface

Δt = time step

$\emptyset^m$ = surface heat flux at m^{th} time step

T_n^m = surface temperature at m^{th} time step

$q^{m-1/2}$ = heat generation rate in half mesh interval bordering outside surface (heat generation caused by metal-water reaction).

Equation set (C-4) was derived by finite differencing the energy balance equation for the half mesh interval bordering the outside surface. The continuous form of the energy balance equation for this half mesh interval is

$$\rho C_p \Delta V \frac{\partial t}{\partial t} = -A_{n-1/2} k \frac{\partial t}{\partial t}\Bigg|_{r = r_n - \Delta r/2} - \emptyset A_n + q\Delta V \qquad \text{(C-5)}$$

where all the terms in Equation (C-5) are defined for Equation (C-4).

The finite difference form of Equation (C-5) is

$$\underbrace{\frac{-0.5 A_{n-1/2} k}{\Delta r}}_{a_n} T_{n-1}^{m+1} + \underbrace{\left(\frac{\rho C_p \Delta V}{\Delta t} + \frac{0.5 A_{n-1/2} k}{\Delta r} \right)}_{b_n} T_n^{m+1} \qquad \text{(C-6)}$$

$$= \underbrace{\frac{\rho C_p \Delta V}{\Delta r} T_n^m \frac{-0.5 A_{n-1/2} k}{\Delta r} (T_n^m - T_{n-1}^m) - 0.5 A_n (\emptyset^m + \emptyset^{m+1}) + q^{m+1/2} \Delta V}_{d_n}$$

By use of information in Equations (C-4) and (C-6), the terms in the equation for surface temperature in Equation set (C-2) can be expanded to give the following equations for A_1 and B_1 in Equation (C-3).

$$A_1 = -(b_n - a_n E_{n-1})0.5A_n$$

$$B_1 = -\left[\frac{0.5\,\phi^m A_n + a_n F_{n-1}\,\frac{-\rho C_p}{\Delta t}\,\Delta V T^m_n - a_n (T^m_n - T^m_{n-1}) - q^{m-1/2}\,\Delta V}{0.5A_n}\right]$$

(C-7)

Empirically dervied heat transfer correlations are available from which surface heat flux due to convection can be computed in terms of surface temperature, geometry parameters, and flow conditions. Also, the equation for radiation heat transfer from a surface to surrounding water is known. Thus, the total surface heat flux can be expressed by the equation

$$\phi^{m+1} = f_i\,(C, G, T^{m+1}_n) + \sigma F_A F_E \left[(T^{m+1}_n)^4 - T^4_w\right] \qquad \text{(C-8)}$$

where

ϕ^{m+1} = surface heat flux at time step m+1

f_i = function specifying rate at which heat is transferred from surface by convective heat transfer during heat transfer mode i. These functions are defined in Table IV of the main text.

i = number identification of convective heat transfer mode (nucleate boiling, film boiling, etc.)

C = set of parameters describing coolant conditions

G = set of parameters describing geometry

T_n = Stefan-Boltzmann constant

F_A = configuration factor for radiation heat transfer

F_E = emissivity factor for radiation heat transfer

T_W = bulk temperature of water surrounding fuel rod surface.

Equations (C-3) and (C-8) are two independent equations with unknowns T_n^{m+1} and Q^{m+1}. Simultaneous solution of the two equations yields the new surface temperature T_n^{m+1}.

APPENDIX D

NUMERICAL SOLUTION OF THE PLENUM ENERGY EQUATIONS

APPENDIX D

NUMERICAL SOLUTION OF THE PLENUM ENERGY EQUATIONS

The Crank-Nicolson finite difference form of the six energy equations presented in Section III-1.5 of the main text is

Plenum Gas:

$$\rho_g V_g C_g \frac{(T_g^{m+1} - T_g^m)}{\tau} = \frac{A_{ep} h_{ep}}{2} (T_{ep}^m - T_g^m - T_g^{m+1} + T_{ip}^{m+1}) + \frac{A_{cl} h_{cl}}{2} (T_{cli}^m - T_g^m + T_{cli}^{m+1} - T_g^{m+1}) + \frac{A_{ss} h_s}{2} (T_{ss}^m - T_g^m + T_{ss}^{m+1} - T_g^{m+1}) \quad \text{(D-1)}$$

Spring Center Node:

$$\rho_s V_{sc} C_s \frac{(T_{sc}^{m+1} - T_{sc}^m)}{\tau} = \bar{q}\cdots V_{sc} + \frac{A_{sc} K_s}{2 R_{ss}} (T_{ss}^m - T_{sc}^m + T_{ss}^{m+1} - T_{sc}^{m+1}) \quad \text{(D-2)}$$

Spring Surface Node:

$$\rho_s V_{ss} C_s \frac{(T_{ss}^{m+1} - T_{ss}^m)}{\tau} = \bar{q}\cdots V_{ss} + \frac{A_{sc} K_s}{2 R_{ss}} (T_{sc}^m - T_{ss}^m + T_{sc}^{m+1} - T_{ss}^{m+1}) + A_{ss} \frac{(h_{rads} + h_{conc})}{2} (T_{cli}^m - T_{ss}^m + T_{cli}^{m+1} - T_{ss}^{m+1}) + A_{ss} \frac{h_s}{2} (T_g^m - T_{ss}^m + T_g^{m+1} - T_{ss}^m) \quad \text{(D-3)}$$

Cladding Interior Node:

$$\rho_{cli} V_{cli} C_{cl} \frac{(T_{cli}^{m+1} - T_{cli}^m)}{\tau} = \bar{q}\cdots V_{cli} + \frac{(A_{cl} h_{radc} + A_{ss} h_{conc})}{2}$$

$$(T^{m}_{ss} - T^{m}_{cli} + T^{m+1}_{ss} - T^{m+1}_{cli}) + \frac{A_{cl}h_{cl}}{2}(T^{m}_{g} - T^{m}_{cli} + T^{m+1}_{g} - T^{m+1}_{cli})$$
$$+ \frac{A_{cl}K_{cl}}{2.\Delta r/2}(T^{m}_{clc} - T^{m}_{cli} + T^{m+1}_{clc} - T^{m+1}_{cli}) \qquad \text{(D-4)}$$

Cladding Center Node:

$$\rho_{cl}C_{cl}V_{clc}\frac{(T^{m+1}_{clc} - T^{m}_{clc})}{\tau} = \bar{q}\cdots V_{clc} + \frac{A_{cl}K_{cl}}{2.\Delta r/2}(T^{m}_{cli} - T^{m}_{clc} + T^{m+1}_{cli} - T^{m+1}_{clc})$$
$$+ \frac{A_{cl}K_{cl}}{2.\Delta r/2}(T^{m}_{clo} - T^{m}_{clc} + T^{m+1}_{clo} - T^{m+1}_{clc}) \qquad \text{(D-5)}$$

Cladding Exterior Node:

$$T^{m+1}_{clo} - T^{m+1}_{cool} \qquad \text{(D-6)}$$

The superscripts m and m+1 represent the values of quantities at the old (m) and new (m+1) time. The steady state finite difference equations are obtained by setting the left side of Equations (D-1) to (D-5) to zero, and by dropping the superscripts m and m+1. Equations (D-1) to (D-5) can be written in the following simplified form by combining constant coefficients and known temperatures (T^{m}_{j}):

Plenum Gas:

$$A_1T^{m+1}_{g} + B_1T^{m+1}_{cli} + C_1T^{m+1}_{ss} = I_1 \qquad \text{(D-7)}$$

Spring Center Node:

$$C_2T^{m+1}_{ss} + D_2T^{m+1}_{sc} = I_2 \qquad \text{(D-8)}$$

Spring Surface Node:

$$A_3T^{m+1}_{g} + B_3T^{m+1}_{cli} + C_3T^{m+1}_{ss} + D_3T^{m+1}_{sc} = I_3 \qquad \text{(D-9)}$$

Combining Equations (D-8) and (D-9):

$$A_3 T_g^{m+1} + B_3 T_{cli}^{m+1} + \bar{C}_3 T_{sc}^{m+1} = \bar{I}_3 \qquad \text{(D-10)}$$

where

$$\bar{C} = C_3 - \frac{D_3}{D_2} C_2$$

$$\bar{I} = I_3 - \frac{D_3}{D_2} I_2$$

Cladding Interior Node:

$$A_4 T_g^{m+1} + B_4 T_{cli}^{m+1} + C_4 T_{ss}^{m+1} + E_4 T_{clc}^{m+1} = I_4 \qquad \text{(D-11)}$$

Cladding Center Node:

$$B_5 T_{cli}^{m+1} + E_5 T_{clc}^{m+1} + F_3 T_{clo}^{m+1} = I_5 \qquad \text{(D-12)}$$

Equations (D-6) through (D-12) represent a set of six equations, with six unknowns.

In the above equations, all material properities and heat transfer coefficients (except convection to the coolant) are shown as constants. For the transient case, the temperature-dependent material properties and heat transfer coefficients are evaluated at the average of the temperatures (TBAR) at the start and end times of each time step. For the steady state calculation, TBAR represents an estimate of the true steady state temperature. Therefore, it is required that the steady state and transient solutions to Equations (D-7) to (D-12) be iterated to convergence on TBAR.

APPENDIX E

FRAP-T LINK TO THERMAL HYDRAULIC CODES

APPENDIX E

FRAP-T LINK TO THERMAL HYDRAULIC CODES

An input option of FRAP-T allows the code to read transient coolant directly from a data storage file. This appendix describes (a) the form of the data set required by FRAP-T, and (b) the description of a routine which converts RELAP4 output to a form usable by FRAP-T as transient coolant condition input.

1. TRANSIENT COOLANT CONDITION DATA SET FORMAT

If NSWC = 2 (Input card 5.1), a data set specifying the transient coolant conditions must be stored on disk or tape. The data set will be accessed by FORTRAN logical unit 4. A control card for FORTRAN unit 4 must be supplied which copies the coolant condition data set to data set with name "TAPE4".

The transient coolant condition data set must be created as follows:

```
      DØ100N=1,NTSTEP
      WRITE(LU)T(N)
      WRITE(LU)PLP(N),HLP(N),TBLP(N)
      DØ50M=1,NZØNE
   50 WRITE(LU)ZB(M),ZT(M),P(M,N),H(M,N),TB(M,N),G(M,N)
  100 WRITE(LU)PUP(N),HUP(N),TBUP(N)
```

where

NTSTEP = number of time points at which coolant conditions are specified
LU = a FORTRAN logical unit
T(N) = time at time step # N (sec).
PLP(N) = pressure of coolant in lower plenum at time T(N) (psia)
HLP(N) = enthalpy of coolant in lower plenum at time T(N) (Btu/lbm)

TBLP(M) = bulk temperature of coolant in lower plenum at time T(N) (°F)

NZØNE = number of coolant zones (same as NZØNE parameter on card 5.1)

ZB(M) = distance from bottom of fuel rods to bottom of coolant zone M (ft)

ZT(M) = distance from bottom of fuel rods to top of coolant zone M (ft)

P(M,N) = pressure of coolant zone M at time T(N) (psia)

H(M,N) = enthalpy of coolant zone M at time T(N) (Btu/lbm)

TB(M,N) = bulk temperature of coolant zone M at time T(N) (°F)

G(M,N) = mass flux of coolant zone M at time T(N) (lbm/ft^2-hr)

PUP(N) = pressure of coolant in upper plenum at time T(N) psia

HUP(N) = enthalpy of coolant in upper plenum at time T(N) (Btu/lbm)

TBUP(N) = bulk temperature of coolant in upper plenum at time T(N) (°F).

The coolant condition parameters in this data set must be input in British units.

2. FRAP-T LINK WITH RELAP4

A FRAP-T subcode is available which reads a RELAP4 plot tape and prepares a data set of coolant conditions for FRAP-T. The required input is described in Table E-I and consists of some editing parameters, the volume index from the RELAP problem which is to be associated with each FRAP-T coolant zone, and some geometry data. Table E-II gives the JCL needed to run the program on the IBM 360/75 at INEL and the input of a sample run. Table E-III shows the printed output for this sample problem. The control cards for running the RELAP4 plot tape to FRAP coolant condition tape conversion program at the INEL CDC 7600 computer are shown in Table E-IV.

TABLE E-1

INPUT FOR RELAP4 TO FRAP-T COOLANT CONDITIONS CONVERSION PROGRAM

Card 0 Columns 1-6. Insert -1, remainder may be used to identify the deck but is not used by program.

Card 1 Control.

Columns	Format	Name	
1-5	I	IPRINT	Print control code. If ≤ 0 - do not print channel data. If > 0 - print the channel data being prepared for FRAP-T every IPRINT data sets.
11-20	F	TMIN	Initial problem time (sec). RELAP4 records at earlier times will be skipped.
21-30	F	TMAX	Final problem time (sec). If left blank or zero, processing will continue to the end of the RELAP4 tape.
26-35	F	TDEL	Minimum FRAP-T data interval (sec). RELAP4 records are skipped if not at least TDEL later than the last point processed. Normally, these columns are left blank.

Card 2 Plenum definition.

Columns	Format	Name	
1-5	I	NLP	Lower plenum number - the RELAP4 problem index for the volume containing the core inlet coolant conditions.
6-10	I	NUP	Upper plenum number - the RELAP4 problem index for the volume containing the core outlet coolant conditions.

TABLE E-1 (continued)

Cards 3-ff — One card for each RELAP volume which surrounds fuel rod being analyzed.

Columns	Format	Name	
1-5	I	M	Volume index in RELAP4 problem.
6-10	I	JA	Junction index in RELAP4 problem, required to define flow for versions (MOD3, update 60 and earlier) that did not write the volume flow rate to the plot tape (edit code WV).
11-20	F	ZB	Distance from bottom of fuel rods to bottom of RELAP volume M (ft). For contiguous coolant zones, ZB may be left blank, and the top of the previous zone will be used for ZB (zero for the first zone).
21-30	F	ZT	Distance from bottom of fuel rods to top of RELAP volume M (ft).
31-40	F	AR	Coolant channel area (ft^2) in the RELAP4 problem - used to convert flow in lb/hr to lb/hr-ft^2 (same as flow area of RELAP volume M).

TABLE E-II

CONVERSION CODE JCL

```
//USER# ROG JOB (D,58101-610-010,1234,X00000),I.A.USER,
// COR=089, CPU=002,WT=010,SR=T2
//X EXEC PGM=COOL,REGION=89K
//STEPLIB DO DISP=SHR,UNIT=DKPRV1,VOL=SER=PERM01,DSN=PERM.R CY FRAPC
//FT06F001 DD SYSOUT=A,DCB=(RECFM=FBA,LRECL=133,BLKSIZE=1590),
//         SPACE=(TRK,40,40),RLSE)
//FT03F001 DD UNIT=TP9ANY,DISP=OLD,VOL=SER=T90622,DSN=RDHL036    RELAP
//FT08F001 DD UNIT=TP9ANY,DCB=(RECFM=VBS,LRECL=52,BLKSIZE=524),  FRAP-T
// DISP=(NEW,KEEP),DSN=L.VTB-L036
//FT05F001 DD *

    -1
 50          0.          5.          .01
 13   1
 14   14                 1.83333     1.86924
 15   15                 2.66667     1.86924
 16   16                 5.5         1.86924
                                          OPTIONAL BLANK CARD

        PINK END-OF-JOB CARD
```

1571 147

TABLE E-III

CONVERSION CODE SAMPLE OUTPUT

```
OLD RELAP4 PROBLEM WAS TITLED
LOFT PA 036    LOCE SIMPLIFIED MODEL, DELAYED CHF
AND HAD  29 VOLUMES,  34 JUNCTIONS AND 17 SLABS.
PLOT RECORD LENGTH =1621

RELAP TO FRAP - COOLANT CONDITIONS
DATA PRINTED EVERY 50   POINTS
INITIAL TIME =   0.0  SEC.     END TIME =  5.000
MINIMUM FRAP DATA INTERVAL = 0.0100 SEC.
RELAP VOLUME FOR LOWER PLENUM IS 13     UPPER PLENUM IS     1

CORE CHANNEL VOLUME DATA

VOL  JUN  BOTTOM    TOP       AREA
NO.  NO.   (FT)     (FT)      (FT**2)
14   14     0.0     1.83      1.869E 00
15   15     1.83    2.67      1.869E 00
16   16     2.67    5.50      1.869E 00
```

TABLE E-IV

CONTROL CARDS FOR RUNNING CONVERSION PROGRAM
ON CDC 7600

```
Job Card
Accounting Card
STAGE, TAPE3,PE,NR,E,VSN=T91234.
ATTACH(FTN44)
ATTACH(FLIB44)
LIBRARY,FTN44,FLIB44.
REQUEST,FRAPC,*PF.
FTN(ØPT=2,R=3,B=FRAPC,A)
CATLOG(FRAPC,FRAPC,ID=RCY,PW=FRAP,RP=999)
FRAPC.
RETURN(FRAPC,TAPE3)
LIBRARY.
RETURN(FTN44,FLIB44)
ATTACH,TAPE,ID=ZZGJT,MR=1.
TAPE,TAPE8.

Card with 7-8-9 punch in column 1
        ----------
source cards for conversion program
        ----------
card with 7-8-9-punch in column 1
        ----------
input data for conversion program
        ----------
end of file card
```

APPENDIX F

CONFIGURATION CONTROL PROCEDURE

APPENDIX F

CONFIGURATION CONTROL PROCEDURE

A Configuration Control Procedure (CCP) has been defined to maintain a traceability of results from developing computer codes. During the development process of a computer code, there are requirements for using the code for generating both checkout results and production results, depending on the stage of development.

The CCP consists of a method by which changes can be made to the code and traceability of results maintained. Any time a modification to the code is made, the following data are recorded in a log book:

(1) Version of code to which modification was made

(2) Reason for modification

(3) Results affected by modification

(4) Date of modification

(5) Person responsible for modification

(6) The change cards used to modify the original version of the code.

The Analytical Model Development Branch at the Idaho National Engineering Laboratory is responsible for recording changes made to FRAP-T in the FRAP-T log book. A tape update routine is used to modify the code. This routine requires only those computer cards defining new statements or deleting old statements. These "change cards" are kept on file so any version of the code can be reproduced if necessary.

A new identification number is assigned to the modified version of the code, and this new number is programmed into the code where it will be listed at the top of each page of output and on each plot produced by the code.

REPORT II

FRAP-T3 MODEL VERIFICATION REPORT

Dennis R. Coleman

E. Thomas Laats

ACKNOWLEDGMENTS

Acknowledgment is given N. L. Hampton and N. R. Scofield who assisted in graphical preparation of results. L. J. Siefken provided model development support.

ABSTRACT

Results of the Fuel Rod Analysis Program-Transient (FRAP-T3) have been compared with data from both operating fuel rod experiments and out-of-pile burst experiments. Consistency between steady state extended burnup results and FRAP-T3 initial conditions has been analytically tested for full-size power reactor rods. This document summarizes the following model verification results, organized in sections according to the various operating conditions indicated below.

(1) Extended burnup steady state analyses for standard design rods - calculated fuel centerline, cladding, and plenum temperature, gap conductance, rod internal pressure, and gap size as a function of heat rating at initiation of accident conditions.

(2) Low and moderate burnup steady state data comparisons - measured and calculated fuel centerline temperature, gap conductance, and the heatup effect on rod internal pressure, fuel stack expansion, and gap closure.

(3) Off-normal data comparisons - measured and calculated burnout flow versus rod power output, and overpower cladding failure threshold versus fuel design and operating parameters.

(4) Transient data comparisons - measured and calculated fuel centerline temperature, rod internal pressure, and cladding surface temperature response as a function of time.

(5) Out-of-pile burst data comparison - measured and calculated cladding internal pressure, temperature, and strain at failure based on either strain- or stress-dependent criteria.

Results are interpreted in terms of physical mechanisms addressed by different modeling areas. Conclusions reached concerning model

capability are limited to operating conditions represented in the data prediction comparison study.

SUMMARY

1. GENERAL

Calculated results from the third version of the Fuel Rod Analysis Program-Transient (FRAP-T3) were compared with measured steady state and transient data for operating fuel rods and also for out-of-pile rupture conditions. The comparisons address the capability of the thermal and mechanical models for a limited range of steady state, off-normal, and transient conditions.

FRAP-T3 results were also evaluated to determine the consistency between steady state FRAP-S2 results and initial conditions reproduced by the transient code at different burnups. The capability of the steady state portion of FRAP-T3 to appropriately use externally supplied permanent burnup effects is evaluated for standard design power reactor rods.

2. STEADY STATE STANDARD DESIGN ANALYSIS

For 7 x 7 and 15 x 15 rods, FRAP-S2 burnup-dependent centerline temperature behavior is initially reproduced in FRAP-T3 within 150°C over the full normal power range. Rod average burnup effects correctly represent initial gap variation versus power for the boiling water reactor (BWR) cases. Input of local burnup effects is required for FRAP-T3 to reproduce FRAP-S2 gap size behavior for pressurized water reactor (PWR) rods at end-of-life. Good agreement for both fuel types is obtained between FRAP-S2 and FRAP-T3 with respect to initial rod internal pressure as a function of power at various burnups. Due to lack of corrosion effects coupling, FRAP-T3 initial cladding temperatures for burnup rods are between 10 and 40°C lower than those predicted by FRAP-S2. Initial plenum gas temperature oscillations in FRAP-T3 are associated with gas mixture properties not dominated by an individual component.

3. STEADY STATE DATA COMPARISONS

Pressurized rod startup centerline temperatures are underpredicted by 50 to 180°C below 10 kW/ft. Unpressurized rod fuel temperatures are within ±10% of the data for rods with low fission gas content. Data comparisons for fuel temperature and gap conductance indicate that calculated effects of gap size and gas composition on the thermal model are too strong. The calculated heatup effect on startup internal pressure response is within ±10% of the data for a wide range of fill gas conditions. The heatup effect on fuel axial expansion is well represented by the model prior to observed gap closure. A fuel relocation adjustment compensating for current error in the gap closure model was found to be proportional to the space available for accommodating pellet cracks. Full implementation of a fuel relocation approach requires some treatment of pellet mechanical deformation, but the model by itself is expected to improve capability of thermal, gas release, and pellet-cladding mechanical interaction (PCMI) calculations.

4. OFF-NORMAL DATA COMPARISONS

Comparison of measured and predicted flow and power conditions at initiation of critical heat flux (CHF) indicates good model performance for bundle geometries with uniform flow and small cold-wall effect. The single-channel enthalpy rise model seems adequate in this case. Single-rod test results exhibit significant scatter due to the effect of channel geometry, flow area, and stand-off devices. Comparing results for various CHF correlation options provides support for using the GE model for BWR conditions and the Babcock & Wilcox model, B&W-2 for Power Burst Facility (PBF) rods with individual flow shrouds.

Low temperature cladding failure probability during power increases is well represented by the FRAIL subcode for those hard gap closure conditions (>15 kW/ft) unaccompanied by a significant bulk fuel plasticity effect. Lower observed failure probabilities associated with

larger gaps and more moderate power levels are underestimated by the model, possibly due to not treating fuel relocation, stress corrosion cracking, and statistical failure effects. More frequency of failure data are needed for core average as opposed to lead rod operating conditions.

5. TRANSIENT DATA COMPARISONS

Transient centerline temperatures were overpredicted for several rods experiencing scram events under normal cooling conditions. Initial calculated temperatures were between 100 and 400°C higher than observed due to the overly strong influence of gap size and gas composition on the steady state thermal model. Transient and equilibrium temperatures for best-estimate initial condition runs were overestimated by up to 300°C, due in part to underpredicting the extent of fuel cracking which remains once power is decreased.

Transient cladding temperatures up to 1000°C were well represented by the model for the low surface heat transfer condition associated with superheated steam flow in two Transient Reactor Test (TREAT) loss-of-coolant accident (LOCA) simulation tests. Transient internal pressure response was generally overpredicted, especially for the small plenum conditions most sensitive to error in calculated stack elongation, active length void volume and temperature, and transient plenum gas temperature. Cladding ballooning and rupture were predicted to occur at significantly lower than observed temperature and pressure levels.

6. OUT-OF-PILE TUBE RUPTURE DATA COMPARISONS

Elevated cladding burst temperatures were underpredicted by the material properties code, MATPRO, by at least 30% for tube heatup tests. Agreement between measured and calculated burst pressure for low temperature (316 to 427°C) isothermal tests was within data scatter.

Cladding rupture deformation was largely overpredicted by MATPRO, due in part to underestimating burst temperature for heatup tests. Underpredicting rupture strain corresponded to isothermal expansion data between 760 and 900°C. Mean failure criteria used as the basis of the FRAIL subcode provided a better representation of observed temperature and pressure conditions at rupture. Overall out-of-pile tube burst results indicate that failure criteria based on the current $\sigma - \varepsilon$ concept used in MATPRO are better applied to normal operating temperature conditions. A different $\sigma - \varepsilon$ form or alternate correlary should be developed to relate cladding stress and temperature conditions, calculated failure probability, and observed deformation behavior.

CONTENTS

FIGURES

FIGURES (continued)

FIGURES (continued)

FIGURES (continued)

FIGURES (continued)

TABLES

FRAP-T3 MODEL VERIFICATION REPORT

I. INTRODUCTION

An essential part of producing an operational computer code, which can be used with a known degree of confidence for conducting reactor safety analysis, is the verification of the models on physical grounds. This report discusses the results of several different verification analyses addressing the present version of the Fuel Rod Analysis Program-Transient (FRAP-T MOD-003), referred to as FRAP-T3[a]. The current model represents an update of the previously documented version of the program, FRAP-T2[1,2,3].

In addition to benchmarking relative capability of subsequent code versions in the development series, a long term verification objective is to determine quantitative indices for characterizing model performance. The scope of the present work addresses the objective of establishing more physical confidence in various controlling aspects of the FRAP-T3 thermal and mechanical model.

FRAP-T3 is intended to predict the transient behavior of fuel rods following perturbations from normal operation such as those caused by a loss-of-coolant accident (LOCA), a power-cooling-mismatch (PCM), or a reactivity initiated accident (RIA). The code treats the coupled effects of fuel rod thermal, mechanical, and internal pressure response, and associated material properties. Documentation pertaining to the present models is presented in three companion volumes. Report 1 of this document contains a description of the code and instructions for its operation. Reference 4, "MATPRO - Material Property Routines for FRAP-T," contains descriptions of the material property models used in the code. This report contains results of the FRAP-T3 model verification study.

---

[a] FRAP-T MOD 003-VER 12/14/76, MATPRO Version 08.

The verification study consists mainly of data prediction comparisons which address various indices of fuel behavior measured for light water reactor (LWR) test rods operated under steady state, transient, and off-normal conditions. Performance of the burnup effects coupling between FRAP-S2[4,5,6], the current steady state model, and FRAP-T3 is also demonstrated for application to analysis of standard commercial fuel designs. Data comparisons for high temperature deformation behavior of zircaloy tubes were added using out-of-pile tests to evaluate the model in an area characterized by limited operating rod data. The overall objective of the verification report is to establish relative ability of the model to compute realistic thermal and mechanical effects expected to impact fuel rod behavior during accidents.

Section II briefly describes the overall model, gives rationale pertinent to choice of data comparisons, and describes input conventions. Section III shows examples of FRAP-S2 coupling with FRAP-T3 to reproduce key initial accident conditions in standard design rods at varying burnup and heat rating. Section IV contains data comparison results for steady state fuel temperature, rod internal pressure, fuel expansion, and gap closure. Section V addresses the onset of off-normal surface heat transfer and cladding stress conditions using burnout and overpower data comparison results. Section VI addresses data comparisons where transient effects are evident in fuel and cladding temperature and rod internal pressure response. Results of out-of-pile tube burst data comparisons are given in Section VII. References are listed in Section VIII.

II. GENERAL APPROACH AND CONSIDERATIONS

Sections giving data comparison and analysis results are preceded by a general description of (a) the model, (b) rationale pertaining to choice of data comparisons and the need to evaluate the model at various conditions, and (c) input conventions used for computer runs.

1. CODE DESCRIPTION AND BASIC STRUCTURE

Detailed description of the FRAP-T3 computer program has been given in other volumes[3,4] of this report series. In summary, the program is capable of calculating fuel rod transient temperature distributions which are driven by changes in power level or surface heat transfer conditions. The transient conduction equation is solved at specified time intervals. Changes in material properties, gap and surface heat transfer, rod internal pressure, mechanical interaction state, and rod deformation are taken into account. The current structural analysis computes deformation for single rods occurring as a result of thermal expansion, hydrostatic pressure differences, gap closure, and high temperature cladding rupture. Output from the mechanical response model interacts with material properties and the transient thermal model because individual node displacement, temperature, and rod internal pressure must all satisfy convergence criteria for the calculation to proceed. Thermal and deformation analyses progress in parallel then, with iteration on mutually dependent variables. Features of the code are intended to facilitate its application to fuel behavior problems having significance in reactor safety analysis.

Early development activity resulted in a modular subroutine framework which fulfills thermal mechanical feedback requirements. Constituent models are not all in final versions, but the overall feedback structure itself is considered firm for single-rod applications. Initial rod and equivalent coolant channel geometry, inlet fluid conditions,

and power history are normally the independent variables available for user input. If required, thermal hydraulic boundary conditions can be externally supplied by way of proper selection of input data from supporting analyses. The code is structured to handle rod arrays of limited size, but currently no feedback is provided to account for subchannel interactions occurring as a result of flow redistribution or cladding deformation. Model differences between FRAP-T3 and FRAP-T2 are listed in Table X of the present model description and user's manual.

2. CHOICE OF ANALYSES

In this section, rationale is given for choosing the various FRAP-T3 analyses described here. The relatively large number of transient data comparisons thought to be necessary for evaluating integrated model performance under accident conditions have not been performed. Key operating rod measurements under typical LOCA, RIA, and PCM conditions are either not yet available or too few in number to establish firm conclusions. The influence of off-normal surface heat transfer seems to govern interpretation of currently available PCM and RIA data comparisons. Calculated rod internal conditions and cladding deformation are, in these cases, controlled by thermal hydraulic input based on either external models or trial-and-error matching of rod surface temperatures. In any event, run identification and design data for all of the operating rod cases considered here are given in Table I. Out-of-pile tube rupture experiments are listed in Table II. Rod design and operating conditions have been cataloged based on the run identification in each case.

FRAP-T3 data comparisons for steady state or slow power ramp conditions are necessary even though the model is meant for application to transients or other events associated with off-normal fuel behavior. Performance of internal fuel rod models is more readily diagnosed when data comparisons can be represented as having normal surface heat transfer. These comparisons minimize perturbations within both the physical model and the material properties package. This damping effect is a result of

Run No.	Reference Standard Design Study	Number of Rods	Cladding ID[a] (in.)	Diametral Gap (mils)	Fuel Density (%)	Enrichment (%)	Fill Gas[a] (psia)	Cold Plenum (in.)
46	7 x 7	1	0.4990	12.0	94.0	2.2	15	16.0
48	15 x 15	1	0.3740	7.5	94.0	2.8	345	6.8
Steady State Data Comparisons								
2,3	HPR-80[7]	2	0.4961	2.4	95.2,95.4	5.0	15	1.58
29,30	AECL-4072[8]	2	0.7346	4.3	97.6,95.8	1.4,1.6	15	0.005
31,32	IFA-255[9]	2	0.4992	5.9	95.0	5.9	15	0.827
36	IFA-226[10]	1	0.3744	7.8	95.9	7.3[U+Pu]	15	7.00
40	HPR-107[11]	1	0.4922	5.9	95.0	5.8	15	1.43
41,42	HPR-107[11]	2	0.4921	7.5	95.7	5.8	15	0.57
273-275 277,278	PBF[12-14, 15,16]	4	0.374	8.0	93.0,94.0	20.0	550,375	2.0
276-280, 281	PBF[17,18]	3	0.346	9.9	92.0	9.5	380(He,Ar)	3.0
318	IFA-208[19]	1	0.4992	11.8	94.9	7.0	15[e]	3.2
335	IFA-181[20]	1	0.4921	11.2	94.0	11.01	15	2.73
351	IFA-224[19]	1	0.4992	11.8	90.1	7.0	15	3.2
372,373	IFA-142[20]	2	0.7480	4.7	94.3	3.0	15[e]	0.12
386	IFA-181[21]	1	0.4921	11.2	94.0	11.0	15[e]	2.73
387-389	IFA-225[22]	3	0.4992	11.8	95.0	5.9	15[e]	0.84
402-404	IFA404 I[23]	3	0.5000	2.4,3.9	94.8	7.0	15[e]	2.8[e]
405,406	IFA-414[24,25]	1	0.3933	2.0,8.7	95.0	7.0	15[e]	1.0[e]
400-410	IFA-404 II[25]	3	0.4988	2.4	90.1-95.8	7.0	15[e]	2.8[e]
415-423	IFA-429[26]	9	0.374	8.0	91.0-95.0	13.0	375	1.0
424-427	IFA-431[27,28]	4	0.4291	1.9-14.9	95.0	10.0	15	0.67-0.94
430	PBF[18]	1	0.345	9.9	92.0	9.5	386	3.04
431,432	PBF[29]	2	0.4252	7.9	95.0	10.0	15	2.17
433-436	PBF[30]	4	0.3740	8.0	93.3	20.0	376,550	2.0
437-440	PBF[31]	4	0.3740	8.0	93.3	20.0	376	2.0
441	HBWR[32]	1	0.3661	9.0	92.2	6.0	514	4.15
442-445	HBWR[32]	4	0.3661	9.0	91.6-95.0	6.0	323	4.15
Overpower Data Comparisons								
OP01-OP04	IFA-4,R2[33-34]	4	0.50236	7.1	96.4	6.05	15	0.512
OP05A,OP05B	IFA-4,229[35,36,37]	2	0.50236	7.1	96.4	6.05	15	0.512
OP06-OP10	IFA-21[38,39]	5	0.4957,0.4961	2.0,6.7	95.2-97.8	5.0	15	0.536,1.579
OP11-OP13	R2[33]	3	0.4959,0.4961	8.1,5.1	95.8[e]	5.0[e]	15	2.5[e]
OP14	R2[33]	1	0.3815	5.5	95.8[e]	5.0[e]	15	2.5[e]
OP15-OP17	R2[38]	3	0.4984,0.4949	3.9,5.5	95.8	5.0[e]	15	2.5
OP18	DR3[40]	1	0.37322	7.5	95.7	3.15	400	0.63
OP19-OP25	IFA-405 I,II[41]	7	0.500	2.4-9.8	94.8	7.0	15	2.95
OP26-OP29 OP46-OP48	IFA-407 II,I[42,43]	7	0.4917,0.4923	8.3-10.6	91.9-92.5	6.08	15	0.96
OP32-OP35	DR3[44]	4	0.5043-0.5067	7.5-10.2	94.3,95.7	5.0,1.5	15	0.50,1.41
OP36-OP45	CIRENE[45]	10	0.7464	7.9	95.0	4.0[e]	15	0.4[e]
OP49	IFA-164[46]	1	0.5039	9.0	94.7	4.0	15	1.79
OP50-OP53	IFA-405 III[47]	4	0.5000	2.4	89.7,94.7	7.0	15	2.95

TABLE I

N IDENTIFICATION FOR OPERATING ROD ANALYSES

Dish (%)	Fuel Length (ft)	Loop Pressure (psia)	Mass Flow (10^6lb/hr-ft^2)	Inlet Temperature (°F)	Peak Power (kW/ft)	Peak/Avg. (axial)	Operating Hours	Output[c]
0.0	12.0	1035	1.3	533	10.3[d]	1.4	32,000	TF,hg,gap,P
1.5	12.0	2250	2.5	552	9.8[d]	1.4	21,000	TF,hg,gap,P
1.3	5.625	406	0.39	446	15.2	1.3	10/4400	TF'
2.0	1.6,1.2	1100	2.1	414	20.6,20.2	1.0	18,105.0	ε'_{cr}
3.6,0.0	1.736	485	0.35	463	22.6	1.2	2140	ε'_{cr}
0.9	1.99	490	0.36	460	15.0	1.4	4800	TF',ε'_{cx}
0.0	1.77	490	0.27	467	17.8	1.26	14	ε'_{fx},ε_{cx}
1.0,0.0	1.76	490	0.33	467	15.8	1.26	14	ε'_{fx}
2.3	3.0	2080.0-2200.0	0.94-2.0	540,620	19.9-24.9	1.35	10	TF',ε_{cx},F,hg',ε_{cx}
4.1	2.89	2160	0.61-2.6	590,620	19.2-20.3	1.32,1.34	23.0,33.0	TF',ε_{cx},P,hg'
1.8	4.82	490	0.33	454	23.7	1.34	3200	ε'_{fx},
2.5	4.83	490	0.28	454	18.5	1.25	5790	ε'_{fx},ε'_{cx},P
3.7	4.82	490	0.34	454	17.6	1.34	150	ε'_{fx}
2.0,2.2	1.57	490	0.31	464	20.3	1.14	4100	P
2.5	4.83	490	0.28	454	18.5	1.25	5700	ε'_{fx},ε'_{cx},P
3.7	1.60	490	0.35	464	15.2	1.27	39	P
2.4	1.64	490	0.17	454	17.9	1.08	1640	ε'_{cr}
2.7[e]	1.31	2000	0.12	491[e]	14.0	1.20	810	ε'_{fx},ε'_{cr}
2.4	1.64	490	0.17	454	16.3	1.08	3900	ε'_{cr}
1.1	0.80	490	0.56	464	7.2-12.0	1.02-1.30	900	TF,P
0.0	1.86,1.89	490	0.36	464	5.6-8.2	1.08	17	TF',hg'
1.3	2.89	2160	2.14-0.0	640,620	13.7	1.10	33	ε'_{cx},T_C'
0.0	2.98	1040	1.9	401	11.7,14.6	1.349	1.5,2.0	hg'
1.0	2.99	2160,2205	2.5,2.6	539,590	15.0-16.2	1.349	2.0,2.8	TF',P,ε'_{cx},TC',hg'
1.0	2.99	2205,2220	1.8,2.4	540,590	16.8-18.5	1.349	2.9,5.0	TF',P,ε_{cx},hg',T_C'
1.4	2.46	490	0.29	460	12.1	1.20	3600	TF
1.4	2.46	490	0.29	460	9.4	1.20	4500	TF'
0.0	2.625	406,490[f],1296,2063[g]	0.18	436,454[f],545,608[g]	19.2[f],16.2,19.8[g]	1.47	24,700	ε_{cr},σ_{cr}
0.0	2.625	406,490[f], 490[g]	0.18	436,454[f],464[g]	19.2[f],20.8-21.9[g]	1.47	24,700	ε_{cr},σ_{cr}
1.3	5.62,5.75	406	0.39	436	15.5[f],17.7[g]	1.22	8640	ε_{cr},σ_{cr}
1.4[e]	0.98[e]	864[e,f],1296[g]	0.5[e]	473[e,f],545[g]	6.3[f],14.0-23.2[g]	1.05[e]	7740	ε_{cr},σ_{cr}
1.8[e]	0.98[e]	864[e,f],1296[g]	0.5[e]	473[e,f],482[g]	20.3[f],21.3[g]	1.05[e]	4630	ε_{cr},σ_{cr}
2.0	0.88,0.98	864[f],1296[g]	0.5[e]	473[f],545[g]	17.5[f],19.6-21.3[g]	1.05[e]	5900	ε_{cr},σ_{cr}
1.2	0.423	2235	1.0[e]	600[e]	15.4[f],16.4[g]	1.05[e]	5080	ε_{cr},σ_{cr}
2.4	1.64	490	0.34	454	10.4[f],16.4-22.6[g]	1.28	8400	ε_{cr},σ_{cr}
0.0,1.5	1.64,1.66	400	0.32	454,464	11.7-21[f]19.4-22.8[g]	1.6	7700	ε_{cr},σ_{cr}
0.0,1.3	0.4,1.07	1043	0.5[e]	549	15.3-17.9[f],8.1-18.3[g]	1.05[e]	15-22,000	ε_{cr},σ_{cr}
2.4[e]	1.56	712[f],870[g]	0.5[e]	504[f],495[g]	10.9[e,f],16.4-21.6[g]	1.1[e]	4500	ε_{cr},σ_{cr}
1.2	2.70	490	0.3	460	14.6	1.09	4195	ε_{cx}
2.4	1.64	490	0.3	460,467	10.2,10.5	1.16,1.23	8400	ε'_{cx}

RUN ID	Reference	Number of Tubes	Cladding ID (in.)	Cladding Thickness (in.)	Unsupported Length (in.)	Int Config
017-028	GEMP-731[62]	11	0.365	0.027	2.5	Em
095-096	GEMP-731	2	0.380	0.022	8.0	Em
097-112	WCAP-3017-6094[63]	16	0.318	0.022	8.0	Em
130-138	WCAP-3385-56[64]	9	0.345	0.023	8.0	Em
139-143	WCAP-3050-3[65]	5	0.436-0.453	0.025	8.0	Em
151-156	WCAP-3850-3	7	0.436	0.017	8.0	Em
157-166	APED 5479[66]	10	0.492	0.035	14.0	Depl Pe
243-254	ORNL-TM-3626[67]	12	0.503	0.030	2.0	Irradi Pe
255-269	ORNL-TM-3626	15	0.503	0.030	2.0	Irradi Pe
270-272	ORNL-TM-3626	3	0.378	0.022	2.0	Irradi Pe
273-276	ORNL-TM-3626	4	0.378	0.022	2.0	Irradi Pe
397-417	JAERI-M-6339[68]	21	0.366	0.028	6.7	Al_2O_3
418-422	BMI[69]	5	0.370	0.024	7.0	Al_2O_3
423-440	ANL[70]	18	0.380	0.025	6.0	Al_2O_3
441-462	ORNL[71,72]	22	0.380	0.025	36.0	Tube H
463-467	AECL-5559[73]	5	0.565	0.017	19.7	E
468-469	AECL-5559	2	0.565	0.017	19.7	Em
470-474	Karlsruhe Spatind76[74]	5	0.367	0.028	12.9	Al_2O_3 w/
475-565	Kwu Spatind76 [75]	91	0.367	0.028	18.1	Al_2O_3 w/
566-568	Karlsruhe RSIF4[76]	3	0.367	0.028	18.1	Al_2O_3 w/
569-583	TRG[77]	15	0.576	0.025	10.4	Em

[a] Integrated Exposure, n/cm^2

[b] Pressurization-Heatup

[c] Restricted

TABLE II

-- OUT-OF-PILE BURST AND EXPANSION DATA
NGLE ZIRCALOY TUBES

ernal uration	Test Mode	Environment	Tube nvt[a]	Pressurization Range (psia)	Clad Max. Temp. Range (°F)	Max. Permanent Hoop ε (in./in.)
pty	P-H Rupture[b]	Steam	0	75-154	1760-2858	0.07-0.34[c]
pty	P-H Rupture	Steam	Irradiated	127-171	1809-1884	0.18-0.75
pty	Pressurization at constant temperature	Air	$1.4\text{-}3.3\times10^{21}$	9000-11,000	625-675	0.02-0.25
pty	Pressurization at constant temperature	Air	$2.2\text{-}3.3\times10^{21}$	5500-11,000	675	0.02-0.46
pty	Pressurization at constant temperature	Air	Irradiated	3600-12,000	650	0.009-0.20
pty	Pressurization at constant temperature	Air	0	7693-8943	600-725	0.13-0.348
ted UO_2 llets	P-H Rupture	Air + Steam	0	170-1560	1338-2227	0.11-0.58
ated UO_2 llets	P-H Rupture	Argon + Steam	0	58-1025	1495-2600	0.25-0.70
ated UO_2 llets	P-H Rupture	Argon + Steam	$0.4\text{-}1.4\times10^{21}$	55-1020	1450-2360	0.15-0.51
ated UO_2 llets	P-H Rupture	Argon + Steam	0	105-509	1650-2025	0.28-0.65
ated UO_2 llets	P-H Rupture	Argon + Steam	$0.9\text{-}1.4\times10^{21}$	106-712	1505-1940	0.16-0.44
Pellets	P-H Rupture	Steam	0	270-697	1481-1598	0.24-0.80
Pellets	Pressurization at constant temperature	Air	0.414×10^{22}	12,310-14,870	600-800	0.018-0.072
Rod	P-H Rupture	Steam	0	146-2466	1368-2322	0.16-0.785
eater	P-H Rupture	Steam	0	116-2094	1497-1980	0.15-0.79
pty	Isothermal expansion at constant pressure	Steam	0	50-54	1922-2372	0.04-0.06
pty	P-H Rupture	Steam	0	51-101.8	1868-2462	0.08-0.70
Pellets eater	P-H Rupture	Air	0	1015-1896	1319-1546	0.023-0.37
Pellets eater	Isothermal expansion at constant pressure	Air	0	279-2190	1276-1659	0.02-1.35
Pellets eater	Isothermal expansion at constant pressure	Air	0	98-142	1832	0.23-0.88
pty	P-H Rupture	Argon + Steam	0	26-87	1724-1814	0.012-0.092

FRAP-T2 verification, additional PBF burnout data have been considered in this study, along with a larger number of Halden overpower tests.

Two types of transient data comparisons were performed for operating rods. Benchmarking of the conduction model was accomplished using an expanded number of centerline scram temperature histories. Secondly, a previous FRAP-T2 data comparison involving an experimental LOCA simulation is repeated to document the effect of model revisions on calculated cladding temperature and rod internal pressure response. Again, the intent of these limited transient analyses is to determine model capability in areas where the physical mechanism can be related to modeling requirements for accident conditions.

Data prediction comparisons are included for out-of-pile burst experiments on zircaloy tubes. This run series was carried over from FRAP-T2 model verification due to relative lack of operating rod tests with observed high temperature cladding ballooning. This measurement sample was also expanded in terms of representing tube deformation conditions for oxidizing environments. All previously used inert environment data were eliminated. The burst data comparisons are used to evaluate the mechanical response model for application to predicting cladding behavior during hypothetical core depressurization events.

3. INPUT CONVENTIONS

Preparation of FRAP-T3 input data is discussed in this section for both as-built and burnup-dependent parameter types.

As-built input parameters were determined directly from fabrication data or loop conditions given in the source references. These parameter values either remain unaffected by prior operation, or have no corresponding models in FRAP-S2 or FRAP-T3 by which a burnup effect can be calculated. Examples of burnup-independent FRAP-T3 input include

surface roughness, cladding thickness, system conditions, dish, spring, and coolant channel dimensions, and axial power distribution. Examples of burnup effects not used by FRAP-T3 include cladding surface condition and hydrogen concentration, retained fission gas concentration, and fuel thermal and mechanical properties.

Burnup-dependent input parameters are affected by fuel rod operation occurring prior to the incident represented by a given FRAP-T3 data comparison or standard design analysis. FRAP-T3 input values have, for these cases, been based on FRAP-S2 output. The burnup parameters reflect permanent fuel and cladding deformation and permanent changes in the amount and composition of internal gas. Specifically for the current models, the following burnup effects are considered: the net effect of pellet densification and fission product swelling, uniform plastic deformation of the cladding due to yield and/or creep, and release of sorbed and fission generated gas. This procedure effectively makes FRAP-T3 results somewhat dependent on FRAP-S2 models. FRAP-S2 verification studies did establish some level of confidence in the steady state code, however. Model results were usually within measurement scatter of the data for experiments exhibiting uniform mechanisms associated with moderate duty, steady power operation without sustained gap closure.

Other input considerations common to all runs are as follows. Radial nodalization was accomplished by specifying ten fuel intervals, one gap interval, and two cladding intervals. Axially, test rods and full-size standard design rods were divided into 7 and 16 intervals, respectively. Equivalent single-channel fluid analysis was usually specified with enthalpy rise calculated internally, based on inlet conditions. When not reported in detail, hydraulic parameters and channel geometry were input to allow surplus cooling conditions to exist. This specification applies to many of the data comparisons because surface heat transfer was usually not a limiting factor for the experiments considered. Radial power distributions were based on the FRAP-S2 model for standard rods, application of diffusion theory[7,78] for high enrichment operating rods, and pretest predictions[79] for PBF rods.

With the exception of two Transient Reactor Test (TREAT) and six scram rods exhibiting transient thermal response, the analytical time scales used to represent the various irradiation histories were usually of long enough duration for the model to always produce steady state temperature distributions.

III. STEADY STATE STANDARD DESIGN RESULTS

Standard design runs discussed here are used to benchmark FRAP-T3 initial conditions for power reactor fuel. No data comparisons are involved. Analytical consistency between FRAP-S2 and steady state FRAP-T3 results is checked across a range of power, design, and burnup conditions expected to be relevant for transient analysis.

Documentation of typical steady state fuel behavior parameters has been a previously described verification result[6,82] applicable to commercial rods. These FRAP-S output parameters reflect a wide range of potential initial accident conditions for full-size rods operated normally from beginning- through end-of-life. Some FRAP-T3 input parameters can be used to account for preaccident operation by defining fuel burnup, integrated cladding fluence, internal free gas content and composition, internal void volume, radial power distribution, and geometry of fuel and cladding. Consideration of retained fission gas distribution, cladding surface condition, and the influence of prior operation on fuel and cladding properties is currently not considered.

The initial FRAP-T3 application of the user input link between extended burnup and transient models is to determine initial hot operating conditions from the input data. Physically, this amounts to the model adding thermal expansion and elastic deformation effects to the input rod geometry and using direct coupling of gas content, gas composition, and power distribution. Results shown in this section are used to determine whether the initial condition FRAP-T3 calculation reproduces the appropriate FRAP-S2 output. The input values for this limited study are based only on the nominal FRAP-S2 standard design runs for core average rods operated at steady power. Results are given addressing initial thermal, pressure, and deformation conditions. Different boiling water reactor (BWR) and pressurized water reactor (PWR) fuel designs have been analyzed, namely 7 x 7, 8 x 8, 15 x 15 and 17 x 17. Both PWR and BWR analyses give consistent trends influenced by

the design parameter range for either fuel type. Results for the 7 x 7 and 15 x 15 cases can be considered typical for the present purpose. FRAP-S2 and FRAP-T3 results are compared as a function of steady state heat rating at beginning-, middle-, and end-of-life. The range of burnup and heat rating represents the range of operating conditions from which point most accident analyses can begin.

Figures 1, 2 and 3 show calculated steady state fuel temperature, gap conductance, and gap size versus local power for 15 x 15 rods at beginning-, middle-, and end-of-life. Results of FRAP-S2 and the coupled FRAP-T3 run appear to be most consistent at beginning-of-life. This observation is consistent with existing differences in burnup dimensions between the FRAP-S2 peak power node and the rod average values used for FRAP-T3 input. Input of the rod average (as opposed to local) burnup geometry was meant to benchmark initial conditions as might be obtained by a code user working without restart tape capability from FRAP-S2.

Maximum difference in centerline temperature for all burnups is less than 100°C, however, as shown in Figure 1. The FRAP-S2 prediction that 15 x 15 gap closure effects result in lower fuel temperature at burnup is reproduced by FRAP-T3. This trend is observed despite some differences in middle- and end-of-life gap conductance behavior seen in Figure 2. Between 6 and 8 kW/ft, the FRAP-S2 mid-life curve shows a discontinuity (believed to be anomalous) which coincides with initiation of nucleate boiling on the surface of the calculated crud and corrosion layer not modeled by FRAP-T3. The lower end-of-life gap conductance predicted by FRAP-T3 and lack of a hard gap closure effect above 10 kW/ft are explained by the larger gap size (Figure 3) which results from input of rod average burnup effects. Pressurized rod gap heat transfer is high enough in any event to moderate fuel temperature differences between the codes. Figure 3 does indicate that an input representation of local burnup effects may be necessary in FRAP-T3 for end-of-life analysis of pellet-cladding mechanical interaction (PCMI) and gas flow conditions.

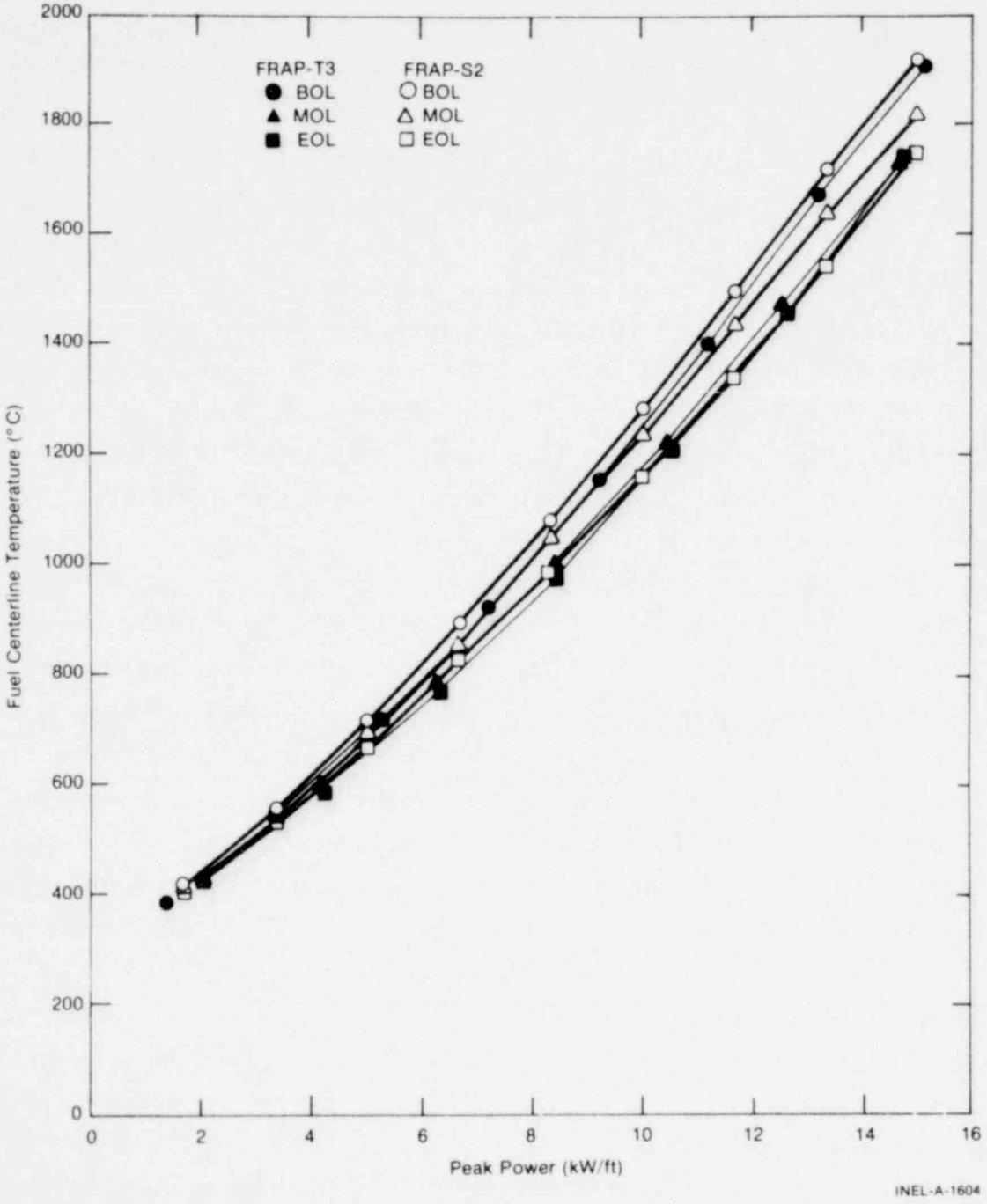

Fig. 1 Initial condition fuel centerline temperature versus local power for a standard 15 x 15 rod at beginning-, middle-, and end-of-life.

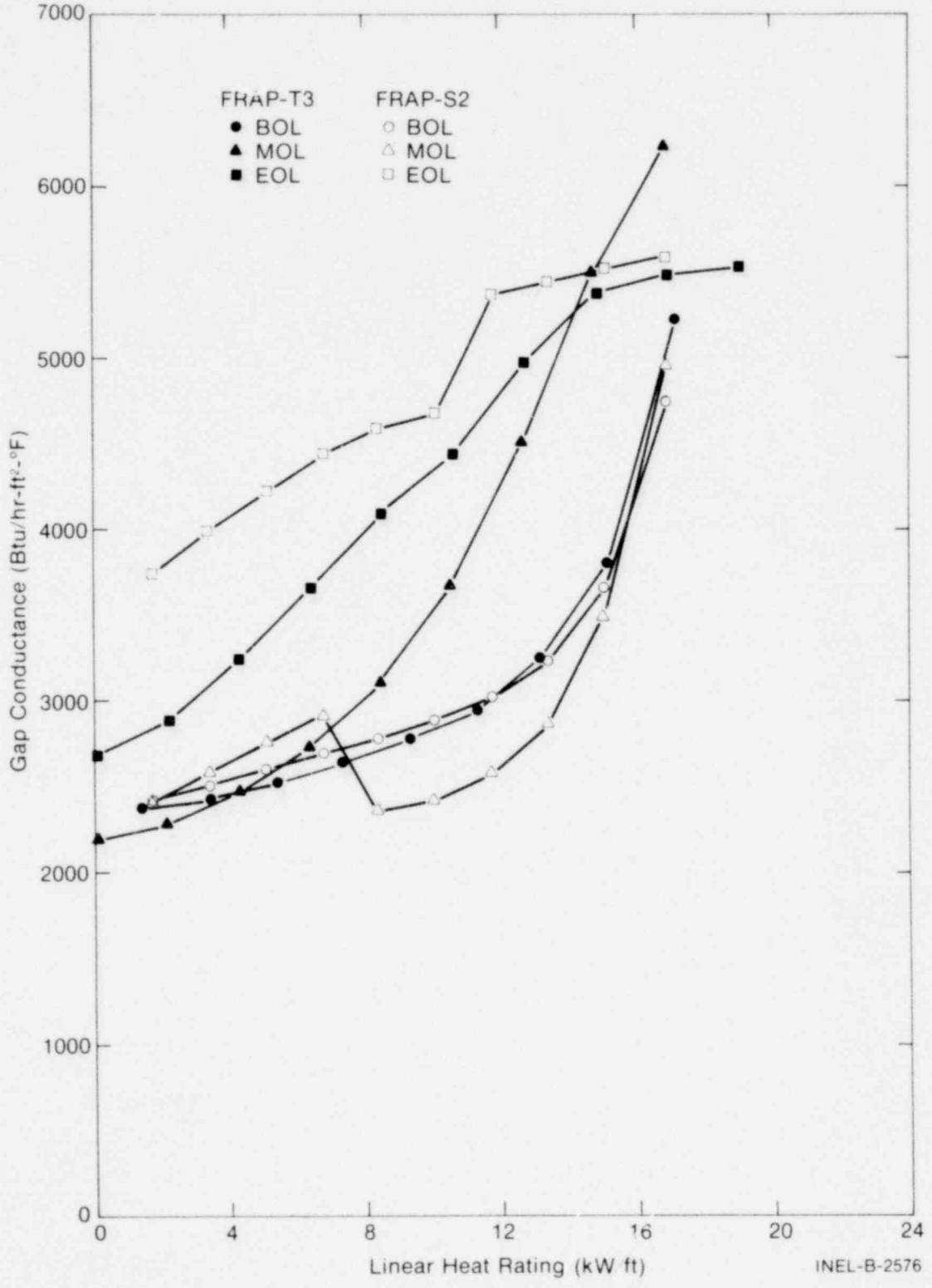

Fig. 2 Initial condition gap conductance versus local power for a standard 15 x 15 rod at beginning-, middle-, and end-of-life.

1571 181

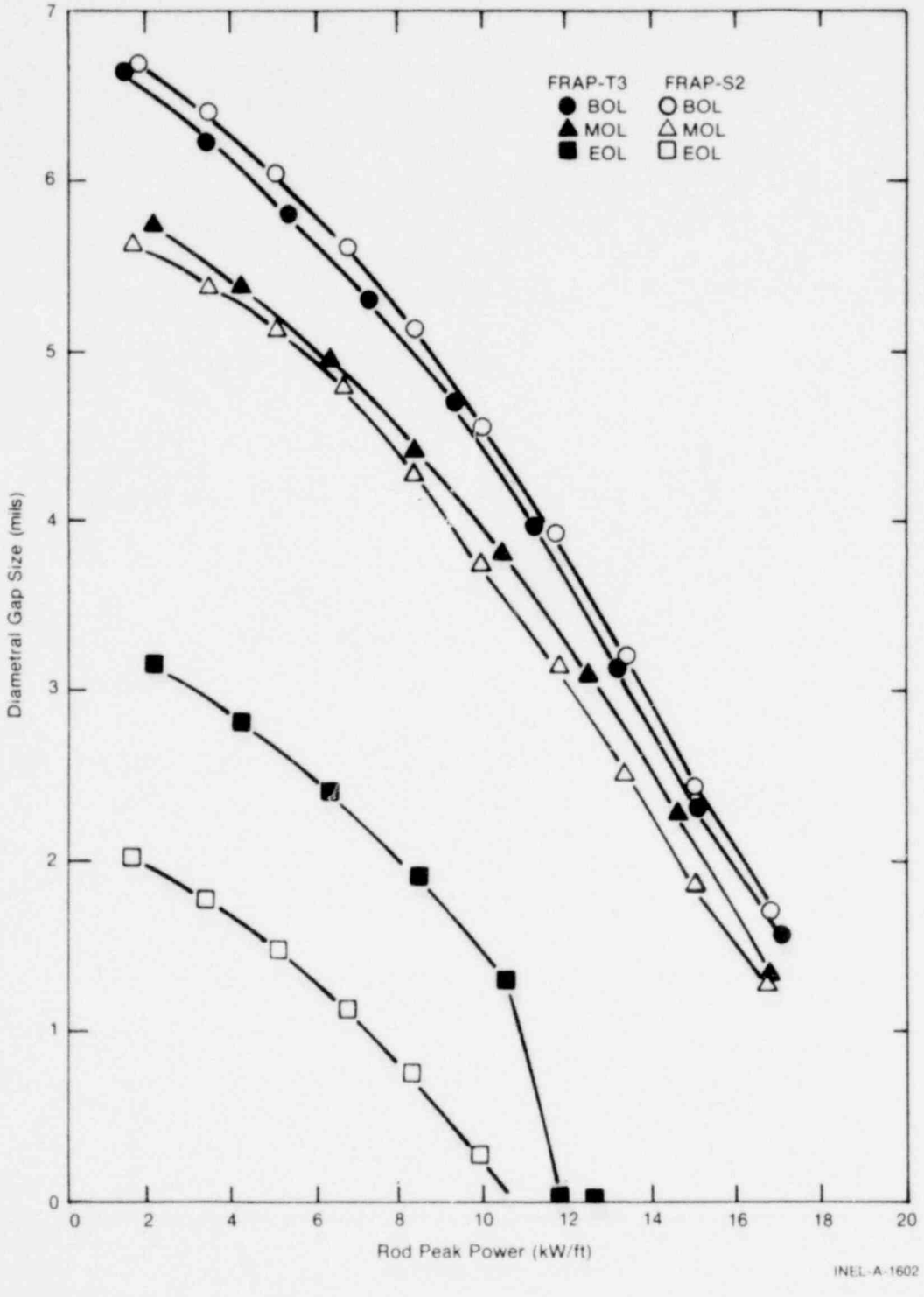

Fig. 3 Initial condition gap size versus local power for a standard 15 x 15 rod at beginning-, middle-, and end-of-life.

Figures 4, 5 and 6 compare FRAP-S2 and steady state FRAP-T3 thermal and gap size response versus local power for 7 x 7 rods at beginning-, middle-, and end-of-life. Again, beginning-of-life conditions are more consistent between the two models. The maximum centerline temperature difference seen in Figure 4 at any burnup is less than 150°C. Unpressurized rod local burnup effects are less easily reproduced by FRAP-T3 due to greater sensitivity of thermal conditions when calculated gap heat transfer is relatively low. Fuel temperatures reflect the comparison of FRAP-S2 and FRAP-T3 gap conductance values shown in Figure 5. Again, FRAP-S2 predicts decreases in gap heat transfer associated with either its additional temperature drops across rod surface corrosion and crud layers, or some other burnup effect entering into gap heat transfer conditions. FRAP-S3 model development activities have addressed this anomaly. Lower gap conductance predicted by both FRAP-S2 and FRAP-T3 at burnup is consistent with linking unpressurized rod gas composition changes to the thermal model. Initial condition gap sizes predicted by FRAP-S2 and FRAP-T3 are consistent, as shown in Figure 6. Rod average and peak power node burnup effects are more comparable for BWR rods than PWR rods due to lower compressive cladding creep.

It was previously reported during FRAP-T2 verification that lack of crud and corrosion coupling with FRAP-S1 caused somewhat lower cladding temperatures to be initially obtained by the transient code. FRAP-T3 has not been changed in this respect. For purposes of documentation, a comparison between FRAP-S2 and FRAP-T3 initial cladding temperatures is shown in Figure 7. The observation is again made that the effect of built up insulating surface layers is greatest at end-of-life. The temperature effect, however, is likely to have smaller impact on accident response than surface condition itself and accompanying material properties at high temperature.

Figures 8 and 9 compare FRAP-S2 and FRAP-T3 rod internal pressure conditions for 7 x 7 and 15 x 15 rods versus steady state power, again at beginning-, middle-, and end-of-life. Rod average dimensional changes and direct coupling of internal gas content was used to link FRAP-T3

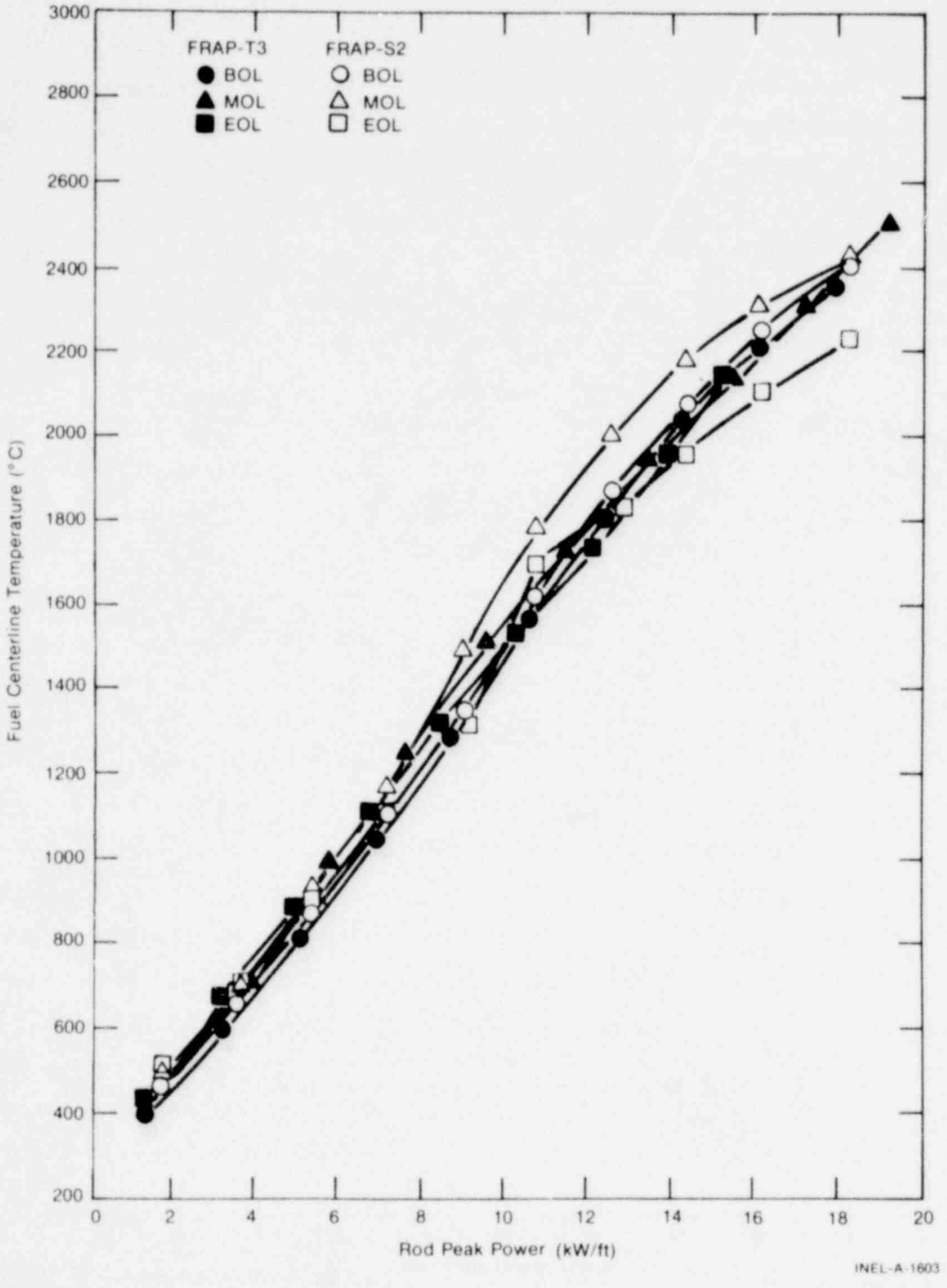

Fig. 4 Initial condition fuel centerline temperature versus local power for a 7 x 7 rod at beginning-, middle-, and end-of-life.

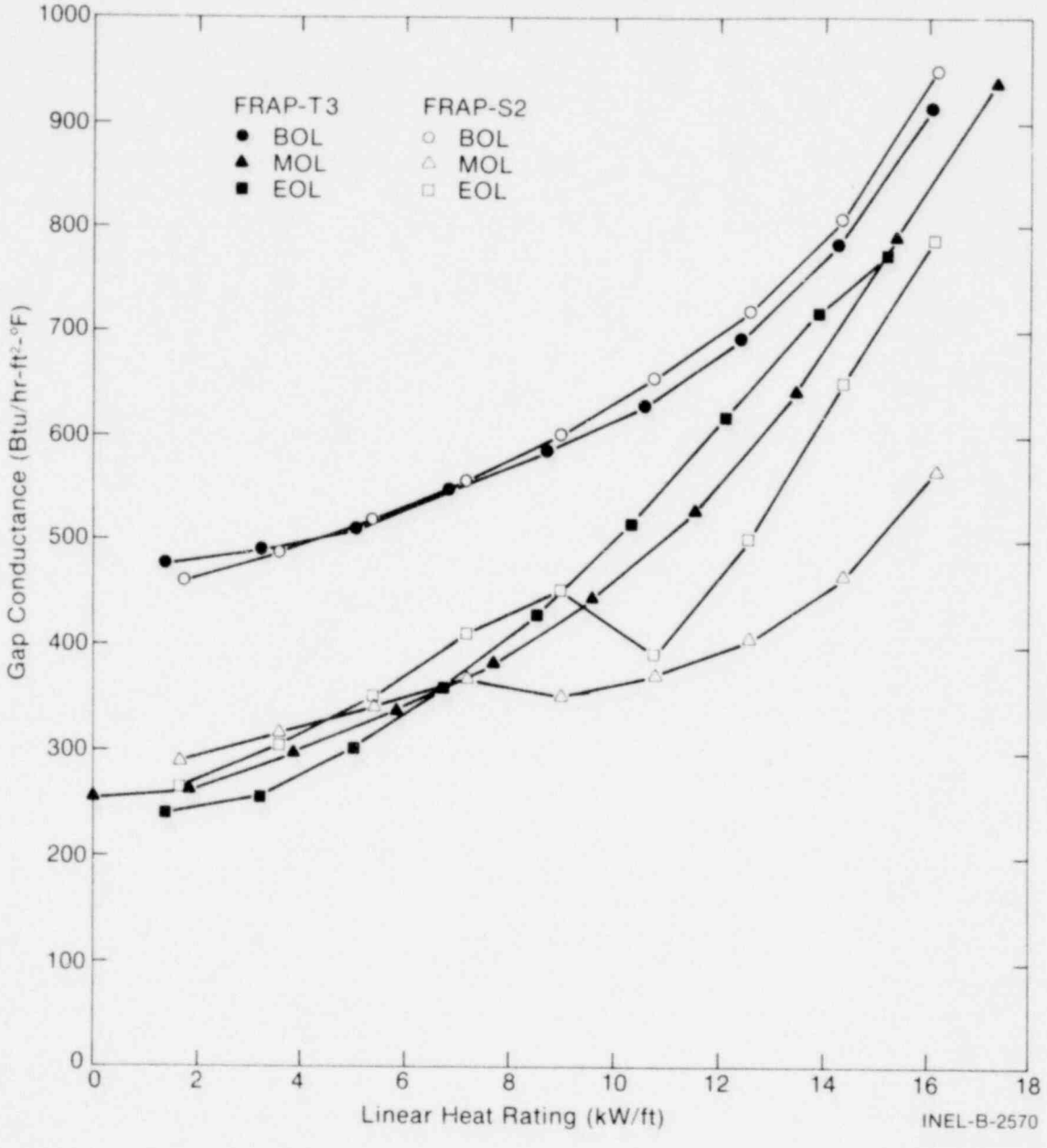

Fig. 5 Initial condition gap conductance versus local power for a 7 x 7 rod at beginning-, middle-, and end-of-life.

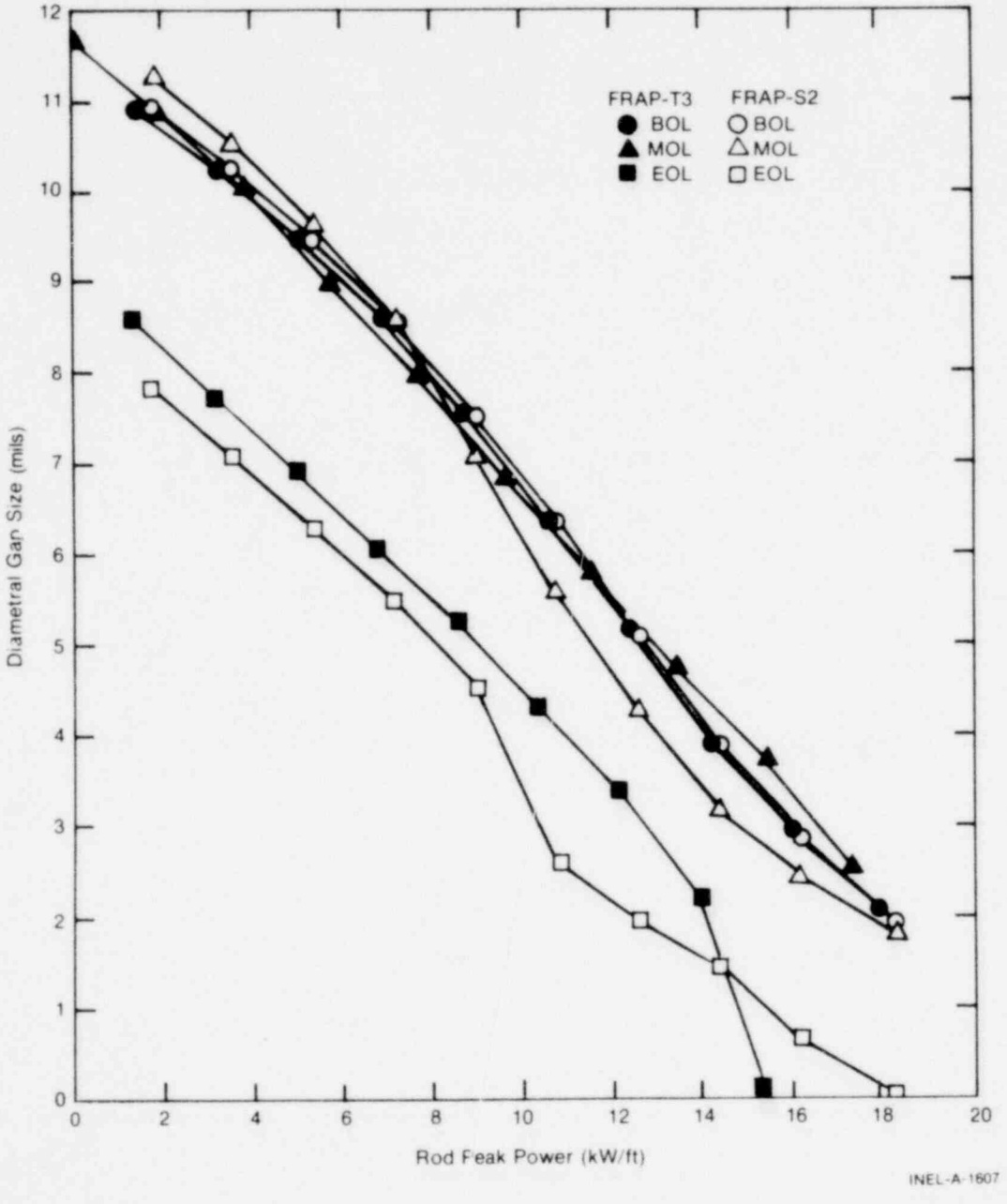

Fig. 6 Initial condition gap size versus local power for a 7 x 7 rod at beginning-, middle-, and end-of-life.

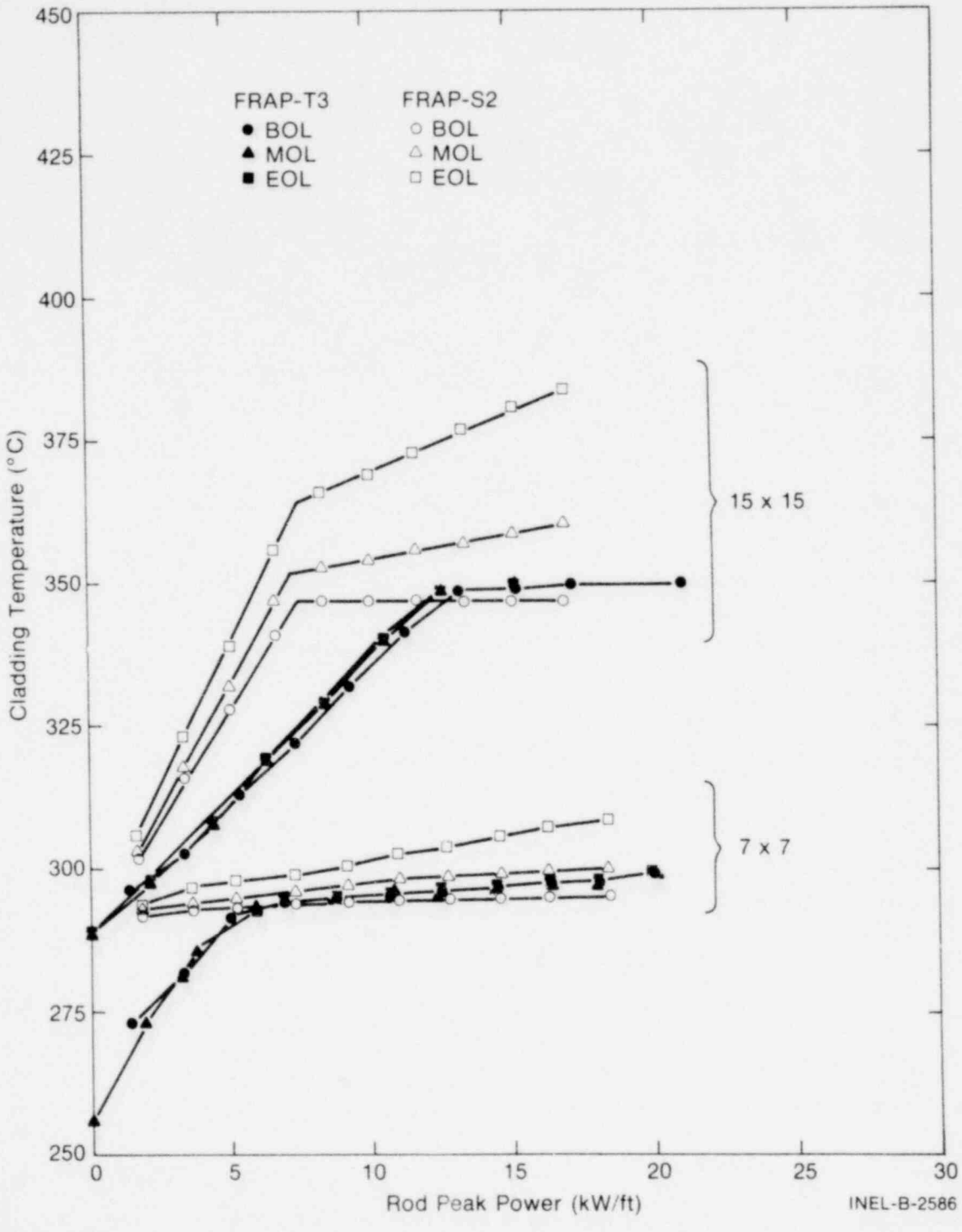

Fig. 7 Initial condition peak cladding surface temperature versus local power for 15 x 15 and 7 x 7 rods at beginning-, middle-, and end-of-life.

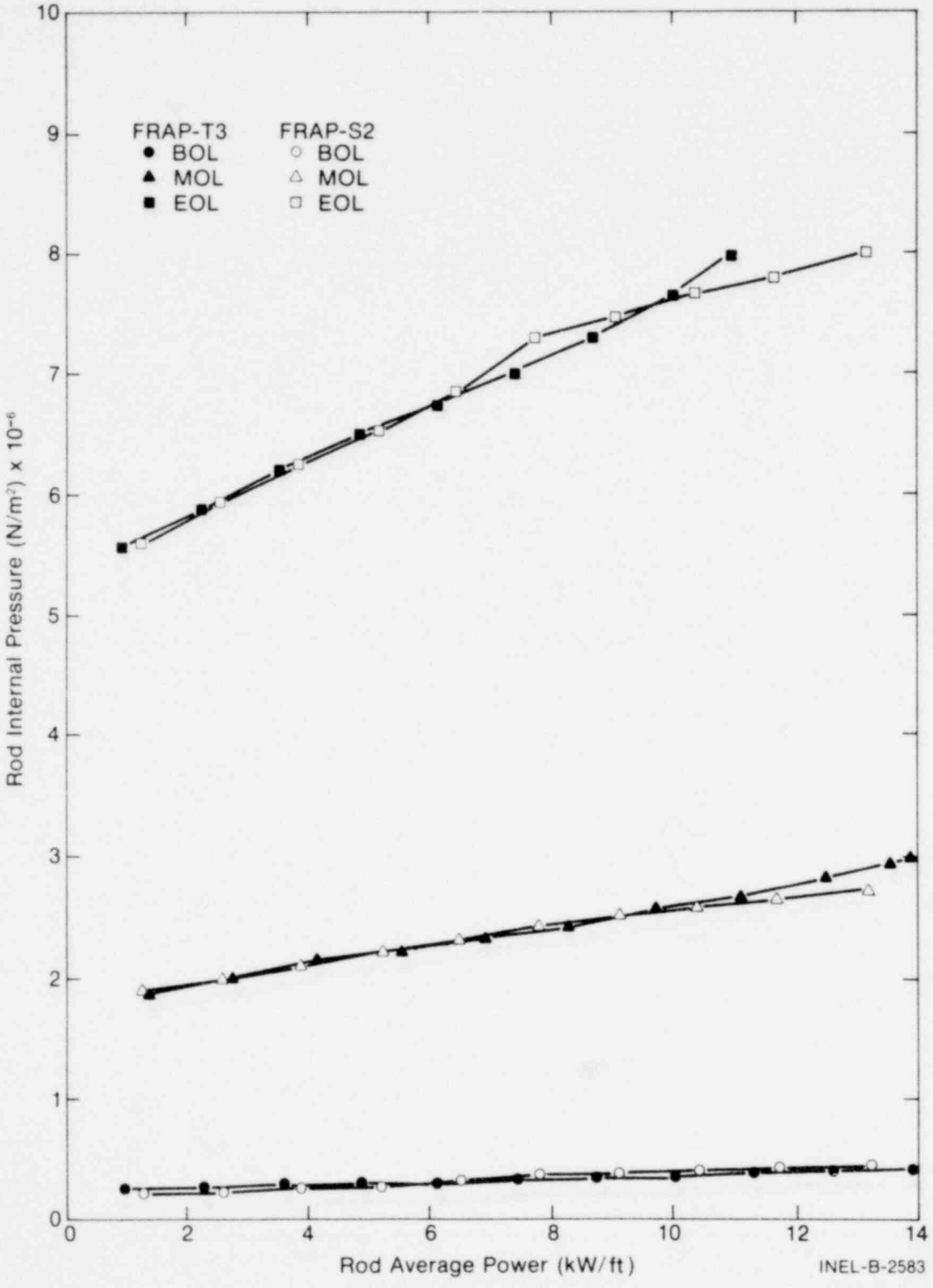

Fig. 8 Initial condition rod internal pressure versus rod average power for a 7 x 7 rod at beginning-, middle-, and end-of-life.

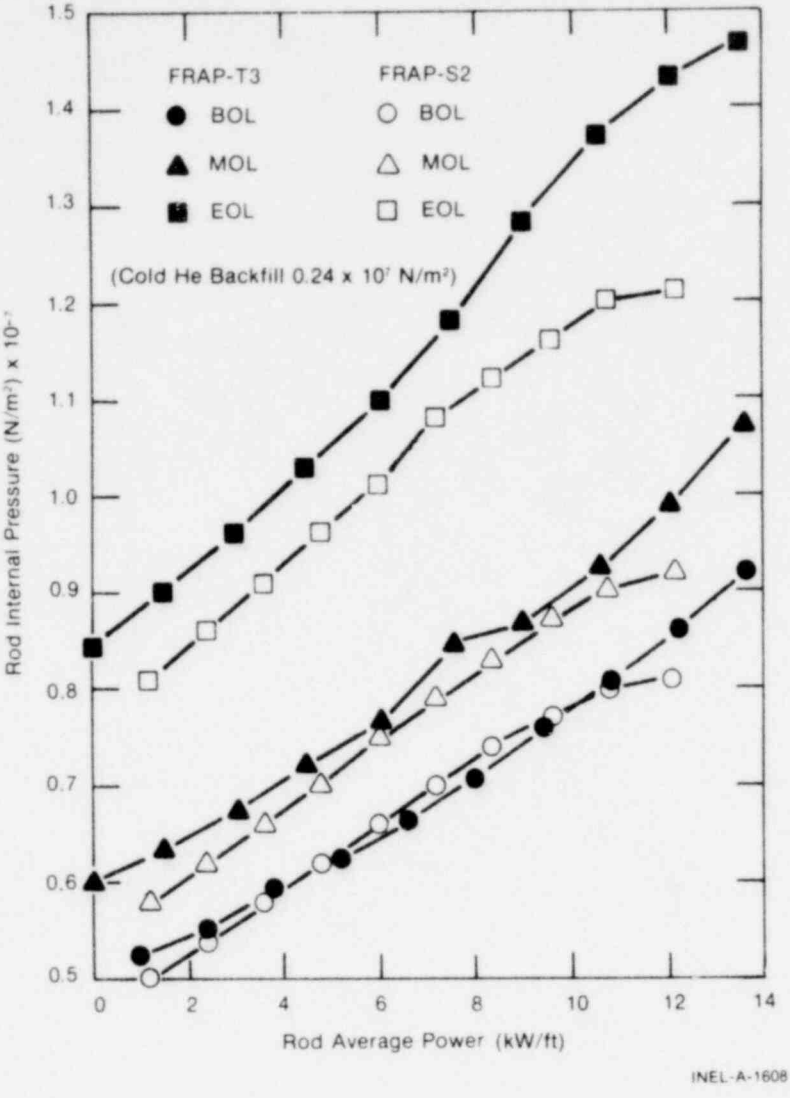

Fig. 9 Initial condition rod internal pressure versus rod average power for a 15 x 15 rod at beginning-, middle-, and end-of-life.

with burnup-dependent FRAP-S2 output. The 7 x 7 results in Figure 8 show good reproducibility between the two codes at all burnups. Previously reported pressure inconsistencies existed, however, between FRAP-S1 and FRAP-T2 for dished pellet 15 x 15 rods. Figure 9 shows that the specification of higher active length void volume temperature in FRAP-T3 results in comparable internal pressure conditions.

The relatively small rod pressure differences which are still evident between FRAP-S2 and FRAP-T3 are consistent with the comparison between calculated plenum temperatures shown in Figure 10. Results indicate that the first principle plenum temperature model in FRAP-T3 is quite sensitive to gas composition. Less evidence of plenum temper-

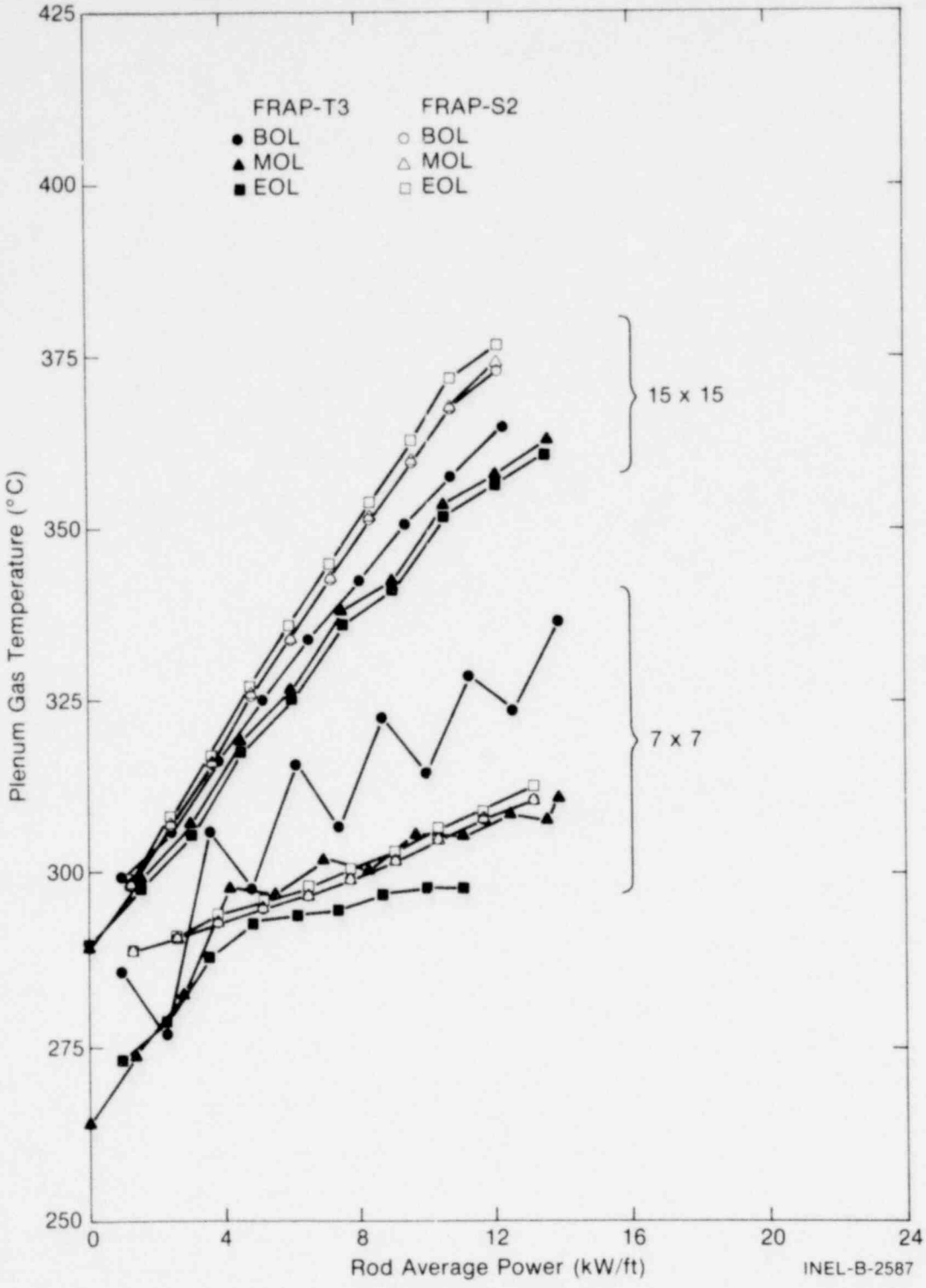

Fig. 10 Initial condition plenum gas temperature versus rod average power for 15 x 15 and 7 x 7 rods at beginning-, middle-, and end-of-life.

oscillation corresponds to conditions when the gas thermal properties are dominated more by an individual component of the mixture. Due to large differences in relative fission and fill gas abundance between 7 x 7 and 15 x 15 rods, this situation occurs at either end-of-life (large fission gas fraction) or beginning-of-life (large fill gas fraction), respectively.

IV. STEADY STATE DATA COMPARISONS

A large number of steady state fuel temperature and rod deformation data comparisons have been reported previously as part of the FRAP-S2 model verification[6]. In this section, a limited number of steady state FRAP-T3 results are given for rods selected largely from the FRAP-S2 data set. More recent pressurized rod thermal data were added to the sample. Fuel temperature and gap conductance results are discussed first, reestablishing applicability of previous conclusions concerning accuracy of the thermal model in characterizing realistic initial accident conditions. Thermal expansion and rod deformation comparisons are then addressed in order to benchmark performance of gap closure and associated mechanical response models.

1. FUEL TEMPERATURE AND GAP CONDUCTANCE

FRAP-S2 data comparisons had shown some tendency for the model to overpredict unpressurized rod temperature (especially for rods with significant calculated fission gas release) and underpredict pressurized rods. Calculated centerline temperatures were generally found to be within ±10% of the data up to 16 kW/ft and 1800°C. Selected FRAP-S2 rods were reanalyzed using FRAP-T3 to verify that the same relative agreement could be obtained. Input coupling of permanent burnup effects on rod geometry, gas, and pressure conditions was made between FRAP-S2 and FRAP-T3. The radial power distribution for Halden rods, previously based on the low enrichment FRAP-S2 model, was changed to be more consistent with the higher enrichments used. Reported values were used for 10 and 20% enriched PBF rods. The codes use similar surface heat transfer, gap conductance, and material properties models.

Figure 11 summarizes measured and predicted steady state fuel temperatures for helium prepressurized rods. A tendency is seen to underpredict centerline temperature in most cases. The data represent

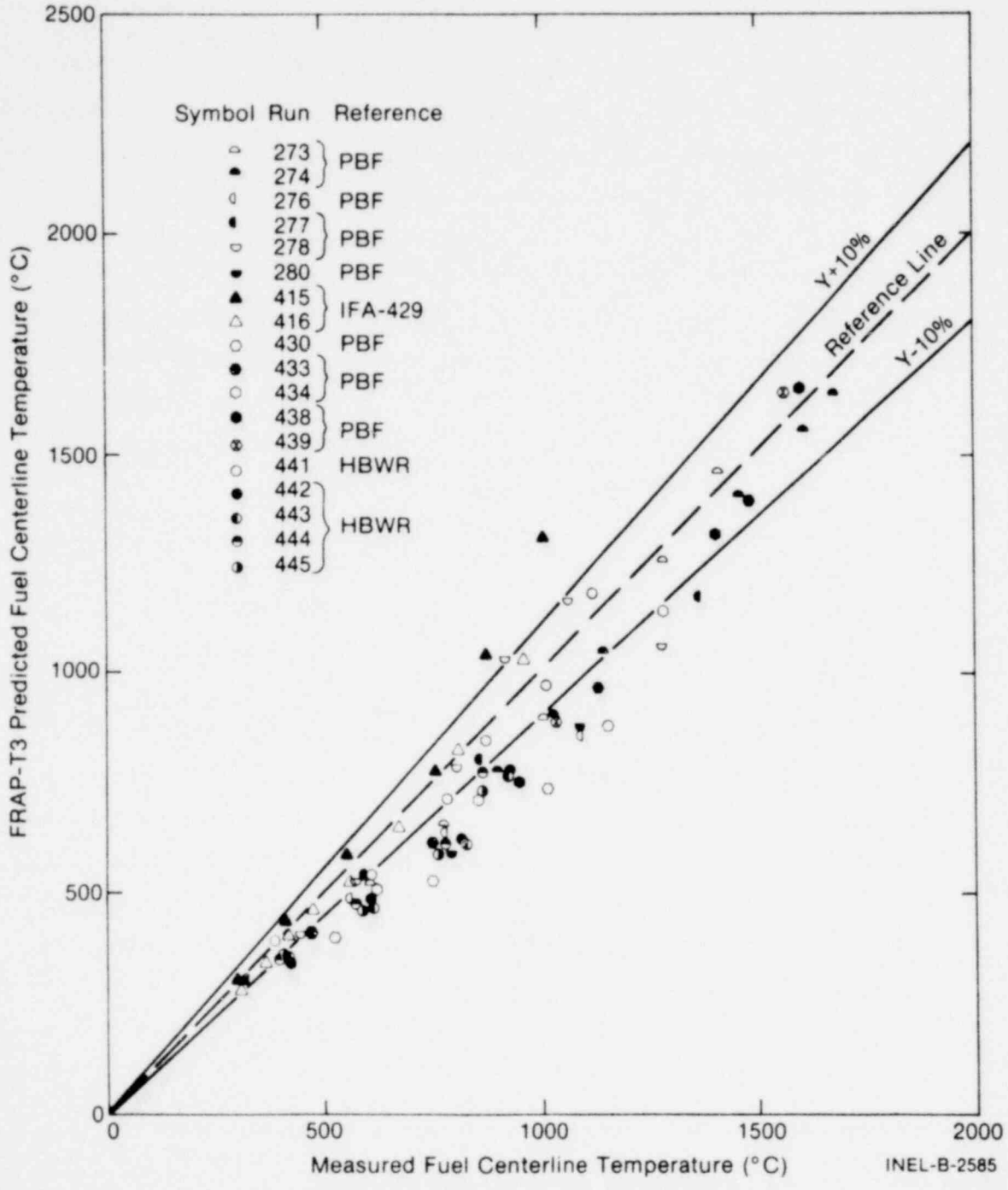

Fig. 11 Predicted versus measured fuel centerline temperature for pressurized rods.

startup measurements for 18 rods in three different experiments. Fractional gap sizes and fuel density ranged from 2.2 to 3% and 91 to 95%, respectively. The general trend is consistent with overpredicting gap conductance for a subset of pressurized rods, as shown in Figure 12. It is likely that rod internal gas composition was well characterized by the code for the early life, low gas release conditions reflected in the data. Also, the same fuel cracking thermal model is used in FRAP-T3 as was shown in FRAP-S2[6] to be within measurement error of thermal data from rods in the 2% gap range. Results indicate then, that the calculated gas composition effect on gap heat transfer remains too strong at high pressure.

Results of unpressurized rod fuel temperature and gap conductance data comparisons are shown in Figures 13 and 14. With the exception of two rods having relatively large calculated or as-built fission gas content, calculated temperatures seem to bracket the reference line within normally expected data uncertainty. This trend is consistent with the previously mentioned strong influence of gas composition. Gap conductance comparisons in Figure 14 reflect startup conditions only. The results show more scatter for small gap rods. Difference between the relatively high level of measured and predicted gap heat transfer in these cases does not result in significant fuel temperature error. Bar figures for some of the data represent the difference due to whether or not startup sorbed gas release is considered. Heat transfer for moderate-size helium filled gap conditions seems well represented by the model.

2. ROD INTERNAL PRESSURE

Previously reported FRAP-T2 data comparisons for rod internal pressure[3] were inconclusive because the available measurements were for small plenum rods, which reflected inseparable heatup and gas release effects. Evaluation of a larger amount of pressure data during FRAP-S2 verification[6] showed that normal operation gas release in unpressurized

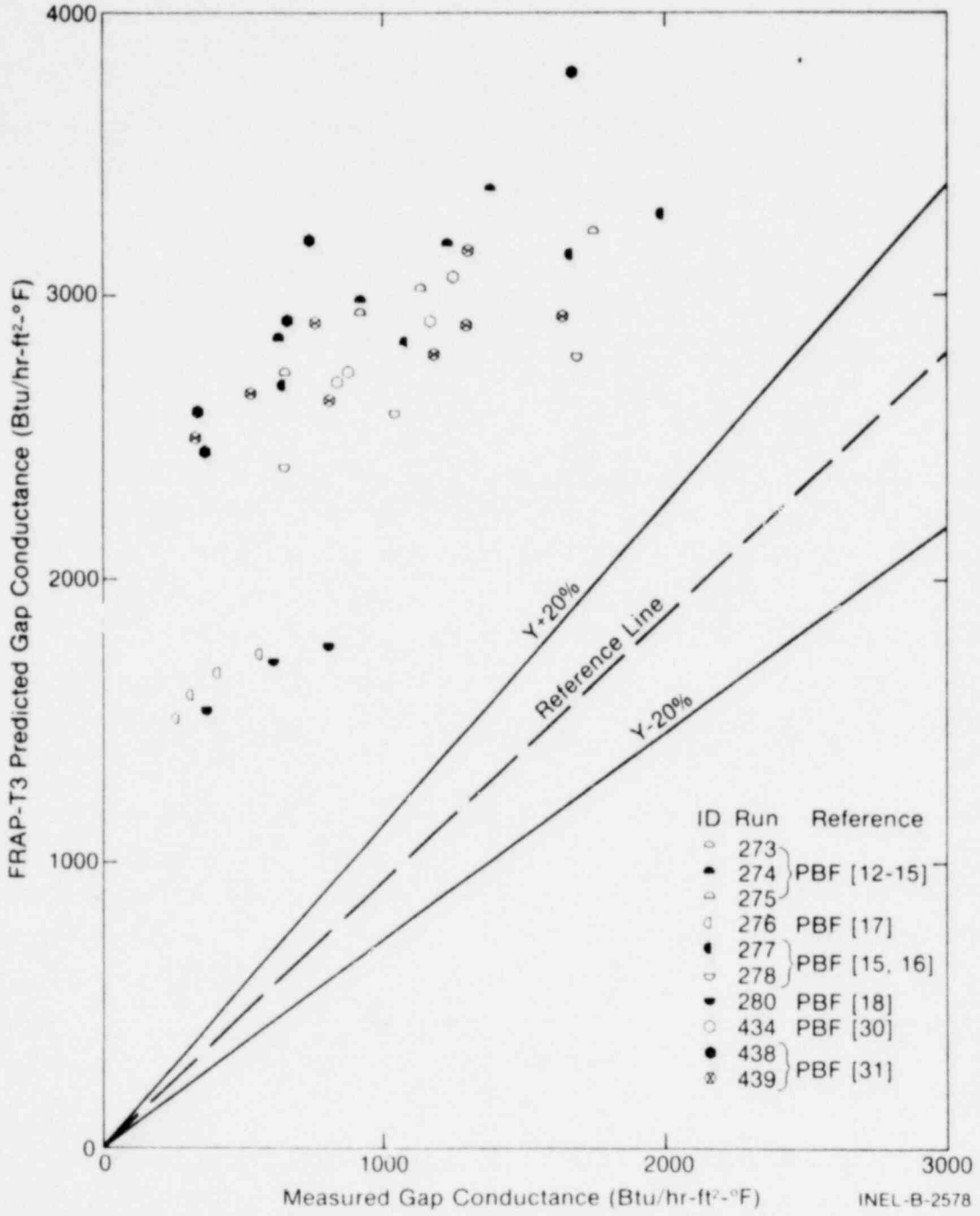

Fig. 12 Predicted versus measured gap conductance for pressurized rods.

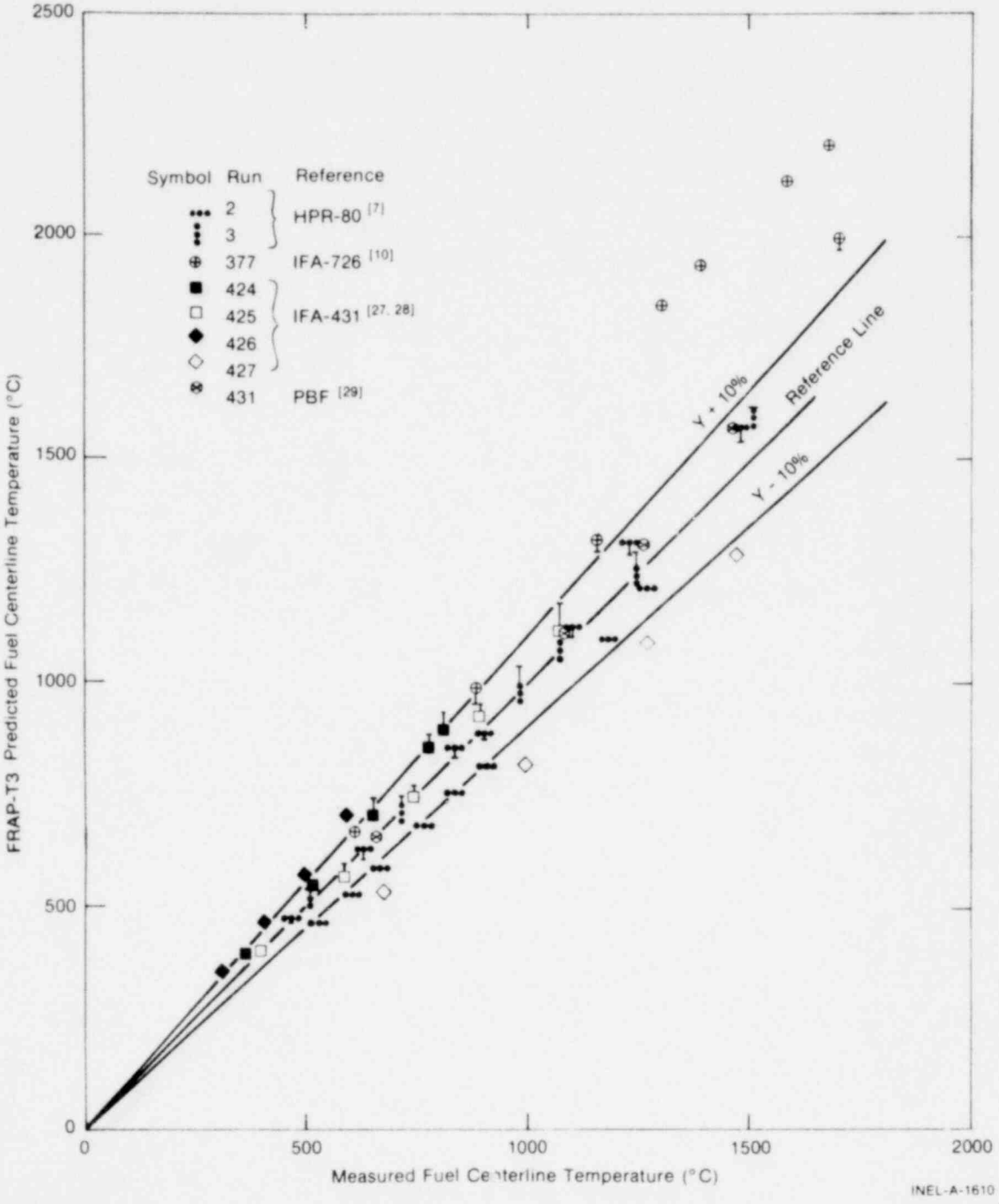

Fig. 13 Predicted versus measured fuel centerline temperature for unpressurized rods.

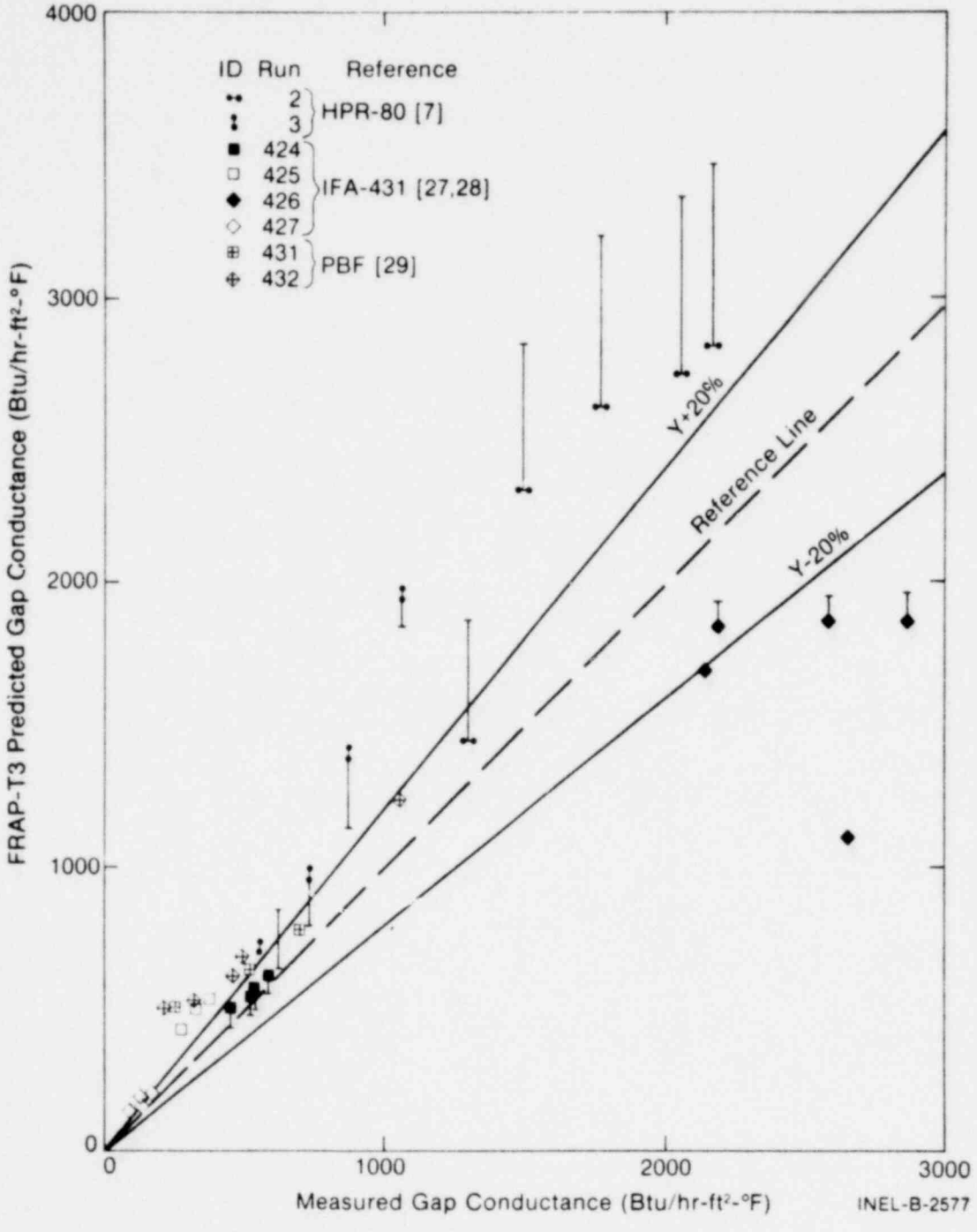

Fig. 14 Predicted versus measured gap conductance for unpressurized rods.

rods could control initial pressure conditions for transients. Pressurized rod conditions are such that the gas release effect does not totally dominate internal pressure levels. Since FRAP-T3 by itself does not consider gas release, only early life data indicative of the heatup effect on internal pressure have been considered here.

Figure 15 compares measured and predicted rod startup pressure for a wide range of conditions. Cold fill gas pressures are either 15, 375, or 550 psia. Most of the high pressure results fall within 10% of the measured values. Unpressurized rod predictions are more scattered due to higher sensitivity to pellet out-gassing and use of relatively small plenums. The latter point is clarified in Figure 16 when the range of relative model error is seen to increase with decreasing relative plenum volume. In this direction, accuracy of calculated pressure becomes more governed by adequacy of less characterized active length gas volume and temperature models.

The pressure predictions as a whole are between 5 and 10% lower than those reported during FRAP-S2 verification. This difference is explained by (a) startup release of sorbed gas not considered by FRAP-T3, (b) somewhat different active length void volume and temperature assumptions between the codes, and (c) higher plenum temperature in FRAP-S2. The effect of rod temperature changes alone on internal pressure level seems well represented by the model. Accuracy of the model for burnup conditions hinges on the ability to characterize steady state and transient fission gas disposition.

3. ROD DEFORMATION COMPARISONS

Unless the cladding is calculated to balloon, the deformation model in FRAP-T3 is essentially the same as that used in FRAP-T2. FRAP-S2 has the same thermal expansion and gap closure model as FRAP-T3, but also accounts for extended burnup effects due to fuel densification and swelling, and uniform cladding creep collapse. Both FRAP-T2 and FRAP-S2

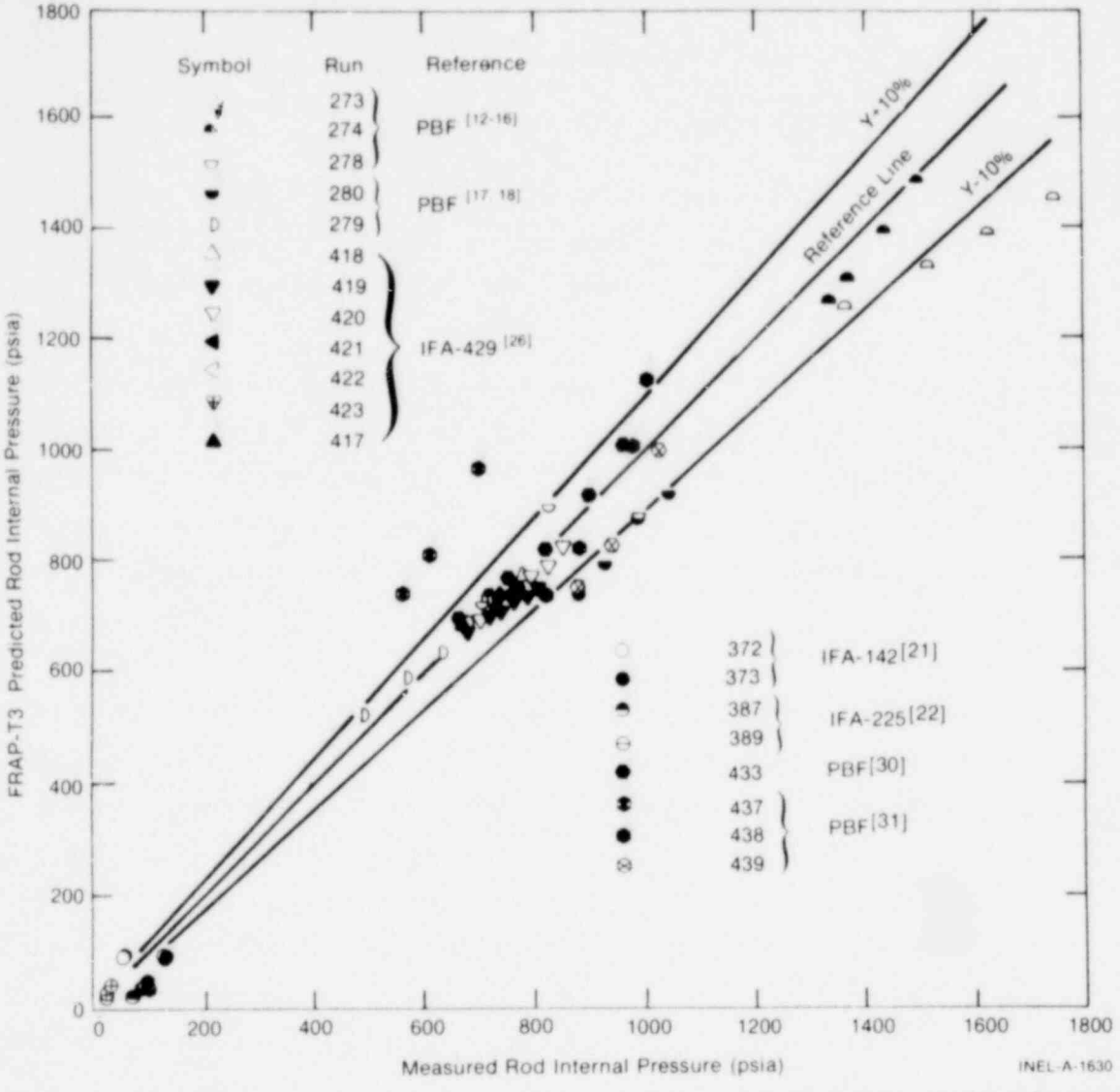

Fig. 15 Predicted versus measured rod internal pressure during heatup.

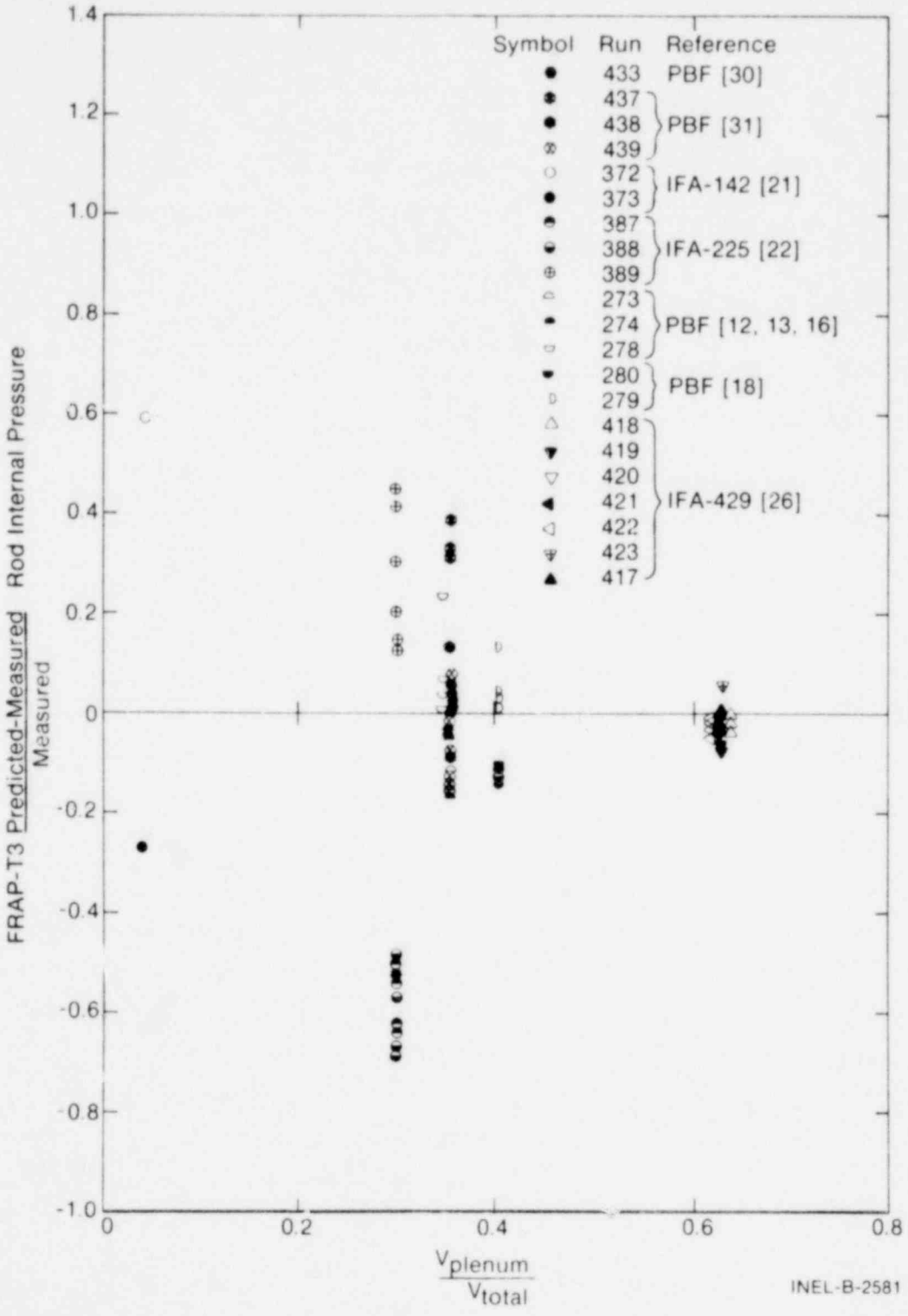

Fig. 16 Predicted-measured/measured rod internal pressure versus V_{plenum}/V_{total}.

1571 199

had shown the capability for calculating fuel axial expansion during power ramps prior to gap closure and below 1700°C. With the exception of small gap conditions, gap closure has not been well represented by any of the codes. Lack of fuel mechanical deformation after gap closure causes PCMI hoop strain to be overestimated above UO_2 plasticity temperatures, while axial PCMI effects are always overpredicted. Rods operated over slow power ramps were chosen from the FRAP-S2 data set and reanalyzed using FRAP-T3. Rod deformation results discussed here, provide updated benchmarking of thermal expansion, gap closure, and PCMI models. These mechanisms are expected to influence fuel behavior, to at least some degree, regardless of operating condition.

3.1 Fuel Elongation

Figure 17 compares initial startup measured and predicted stack axial expansion relative to system temperature for several rods. Since the instruments in this case read length change relative to the cladding, the reference data have been adjusted upward by measured cladding elongation when available. Otherwise, observed and predicted fuel thermal expansions are only compared up until the point when PCMI becomes evident.

The same heatup elongation trends are seen as reported previously from FRAP-S2, using the same data. Low values of expansion are better represented by the model. This is because at low fuel temperature, PCMI stresses are less likely to have increased to the point of allowing the data to reflect fuel mechanical deformation not considered by the model. Since the model effectively assumes the fuel to have infinite strength, it is expected that fuel expansion would be overestimated by FRAP-T3 for operating conditions accompanied by hard gap closure and fuel plasticity.

3.2 Gap Closure Conditions

Rather than regenerate prior verification conclusions, results of cladding strain data comparisons are indirectly used to diagnose

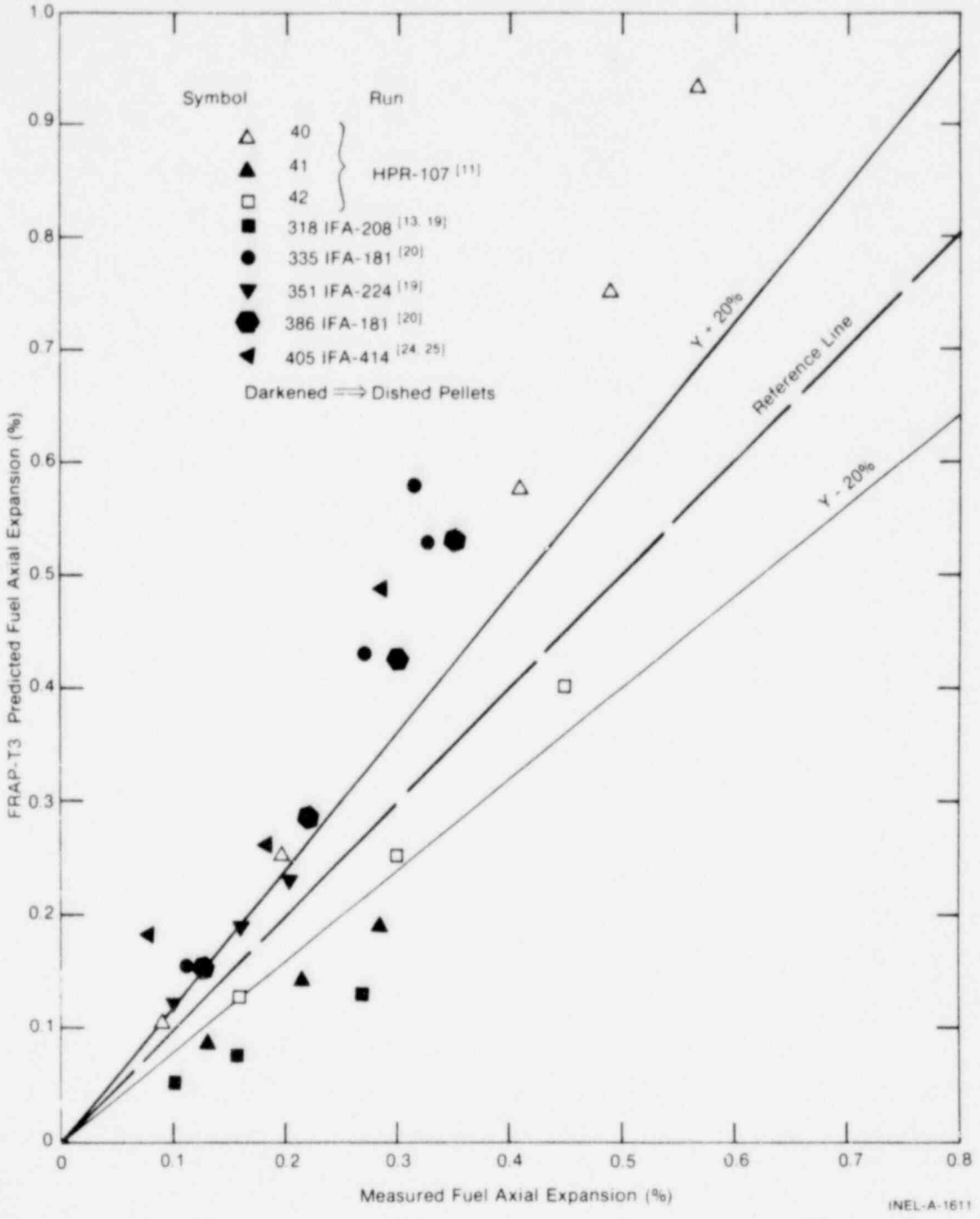

Fig. 17 Predicted versus measured fuel heatup expansion.

differences between measured and predicted gap closure conditions. Improvement of fuel relocation models is a prerequisite for both FRAP-S and FRAP-T treating stress-dependent fuel deformation, as well as providing a better representation of relative cracked pellet and gap heat transfer effects.

Cladding strain measurements during slow power changes were analyzed in order to at least bracket power conditions corresponding to the onset of gap closure. Interpretation of slope changes for circumferential and axial strain data was based respectively on local and average heat rating. The uniform (mid-pellet) gap predicted by FRAP-T3 to still exist at the measured gap closure heat rating was then related to fuel design and operating conditions. Results indicate the magnitude of geometry adjustment needed to revise free thermal expansion, PCMI, and fuel cracking models to be more consistent with observed trends.

Two approaches were used to represent the required gap closure adjustment. In one case (I), fuel relocation is described in terms of fractional pellet dimension. In the second approach (II), gap closure is related to the fractional space calculated to still be available when relocation effects become evident.

Case I results are shown in Figures 18, 19 and 20. The range of results for an individual rod in both x and y directions represents uncertainty in interpreting gap closure heat rating from cladding deformation response. The ordinate corresponds to gap closure adjustment divided by fuel diameter. The pellet diameter is less sensitive than the gap to temperature and burnup changes. The fuel then, should provide a relatively stable dimensional parameter by which to represent its own relocation. Figures 18 and 19 show that Case I relocation is not strongly related to fuel temperature or density in the indicated range. This observation is not surprising if the gap closure mechanism is also strongly dependent on gap space itself, in addition to fuel dimension. Figure 20 supports this view by indicating a more orderly trend between fractional pellet relocation and initial gap size. This trend is consistent with the physical expectation that gap closure is an inevitable

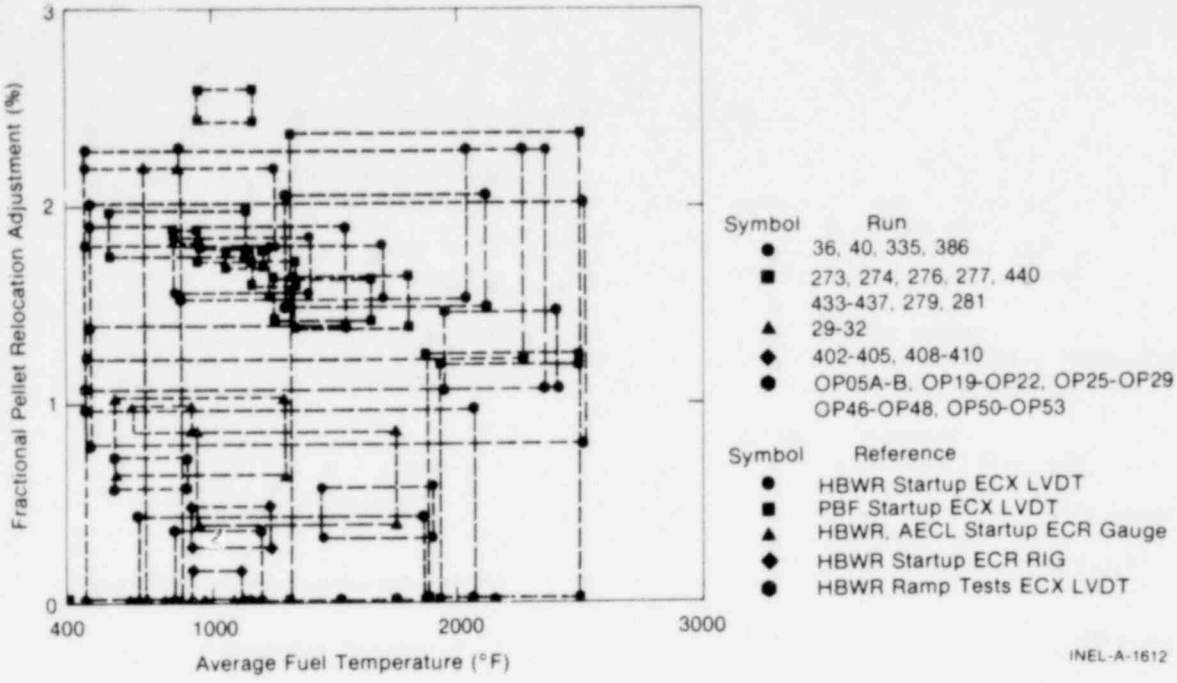

Fig. 18 FRAP-T3 fractional pellet relocation adjustment versus average fuel temperature.

operating mechanism with macroscopic effects limited by the space available for open cracks. Previously reported verification analysis for cladding strain had always indicated little need of adjustment for modeling fuel relocation for very small gap rods.

Case II results are shown in Figures 21 and 22. Here, the ordinate value corresponds to gap closure adjustment divided by cold gap size. Consistent with the Case I analysis, bulk fuel indices such as fuel temperature, density, and diameter were observed to have an indeterminant influence on fuel relocation. Figures 21 and 22 show that the gap size effect on the Case II relocation index exhibits an identifiable trend. This trend, however, is less well characterized than the Case I results in Figure 20. The increased scatter is due to strong temperature and burnup sensitivity for both numerator and denominator in the purely gap-dependent Case II representation of fuel relocation.

Observed gap closure appears then, to behave in a more stable manner when physically expressed in terms of fractional pellet redistribution into an initially present gap. The Case I relocation index incorporates the more appropriate combination of both driving pellet dimension and crack space availability.

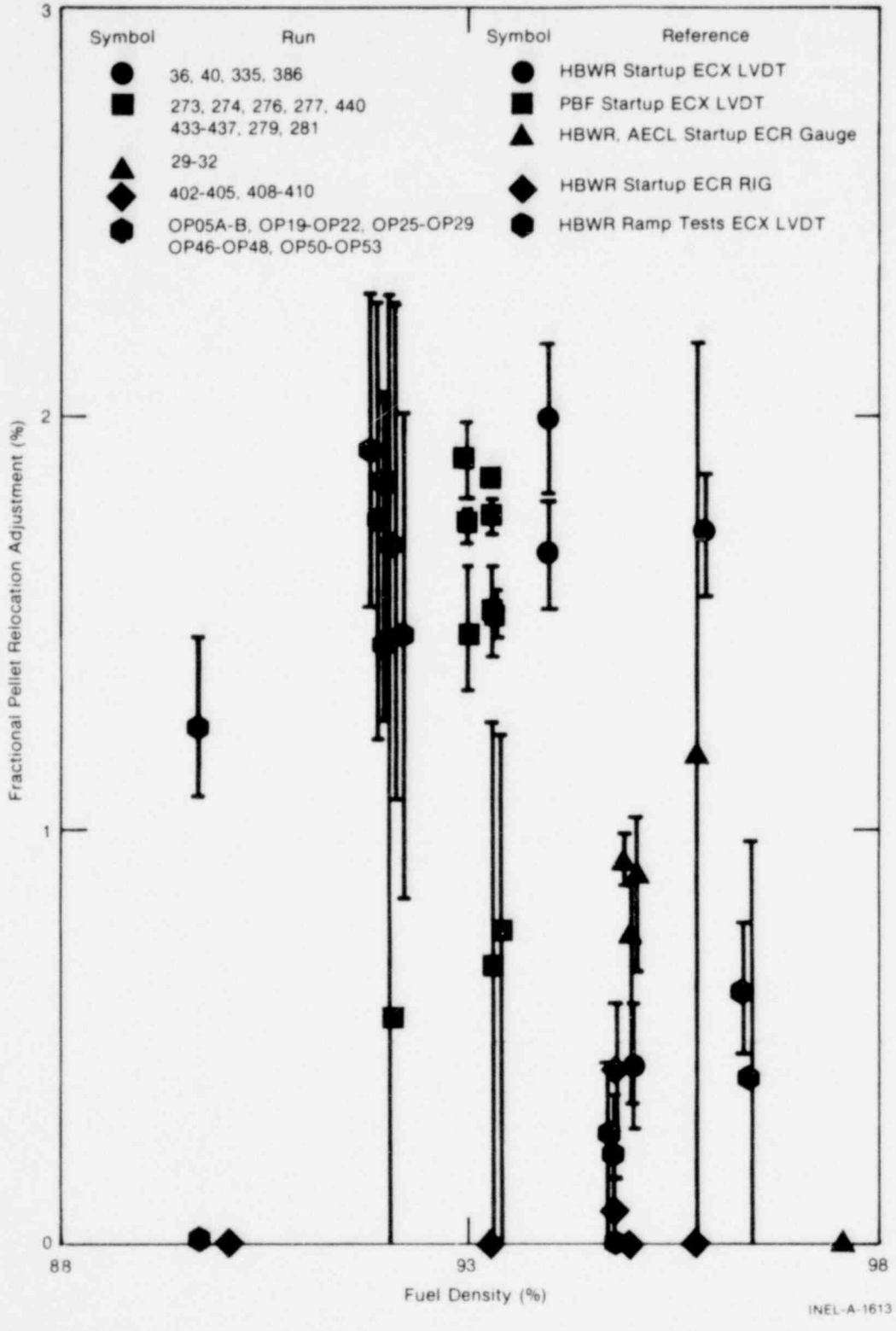

Fig. 19 FRAP-T3 fractional pellet relocation adjustment versus fuel density.

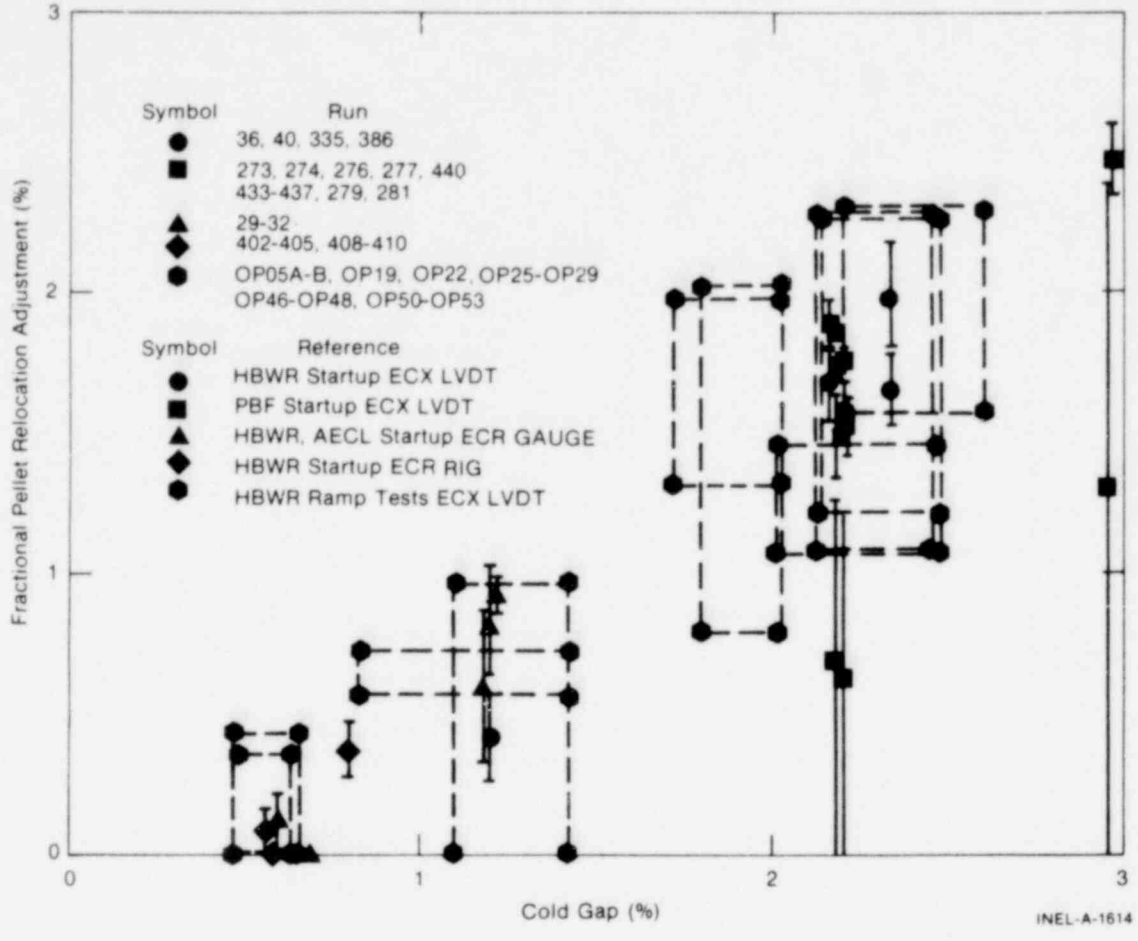

Fig. 20 FRAP-T3 fractional pellet relocation adjustment versus cold gap.

The Case I gap closure adjustment from Figure 20 is also amenable, in a programming sense, to modifying the currently calculated hot pellet diameter. A varying amount of fractional relocation can be directly added to the fractional free thermal expansion. Figure 20 bar symbols for rods with calculated permanent burnup effects indicate that the amount of relocation seems equally related to either as-built or burnup-dependent cold gap sizes. Cladding deformation after calculated gap closure would be greatly overestimated, however, by the revised model, unless crack closure during soft interaction and both fuel and cladding plasticity during hard interaction acted to accommodate stress and increase the unadjusted gap size for subsequent thermal cycles.

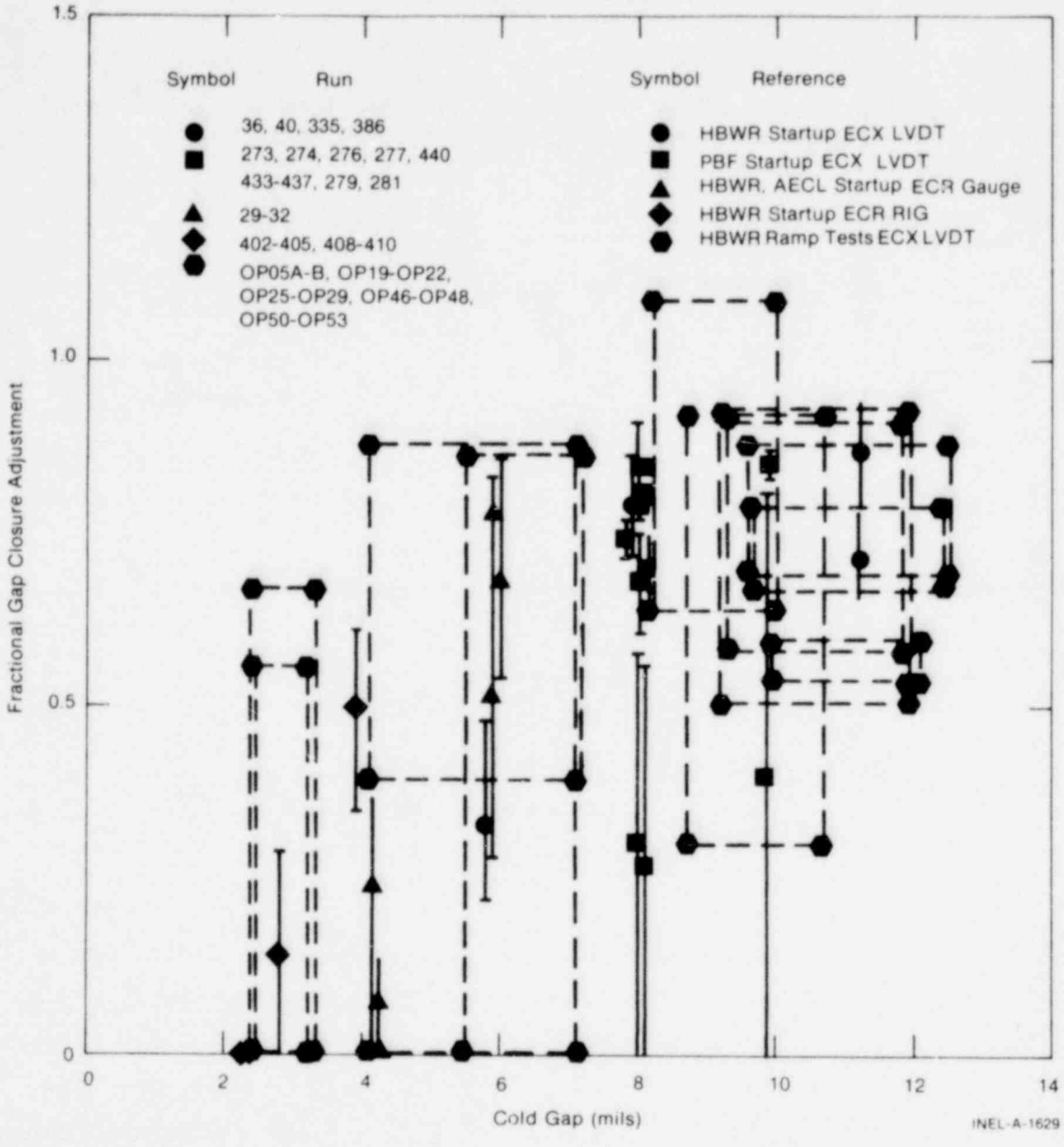

Fig. 21 FRAP-T3 fractional gap closure adjustment versus cold gap.

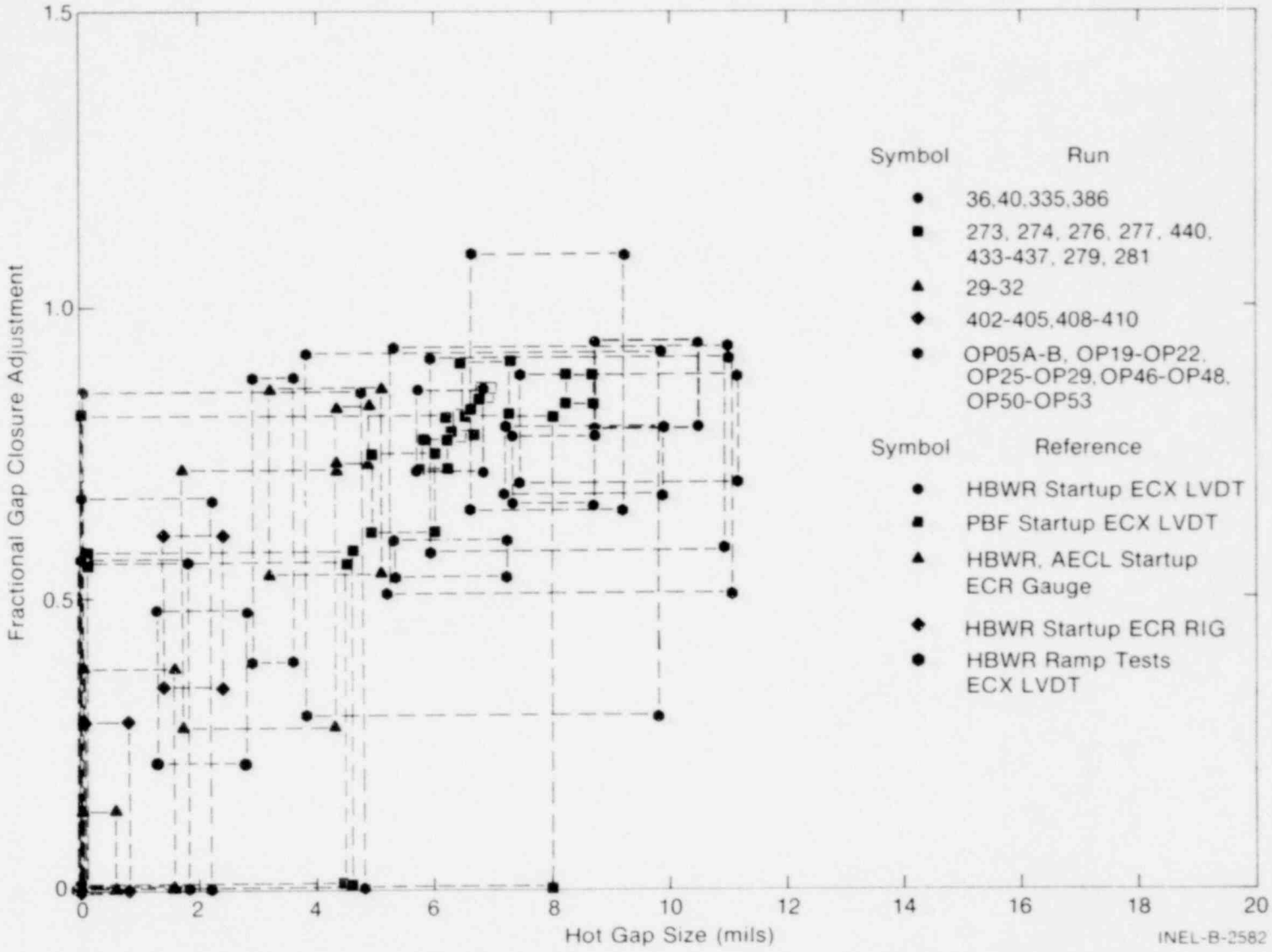

Fig. 22 FRAPT-T3 Fractional gap closure adjustment versus hot gap size.

V. OFF-NORMAL DATA COMPARISONS

This section gives results for burnout and overpower data prediction comparisons. How the fuel ultimately performed in these experiments or whether the governing fuel operating mode was steady state or transient is not the main point here. The available measurements describe conditions which coincide only with the beginning of some off-normal response. Even if data existed to show that subsequent cladding heatup or deformation rates were well represented by transient predictions, the model's ability to initiate off-normal response at the appropriate time or operating conditions is a prerequisite for demonstrating overall predictive capability.

1. ONSET OF BURNOUT

As shown in Table I, the burnout experiments were done under three different sets of system and geometry conditions. Namely, these were 500 psi - small bundle geometry; 900 psi - large bundle geometry; and 2200 psi - single-rod geometry. For the bundle tests, inlet mass flux was slowly decreased while the rods operated at nominally constant power. For the high pressure tests, rod power was either increased while constant inlet mass flux was maintained, or held constant while inlet mass flux was decreased. In all cases, cladding temperature or thermal expansion detectors responded when dryout occurred at various measured combinations of flow and heat rating.

FRAP-T3 was used to generate a set of burnout curves for each experiment. A relationship was determined between channel inlet mass flux and rod power input to the channel at the calculated point of departure from normal surface heat transfer. This point was identified in FRAP-T3 with the calculated occurrence of a heat transfer mode other than forced convection to liquid (mode 1) or nucleate boiling (mode 2). For various levels of constant heat rating or mass flux input, burnout

was predicted to occur as either flow or power was slowly changed so as to approach a deficient heat transfer condition. Use of different CHF correlations was specified by varying an input switch. Equivalent single-channel analysis was applied in all cases. Relative agreement shown by the data comparisons then, is influenced by unknown system-dependent experiment factors, mainly cold-wall and cross flow effects.

Figure 23 shows the measured and predicted burnout curves for a large cluster test at essentially BWR conditions (940 psia). There is little uncertainty with respect to inlet fluid conditions input for this case. The full length bundle configuration with 36 rods and relatively small equivalent cold-wall effect also tends to promote development of uniform flow conditions. The range of values shown in Figure 23 reflects sensitivity of both measured and predicted burnout response to three different inlet enthalpy levels. As expected, the high fluid quality BWR correlation (GE)[a] represents the data well for these flow conditions. For well characterized inlet conditions and uniform flow, FRAP-T3 seems to correctly apply the pre-CHF fluid enthalpy increase along the channel.

In Figure 24, measured and predicted burnout curves are shown for three different heavy boiling water reactor (HBWR), small-bundle experiments (490 psi). Again, there is little uncertainty associated with the inlet fluid conditions input to FRAP-T3. Since the restricted bundle geometry in this case includes cold walls, uncertainty exists as to whether the bundle inlet mass flux data are correctly associated with a burnout event in the hot subchannel. Assuming that the data are correct, all correlations shown in Figure 24 appear to predict burnout at somewhat lower than observed mass flux. It would require only a 10 to 15% decrease in the subchannel flow, however, to bring the bundle flow data into agreement with the equivalent channel analysis considered by FRAP-T3.

---

[a] See Report I of this document.

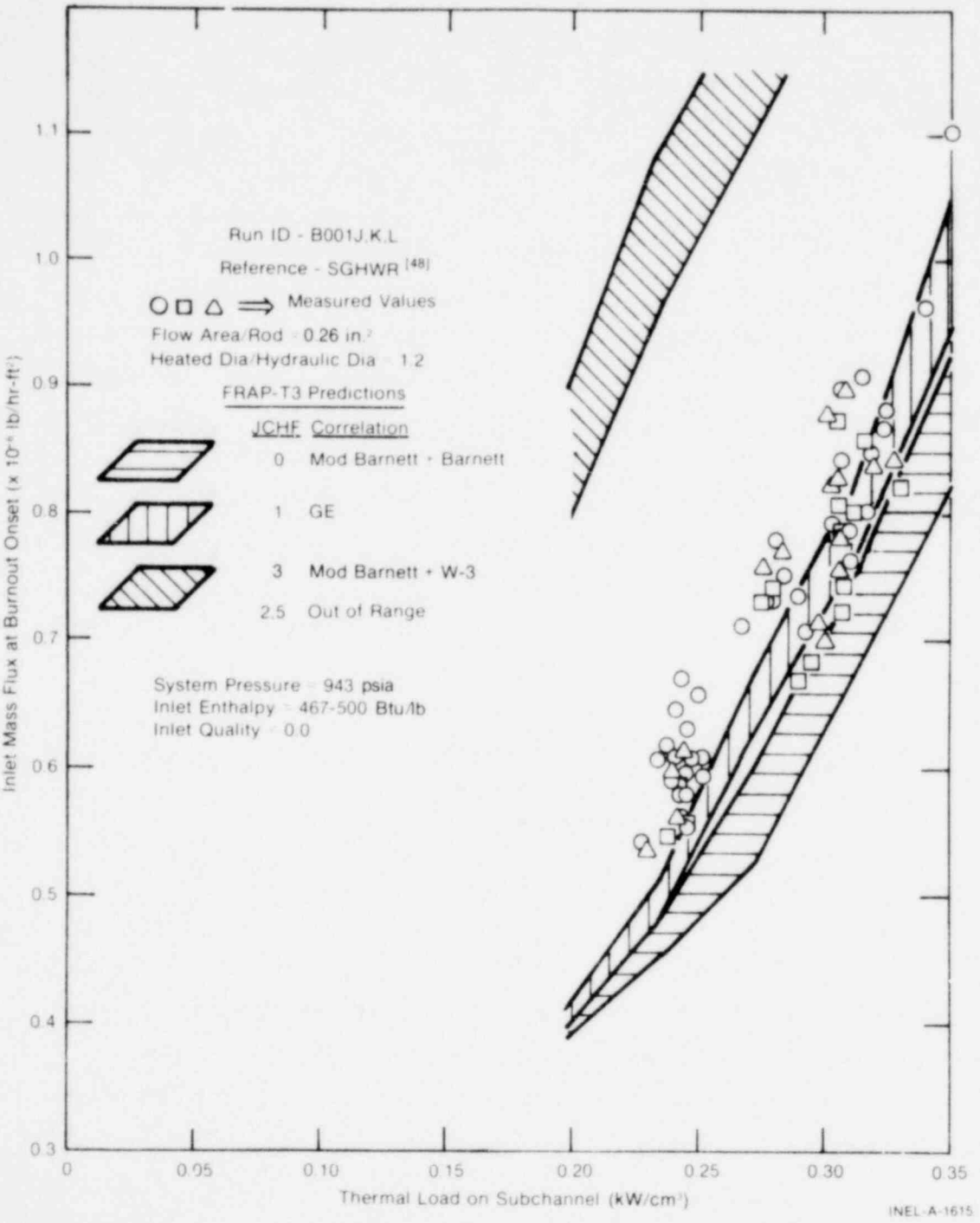

Fig. 23 SGHWR inlet mass flux at burnout versus rod thermal output, circular pitch large bundle geometry, small cold-wall effect, no inlet enthalpy uncertainty (BØ01).

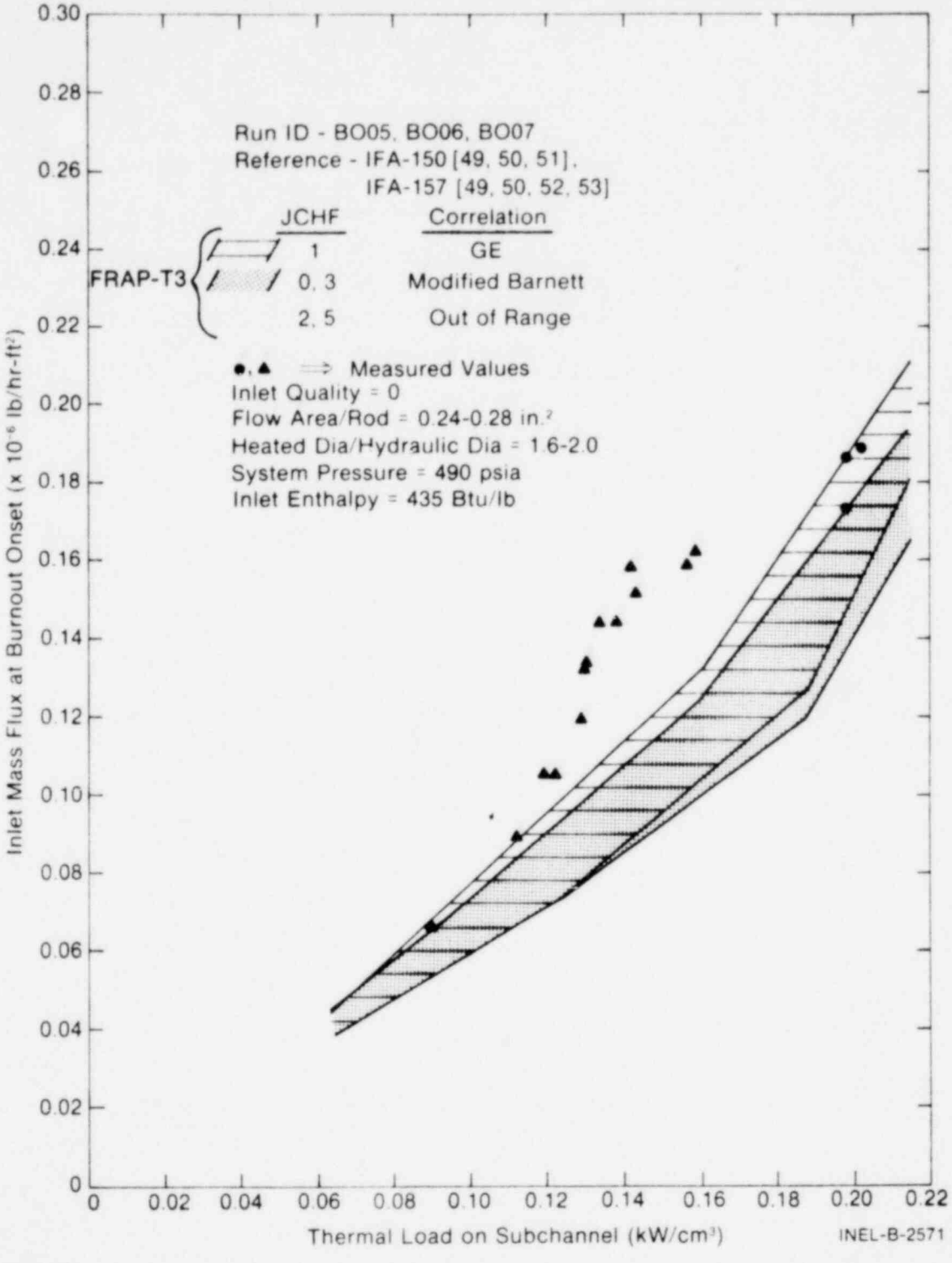

Fig. 24 HBWR Inlet mass flux at brunout versus rod thermal output, 3 x 3 small bundle geometry, shroud cold wall, no inlet enthalphy uncertainty (BØ05, 06, 07).

1571 211

In Figure 25, the measured and predicted burnout curves are presented for two, small-bundle, HBWR experiments of different designs. In both cases, a separate fuel bundle occupied a position below the inlet to the burnout cluster. As a result, a range of inlet qualities was specified for separate runs in an attempt to reduce the additional uncertainty with respect to inlet enthalpy conditions to the burnout cluster. As a result of this analysis, an inlet fluid quality of between 0.1 and 0.3 was found to represent the data best.

The range of predicted values shown in Figure 25 for Run BØ04 reflect a range of inlet conditions varying from slightly subcooled to a quality of 0.2. Use of the BWR correlation provides better agreement with the data. Scattered results for Run BØ09 reflect low flow conditions and a somewhat atypical four-rod geometry. This combination prevents the drawing of firm conclusions as to adequacy of any one correlation.

Figure 26 indicates that increasing the flow area per rod and the relative cold-wall factor (heated diameter/hydraulic diameter) has an effect on the model but not on the data. When comparing the measured and predicted burnout values for Runs BØ05, BØ06, BØ07, and BØ08, the measured values show similar behavior among experiments. Even though the inlet fluid conditions are well characterized for all cases, Run BØ09, with its combination of larger flow area and cold-wall factor, is the only experiment for which both correlations predicted burnout at higher than observed inlet mass flux.

Figures 27, 28, and 29 show the measured and predicted onset of burnout curves for several single-rod experiments conducted in the PBF[12-13,15-18,30-31] at system pressures of about 2200 psi. Previous verification results had indicated that unknown shroud flow distribution effects resulted in low sensitivity of the measured burnout flow to power for the only two experiments available at that time. Summary verification analysis of an expanded number of tests now shows that sensitivity of the data to power was well within the range of measurement scatter. The data, as a whole, seem most affected by some combi-

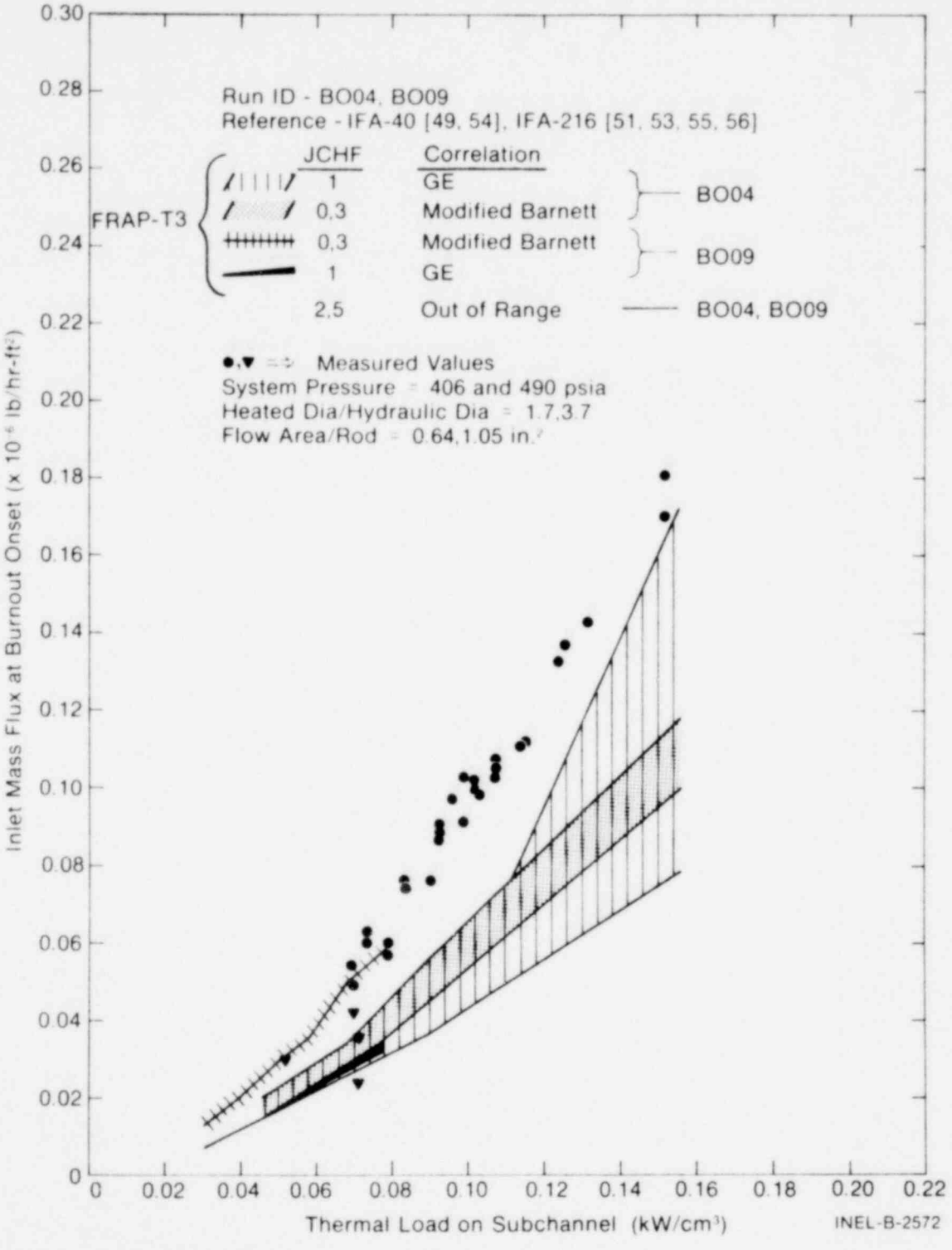

Fig. 25 HBWR Inlet mass flux at burnout versus rod thermal output, circular pitch small bundle geometry, shroud cold wall, significant inlet enthalpy uncertainty (BØ04, BØ09).

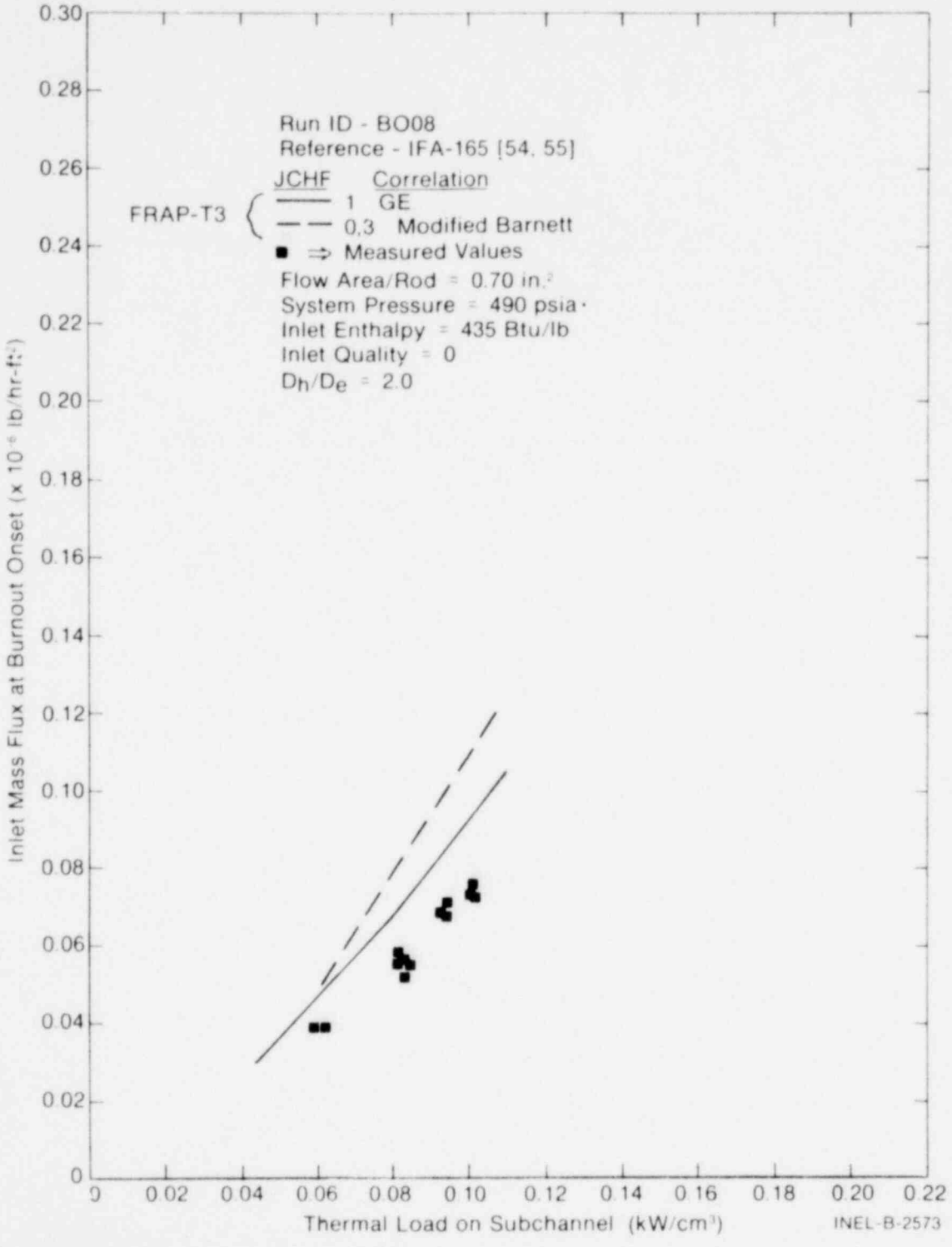

Fig. 26 HBWR Inlet mass flux at burnout versus rod thermal output, circular pitch small bundle geometry, shroud plus instrument tube cold wall, no inlet enthalpy uncertainty (BØ08).

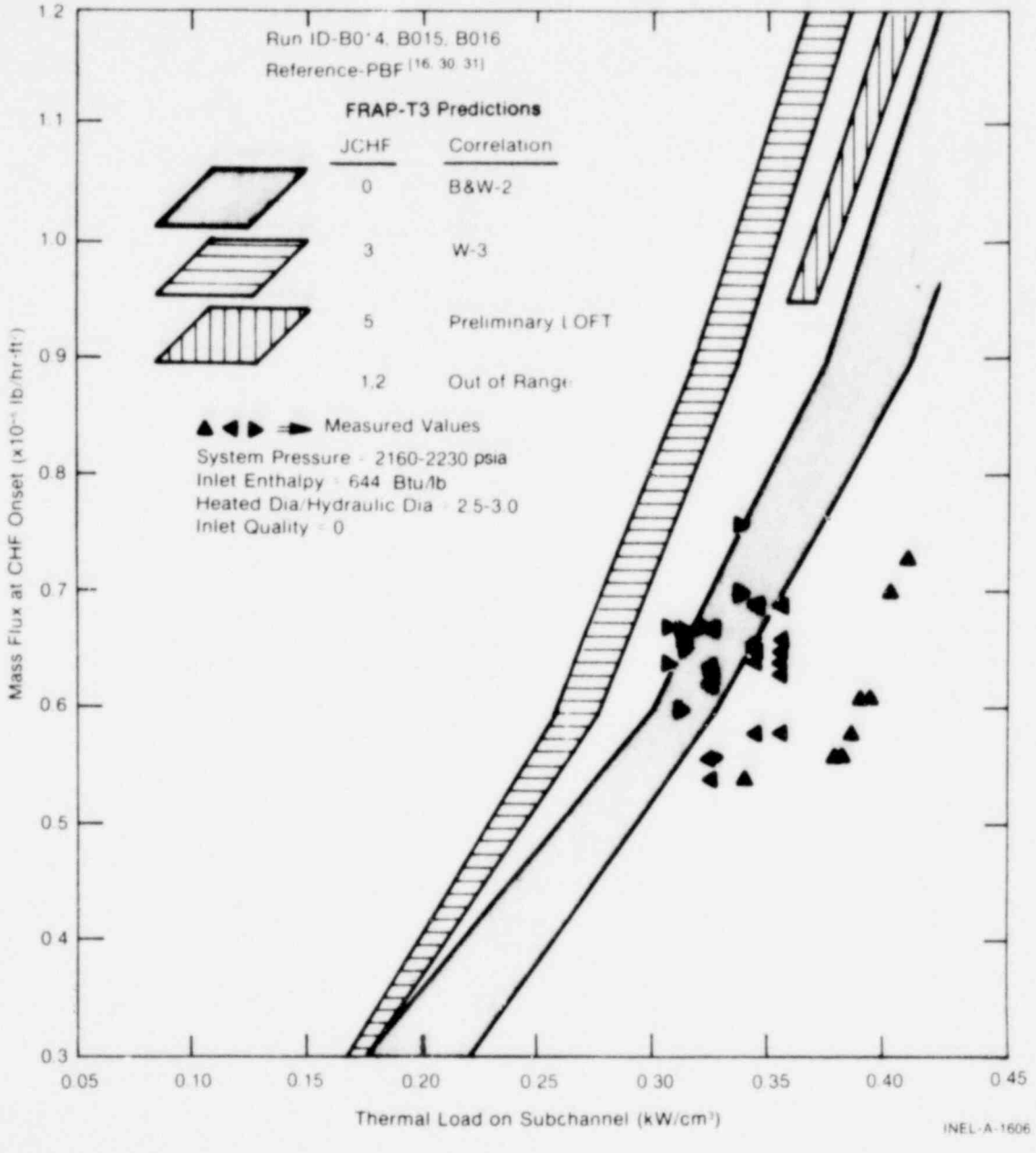

Fig. 27 PBF Inlet mass flux at burnout versus rod thermal output-(BØ14, 15, 16) - low flow area tests.

1571 215

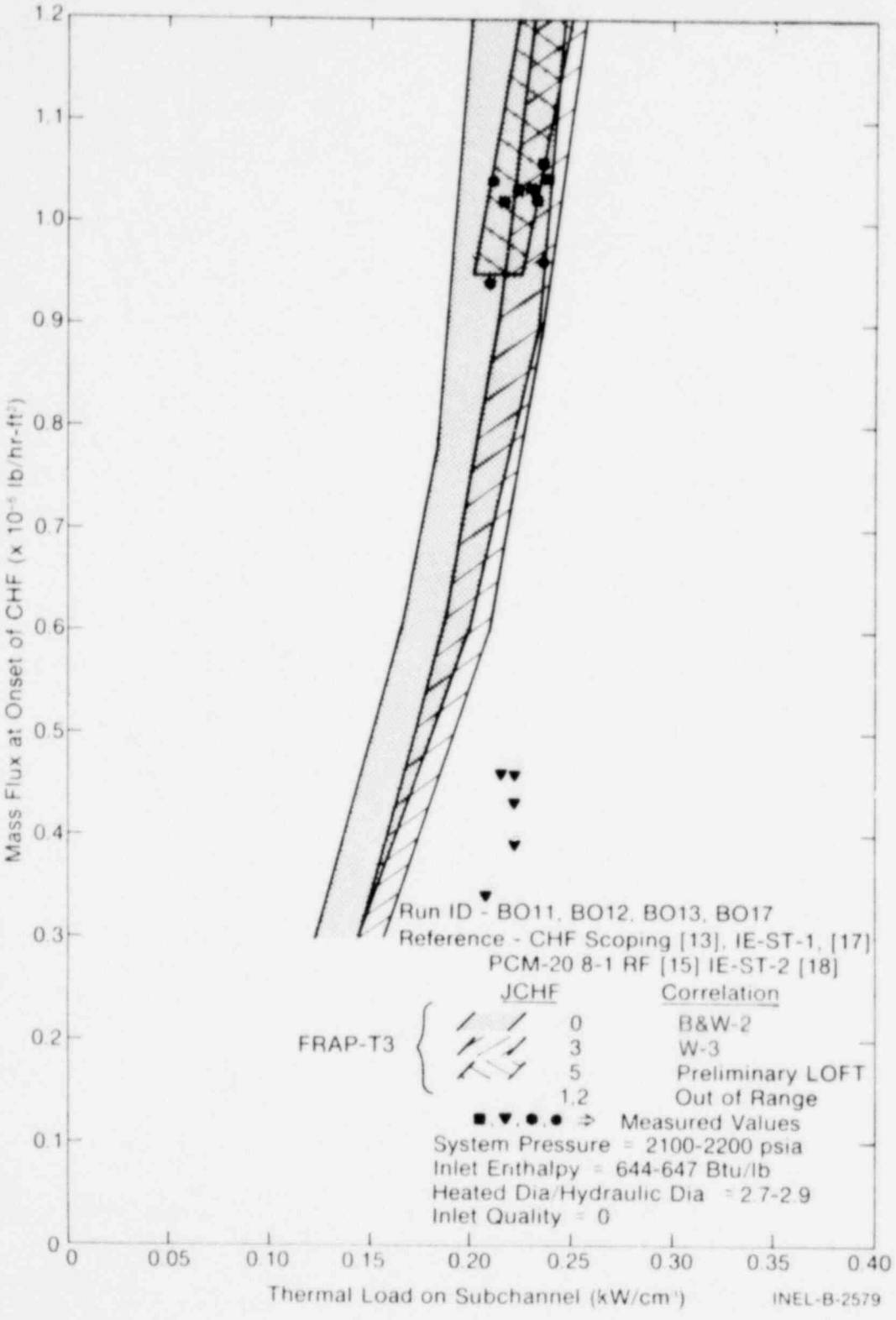

Fig. 28 PBF Inlet mass flux at burnout versus rod thermal output (BØ11,12, 17) - high flow area tests.

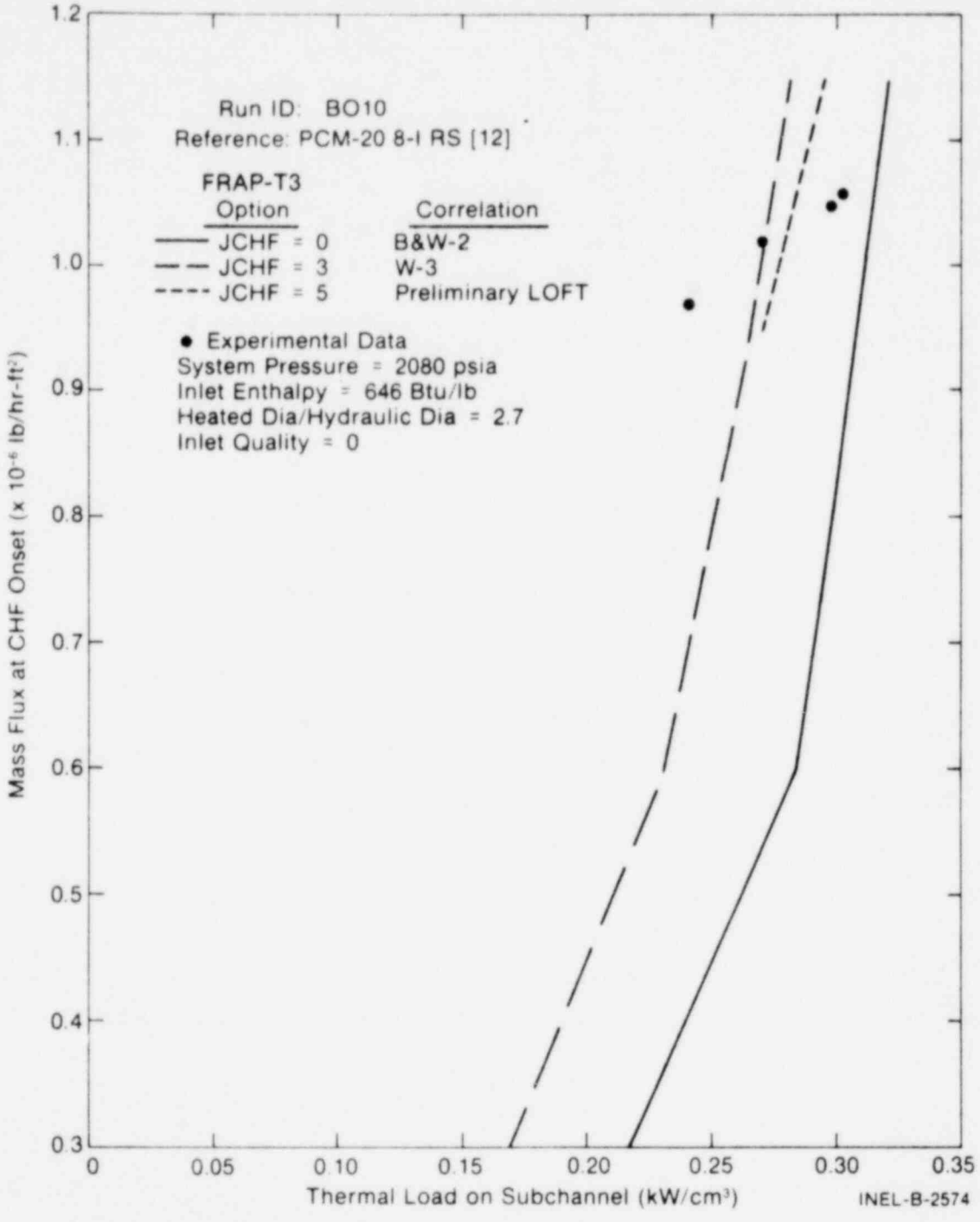

Fig. 29 PBF Inlet mass flux at burnout versus thermal output (BØ10) - moderate flow area test.

nation of flow area and whether or not standoff screws are present between the rod and flow shroud. These effects indicate that the PBF rig configuration and shroud flow velocity (rather than power or flow rate), cause development of different fluid heat transfer regimes as CHF is approached. Since the equivalent single-channel model in FRAP-T3 is mainly sensitive to flow area as opposed to other geometry effects, the data have been distinguished on this basis.

A comparison of measured and predicted burnout curves for low flow area (0.184-in.^{2}/rod) PBF tests is presented in Figure 27. The three experiments had rods and test rigs of similar dimension, and were conducted at about the same system pressure and inlet conditions. The range of predicted values for each correlation reflects calculated response to these variations. As can be seen, the measured burnout points are better represented by correlation 0 (B&W-2). Scatter in the measured values is greater than the range of predictions. In this case, more reproducibility of test results is desirable.

The measured and predicted onset of burnout curves for high flow area (0.31- to 0.33-in.^{2}/rod) PBF tests with similar design and operating conditions are presented in Figure 28. For each CHF correlation, a range of predicted values again corresponds to known differences between the tests. The burnout mass flux data for test PCM-20 8-1 RF appears to be low in comparison with the other measurements, as well as in comparison with FRAP-T3 results. Otherwise, the overall level and range of all predicted values is consistent with the data. Further interpretation is not clear, since the data are located in the steepest slope region of the burnout curve.

Results for the single moderate flow area (0.25-in.^{2}/rod) test are shown in Figure 29. In this case, the Westinghouse W-3, and preliminary Loss-of-Fluid Test (LOFT) correlations seem to represent the data better than B&W-2.

Figures 30 and 31 are shown in order to present summary FRAP-T3 burnout results in a more quantitative manner. These figures illustrate overall relative agreement between FRAP-T3 and the data for each CHF correlation. Comparisons in Figures 30 and 31 correspond to BWR and PWR fluid conditions, respectively.

For relatively low system pressure, the BWR (GE) correlation appears to represent the data more often than the other CHF models. Figure 30 indicates that (a) the BWR correlation (JCHF = 1) underpredicts the measured inlet mass flux at burnout by an average value of 8%, (b) the combination of Barnett - Modified Barnett correlation (JCHF = 0) underpredicts burnout mass flux by 15%, and (c) the Modified Barnett - W-3 correlation (JCHF = 3) overpredicts the data by 33%.

The current burnout data at high system pressure are best represented by the B&W-2 correlation (option 0). As shown in Figure 31, the inlet mass flux at burnout is overpredicted by an average value of 17% when option 0 is specified. Use of option 3 (W-3) results in an average overprediction of 48%, and use of option 5 (preliminary LOFT) results in an overprediction of 46%. Results for option 5 are incomplete due to low flow limits imposed by the model.

2. ONSET OF OVERPOWER CLADDING FAILURE

The overpower experiments employ rods of various design, operated with normal cooling but at increased heat rating relative to base irradiations of varying duration and severity. The measurements include power history, heat rating at failure where applicable, and cladding axial and circumferential elongation for some cases. The localization of cladding damage, so often observed during posttest examination, indicates that nonuniform PCMI effects certainly contribute to the failure process. Both PCMI and stress corrosion cracking (SCC) theories have alternately been used to explain failure results from individual experiments, gathered together here in the overpower run series. FRAP-T3

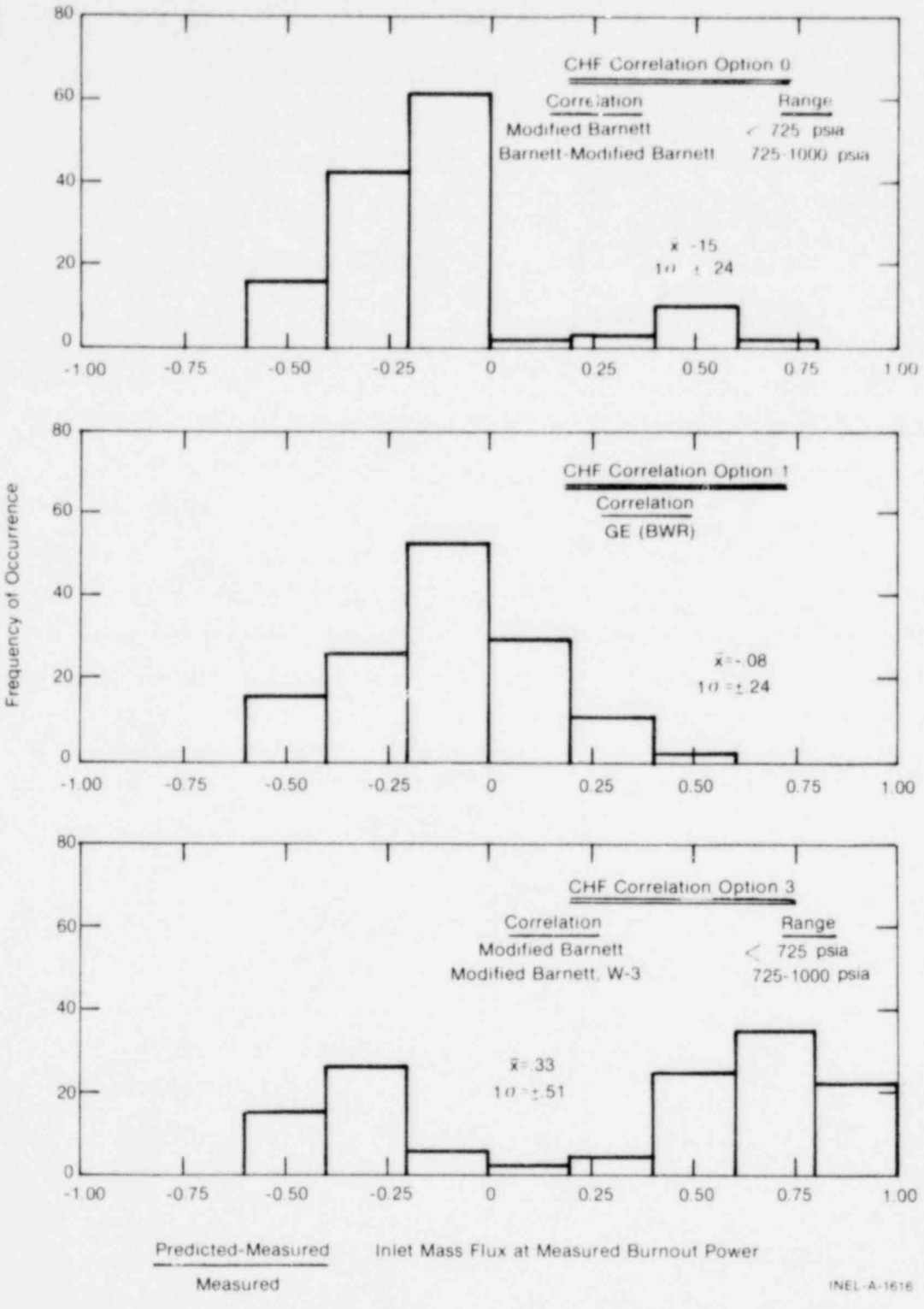

Fig. 30 Frequency of occurrence of predicted-measured/measured inlet mass flux at measured burnout power (BØ01 through BØ09).

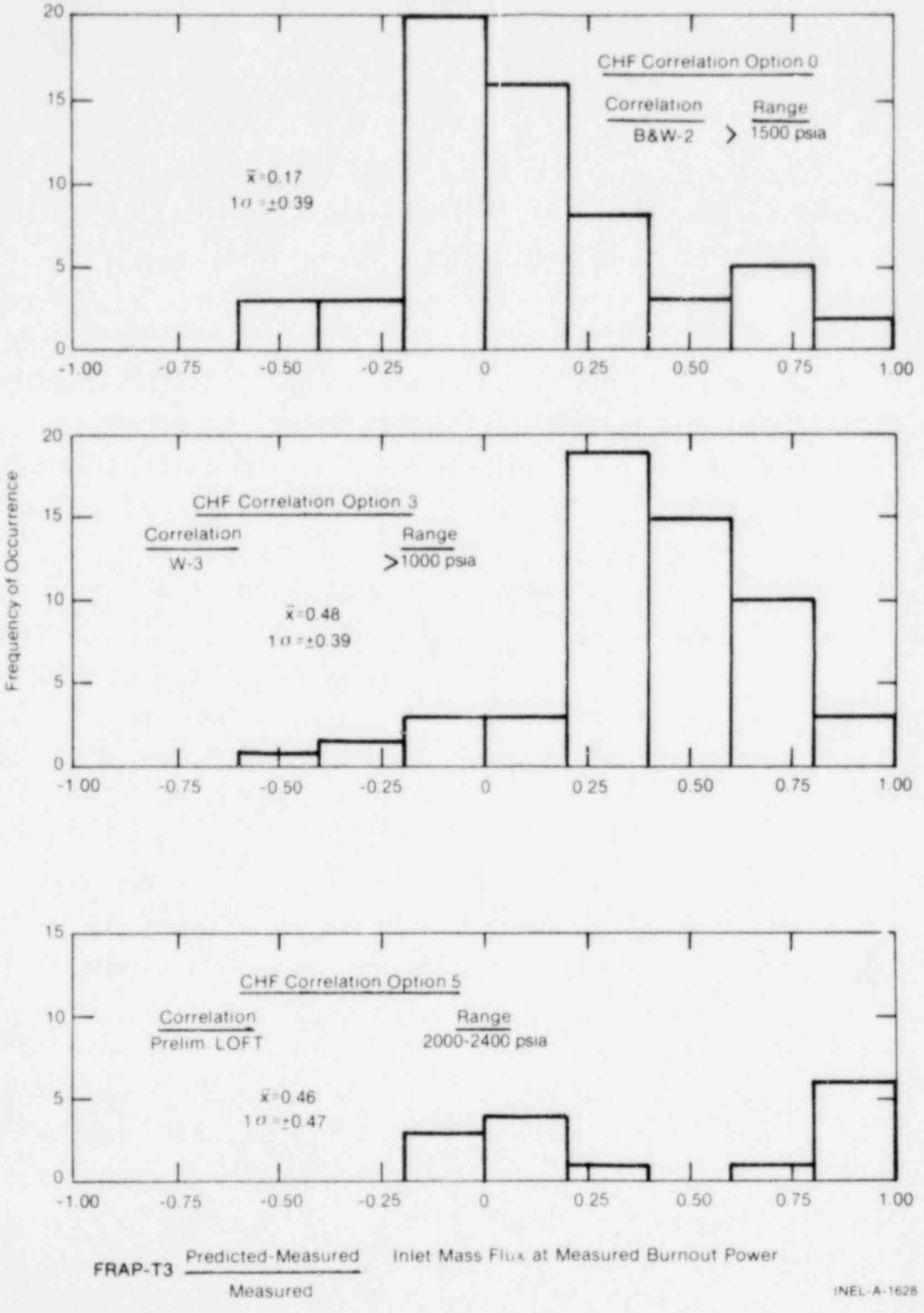

Fig. 31 Frequency of occurrence of predicted-measured/measured inlet mass flux at measured burnout power (BØ11 through BØ17).

is now applied to analyze the data strictly from the viewpoint of mechanical considerations. Further distinction of an SCC contribution (other than random) to rod failure probability requires implementation of an improved fuel relocation model and more data on frequency of moderate power defects, less dominated by hard gap closure.

FRAP-T3 with burnup effects input from FRAP-S2 was used to follow the experimental power histories. Failure probability was calculated by the empirically determined failure stress versus temperature model used in the FRAIL subcode. Hoop stress input to the subcode is a result of both the FRACAS and MATPRO subcodes. Calculated and observed failure probability is compared and interpreted with respect to relative gap size, fuel density, and burnup effects. At issue here is the relative capability of FRAP-T3 for calculating low temperature cladding failures, a probable consequence for at least some rods during PCM or RIA accidents.

The particular design, burnup, and operating conditions reflected in the results of many overpower tests seems to promote the occurrence of failure. In most cases the experimental objective actually involves determination of fuel performance limits. This fact is illustrated in Figure 32 by the relative dominance of high power operation within the current sample of 51 rods. All but one of the rods are unprepressurized. Figure 33 shows that performance for most of the rods can be interpreted as representing moderate burnup conditions. The observed failure probability plotted in Figure 34 for rods in given burnup intervals, does not support existence of a dominant burnup effect on the results. The observed failure probability, shown in Figure 35, versus peak power interval, does indicate dominance of this sample by PCMI effects. Due to the influence of gap and fuel density on both measured and calculated stress, Figures 36, 37, and 38 are used to characterize the sample in this respect. The as-built gap in Figure 36 should be distinguished from the burnup gap value in Figure 37. The burnup gap reflects calculated permanent geometry effects of pretest operation, and was reflected in FRAP-T3 input for all cases. Figure 38 indicates that fuel densities $\geq$95% dominate the sample. For this reason, lack of a fuel mechanical deformation model should compromise only the highest heat rating results.

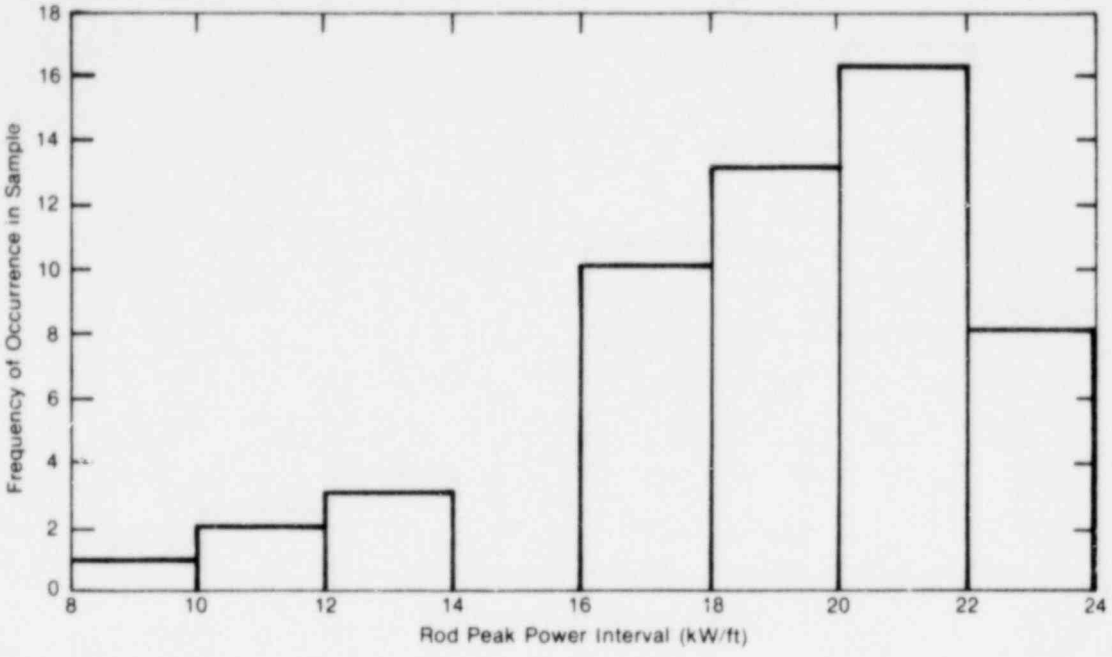

Fig. 32 FRAP-T3 rod peak power frequency for overpower rods.

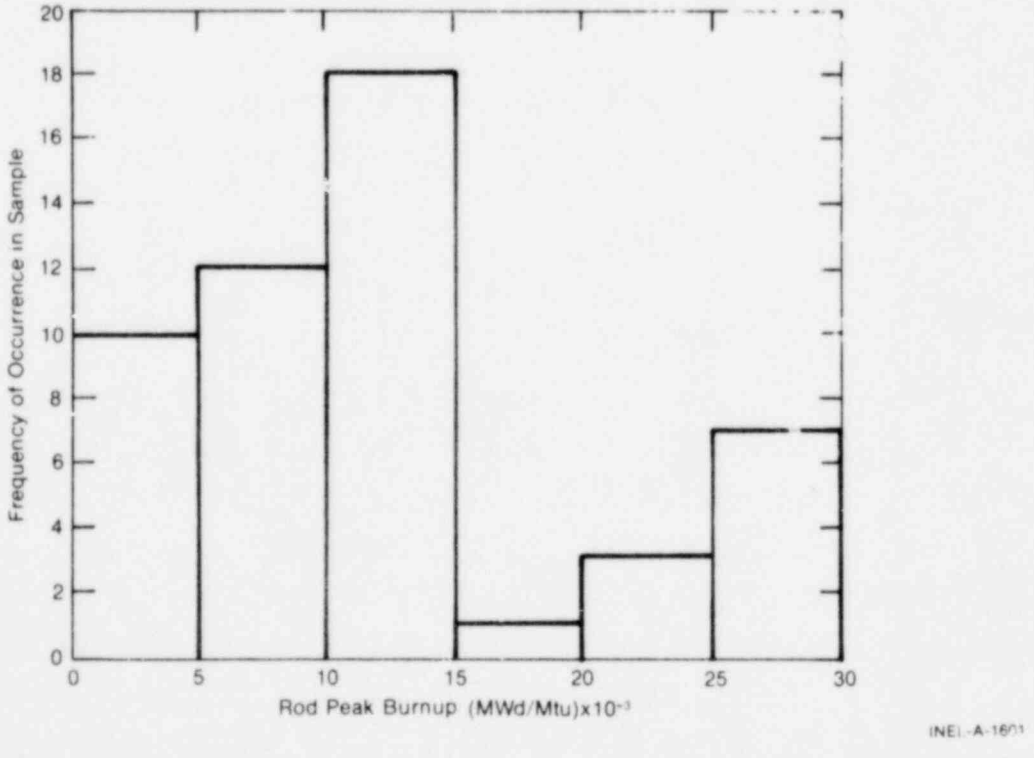

Fig. 33 FRAP-T3 rod peak burnup frequency for overpower rods.

1571 223

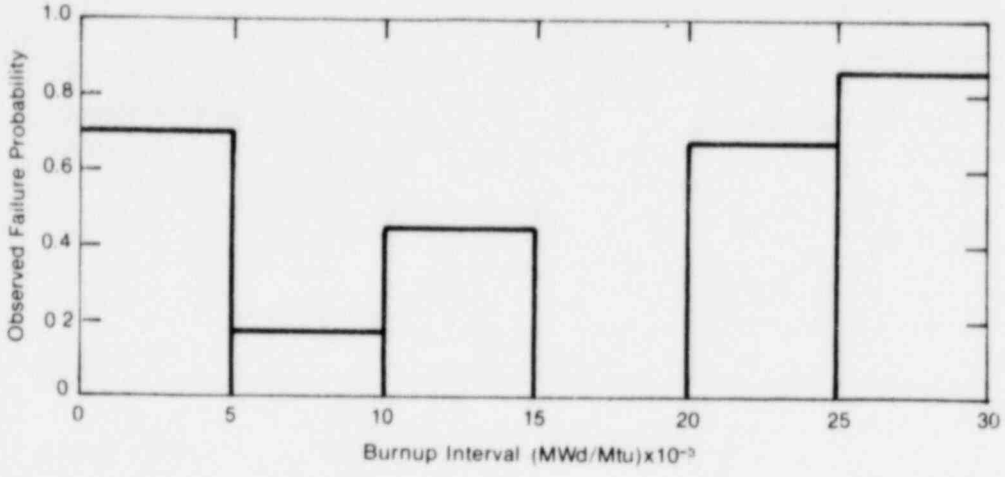

Fig. 34 Observed failure probability versus burnup interval.

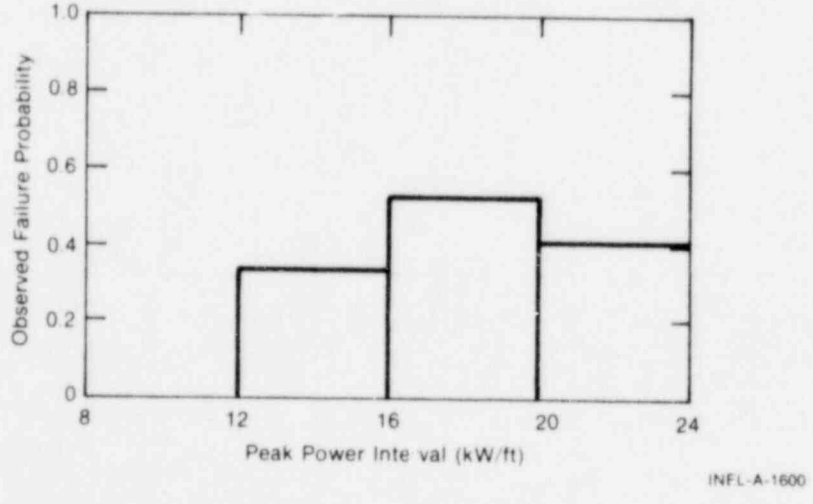

Fig. 35 Observed failure probability versus peak power interval.

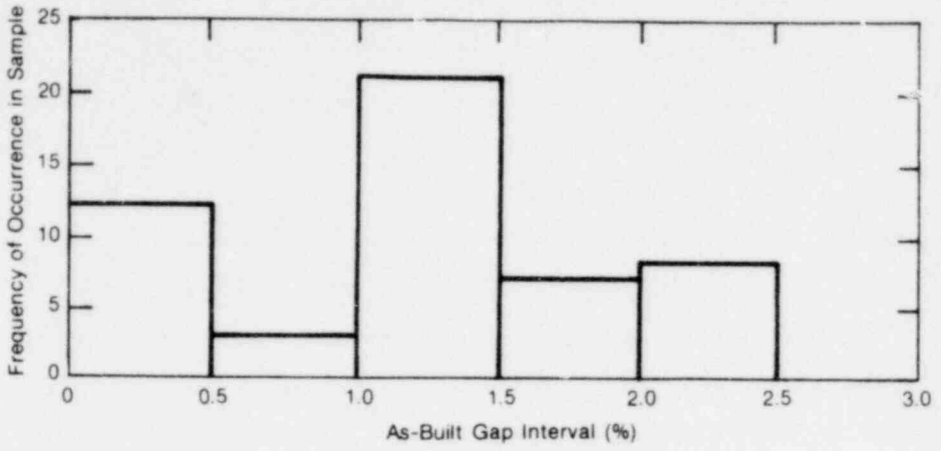

Fig. 36 FRAP-T3 as-built gap frequency for overpower rods.

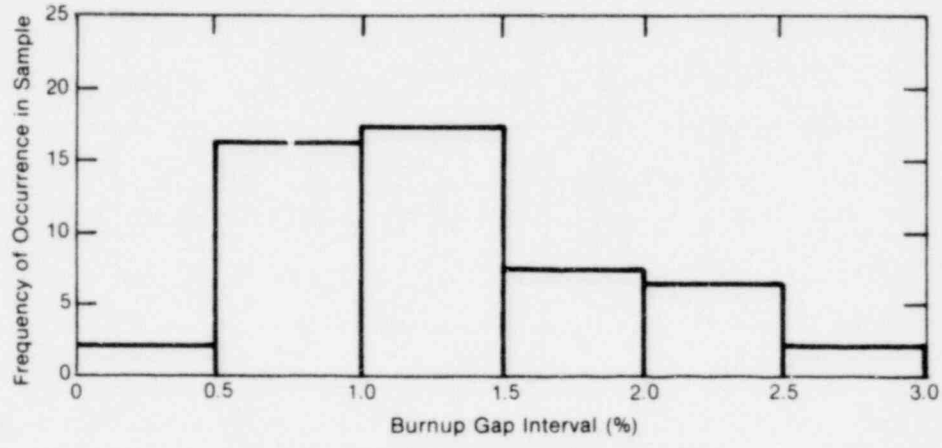

Fig. 37 FRAP-T3 burnup gap frequency for overpower rods.

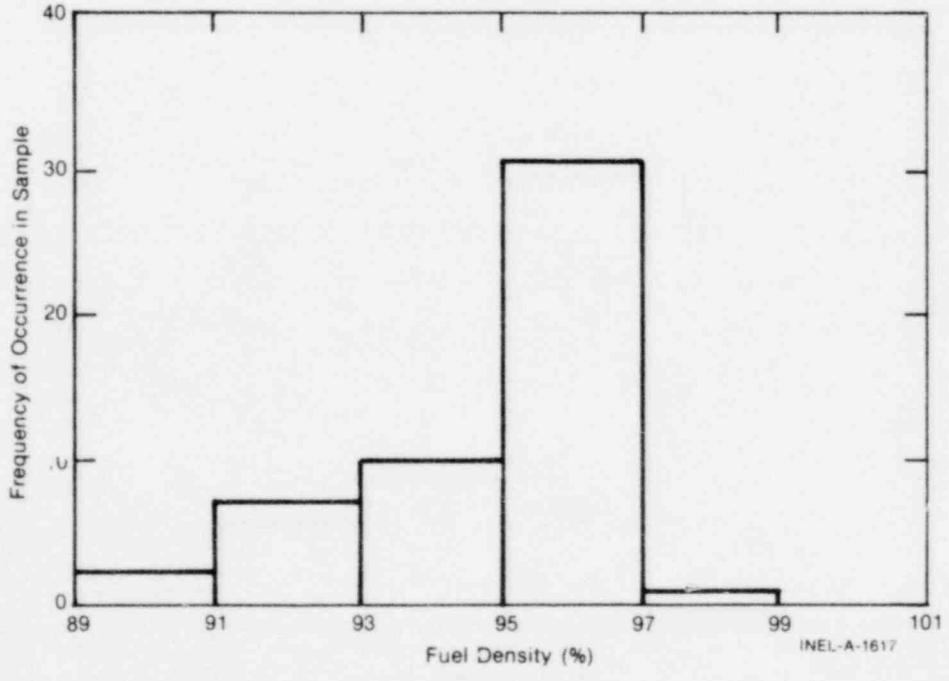

Fig. 38 FRAP-T3 fuel density frequency for overpower rods.

The observed frequency of occurrence for given FRAIL output intervals indicates that fairly high failure probabilities are calculated for most of the rods, as shown in Figure 39. This high stress situation is expected, given high power operation of relatively small-gap rods. Without FRACAS accounting for fuel mechanical deformation, the uniformily applied calculated stress should be too high. Lack of PCMI stress concentration factors compensates, to at least some degree, making the maximum stress more realistic than constituent model limitations would indicate. Summary results in Figure 40, relating measured and observed failure probability, suggest that the combined stress and failure model is only adequate for hard gap closure conditions without occurrence of a large fuel plasticity effect. For intervals populated by at least several rods, the calculated failure probability does tend to increase in proportion to the observed value. Either lack of data for rods with >80% calculated failure probability, or the experimental impact of bulk fuel plasticity with both high stress and temperature causes anomalies between 0.8 and 1. The code is also limited when it results in a low-to-moderate failure probability (<0.2). Gap closure is either not calculated to occur, or is just beginning at the maximum heat rating in these cases. Lack of a realistic fuel cracking model, and other unaccounted for experimental effects such as fuel handling and SCC, cause failure probability to be under predicted.

Figure 41 provides some indirect verification of the FRAP-S2 permanent burnup effects which provided the FRAP-T3 input rod geometry. These effects included fuel swelling, densification, cladding creep, and yield. In terms of the pretest cold-gap dimension, both the observed and calculated failure probability show consistent and continuous trends in Figure 41. The measurements, when related to the as-built gap dimension, are more scattered and, to some extent, contrary to physical expectations.

Figure 42 compares measured and predicted failure probability with respect to fuel density interval. A density effect appears in the data, but not in the predictions. The measurement trend supports the contention

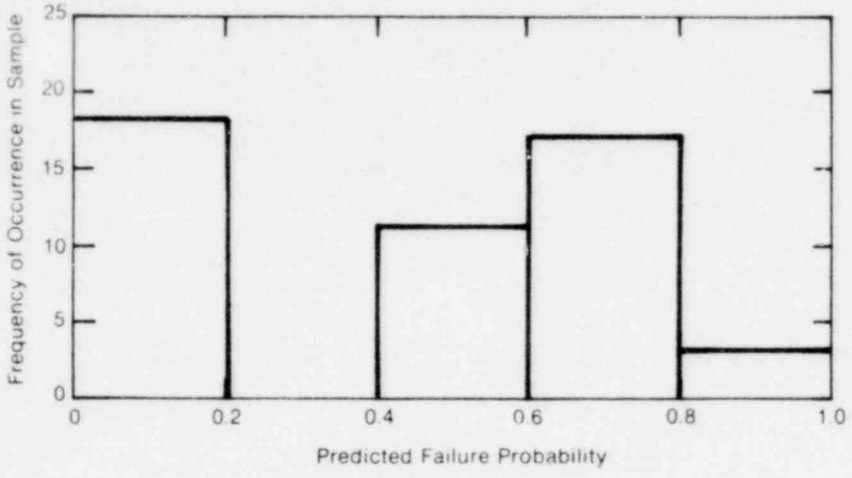

Fig. 39 FRAP-T3 predicted failure probability frequency.

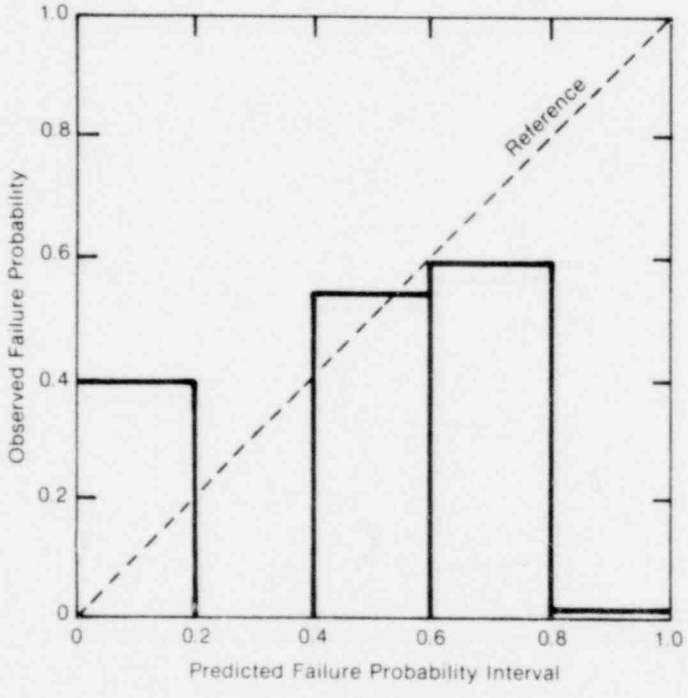

Fig. 40 FRAP-T3 measured versus predicted failure probability.

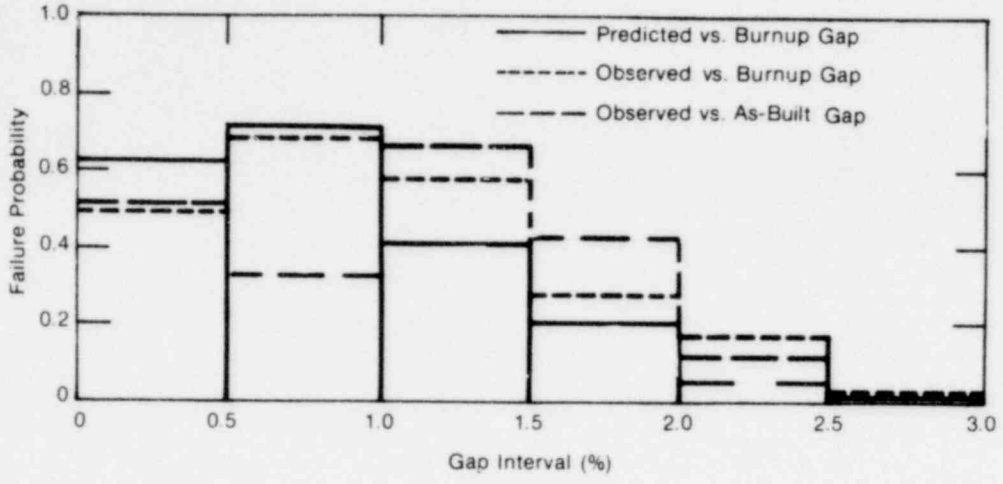

Fig. 41 FRAP-T3 failure probability versus gap interval.

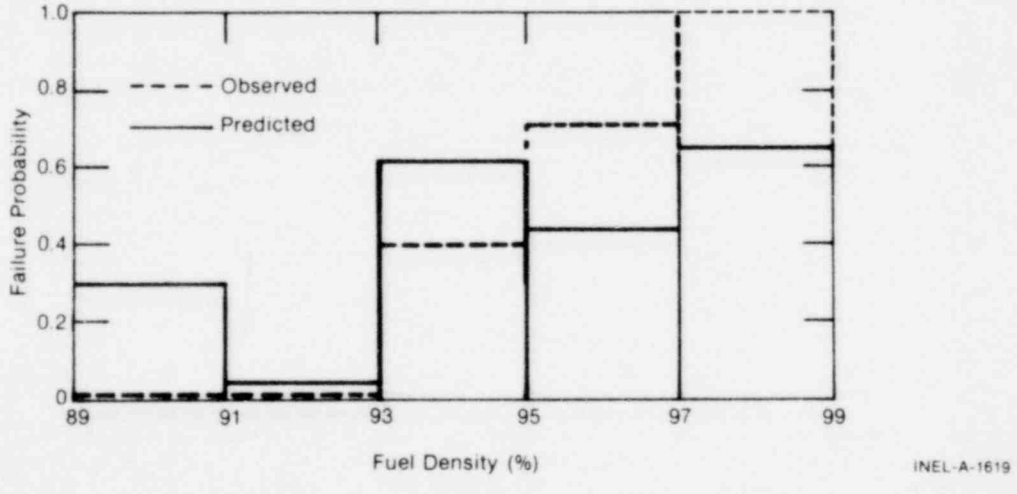

Fig. 42 FRAP-T3 failure probability versus fuel density.

that PCMI dominates this data set. This is said because PCMI stress and pellet resistance to deformation should be proportional to fuel density. Lack of a consistent predicted trend reflects the fact that the model does not consider fuel mechanical deformation.

VI. TRANSIENT DATA COMPARISONS

Two types of transient data comparisons for operating rods were performed with FRAP-T3. Comparisons for fuel temperature response at shutdown are followed by limited results for rod surface temperature and pressure response under deficient cooling conditions.

1. FUEL TEMPERATURE RESPONSE

Transient data comparisons based on fuel centerline temperature response are used here to benchmark internal heat conduction models. Adequately calculating the dissipation of stored energy and decay heat immediately after scram is especially important for analyzing expected accident situations. Given normal surface cooling in these experiments, there is less uncertainty in interpreting performance of pellet stored energy, heat transfer, and gap conductance models. Data were available for six rods whose centerline temperature histories were measured with high frequency during operation of the HBWR slow scram system. Local power at the instrument positions decreased from an operating level of between 6 and 10 kW/ft, to the decay heat level (initially ≈ 6%) within 0.8 seconds. Differences in design, fabrication, initial power, burnup, and thermocouple decalibration contribute to wide measurement variation.

In Figures 43, 44, and 45, scram temperature histories and associated predictions are considered for three rods with varying gap sizes. For two of the rods, scram data have been reported for different burnups and initial conditions. The data are consistent with physical expectations as to the effect of initial stored energy and decay heat on centerline temperature coastdown. Equilibrium conditions somewhat above the 236°C system temperature seem reasonable. The rate of temperature decrease is observed to be proportional to gap size. The large gap rod reaches the lowest equilibrium temperatures.

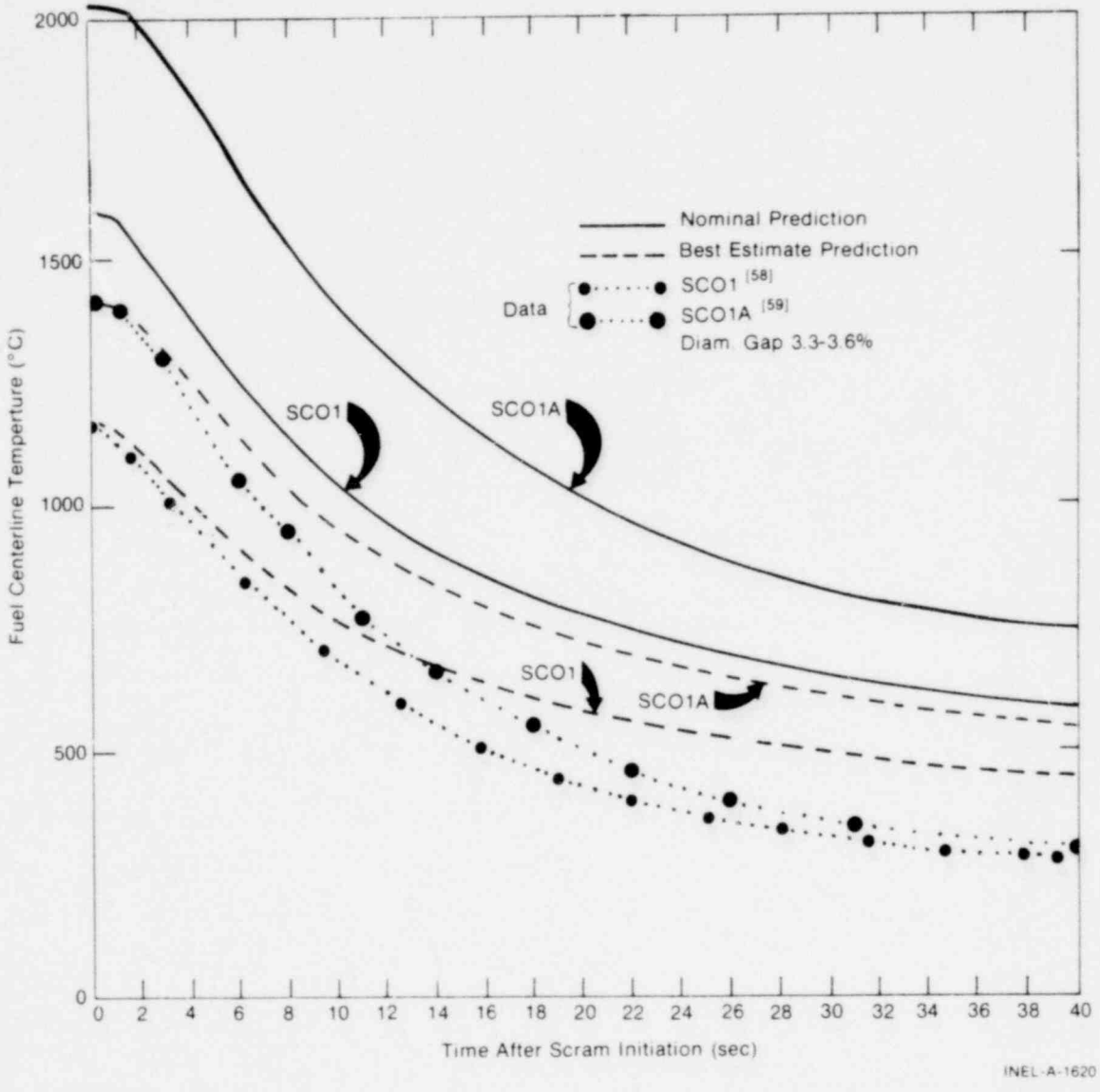

Fig. 43 FRAP-T3 fuel temperature response during scram at 5600 and 8700 MWd/t.

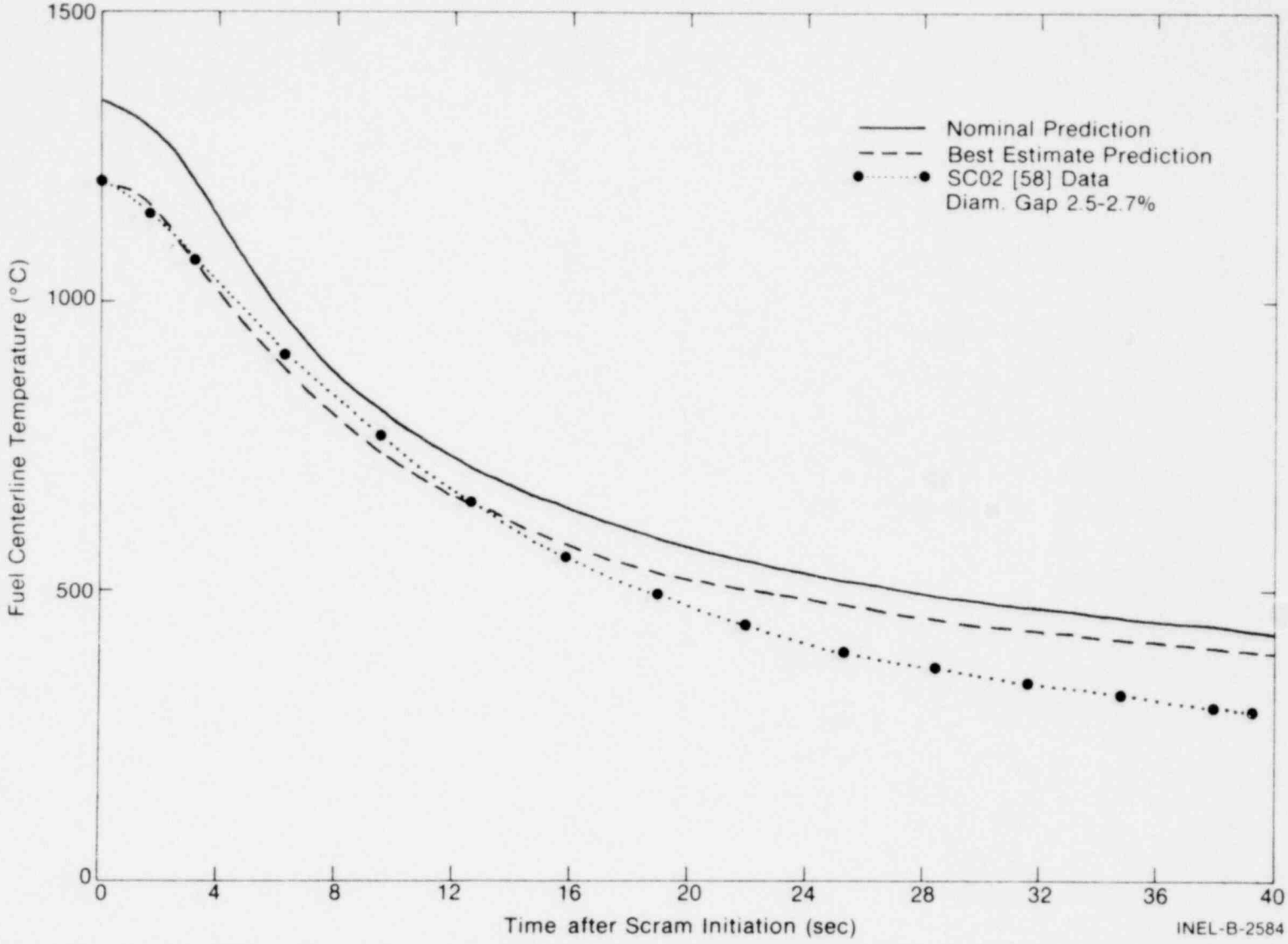

Fig. 44 FRAP-T3 fuel temperature response during scram at 5600 MWd/t.

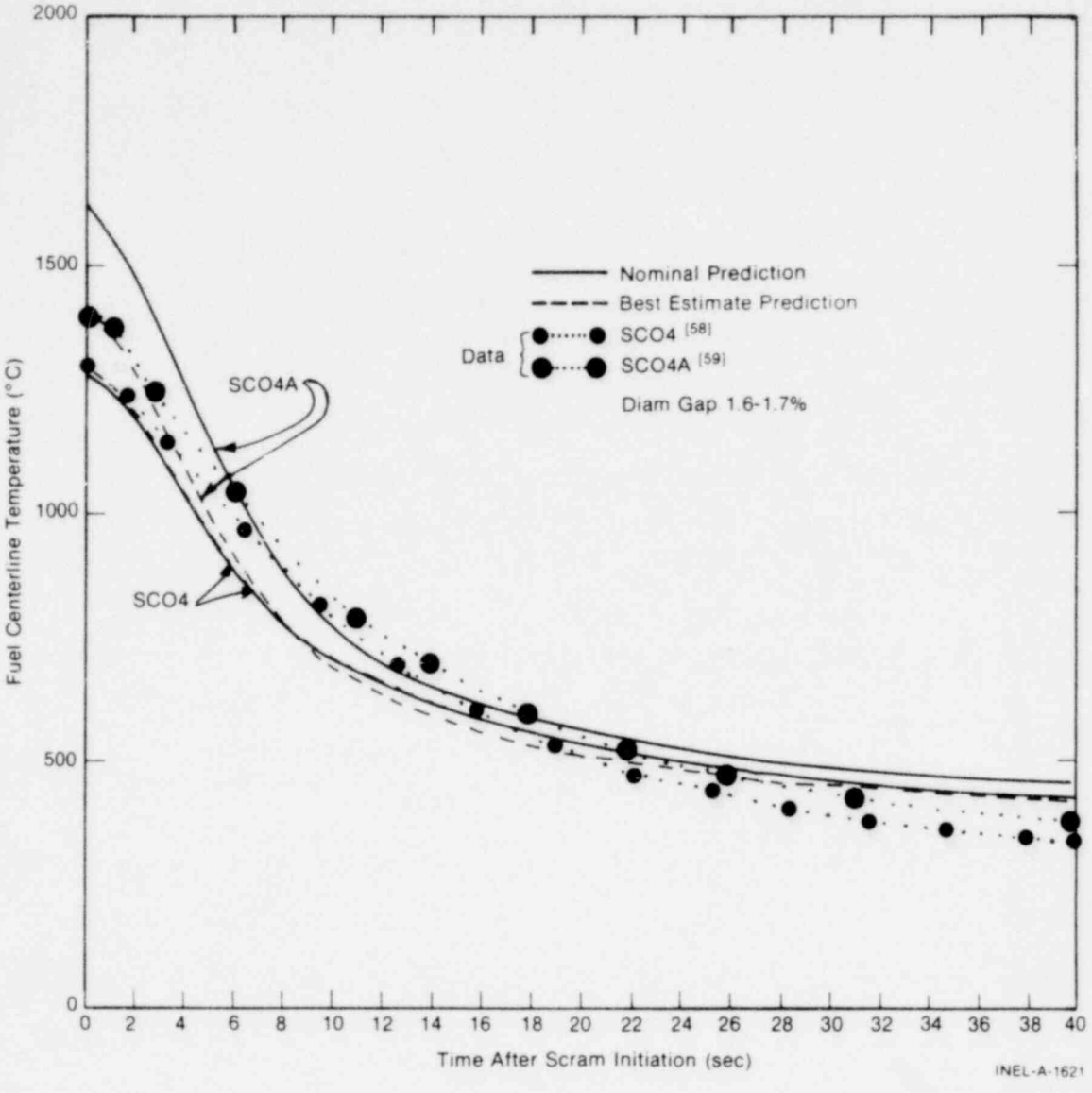

Fig. 45 FRAP-T3 fuel temperature response during scram at 2000 and 8700 MWd/t.

All predictions utilized a current best-estimated decay heat relationship[80] to restrict error in calculated temperature to that caused by the thermal model. Nominal predictions correspond to the measured local power at initiation of the scram. In this case, initial stored energy from the steady state model, in addition to fuel properties and gap conductance, contributes to the observed overprediction of temperature. The best-estimate predictions reflect matching initial stored energy at the expense of underestimating the power history somewhat. Fuel temperature is still overpredicted, however, by an amount increasing with gap size. Underestimating removal of heat from the pellet corresponds to underestimating fuel relocation and gap conductance. It is likely

that permanent fuel relocation actually increases during a rapid fuel temperature decrease. Results of the temperature comparison do not support the crack recovery process applied by the current gap conductance model as power decreases.

A consistent trend of underestimating the rate of fuel temperature decrease and overestimating equilibrium temperature was seen in the scram results for two other unpressurized rods. One of the rods exhibited a thermocouple decalibration effect, while the other was scrammed from an initial power level of only 4 kW/ft. Incomplete data were available for the single pressurized rod test considered. Temperature comparisons over a limited time period did provide some support for maintaining a high gap heat transfer level during rapid power decreases.

2. TREAT ANALYSIS

Fuel rod transient behavior during sustained periods of deficient surface heat transfer is of particular interest for off-normal analysis. With net positive internal pressure, high cladding temperatures can lead to local rod deformations having feedback on subchannel geometry and bundle flow resistance. Operating data for instrumented LWR rods is very limited for these conditions. This section gives data comparisons for two experiments in which plenum pressure and cladding temperature were measured during short-term irradiations with low surface heat transfer.

FRAP-T3 results were compared with TREAT data[60,61] for two different rods. A flowing steam LOCA environment was simulated in seven-rod cluster Tests FRF-1 and FRF-2. Fluid conditions were meant to be typical of residual steam boil-off immediately following blowdown from BWR conditions. Use of slightly pressurized rods resulted in multiple-rod ballooning followed by cladding ruptures between 927 and 1204°C. Deposition of residual fission heat under LOCA conditions was to be simulated by steady power operation, although significant power changes occurred in each test. Peak heat ratings in Tests FRF-1 and FRF-2 were near 7 and 11 kW/ft, respectively.

Figures 46 and 47 compare measured and predicted rod surface temperature and internal pressure response for Tests FRF-1 and FRF-2. Predictions from three different runs are shown on each plot. The designations "hot" and "cold" refer to runs with channel average enthalpy input based on different local conditions calculated by a transient fluid model, COBRA-IIIC[81]. Specifying two different enthalpy histories for each TREAT run is intended to bracket the range of values applicable between the benchmark instrument position above, and another point the same distance below, the midplane rupture location. Predictions from the "internal" model utilize the single-channel enthalpy rise calculation in FRAP-T3. The internal model in this case would allow higher fluid temperatures to occur over the plenum region, resulting in higher calculated internal pressure.

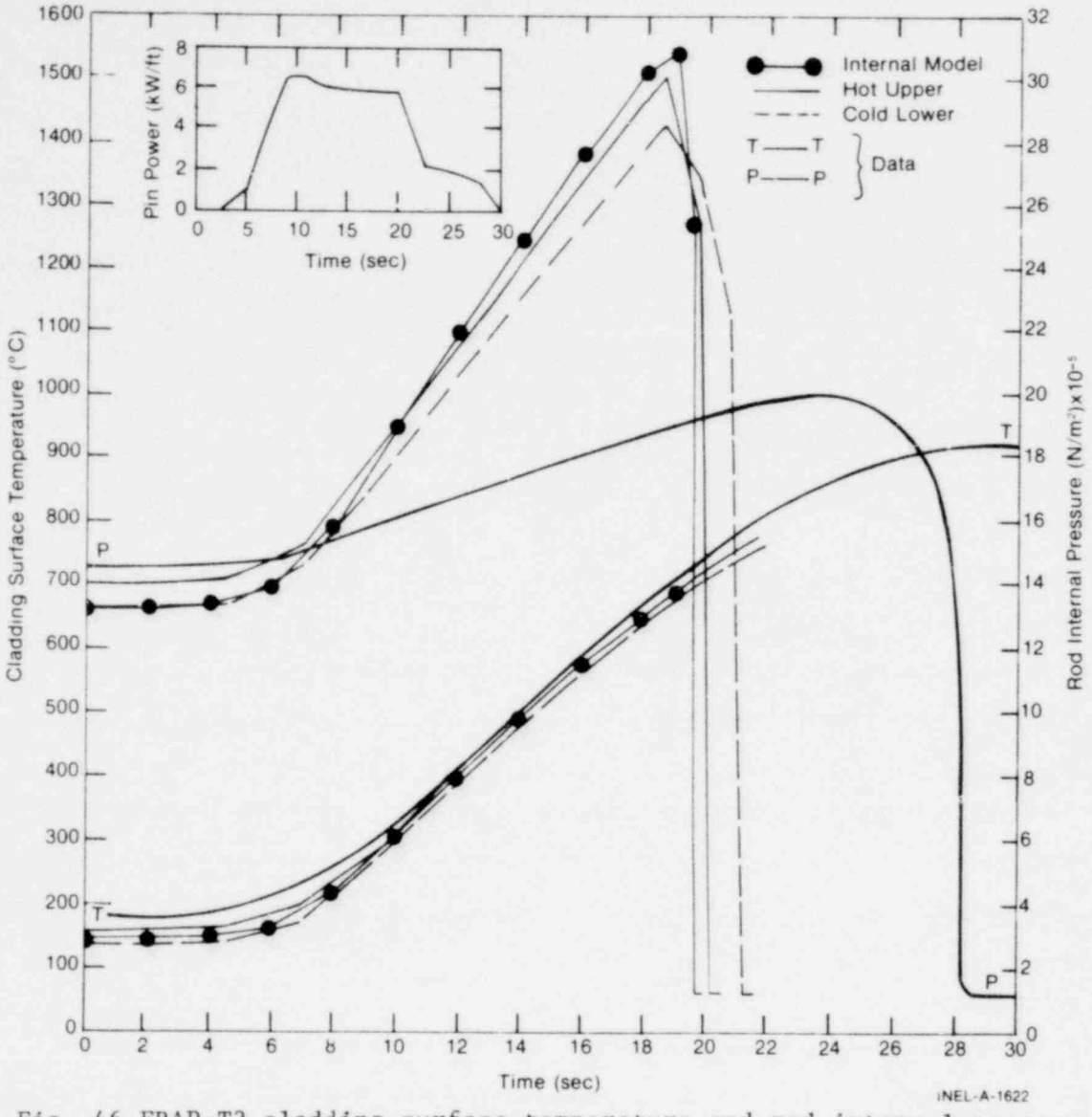

Fig. 46 FRAP-T3 cladding surface temperature and rod internal pressure histories for TREAT Test FRF-1.

For both experiments, cladding temperature is well represented by all the runs up until the point of calculated cladding burst. For the cold channel run in Figure 47, instability strain is exceeded, ballooning occurs, and a stable tube configuration is reached, without the run being terminated due to nonconvergence on pressure and deformation. Increased heat transfer area starts to cool the rod prior to observed rupture time. Close agreement in calculated cladding temperature among the runs for each test is a result of consistently low surface heat transfer ($\approx$ 5 Btu/hr-ft^2°F) assigned by the model to pure superheated steam conditions.

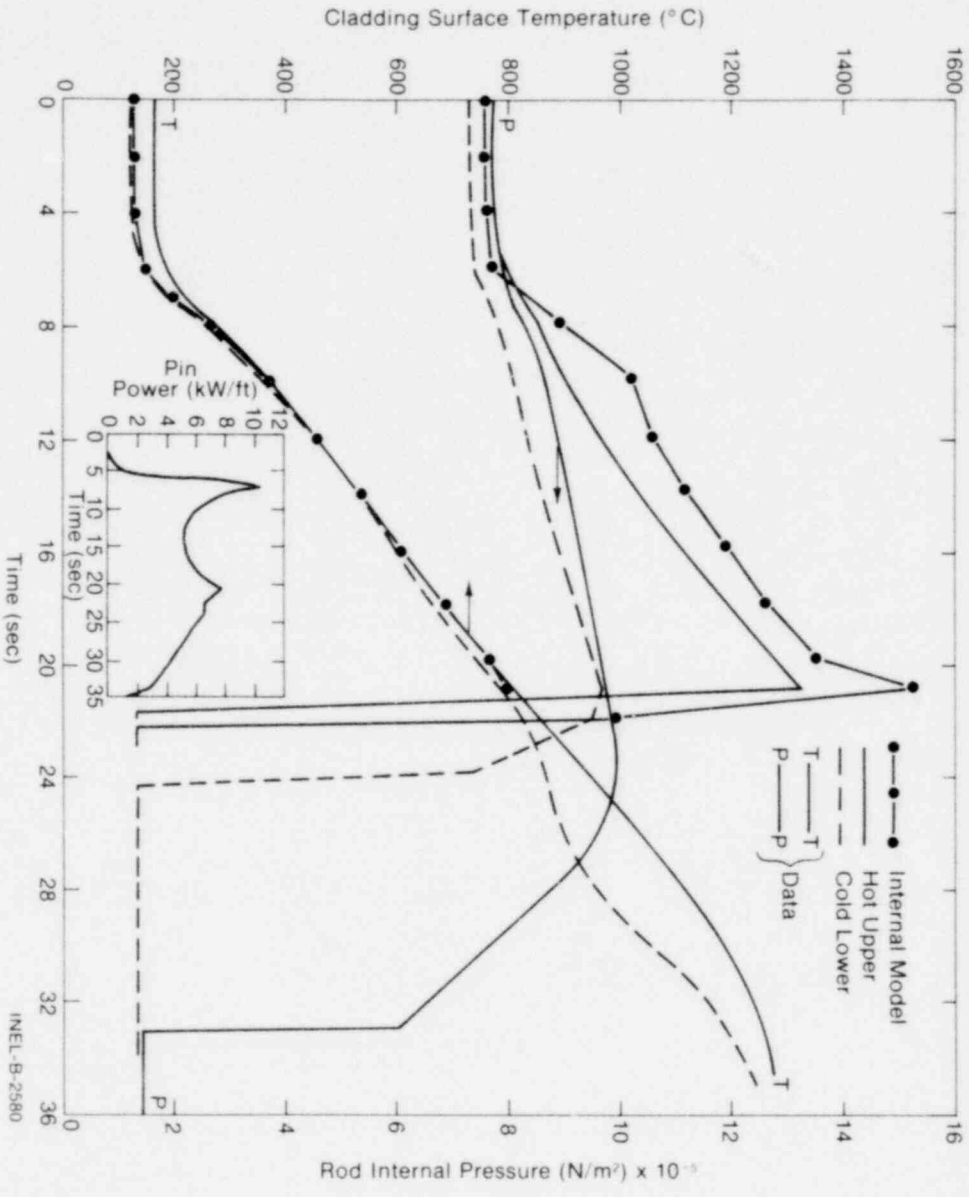

Fig. 47 FRAP-T3 cladding surface temperature and rod internal pressure histories for TREAT Test FRF-2.

Calculated pressure history shows strong sensitivity to fluid temperature conditions, especially for the higher power Test FRF-2. Without a significant gas flow effect, calculated rod pressure is largely controlled by heat transfer between the plenum region and adjacent fluid. Pressure response for the FRF-1 rod shown in Figure 46 is overpredicted by each fluid condition option. Since this rod had the combination of smallest plenum and highest pressurization between the two cases, the calculated pressure history is much more sensitive to error in fuel stack expansion and plenum heat transfer conditions. The cold channel result in Figure 47 indicates that the premature calculation of cladding rupture is not only a result of overpredicting rod pressure in FRAP-T3, but also a result of MATPRO error in high temperature σ - ε properties. On the basis of the FRAIL subcode, maximum failure probabilities, corresponding to the time of calculated rapid pressure decrease, are only 1% and 15% for Tests FRF-1 and FRF-2, respectively. The difference in calculated rupture conditions between MATPRO and FRAIL is discussed further in Section VII.

VII. OUT-OF-PILE TUBE RUPTURE DATA COMPARISONS

This section gives data comparison results for out-of-pile tube rupture experiments. FRAP-T3 predictions were generated using a special version of the code supplied by model development[a]. The objective was to isolate the tube mechanics model from the rest of the program. In this way, calculated zircaloy behavior could be checked for a relatively large sample size under known pressure and temperature conditions in the off-normal range.

The modified code version bypassed the heat conduction, void volume, and rod internal pressure calculations. Cladding temperature and internal pressure histories could then be forced through the deformation model via input specification. Active parts of the model for these runs were stress calculation, the failure subcode, material properties, and the ballooning model. In the fully coupled program, these submodels form the basis of the cladding structural response and failure analysis within the iteration procedure involving fuel rod temperature distribution and internal pressure.

Table II previously listed the tube burst and expansion tests that form the data base. All of the data represent single-rod tests. Tube dimensions were typical of both PWR and BWR fuel types. Reported fast neutron exposure for previously irradiated samples ranged from 0.09 to 4.1×10^{22} ($n/cm^2 > 1$ meV). Much of the previously used data base[3] was eliminated from consideration. External atmosphere for the current sample is restricted to oxidizing atmospheres (air or steam) more representative of accident conditions. Some of the data reflect behavior of empty tubes but, in most cases, simulated fuel pellets provide for more typical levels of gas stored energy. It was assumed that effects due to differences in tube end constraints did not invalidate treatment of the

---

[a] FRAP-T MOD 003 VER OP-12-16-76, MATPRO Version 08.

data on the basis of temperature, pressure, and strain only. Three different test procedures were used; nominally constant pressurization followed by heatup to failure ("T" runs), pressurization to failure at nominally constant cladding temperature ("P" runs), and pressurization to nominally constant load while maintaining cladding temperature over a given time period ("E" runs). In all cases, between 500 and 1000 time steps were specified to represent the experiment history.

The FRAP-T1 rupture model used an assumed mathematical form to obtain temperature-dependent σ - ε curves from CSTRAN. An ultimate stress burst criteria was used to determine temperature conditions at rupture. Instability strain was equal to a fit of work-hardening coefficient versus temperature. Rupture strain itself came from a temperature-dependent empirical model based on uniaxial tensile failures. FRAP-T2 also used CSTRAN to drive the burst model. Failure was defined when an ultimate strain at temperature threshold (empirically determined from tube test data) was met or exceeded. Instability strain was effectively the same work-hardening coefficient used in FRAP-T1, which initiated the flat region of the σ - ε curve. FRAP-T3 incorporates a strain rate term in the mathematical form assumed to describe σ - ε behavior. Strain rate is based on current and previous time steps. Meeting an instability strain criteria (now equal to one-fourth the ultimate strain at temperature), passes control to the BALLOON model. BALLOON effectively distributes strain according to membrane theory and geometrical tube stability relationships. Maximum strain at rupture is again, based on ultimate strain at temperature. Since FRAP-T3 also includes the failure probability subcode FRAIL, tubes may also be calculated to burst in FRACAS on the basis of stress and temperature alone. The FRAIL calculation is independent of burst criteria in MATPRO.

Figures 48 through 51 compare measured and MATPRO calculated burst temperature, pressure, and strain at failure. With the exception of low temperature (316- to 427°C) irradiated tube tests, burst criteria were met through CSTRAN and BALLOON prior to satisfying nominal FRAIL criteria

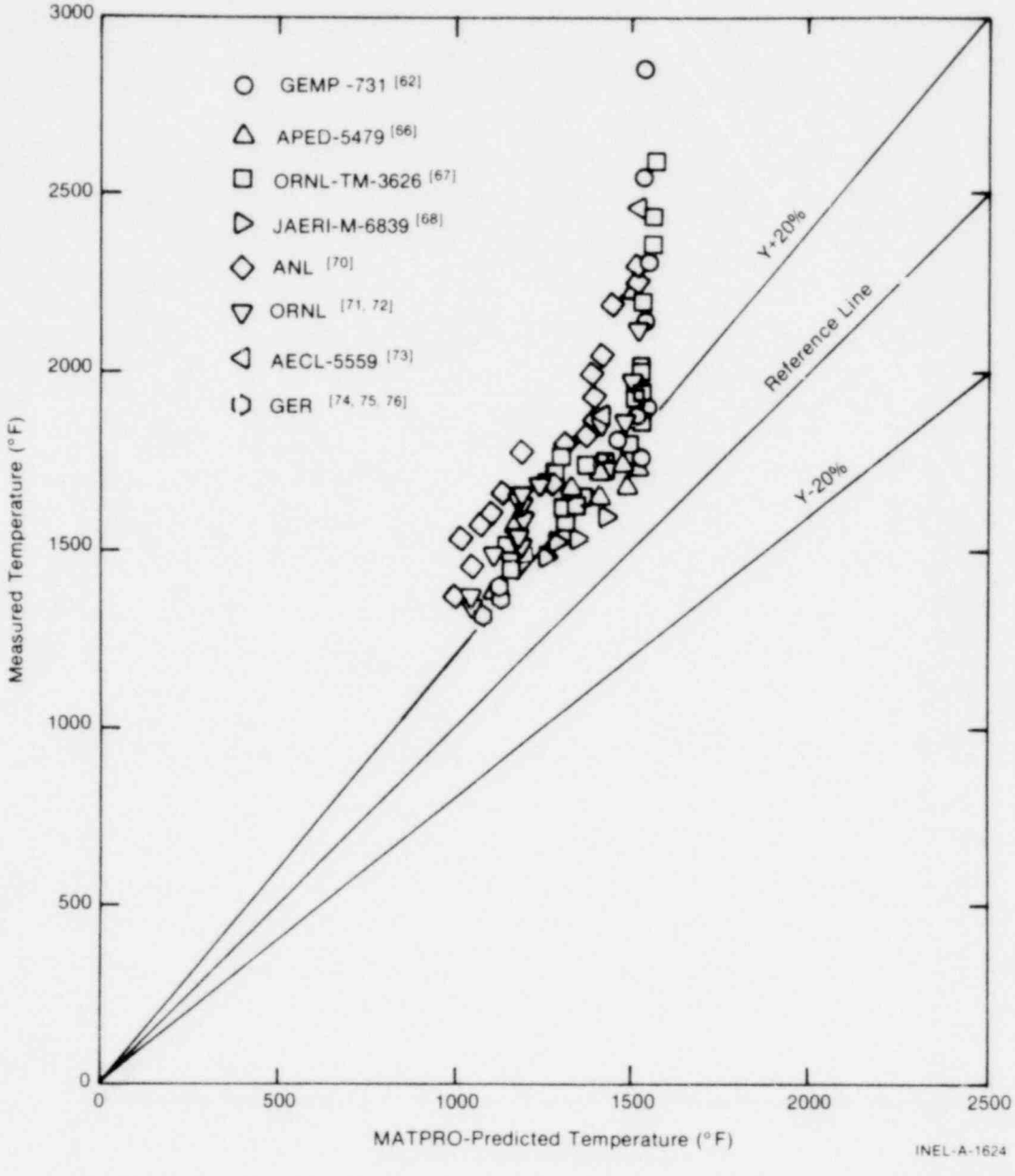

Fig. 48 FRAP-T3 measured versus predicted cladding temperature at burst.

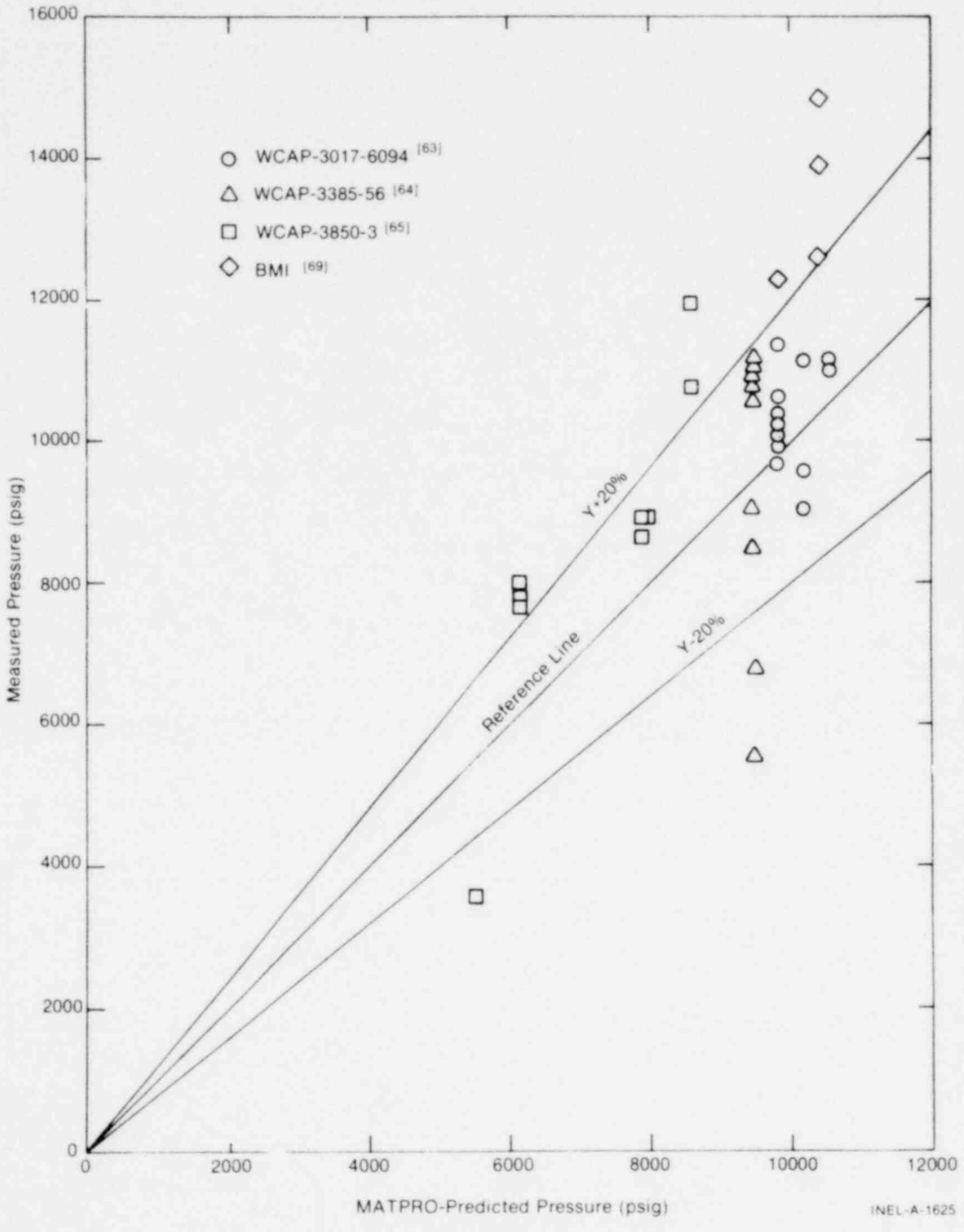

Fig. 49 FRAP-T3 measured versus predicted internal pressure at burst.

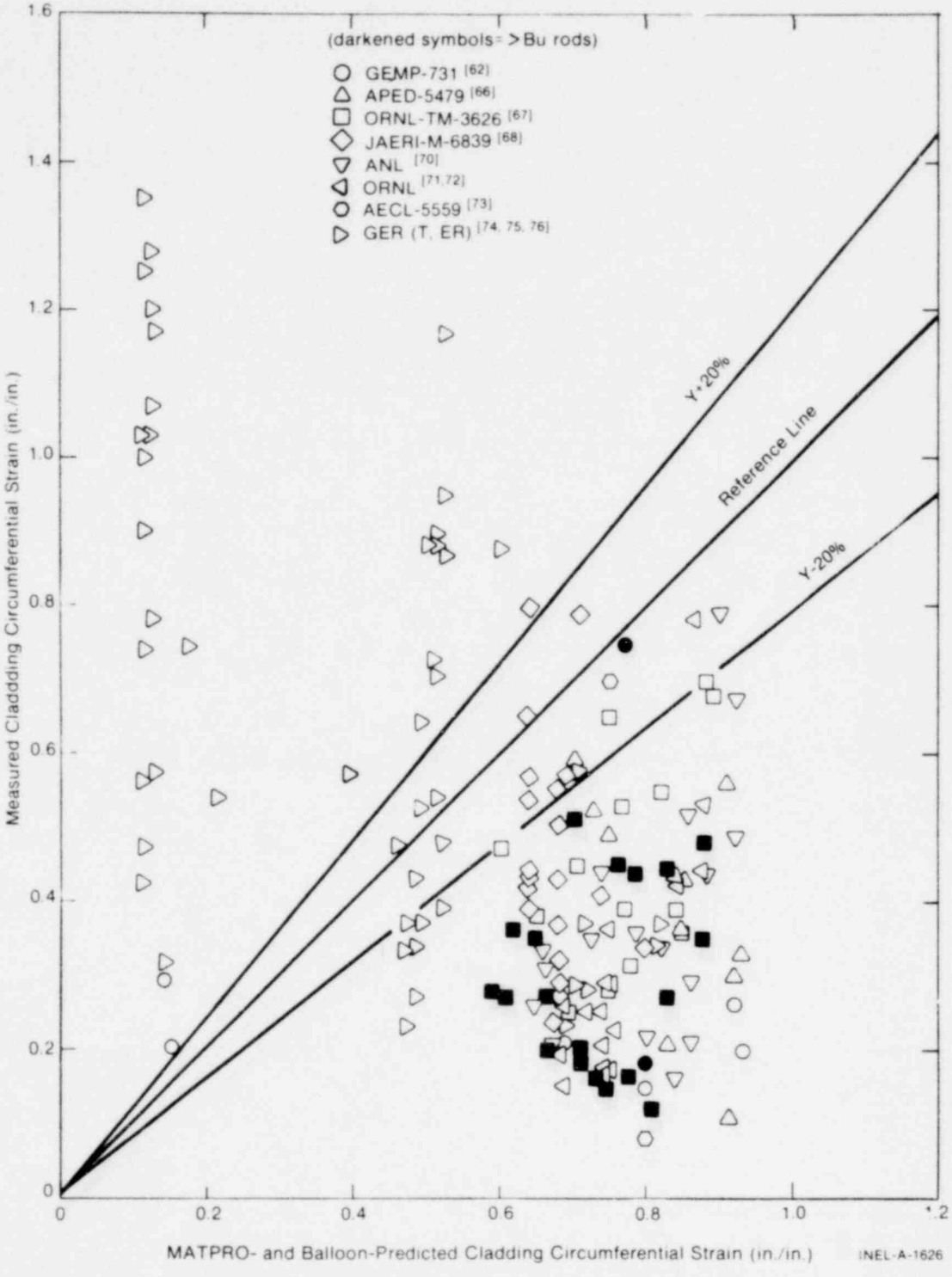

Fig. 50 FRAP-T3 measured versus predicted cladding circumferential strain at burst, as predicted by balloon model.

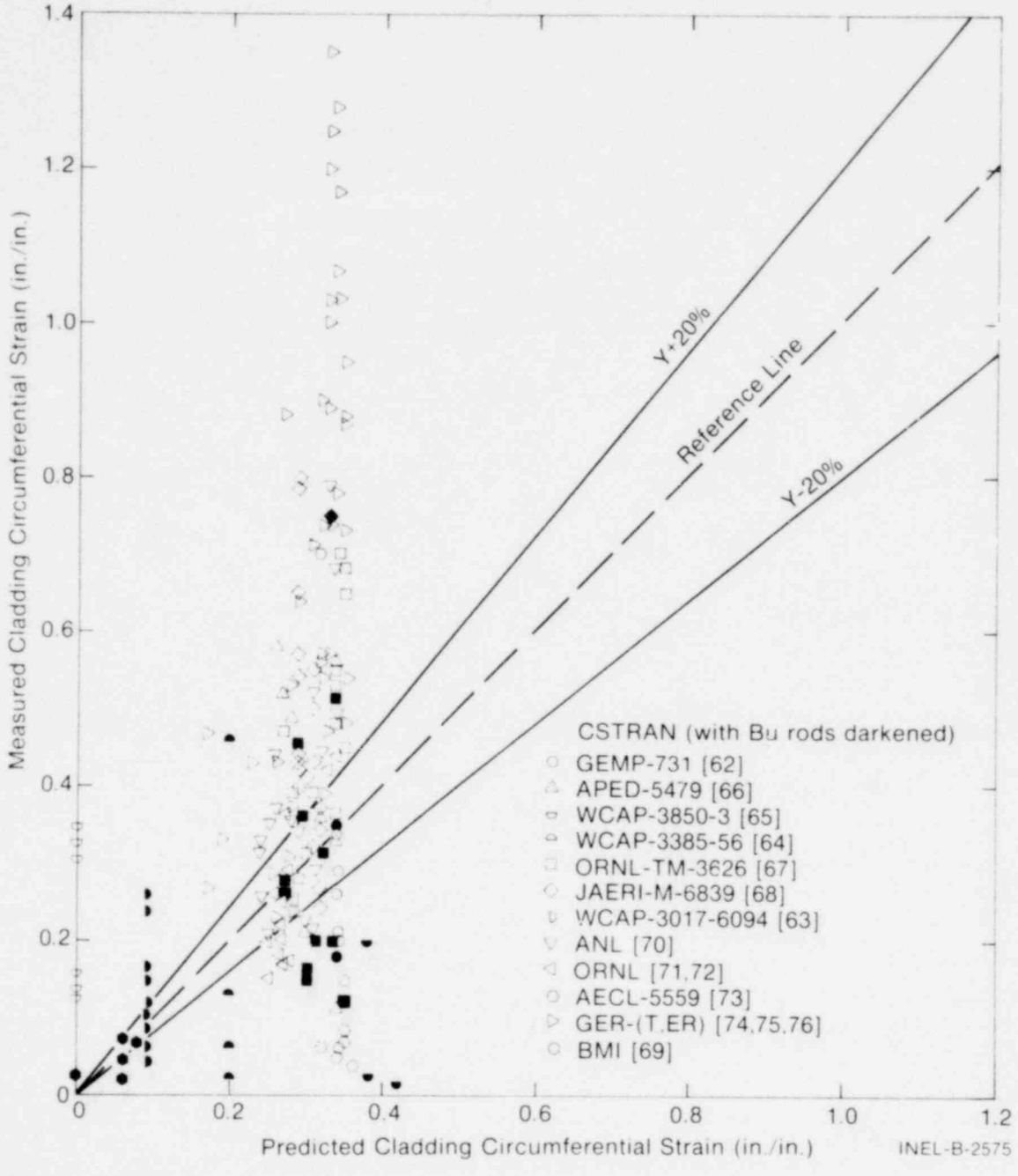

Fig. 51 Measured versus predicted cladding circumferential strain at burst as predicted by CSTRAN model.

(50% failure probability). The FRAIL threshold was set at 100% for the irradiated tubes to allow all burst runs to reach instability strain conditions under MATPRO control.

Temperature results in Figure 48 reflect measured pressure input during heatup ramps ("T" runs). Rupture temperature is underpredicted by at least 30%. There seems to be a maximum predicted burst temperature near 816°C which corresponds to zircaloy phase transition and an abrupt decrease in calculated instability strain. As was the case in FRAP-T2, results indicate that current formulation of the σ - ε curves does not provide enough continuity on which to base threshold numerical decisions over finite-length time steps. The very rapid high temperature deformation rates effectively calculated by MATPRO are a direct result of extrapolating a traditional σ - ε concept of material behavior into the off-normal range.

Pressure results in Figure 49 reflect measured temperature input during pressurization ramps ("P" runs). Unfortunately, no "P" run data were available for the high temperature (>538°C), low pressure (<2000 psig) conditions of most interest. There is more tendency however, for these low temperature (316- to 427°C) predictions to bracket the reference line representing observed behavior. The current σ - ε approach seems more applicable then, to characterizing cladding failures under more normal operating conditions.

The comparison of measured and predicted rupture strain shown in Figures 50 and 51 includes results from "T" runs, "P" runs, and isothermal expansion tests in which rupture was observed ("ER" runs). Interpretation is confounded since burst temperature was so consistently underpredicted for "T" runs. Calculated strains in Figure 50 come from BALLOON and are consistent with its associated ultimate strain model between 538 and 817°C. BALLOON was not activated for the low temperature "P" runs shown previously in Figure 49. Observed deformation for the remaining "T" runs is largely overpredicted, but this trend is expected. Many of the tubes were observed to burst between 816 and

1038°C, a region of lower calculated strain which was not reached by the model due to premature bursts below 816°C. Underpredictions below 20% strain correspond to constant condition "ER" runs with cladding temperatures beween 816 and 829°C. Better agreement is obtained for "ER" runs at cladding temperatures between 832 and 899°C. Comparisons between measured and CSTRAN-predicted strain are shown in Figure 51 for the same tubes. The predictions essentially correspond to instability strain values. The range of predictions for both low and high temperatures is very tight compared to the range of observations. Thus, even though the range of predictions largely brackets the reference line, it appears that basic mechanisms associated with rupture events are not entirely represented by instability strain alone.

Figures 52 and 53 compare measured and calculated burst temperature and pressure. Pressure is expressed in terms of hoop stress. In this case, predicted values are based on the temperature and pressure failure relationship in FRAIL, here considered independently of FRAP-T3 and MATPRO. Predicted burst temperature represents the mean value of the FRAIL distribution obtained at the measured pressure. Conversely, predicted burst stress is the expected FRAIL value at the measured burst temperature. Data common to both the FRAIL and verification data sets have been labeled as such. Results of this data comparison show more consistency between measured and predicted conditions of rupture than was shown by the MATPRO analysis. It seems worthwhile to expand the mechanical response model based on this capability for predicting physical conditions associated with observed cladding failure events. Consequences of failure in terms of strain measurements could be statistically evaluated at various temperature and stress conditions in an attempt to arrive at the operant σ - ε form or alternate strain relationship.

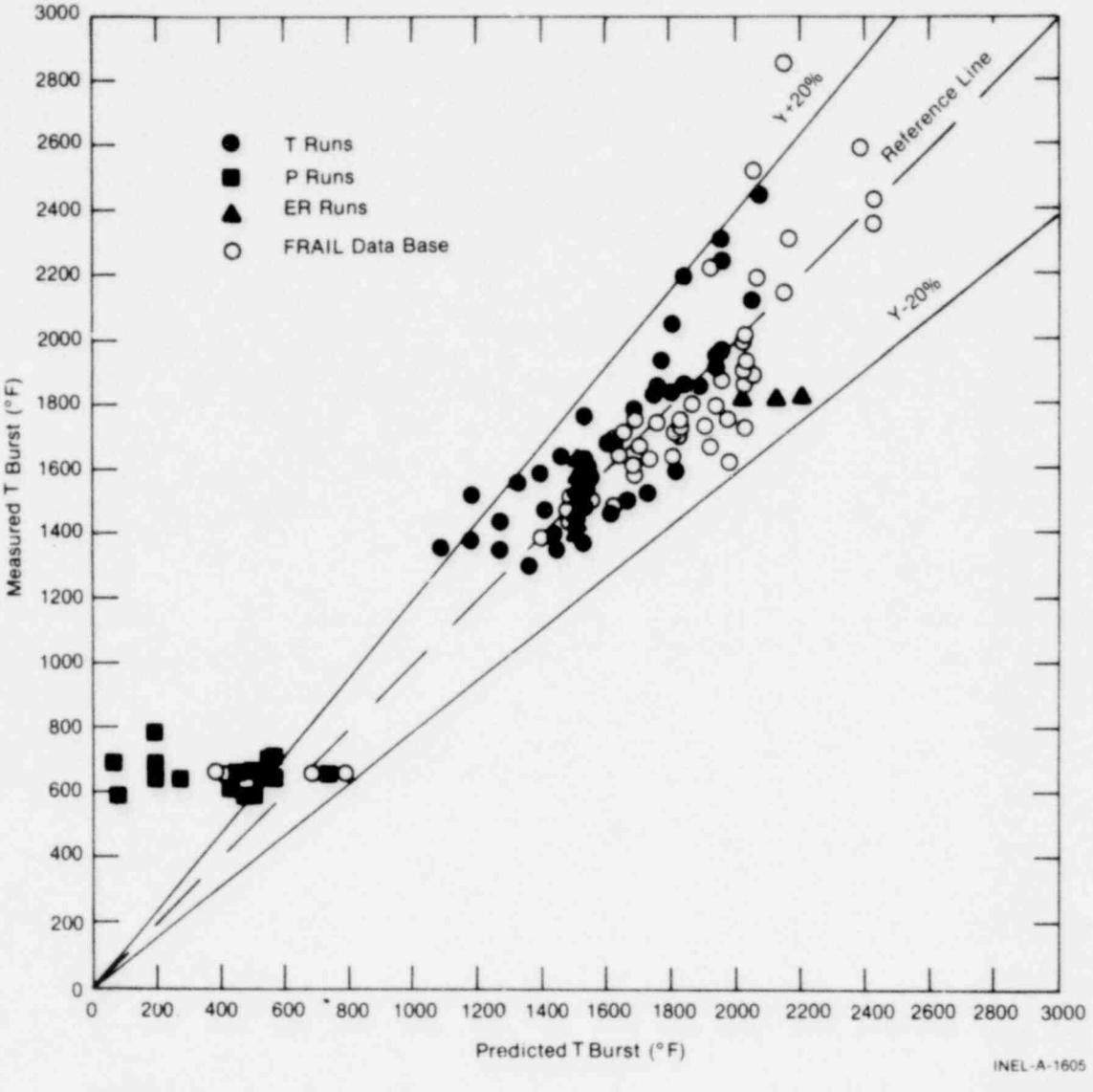

Fig. 52 FRAP-T3 measured versus predicted burst temperature at the measured burst pressure - FRAIL model.

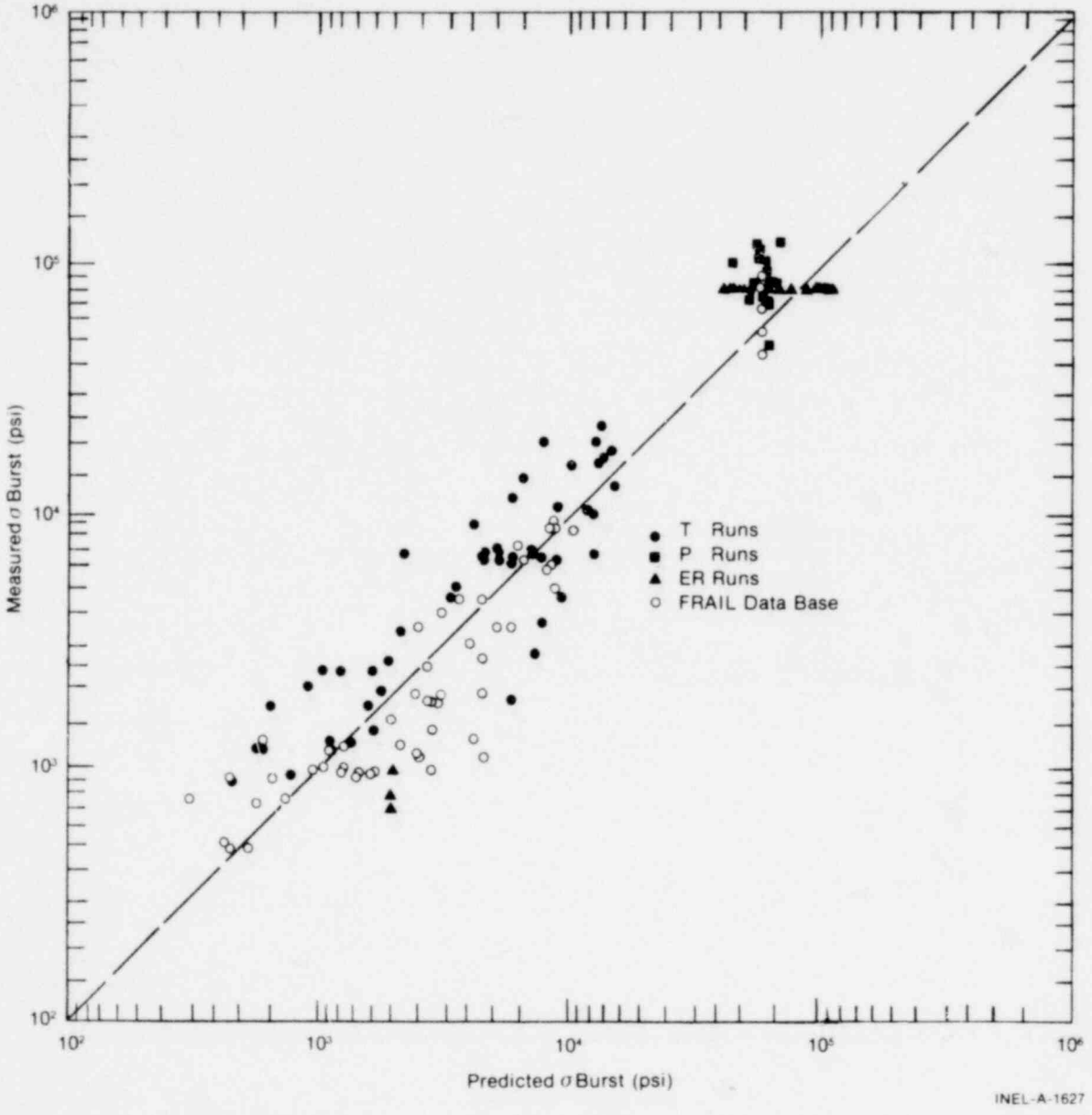

Fig. 53 FRAP-T3 measured versus predicted burst pressure at the measured burst temperature - FRAIL model.

VIII. REFERENCES

1. J. A. Dearien et al, *FRAP-T2: A Computer Code for the Transient Analysis of Oxide Fuel Rods - Vol. I - Analytical Models and Input Manual*, TREE-NUREG-1041 (February 1977).

2. P. E. MacDonald et al, *MATPRO Material Properties Library - Version 005*, ANCR-1263 (June 1975).

3. D. R. Coleman and E. T. Laats, *FRAP-T2: A Computer Code for the Transient Analysis of Oxide Fuel Rods - Report II - Model Verification Report*, TREE-NUREG-1041 (February 1977).

4. P. E. MacDonald et al, *MATPRO: A Handbook of Materials properties for Use in Analysis of Light Water Reactor Fuel Rod Behavior*, TREE-NUREG-1005 (December 1976).

5. J. A. Dearien et al, *FRAP-S2: A Computer Code for Steady State Analysis of Oxide Fuel Rods - Vol. I - Analytical Models and Input Manual*, TREE-NUREG-1107, July 1977.

6. D. R. Coleman and E. T. Laats, *FRAP-S2: A Computer Code for Steady State Analysis of Oxide Fuel Rods - Vol. III - Model Verification Report*, TREE-NUREG-1107, July 1977.

7. G. Kjaerheim and E. Rolstad, *In-Pile Determination of UO_2 Thermal Conductivity, Density Effects and Gap Conductance*, HPR-80, (1967).

8. M. J. F. Notley et al, *Measurements of the Circumferential Strains of the Sheathing of UO_2 Fuel Elements During Reactor Operation*, AECL-4072 (1972).

9. [a] M. J. Brakas, "Cladding Strain Measurements Using Strain Gauges," *Englarged Halden Programme Group Meeting, Sanderstolen, March 1973.*

[a] Halden Project use only.

10. E. T. Laats et al, *US-NRC-OECD Halden Project Fuel Behavior Test Program - Experiment Data Report for Test Assemblies IFA-226 and IFA-239*, ANCR-1270 (December 1975).

11. G. Kjaerheim and E. Rolstad, *In-Core Study of Fuel/Clad Interaction and Fuel Centre Temperature*, HPR-107 (1969).

12. Z. R. Martinson et al, *Power-Coolant-Mismatch Test Series, 8-1 Reduced Shroud Test*, TFBP-TR-109 (October 1975).

13. J. R. Larson et al, *Power-Cooling-Mismatch Test Series, CHF Scoping Test*, TFBP-TR-114 (March 1976).

14. R. W. Garner et al, *Gap Conductance Thermal Oscillator Feasibility Test 1-1*, TFBP-TR-108 (September 1975).

15. Z. R. Martinson et al, *Power-Cooling-Mismatch Test Series, Test PCM 8-1 RF, Test Results Report*, TFBP-TR-119 (June 1976).

16. G. W. Cawood et al, *Power-Cooling-Mismatch Test Series - Test PCM-2A, Test Results Report*, ANCR-NUREG-1347 (September 1976).

17. W. J. Quapp et al, *Irradiation Effects Test Series, Scoping Test 1*, TFBP-TR-110 (January 1976).

18. W. J. Quapp et al, *Irradiation Effects Test Series, Scoping Test 2 Test Results Report*, TFBP-TR-137 (September 1976).

19. K. Taketani and M. Ichikawa, "Fuel Irradiation Experiments by JAERI for Light Water Reactors," *Crest Specialist Meeting, Sacley, France, October 21-24, 1973.*

20. *OECD Halden Reactor Project Quarterly Progress Report, April to June 1971*, HPR-140 (August 1971).

21. *OECD Halden Reactor Project Quarterly Progress Report, July to September 1970*, HPR-128 (November 1970).

22. *OECD Halden Reactor Project Quarterly Progress Report, April to June 1972*, HPR-152 (August 1972).

23.[a] E. Kolstad, "The 3-Rod Diameter Rig Experiment IFA-404 I (HP) and IFA-404 II (HP)," *Enlarged Halden Programme Group Meeting, Geilo, Norway, March 16-21, 1975.*

24.[a] E. Kolstad and E. Rolstad, "The High Pressure Rig Experiment IFA-414 (N) In-Pile Results Obtained with First Test Rod, *Enlarged Halden Programme Group Meeting, Geilo, Norway, March 16-21, 1975.*

25.[a] E. Kolstad et al, "The High Pressure PWR Rig IFA-414(N), A Short Description of the Design and the Performance Characteristics," *Enlarged Halden Programme Group Meeting, Geilo, Norway, March 16-21, 1975.*

26. W. F. Domenico et al, *IFA-429 Data Report No. 1*, TREE-NUREG-1009 (December 1976).

27. C. R. Hann et al, "Experimental Verification of Nuclear Fuel Rod Stored Energy Calculations," *Enlarged Halden Programme Group Meeting, Sanderstolen, Norway, March 8-12, 1976.*

28.[a] *OECD Halden Reactor Project Quarterly Progress Report, April to June 1975*, HPR-187 (September 1975).

29. R. W. Garner and D. T. Sparks, *Gap Conductance Test Series, Test GC 1-3, Quick Look Report*, TFBP-TR-124 (May 1976).

30. Z. R. Martinson et al, *Power-Cooling-Mismatch Test Series, Test PCM-3, Quick Look Report*, TFBP-TR-129 (July 1976).

---

[a] Halden Project use only.

31. Z. R. Martinson et al, *Power-Cooling Mismatch Test Series, Test PCM-2, Quick Look Report*, TFBP-TR-120 (May 1976).

32.[a] B. Brzoska and P. Dewes, "Measurement and Analysis of Central Fuel Temperatures," *Enlarged Halden Program Group Meeting, Sanderstolen, Norway, March 1976.*

33. H. Mogard et al, "Power Increases and Fuel Defection," *Fourth Geneva Conference, 1971.*

34.[a] G. Lysell, "Overpower Experiments on IFA-4 Fuel Rods in R2 at Studsvik," *Enlarged Halden Programme Group Meeting, Sanderstolen, Norway, 1973.*

35. E. Rolstad and K. Svanholm, "Overpower-to-Failure Experiment on a High Burnup Fuel Rod," *BNES Conference, 1973.*

36.[a] E. Rolstad and K. Svanholm, "The IFA-229^{I} (N) Overpower-To-Failure Experiment on a High Burnup Fuel Rod," *Enlarged Halden Programme Group Meeting, Sanderstolen, Norway, 1973.*

37. OECD Halden Reactor Project, *Fourteenth Annual Report* (1973).

38. S. Djurle et al, "Some Irradiation Studies of Fuel/Clad Interaction and Clad Cracking," *Fourth Geneva Conference, 1971.*

39. S. Djurle and H. Taylor, *Post-Irradiation Evaluation of the Third Swedish Fuel Assembly, IFA-21, Irradiated in the Halden Boiling Water Reactor*, HPR-114 (1969).

40. P. Knudsen et al, "Power Ramp Test With a PWR Fuel Pin," *Atomwirtschaft 514*, (October 1975).

---

[a] Halden Project use only.

41.[a] K. Svanholm, "The Overpower Tests on IFA-405 (HP)," *Enlarged Halden Programme Group Meeting, Geilo, Norway, 1975.*

42.[a] I. Ruyter, "Analysis of the German IFA-407[II] Overpower Experiment," *Enlarged Halden Programme Group Meeting, Geilo, Norway 1975.*

43.[a] OECD Halden Reactor Project, *Quarterly Progress Report,* HPR-165 (July to September 1973).

44. P. Knudsen et al, "Overpower Testing of UO_2-Zr Fuel Pins at 20,000 and 35,000 MWd/t," *Atomwirtschaft 140, March 1974.*

45. G. Lysell and G. Valli, "Overpower Ramp Tests on CIRENE Prototype Fuel Pins," *BNES Conference, 1973.*

46. N. Hansen, "Risø Power Ramp Experience," *Fourth Water Reactor Safety Research Information Meeting, September 27-30, 1976.*

47.[a] K. Svanholm, "Overpower Tests in IFA-405 III," *Enlarged Halden Programme Group Meeting, Sanderstolen, Norway, March 8-12, 1976.*

48. W. Redpath, "Winfrith SGHWR In-Reactor Dryout Tests," *BNES Journal,* (1973) pp 87-97.

49. E. Rolstad and G. Kjaerheim, "BWR Burnout Experiments," *Nuclear Engineering International* (December 1968).

50. OECD Halden Reactor Project, *Ninth Annual Report* (1968).

51. OECD Halden Reactor Project, *Twelfth Annual Report* (1971).

52. OECD Halden Reactor Project, *Eleventh Annual Report* (1970).

---

[a] Halden Project use only.

53. OECD Halden Reactor Project, *Thirteenth Annual Report* (1972).

54. OECD Halden Reactor Project, *Tenth Annual Report* (1969).

55. HBWR Quarterly Progress Report, HPR-117 (October to December 1969).

56. OECD Halden Reactor Project, *Quarterly Progress Report*, HPR-156 (July to September 1972).

57. J. G. Crocker et al, *PCM-20 8-l RS Quick Look Report*, TFBP-TR-159 (May 1975).

58.[a] E. Kolstad, "Temperature and Stored Heat Decrease in Fuel Rods Following a Reactor SCRAM," *Enlarged Halden Programme Group Meeting, Geilo, Norway, 1975.*

59.[a] T. J. Bjorlo, "Application of the Thermal Models STTEMP and TRTEMP for Analysis of In-Pile Fuel Temperature Measurements," *Enlarged Halden Programme Group Meeting, Sanderstolen, Norway, March 1976.*

60. R. A. Lorenz et al, *Final Report on the First Fuel Rod Failure Transient Test of a Zircaloy-Clad Fuel Rod Cluster in TREAT*, ORNL-4635 (1971).

61. R. A. Lorenz and G. W. Parker, *Final Report on the Second Fuel Rod Failure Transient Test of a Zircaloy-Clad Fuel Rod Cluster in TREAT*, ORNL-4710 (1972).

62. E. E. Juenke and J. F. White, *Physical-Chemical Studies of Clad UO_2 Under Reactor Accident Conditions*, GEMP-731 (1970).

63. J. B. Melehan, *Yankee Core Evaluation Program, Final Report*, WCAP-3017-6094 (1971).

---

[a] Halden Project use only.

64. W. R. Smalley, *Saxton Core II Fuel Performance Evaluation, Part I. Materials*, WCAP-3385-56 (1971).

65. M. G. Balfour (ed.), *Post-Irradiation Examination of CVTR Fuel Assemblies. Semi-Annual Progress Report for the Period Ending June 30, 1968*, WCAP-3850-3 (1968).

66. F. A. Schraub and R. G. Bock, *Fuel Rod Failures During Simulated Loss-of-Coolant Conditions*, APED-5479 (1968).

67. M. F. Osborne and G. W. Parker, *Effect of Irradiation on the Failure of Zircaloy-Clad Fuel Rods*, ORNL-TM-3626 (1972).

68. T. Furuta et al, *Deformation and Inner Oxidation of the Fuel Rod in a Loss-of-Coolant Accident Conditions*, NR-TR-005, JAERI-M-6339 (November 1975).

69. A. A. Bauer et al, "Evaluating Strength and Ductility of Irradiated Zircaloy," *Quarterly Progress Report, January - March 1976.* BMI-NUREG-1948 (March 1976).

70. H. M. Chung et al, "Deformation and Rupture Behavior of Zircaloy Cladding Containing Oxygen Under Simulated Loss-of-Coolant Accident Conditions," *Symposium on Zirconium in the Nuclear Industry, Quebec City, Quebec, Canada, August 10-12, 1976.*

71. R. H. Chapman, *Multirod Burst Test Program Quarterly Progress Report for July-September 1975*, ORNL-TM-5154 (December 1975).

72. R. H. Chapman, *Multirod Burst Test Program Quarterly Progress Report for October-December 1975*, ORNL/NUREG/TM-10 (May 1976).

73. E. E. L. Hunt et al, *The Effect of Steam Oxidation on the Strain of Fuel Sheathing at High Temperature*, AECL-5559 (August 1976).

74. F. Erbacher et al, "Out-of-Pile Experiments on Ballooning in Zircaloy Fuel Rod Claddings in the Low Pressure Phase of a Loss-of-Coolant-Accident," *Specialists Meeting on the Behavior of Water Reactor Fuel Elements Under Accident Conditions, Spatind, Norway, September 13-16, 1976.*

75. H. G. Weidinger et al, "LOCA Fuel Rod Behavior of KWU-Pressurized Water Reactors," *CSNI Specialist Meeting on the Behavior of Water Reactor Fuel Elements Under Accident Conditions, Spatind, Norway, September 13-16, 1976.*

76. M. Bocek and M. Fischer, "Cladding Reserach in Germany," *Summary of Paper Presented at the USNRC Fourth Water Reactor Safety Research Information Meeting, Washington, D.C., September 27-30, 1976.*

77. E. D. Hindle and J. A. S. Mowat, *The Effect of Oxygen Uptake on the Deformation and Rupture on SGHWR Fuel Cladding*, TRG Report 2899(S) (August 1976).

78. I. Devold, *A Study of the Temperature Distribution in UO_2 Reactor Fuel Elements*, AE-318, (1968).

79. T. G. Odekirk, *Detailed Test Plan Report for PBF Test PCM-20: The Behavior of Unirradiated PWR Fuel Rods Under Power-Cooling-Mismatch Conditions*, ANCR-1095 (April 1974).

80. B. Spinrad, "OSU Decay Heat Studies," *USNRC Fourth Water Reactor Safety Research Information Meeting, Washington, D.C., September 27-30, 1976.*

81. D. S. Rowe, *COBRA-IIIC: A Digital Computer Program for Steady State and Transient Thermal-Hydraulic Analysis of Rod Bundle Nuclear Fuel Elements*, BNWL-1695 (1973).

82. D. R. Coleman, FRAP-S1: *A Computer Code for Steady State Analysis of Oxide Fuel Rods, Vol III, Model Verification Report, SSRD-6-76, September 1975*, (Public Document Room).